20 May 2011 | $10

Science

AAAS

CONTENTS continued >>

page 908

page 918

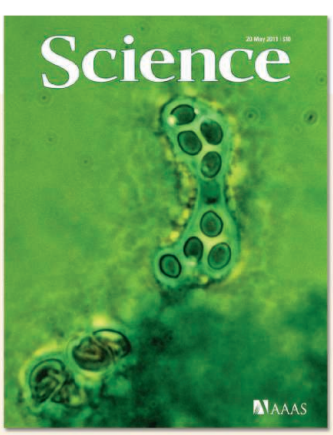

COVER

Phase contrast photomicrograph of a *Schizosaccharomyces octosporus* ascus, a sac-like cell that typically contains eight spores (each ~2 micrometers across). *S. octosporus* and other fission yeasts are important models of eukaryote biology and have evolved a single-celled lifestyle independently from their budding yeast cousins. On page 930, Rhind *et al.* present a comparative genomic analysis of fission yeasts that sheds light on their genome structure and gene regulation.

Image: Dr. George Wilder/Visuals Unlimited, Inc.

DEPARTMENTS

RESEARCH ARTICLE

REPORTS

CONTENTS continued >>

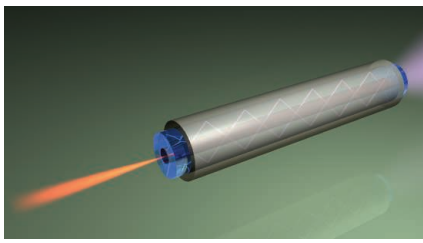

page 921

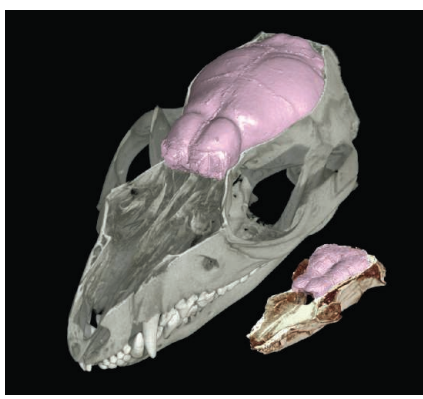

pages 926 & 955

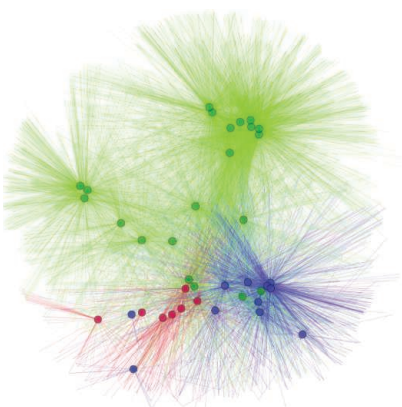

page 970

CREDIT: (MIDDLE PHOTO) UNIVERSITY OF TEXAS HIGH RESOLUTION CT FACILITY

SCIENCEONLINE

SCIENCEXPRESS

www.sciencexpress.org

The Visual Impact of Gossip
E. Anderson et al.
Negative gossip about a person renders that person's face more visible to the onlooker.
10.1126/science.1201574

Predicting a Human Gut Microbiota's Response to Diet in Gnotobiotic Mice
J. J. Faith et al.
Model microbial communities in mouse guts respond quickly and predictably to dietary shifts.
10.1126/science.1206025

Widespread RNA and DNA Sequence Differences in the Human Transcriptome
M. Li et al.
All 12 categories of discordances can be observed where the RNA sequence does not match that of the DNA.
10.1126/science.1207018

Thermal Structure and Dynamics of Saturn's Northern Springtime Disturbance
L. N. Fletcher et al.
Satellite and ground-based observations characterize a massive storm on Saturn and its effects on the atmosphere.
10.1126/science.1204774

Endotoxin-Induced Structural Transformations in Liquid Crystalline Droplets
I.-H. Lin et al.
Bacterial lipid A was detected by its interactions with defects in droplet-confined liquid crystals.
10.1126/science.1195639

The 2011 Magnitude 9.0 Tohoku-Oki Earthquake: Mosaicking the Megathrust from Seconds to Centuries
M. Simons et al.
10.1126/science.1206731

Shallow Dynamic Overshoot and Energetic Deep Rupture in the 2011 M_w 9.0 Tohoku-Oki Earthquake
S. Ide et al.
10.1126/science.1207020

Displacement Above the Hypocenter of the 2011 Tohoku-Oki Earthquake
M. Sato et al.
Detailed geophysical measurements reveal features of the 2011 Tohoku-Oki megathrust earthquake.
10.1126/science.1207401
>> News story p. 911

TECHNICALCOMMENTS

Comment on "Positive Selection of Tyrosine Loss in Metazoan Evolution"
Z. Su et al.
Full text at www.sciencemag.org/cgi/content/full/332/6032/917-a

Response to Comment on "Positive Selection of Tyrosine Loss in Metazoan Evolution"
C. S. H. Tan et al.
Full text at www.sciencemag.org/cgi/content/full/332/6032/917-b

SCIENCENOW

www.sciencenow.org
Highlights From Our Daily News Coverage

Bright Lights, Rich Cities
Satellite images of nighttime lights could help economists model GDP in regions where it is poorly reported.
http://scim.ag/bright-lights

Controversial Computer Is at Least a Little Quantum Mechanical
Skepticism of the system remains, however.
http://scim.ag/quantum-computer

Mice Reject Reprogrammed Cells
Finding underscores challenges of using iPS cells as a potential therapy for humans.
http://scim.ag/ips-rejection

SCIENCESIGNALING

www.sciencesignaling.org
The Signal Transduction Knowledge Environment
17 May issue: http://scim.ag/ss051711

RESEARCH ARTICLE: Ca^{2+} Signaling Tools Acquired from Prostasomes Are Required for Progesterone-Induced Sperm Motility
K.-H. Park et al.

PERSPECTIVE: Calcium Signaling in Sperm—Help from Prostasomes
D. Ren
Proteins involved in calcium signaling are delivered to sperm through fusion with prostate-derived vesicles.

RESEARCH ARTICLE: Stomatal Closure by Fast Abscisic Acid Signaling Is Mediated by the Guard Cell Anion Channel SLAH3 and the Receptor RCAR1
D. Geiger et al.
Plant survival during periods of drought may involve SLAH3, a nitrate-conducting anion channel activated by abscisic acid.

PRESENTATION: Network-Based Tools for the Identification of Novel Drug Targets
I. J. Farkas et al.
Analysis of network topology and dynamics holds promise for identifying new sets of potential drug targets.

SCIENCECAREERS

www.sciencecareers.org/career_magazine
Free Career Resources for Scientists

Focus on Aging: Engineering Safer Drivers
L. Chiu
MIT engineer Bryan Reimer designs systems to monitor and improve drivers' performance behind the wheel.
http://scim.ag/aging-engineering

Tooling Up: I've Got a Great Idea
D. Jensen
Two recent entrepreneurs offer advice on starting a new company.
http://scim.ag/startup_success

SCIENCETRANSLATIONAL MEDICINE

www.sciencetranslationalmedicine.org
Integrating Medicine and Science
18 May issue: http://scim.ag/stm051811

EDITORIAL: NCATS Purrs—Emerging Signs of Form and Function
G. A. FitzGerald
Derisking and repurposing therapeutics will be among the aims of the National Center for Advancing Translational Science.

RESEARCH ARTICLE: Functional Regulatory T Cells Produced by Inhibiting Cyclic Nucleotide Phosphodiesterase Type 3 Prevent Allograft Rejection
G. Feng et al.

RESEARCH ARTICLE: Massive ex Vivo Expansion of Human Natural Regulatory T Cells (T_{regs}) with Minimal Loss of in Vivo Functional Activity
K. L. Hippen et al.

RESEARCH ARTICLE: Human Regulatory T Cells with Alloantigen Specificity Are More Potent Inhibitors of Alloimmune Skin Graft Damage than Polyclonal Regulatory T Cells
P. Sagoo et al.

PERSPECTIVE: Regulatory T Cells—Customizing for the Clinic
X. Wang et al.
A collection of new data provides a platform for clinical use of regulatory T cells as personalized therapeutic agents.

SCIENCEPODCAST

www.sciencemag.org/multimedia/podcast
Free Weekly Show

On the 20 May *Science* Podcast: diet and mammalian gut microbiomes, the science of alchemists, inquiry-based writing, and more.

SCIENCEINSIDER

news.sciencemag.org/scienceinsider
Science Policy News and Analysis

SCIENCE (ISSN 0036-8075) is published weekly on Friday, except the last week in December, by the American Association for the Advancement of Science, 1200 New York Avenue, NW, Washington, DC 20005. Periodicals Mail postage (publication No. 484460) paid at Washington, DC, and additional mailing offices. Domestic individual membership and subscription (51 issues): $149 ($74 allocated to subscription). Domestic institutional subscription (51 issues): $990; Foreign postage extra: Mexico, Caribbean (surface mail) $55; other countries (air assist delivery) $85. First class, airmail, student, and emeritus rates on request. Canadian rates with GST available upon request, GST #1254 88122. Publications Mail Agreement Number 1069624. **Printed in the U.S.A.**

Change of address: Allow 4 weeks, giving old and new addresses and 8-digit account number. **Postmaster:** Send change of address to AAAS, P.O. Box 96178, Washington, DC 20090–6178. **Single-copy sales:** $10.00 current issue, $15.00 back issue prepaid includes surface postage; bulk rates on request. *Science* is indexed in the *Reader's Guide to Periodical Literature* and in several specialized indexes.

AAAS
ADVANCING SCIENCE, SERVING SOCIETY

Dissecting the Spikemoss Genome

The lineage to modern lycophytes (club mosses, quilworts, and spikemosses) diverged from that of flowering plants long ago. **Banks *et al.*** (p. 960, published online 5 May) have now sequenced the genome of the lycophyte, *Selaginella moellendorffii*, whose genome, compared to other plants, is particularly compact at 110 megabase pairs. The gene density is similar to that of *Arabidopsis*, but the genome does not carry traces of polyploidization. This analysis of the genome lends insight into unique deployments of small RNA and RNA editing functions, and hints at the evolutionary transitions needed to go from nonvascular to vascular plants.

Understanding Yeast

Fission yeast, *Schizosaccharomyces pombe*, is a key model eukaryote that has been studied in context of its distant relationship to other organisms. **Rhind *et al.*** (p. 930, published online 21 April; see the cover) compared genome sequences of four fission yeast species, including *S. pombe*. Transposon structure and number differ significantly among species, and—while gene content, gene structure, and gene order are conserved—the degree of amino acid substitution is high. Antisense transcription was enriched for meiotic genes, suggesting that these transcripts may help to coordinate their expression. Furthermore, regulatory motif evolution and innovations in gene content and regulation may underlie the parallel evolution of ethanol metabolism in fission and budding yeast.

CREDITS (TOP TO BOTTOM): JING-KE WENG; FRANKE *ET AL.*

Prescribing Order

Interfaces between transition metal oxides exhibit a wide range of behavior; insulating, metallic, magnetic, and superconducting behaviors can all be induced by a gate voltage. Moving into bulk systems, **Boris *et al.*** (p. 937; see the Perspective by **Hammerl and Spaldin**) found that varying the thickness and number of layers of a heterostructure of thin $LaNiO_3$ and $LaAlO_3$ layers could control the dimensionality of the superlattice. This approach provides a route to manipulate the collective behavior of charge and spin order within metal oxide superlattice systems.

Organic Devices Find a Closer Match

Indium tin oxide (ITO) electrodes are transparent and robust and are often used as an electrode in many organic devices, such as light-emitting diodes (LEDs). **Helander *et al.*** (p. 944, published online 14 April) report a method for chlorinating ITO that increases its work function—the energy needed to emit an electron—so that the electron energy better matches that of the typical organic active layers. The need to use multiple layers of different materials to build a stepwise charge injection process is avoided, and device efficiency for green organic LEDs is high.

Indecisive Magnetic Interactions

A magnetic atom adsorbed on the surface of a superconductor could undergo two different types of interactions: It could be screened by free electrons that remain in the normal metal state through the Kondo effect, or it could couple with electron pairs of the superconducting state. **Franke *et al.*** (p. 940) used scanning tunneling microscopy and spectroscopy to study manganese phthalocyanine molecules adsorbed on a lead surface. Both types of magnetic ground state that could be produced through these interactions were observed. The states alternated spatially on nanometer length scales and formed a superstructure with a Moiré-like pattern.

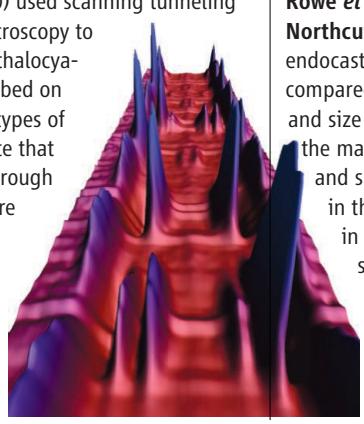

The Fingerprints of Tides

Ocean tides result in substantial variations of the amount of stress that is applied by the ocean to the sea floor and nearby continents. This stress can influence the motion of the crust—a response that could be used to determine properties of Earth's interior. By monitoring the response of Earth's crust to the tides with a dense Global Positioning System array, **Ito and Simons** (p. 947, published online 14 April) determined the regional structure of the mantle below the western United States. The crustal motion data are compatible with independent seismic data and provide direct estimates of previously inaccessible properties such as density.

Ozone and Rainfall

The widespread commercial and industrial use of chlorofluorocarbons during the second half of the 20th century caused a stratospheric ozone hole over Antarctica. The resulting modification of the thermal structure of the atmosphere led to dynamic changes in atmospheric circulation both within the Antarctic atmospheric vortex and at lower latitudes. **Kang *et al.*** (p. 951, published online 21 April; see the Perspective by **Feldstein**) report on one of the consequences of this process—a summertime increase in precipitation in the southern subtropics. This change resulted from a poleward shift of the extratropical westerly jet in the Southern Hemisphere, illustrating the importance of the polar regions to the hydrology of the subtropics.

The Better to Smell You With

Mammals possess advanced olfactory and tactile senses. Enlargement of sensory regions in the mammalian brain reflect these specializations. **Rowe *et al.*** (p. 955; see the Perspective by **Northcutt**) used x-ray tomography to create endocasts of two pre-mammal species and compared these to existing data on brain shape and size in extinct and extant species within the mammalian lineage. Brain enlargement and specialization in mammals proceeded in three pulses. First, there was an increase in the ability to perceive and process sensory cues, including tactile stimuli through body hair and olfactory cues from the environment. This was followed by improved neuromuscular coordination, and finally, in the first

Continued on page 893

Continued from page 891

true mammals, development of nasal architecture increased the surface area available for olfactory receptors and water balance.

Black or Light

The evolution and spread of industrial melanism in the peppered moth (*Biston betularia*) is one of the most well known examples of evolution by natural selection. However, the genetic basis of the polymorphism remains unclear, as does whether the melanic form evolved once or multiple times. **Van't Hof *et al.*** (p. 958, published online 14 April) go some way to answering these questions by mapping the *carbonaria* locus, which shows that all melanic individuals carry the same haplotype. This finding suggests the rapid spread of the melanic form from a single mutation event. Furthermore, the genomic region responsible for the polymorphism also explains wing pattern and color variation in other lepidopteran species.

Break Down to Build Up

At certain points during development and aging, cells appear to catabolize their own constituents in order to provide the amino acids required for new protein synthesis. **Narita *et al.*** (p. 966, published online 21 April; see the Perspective by **Zoncu and Sabatini**) identified a protein recycling factory that can be formed to enhance protein synthesis in order to facilitate en masse secretion. This mTOR-autophagy spatial coupling compartment allows the simultaneous activation of both mTOR and autophagy, leading to concurrent protein synthesis and degradation and significantly enhancing protein turnover.

Tolerance by TLR

Our bodies harbor over a billion bacteria, the majority of which are commensal rather than pathogenic. Why does the immune system attack only pathogenic bacteria? **Round *et al.*** (p. 974, published online 21 April) examined the underlying immune mechanisms that allow for the colonization of colonic mucosal tissue by the human commensal, *Bacteroides fragilis*. In germ-free mice and in mice colonized with only *B. fragilis*, the *B. fragilis*–secreted molecule, polysaccharide A, signaled through Toll-like receptor 2 (TLR2) to promote immune tolerance. This finding is rather unexpected because TLR2 signaling is typically associated with immune activation and bacterial clearance. Thus, commensal bacteria may produce factors that promote tolerance by signaling through classical innate immune response pathways.

Reconstituting Nucleosome Positioning

Nucleosomes occupy specific defined positions around the transcription start sites of many genes, and up to half of all specific nucleosome positions are defined by the underlying DNA sequence. To determine whether histones and DNA are sufficient to determine proper nucleosome positions, **Zhang *et al.*** (p. 977) reconstituted chromatin in vitro. Most nucleosome positions were not predominantly sequence-intrinsic, nor were they determined by statistical positioning, where fixed barriers act as guides, nor were they driven by transcription. Rather, reconstitution of nucleosome position and occupancy level around the 5′ ends of many yeast genes required the presence of whole-cell extract and adenosine triphosphate (ATP), implying that an ATP-driven chromatin remodeler is involved.

Ribosome Times Two

The ribosome is the molecular machine responsible for protein synthesis. During synthesis, a ratchet-like rotation of the small ribosomal subunit relative to the large subunit facilitates translocation of messenger RNA (mRNA) and transfer RNA (tRNA). A key intermediate is a hybrid state in which tRNA is bound simultaneously to the peptidyl-tRNA site (P-site) on the small subunit and to the exit site (E-site) on the small subunit. **Dunkle *et al.*** (p. 981) describe two high-resolution structures of the *Escherichia coli* ribosome. The first positions tRNA in the P-sites of both the small and large subunits. The second has tRNA bound in the P/E state, stabilized by the ribosome recycling factor. Together, the structures provide insight into the ratcheting mechanism of the ribosome.

CREDIT: ILIK SACCHERI

David J. Asai is director of the Precollege and Undergraduate Science Education Programs for the Howard Hughes Medical Institute, Chevy Chase, MD.

Measuring Student Development

FOR THE PAST TWO DECADES, FUNDING ORGANIZATIONS SUCH AS MINE HAVE SUPPORTED initiatives at U.S. colleges and universities with the goal of transforming undergraduate science education. Now it is time to ask the tough questions: How effective have these efforts been? How can educators and funders build on the lessons learned? Undergraduate education is an absolutely critical enterprise. Regardless of the future profession that a student chooses, this is the time when undergraduates acquire the fundamental skills for making creative contributions to society, including the process of scientific thinking that will empower them to be more effective citizens.

The achievements over the past 20 years have identified some key practices that contribute to a successful science education program. Research experiences ensure that students truly understand what it's like to be a scientist, an impact that is reinforced through incremental achievements and longer-term success, such as publishing results. Interdisciplinary research and curricula need to be more than the sum of the individual disciplines, and making room for new ways of teaching requires doing away with the old ways. And U.S. colleges and universities can use outreach, such as professional development for early education and precollege (K-12 grades) teachers, to inspire and prepare undergraduates to become science teachers themselves.

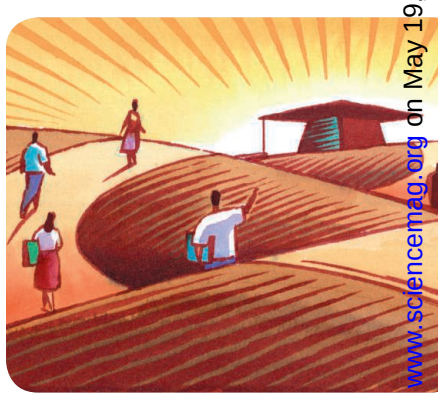

To move to the next level of strengthening science education, more sophisticated assessments are needed of programs that attempt to improve the undergraduate science experience. Counting up participants can gauge a program's scale, but not its impact on developing scientific abilities. Selecting students based on their past achievements is relatively straightforward. But what happens after a student arrives on campus? How well do the faculty and programs enable the student to develop, and how much does that student change relative to his or her potential? Education programs must be evaluated for their ability to reach key goals. An effective program should enable students to demonstrate an understanding of the process of science, regardless of their academic discipline. Therefore, a student's ability to formulate a hypothesis, design a meaningful experiment, deal with uncertainty, critically evaluate evidence, and engage in effective discourse should be measured.

Persistence is another challenge. The minority and majority undergraduates who enter U.S. colleges and universities with similar precollege education backgrounds have similar graduation rates. But the minority students switch from science to nonscience majors at a rate more than twice that of the majority students.* Educators and funders need to understand why students leave science, and create strategies that encourage students from all backgrounds to succeed as science majors.

A few organizations seek to understand and measure which components of undergraduate science education programs are most successful. Last month, the Howard Hughes Medical Institute (HHMI) invited primarily undergraduate institutions to compete for up to $60 million in science education grants. With nearly 25 years of experience in supporting undergraduate science education, HHMI can now ask applicants to evaluate the impact of their programs by measuring student development rather than simply counting beings. Over the long run, we hope that this new emphasis will provide better information about what strategies succeed in developing better scientists, science teachers, and a more science-literate society. Only if institutions approach the evaluation of teaching and learning as a science—that is, by creating continuous improvement cycles through information gained from research—will they be able to thoroughly engage the creative capacities of all students and to develop the interdisciplinary scientific thinkers that the world so badly needs.

– David J. Asai

10.1126/science.1207680

*G. Huang, N. Taddese, E. Walter, S. Peng. *Entry and Persistence of Women and Minorities in College Science and Engineering Education* (National Center for Education Statistics, U.S. Department of Education, Washington, DC, 2000).

Published by AAAS

EDITED BY KRISTEN MUELLER AND JAKE YESTON

EVOLUTION

Nitrogenase's Nascence

On early Earth, abiotic processes formed the initial supply of fixed (bioavailable) nitrogen necessary to maintain basic metabolic functions. As life began to flourish, this supply probably couldn't meet demand, and evolutionary pressures selected for a means of biological nitrogen fixation. How did the requisite enzymatic machinery—nitrogenase proteins that catalyze the reduction of N_2 into bioavailable ammonium—develop, and which microorganisms possessed it? By examining phylogenetic relationships between nitrogenases and other related proteins from modern bacteria and archaea (such as the one at left), Boyd *et al.* show that molybdenum (Mo)–dependent nitrogenases, which are currently the most common form of nitrogen-fixing enzymes, originated after vanadium- and purely iron-based variants. The first Mo-nitrogenase probably appeared 1.5 to 2.2 billion years ago in an ancestor of methanogenic archaea, and later transferred to bacteria through lateral gene transfer. At that time, the ocean was still adjusting to widespread oxygenation from oxygenic photosynthesis. Because the N_2 reduction is an anaerobic process, however, it must have occurred in anoxic layers of a stratified ocean, where fixed nitrogen was limited and Mo was available from oxidative weathering of the continents. — NW

Geobiology **9**, 221 (2011).

CELL SIGNALING

Finding NEMO in the Clock

Living organisms have intrinsic clocks that have an approximately 24-hour period. The specific biochemical mechanism that sets the pace of the clock, however, has not been fully described. Chiu *et al.* expand on earlier indications that changes in daily cycles of phosphorylation of PER (which recruits transcriptional repressors controlling the central transcriptional clock mechanism) can alter the period of the clock. Studies using cultured cells and genetically altered *Drosophila* showed that complex interactions of sequential phosphorylation of multiple clusters of phosphorylation sites on PER by multiple protein kinases dictated the rate at which PER became fully phosphorylated and thus targeted for degradation. The protein kinase NEMO was identified as being critical for an initial phosphorylation event that was permissive for further phosphorylation by the protein kinase DOUBLETIME. Intriguingly, NEMO functions (as do several regulators of the circadian clock) in the Wnt or Wingless signaling pathway. Yu *et al.* also implicate NEMO in pacing the *Drosophila* clock and found that NEMO is present in nuclear protein complexes with clock components PER, TIM, and CLK, and appears to influence phosphorylation and abundance of the transcriptional activator CLK. — LBR

Cell **145**, 357 (2011); *Curr. Biol.* **21**, 756 (2011).

PSYCHOLOGY

Ambiguous Evidence

Two of the methodologies used to compare the efficacies of treatments are randomized placement of participants in experimental studies and statistical or propensity matching of participants on confounding variables in observational studies. Both approaches have their proponents and might plausibly carry comparable weight in evidentiary assessments. Bastardi *et al.* developed a scenario in which a matching study (in comparison to a randomized one) was described as favoring home care of children to one group of participants, whereas a second group of participants received the information that the matching study favored day care. All of the participants were soon to become parents, and their preexisting belief was that home care was superior, although half of them were intending to use day care. When confronted with these scenarios in a crossed design, those who intended to use home care for their children did not judge one methodology to be more reliable than the other and maintained their stance about the superiority of home care. On the other hand, the internally conflicted participants (that is, those who intended to use day care) did regard the matching protocol as better when it favored day care, and this sufficed to shift their belief to the point where home care and day care were viewed as equivalent. — GJC

Psychol. Sci. **22**, 10.1077/0956797611406447 (2011).

BIOMATERIALS

TREEting Rheumatoid Arthritis

Rheumatoid arthritis is an autoimmune inflammatory disorder that can cause swelling of the joints, cartilage degradation, and eventual bone erosion. The immunological processes are controlled by a set of cytokines (cell signaling

CREDIT: DR. RACHEL A. FOSTER

Published by AAAS

molecules) that trigger an inflammatory response, diminish anti-inflammatory responses, and promote the differentiation of monocytes into osteoclasts. Current treatments, based on monoclonal antibodies and soluble receptors, typically target only the proinflammatory cytokines. Hayder *et al.* synthesized dendrimers—highly branched tree-like polymers—in which the outer branches were capped with azabisphosphonate (ABP), which has been shown to selectively target monocytes in culture. These dendrimers were tested in mice with a deficiency in the interleukin-1 receptor antagonist and in mice undergoing K/BxN serum transfer, which are two established inflammatory arthritis models. At the highest doses tested (1 and 10 mg/kg), intravenous injections completely suppressed inflammation, as evidenced by a decrease in paw swelling and little or no damage to the synovial fluid and cartilage in the ankle joints. Further tests using ex vivo human synovial tissue and human peripheral blood monocytes in vitro showed that the ABP dendrimers prevented the conversion of monocytes into osteoclasts. Because the dendrimers promote anti-inflammatory responses in addition to preventing bone loss, they may prove more effective than current treatments for rheumatoid arthritis. — MSL

Sci. Transl. Med. **3**, 81ra35 (2011).

CELL BIOLOGY

New Actions for Actin

Actin is a major component of the cytoskeleton and regulates fundamental cellular processes such as cell motility, cell division, and organelle movement. Actin is also present in the nucleus, participating in transcription, chromatin remodeling, and nuclear export, although additional roles for nuclear actin are still being defined. In a search for factors that regulate cellular reprogramming of differentiated cells into pluripotent cells, Miyamoto *et al*. identified nuclear actin as a candidate cell reprogramming factor. When somatic nuclei were transplanted into amphibian oocytes, filamentous actin localized to the nuclear envelope. One day after nuclear transfer, filamentous actin was detected in the transplanted nucleus. Polymerized nuclear actin was required for the transcriptional reactivation of *Oct4*, which is critical for cellular reprogramming. The actin signaling protein Toca-1 enhanced polymerization of actin and stimulated *Oct4* reactivation. Actin bound to RNA polymerase and the chromatin complex BAF, suggesting that it may regulate gene expression by promoting transcription and chromatin remodeling. — BAP

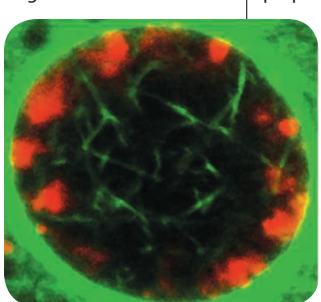

CREDIT: MIYAMOTO *ET AL.*, *GENES DEV.* **25**, 946 (2011)

Genes Dev. **25**, 946 (2011).

GENETICS

Pseudo Regulators No More

For many years, pseudogenes were thought to just be "junk" DNA: present in the genome but noncoding and therefore without function. Many recent studies now indicate that this is not the case, and studies in mice and rice suggest that pseudogenes generate small RNAs that have regulatory function. Wen *et al.* investigated pseudogene expression in the ancient eukaryote *Trypanosoma brucei*, a significant human pathogen. Earlier studies suggested that *T. brucei* pseudogenes were important for generating chimeric genes for antigenic variation and immune escape, but it appears that by pairing with the complementary coding gene, pseudogenes in *T. brucei* generate small RNAs that modulate the expression of the coding gene by RNA interference. The pseudogene-derived siRNAs appear to regulate genes of diverse functions, including genes involved in metabolic processes. This discovery in an ancient protist, as well as in mice and plants, indicates that pseudogene-RNAi regulation is widespread among eukaryotes. — CA

Proc. Natl. Acad. Sci. U.S.A. **108**, 10.1073/pnas.1103894108 (2011).

PHYSICS

Focusing On Disorder

The ability of high-end optical microscopes to image the smallest of features is very much dependent on the quality of the lenses. However, the preparation and milling of the best-quality lenses add a hefty premium to the cost. In a somewhat counterintuitive approach to improving resolving capability, van Putten *et al.* explore the use of lenses that are completely disordered. Laser light hitting such a disordered lens creates a random pattern, or speckle, of intense, highly focused spots. By manipulating the wavefront of the laser beam with a spatial light modulator before it hits the lens, the authors show that the multiple spots can be made coincident, thereby forming a spot smaller than that from a conventional lens. They then go on to demonstrate imaging of gold particles with sub–100-nm resolution. Such an adaptive optics approach might prove a useful and ultimately cheaper method of high-resolution microscopy. — ISO

Phys. Rev. Lett. **106**, 193905 (2011).

Published by AAAS

www.sciencemag.org

Science

1200 New York Avenue, NW
Washington, DC 20005
Editorial: 202-326-6550, FAX 202-289-7562
News: 202-326-6581, FAX 202-371-9227
Bateman House, 82-88 Hills Road
Cambridge, UK CB2 1LQ
+44 (0) 1223 326500, FAX +44 (0) 1223 326501

Subscription Services For change of address, missing issues, new orders and renewals, and payment questions: 866-434-AAAS (2227) or 202-326-6417, FAX 202-842-1065. Mailing addresses: AAAS, P.O. Box 96178, Washington, DC 20090-6178 or AAAS Member Services, 1200 New York Avenue, NW, Washington, DC 20005

Institutional Site Licenses please call 202-326-6755 for any questions or information

Reprints: Author Inquiries 800-635-7181
Commercial Inquiries 803-359-4578

Permissions 202-326-7074, FAX 202-682-0816

Member Benefits AAAS/Barnes&Noble.com bookstore www.aaas.org/bn; AAAS Online Store www.apisource.com/aaas/ code MKB6; AAAS Travels: Betchart Expeditions 800-252-4910; Apple Store www.apple.com/eppstore/aaas; Bank of America MasterCard 1-800-833-6262 priority code FAA3YU; Cold Spring Harbor Laboratory Press Publications www.cshlpress.com/affiliates/aaas.htm; GEICO Auto Insurance www.geico.com/landingpage/go51.htm?logo=17624; Hertz 800-654-2200 CDP#343457; Office Depot https://bsd.officedepot.com/portalLogin.do; Seabury & Smith Life Insurance 800-424-9883; Subaru VIP Program 202-326-6417; VIP Moving Services www.vipmayflower.com/domestic/index.html; Other Benefits: AAAS Member Services 202-326-6417 or www.aaasmember.org.

science_editors@aaas.org	(for general editorial queries)
science_letters@aaas.org	(for queries about letters)
science_reviews@aaas.org	(for returning manuscript reviews)
science_bookrevs@aaas.org	(for book review queries)

Published by the American Association for the Advancement of Science (AAAS), *Science* serves its readers as a forum for the presentation and discussion of important issues related to the advancement of science, including the presentation of minority or conflicting points of view, rather than by publishing only material on which a consensus has been reached. Accordingly, all articles published in *Science*—including editorials, news and comment, and book reviews—are signed and reflect the individual views of the authors and not official points of view adopted by AAAS or the institutions with which the authors are affiliated.

AAAS was founded in 1848 and incorporated in 1874. Its mission is to advance science, engineering, and innovation throughout the world for the benefit of all people. The goals of the association are to: enhance communication among scientists, engineers, and the public; promote and defend the integrity of science and its use; strengthen support for the science and technology enterprise; provide a voice for science on societal issues; promote the responsible use of science in public policy; strengthen and diversify the science and technology workforce; foster education in science and technology for everyone; increase public engagement with science and technology; and advance international cooperation in science.

Information for Authors
See pages 784 and 785 of the 11 February 2011 issue or access www.sciencemag.org/about/authors

AROUND THE WORLD

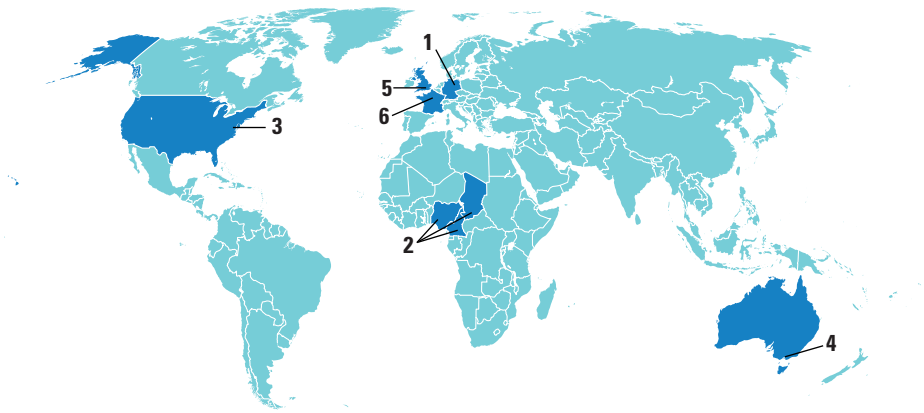

Berlin **1**

Ethics Commission Calls For Swift Nuclear Phaseout

Germany should phase out nuclear power by 2021, according to a leaked draft of a report from the Ethics Commission on Safe Energy Supply created by Chancellor Angela Merkel in the wake of the Fukushima catastrophe. The commission, chaired by two scientists and comprising representatives from industry, research, politics, and religion, recommends permanently shutting down the country's seven oldest nuclear reactors, followed by "a complete withdrawal from nuclear energy" within 10 years or less.

The seven reactors were taken off line shortly after problems started at Fukushima; the commission says this demonstrates that the 8.5 gigawatts they produce can be obtained elsewhere. Renewable energy, natural gas, and coal can take care of the rest without increasing Germany's carbon dioxide emissions or shaking the economy, the report says.

A law enacted in 2002 would have closed all of Germany's 17 nuclear power plants by 2023, but Merkel's coalition passed a new law last autumn that delayed that phaseout by more than a decade. The leaked report could change significantly before the official version is released at the end of the month. In any case, it is expected to strongly influence the direction the government takes. **http://scim.ag/german-nuclear**

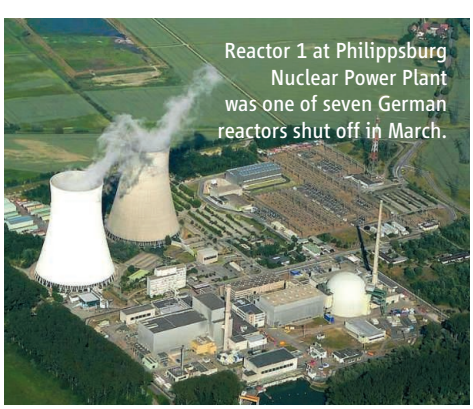
Reactor 1 at Philippsburg Nuclear Power Plant was one of seven German reactors shut off in March.

Cameroon, Chad, Nigeria **2**

More of New Meningitis Vaccine for Africa

An affordable, effective vaccine against deadly bacterial meningitis A will be rolled out in three more African countries this year, thanks to $100 million in new funds from the GAVI Alliance, a public-private global health partnership. Massive immunization campaigns will start in Cameroon, Chad, and Nigeria by December, ahead of the dry season when epidemics sweep across the so-called meningitis belt of Africa. MenAfriVac is the first vaccine developed specifically for Africa, at a price poor governments can afford—roughly 50 cents per dose. Since its initial introduction last year in Burkina Faso, Mali, and Niger, cases have dropped dramatically. "Men A has disappeared from Burkina Faso," says Marc LaForce, head of the Meningitis Vaccine Project, which developed the vaccine. LaForce hopes the donor community will commit enough money so that all 25 countries in the belt are covered by 2015.

Washington, D.C. **3**

NIH Grant Applicants Face Low Odds

U.S. National Institutes of Health (NIH) Director Francis Collins warned last week that the fraction of NIH grant applications that are funded this year could drop to 18% or 17%, the lowest percentage ever. The crash in so-called success rates comes because NIH's budget was cut by $322 million, or 1%, in last month's budget agreement for the current fiscal year. Collins's warning was part of his testimony to the Senate appropriations subcommittee that oversees NIH's budget. Subcommittee chair Senator Tom Harkin (D–IA) also worried about next year, noting that if a House of Representatives proposal to cut health spending by 9% prevails, "severe reductions to NIH research would be unavoidable." **http://scim.ag/low-odds**


Australia's budget plan doesn't address funding for the Australian Synchotron.

Melbourne, Australia **4**

Synchrotron Funding Up in the Air

When the Australian government released its new budget proposal last week, it didn't contain the drastic cuts many scientists had feared. But anxiety is still rippling through users of the Australian Synchrotron. Neither the federal government nor the Victoria state government, which also released budget plans recently, addressed how the world-class facility will be funded beyond June 2012, when its original 5-year financial plan ends. The bulk of the facility's funding comes from the two governments. Andrew Peele, a physicist at La Trobe University in Victoria who has been head of science at the synchrotron since late last year, says the facility's leadership had applied for additional government funding to expand the facility. He's hopeful a decision will be made soon. Long-term funding "is always an issue for major research institutions, [and] there are a number of alternatives," he says. **http://scim.ag/oz-synch**

London **5**

Astronomy, Particle Physics Cuts Decried

A U.K. parliamentary committee has warned that budget cuts planned for astronomy and particle physics will jeopardize Britain's ability to stay at the forefront of those disciplines.

CREDITS (TOP TO BOTTOM): DANIEL MENDELBAUM/STATE OF VICTORIA; LOTHAR NEUMANN, GERNSBACH/WIKIPEDIA

Published by AAAS

THEY SAID IT

"Climate change is occurring, is very likely caused primarily by the emission of greenhouse gases from human activities, and poses significant risks for a range of human and natural systems. Each additional ton of greenhouse gases emitted commits us to further change and greater risks."

—The National Research Council Committee on America's Climate Choices, in its fifth and final report to the United States Congress on climate change.

Although science in general was relatively well protected from severe government spending cuts announced last year, astronomy and particle physics took a big hit. A report released last week by the House of Commons Science and Technology Committee says the two fields will have 50% less funding in 2014–15 than they did in 2005.

The committee was particularly scathing about the decision to withdraw support from all ground-based optical and infrared telescopes in the Northern Hemisphere, noting that British astronomers will lose access to cutting-edge instruments and the country's reputation as an international partner could suffer. "The idea that subjects like astronomy and particle physics do not provide immediate economic returns and therefore can be sacrificed at the altar of cutbacks is nonsense," says committee chair Andrew Miller. Welcome words for Britain's big-science supporters, but the impact will be limited: the committee has no direct legislative power. **http://scim.ag/UKastro**

Paris **6**

Goodbye, Rinderpest

Animal health officials are about to report that rinderpest, which has decimated cattle herds for millennia, has been eradicated worldwide after a 17-year vaccination effort. On 25 May in Paris, the World Organization for Animal Health will certify the last eight countries, which include Micronesia, Sri Lanka, and Kazakhstan, as free of the disease. Then on 28 June in Rome, the governing body of the United Nations' Food and Agriculture Organization is expected to issue a declaration of global eradication. Rinderpest, a viral disease, was once endemic across Eurasia and Africa with periodic outbreaks killing calves and devastating herders. The virus was last detected in 2001 in Kenya. It will be the first animal disease to be eradicated and only the second disease in human history after smallpox.

FINDINGS

Is That Fish Worth Chasing?

Harbor seals in the murky North Sea rely on their whiskers to follow the wake a fish leaves behind. A new study reveals that whiskers can also gather detailed information about what the seal is hunting.

Biologist Wolf Hanke of the University of Rostock in Germany and colleagues worked with a harbor seal named Henry, a veteran research participant. First, they created wakes in a box of still water at the bottom of a pool using motorized paddles of different sizes; Henry waited outside the box wearing noise-blocking headphones and a blindfold. Once the paddle stopped, Henry dunked his front half inside and let the eddies swirl around his whiskers. He then pressed one of two buttons with his nose, indicating whether the wake had been made by one of three paddle sizes he'd been trained to recognize or by an unfamiliar one.

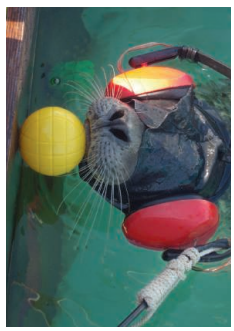

Henry chose correctly more than 90% of the time, as long as the familiar and unfamiliar paddles differed in width >>

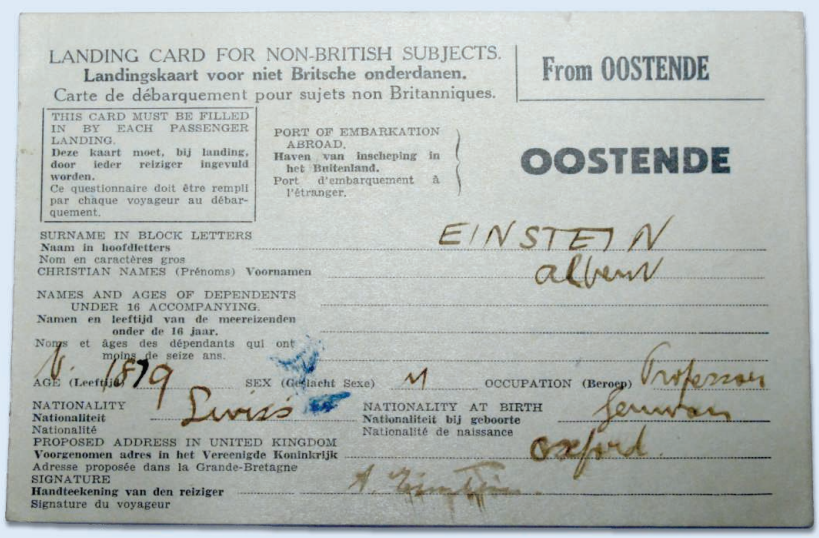
LANDING CARD FOR NON-BRITISH SUBJECTS.
Landingskaart voor niet Britsche onderdanen.
Carte de débarquement pour sujets non Britanniques.

From OOSTENDE

THIS CARD MUST BE FILLED IN BY EACH PASSENGER LANDING.
Deze kaart moet, bij landing, door ieder reiziger ingevuld worden.
Ce questionnaire doit être rempli par chaque voyageur au débarquement.

PORT OF EMBARKATION ABROAD, Haven van inscheping in het Buitenland, Port d'embarquement à l'étranger.
OOSTENDE

SURNAME IN BLOCK LETTERS
Naam in hoofdletters
Nom en caractères gros
EINSTEIN

CHRISTIAN NAMES (Prénoms) Voornamen
albert

NAMES AND AGES OF DEPENDENTS UNDER 16 ACCOMPANYING.
Namen en leeftijd van de meereizenden onder de 16 jaar.
Noms et âges des dépendants qui ont moins de seize ans.

AGE (Leeftijd) 1879
SEX (Geslacht Sexe) M
OCCUPATION (Beroep) Professor

NATIONALITY
Nationaliteit
Nationalité
Swiss

NATIONALITY AT BIRTH
Nationaliteit bij geboorte
Nationalité de naissance
German

PROPOSED ADDRESS IN UNITED KINGDOM
Voorgenomen adres in het Vereenigde Koninkrijk
Adresse proposée dans la Grande-Bretagne
Oxford

SIGNATURE
Handteekening van den reiziger
Signature du voyageur
A Einstein

Spacetime Souvenir

On 26 May 1933, a wild-haired German physics professor stepped off a ferry from Oostende, Belgium, and handed this landing card to border authorities in Dover, England. This year, museum curators on an artifact-hunting trip to a border agency office near Heathrow Airport found the card, signed by Albert Einstein, among the personal collections of immigration officers.

Einstein "already had his Nobel Prize," so the border agent who stamped it "might have thought, 'Ooh, I'll keep this,' " says Lucy Gardner, assistant curator at the Merseyside Maritime Museum in Liverpool, where the card went on display 10 May. On the card, Einstein records his nationality as Swiss; he had left Germany, where the Nazis had denounced his theory of relativity and burned his books, in 1932. He lists Oxford, where he would give a series of lectures, as his expected address. Later that year, Einstein immigrated to the United States, never to return to Germany.

CREDITS (TOP TO BOTTOM): MARINE SCIENCE CENTER, ROSTOCK; NATIONAL MUSEUMS LIVERPOOL

Published by AAAS

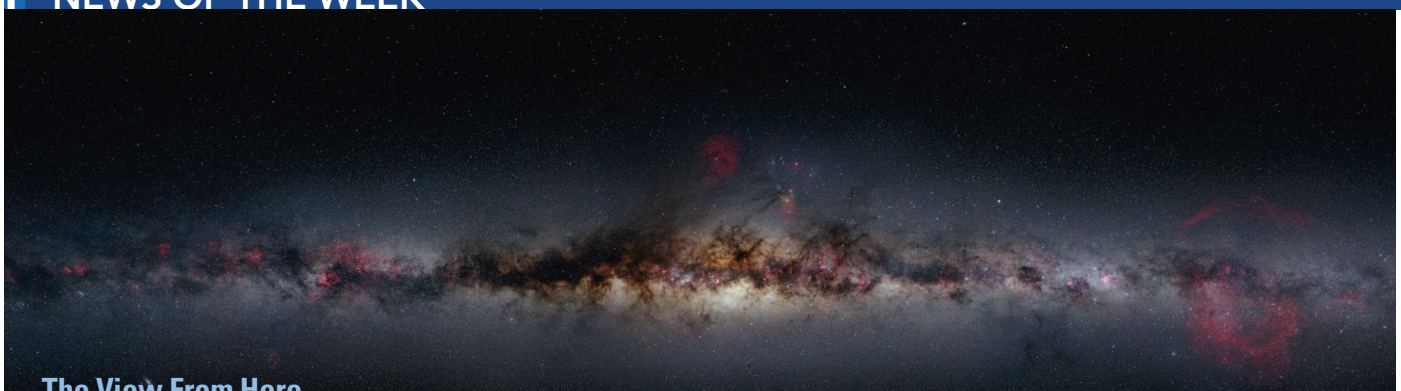

The View From Here

Ever wonder what the night sky would look like if all the stars grew thousands of times brighter? Go see for yourself at www.skysurvey.org.

The Photopic Sky Survey is the labor of love of amateur astronomer Nick Risinger, who quit his job as a marketing director in Seattle, Washington, and spent a year lugging sensitive cameras almost 100,000 kilometers around the United States and to South Africa. He then stitched together the 37,440 images to create the largest ever true-color sky survey—a zoomable, 360° panorama of the universe from Earth's point of view.

"Its main value is as an educational tool," Risinger says. But Jonathan McDowell, an astrophysicist at Harvard University, says astronomers could use the survey's 5000 megapixels to identify objects to observe. "The human eye is very good at spotting things that are unusual in shape or color," he says. "And of course, it's very pretty."

>>FINDINGS

by at least 4 cm, the team reported last week in *The Journal of Experimental Biology*. Laser-aided analysis of the eddies revealed that he could "read" information such as the width of the wake and its velocity—clues to the size of a passing fish, Hanke says, and whether it's worth chasing.

http://scim.ag/chase-fish

Mice Reject Reprogrammed Cells

Scientists have high hopes that stem cells called induced pluripotent stem (iPS) cells can be turned into replacement tissues for patients with injury or disease. Derived from a patient's own cells, scientists had assumed they wouldn't be rejected—a common problem with organ transplants. But a new study suggests otherwise.

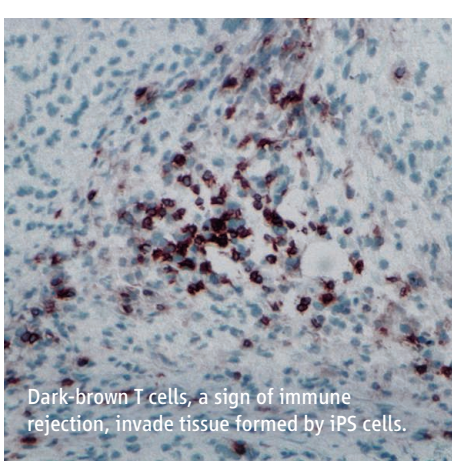

Dark-brown T cells, a sign of immune rejection, invade tissue formed by iPS cells.

Immunologist Yang Xu of the University of California, San Diego, and his colleagues implanted iPS cells, which are reprogrammed from adult cells, into mice that were genetically identical to the iPS cell donor. To the scientists' surprise, the cells were attacked by the recipients' immune systems and were rejected, the team reported online last week in *Nature*. The culprit seems to be incomplete reprogramming that leaves some genes in iPS cells misexpressed, Xu says.

The results add to a series of findings that iPS cells differ in subtle but potentially important ways from more controversial embryonic stem cells. Meanwhile, dozens of labs are working on ways to improve the reprogramming process so that the stray gene expression is eliminated.

http://scim.ag/iPSC-problems

HIV Treatment Prevents Heterosexual Transmission

HIV-infected people who start antiretroviral (ARV) treatment at earlier stages of the disease lowered their risk of transmitting the virus to their sexual partners by 96%, according to a multicountry study that ended abruptly last week.

The $73 million study by the U.S. National Institute of Allergy and Infectious Diseases recruited 1763 couples (97% heterosexual) in which only one partner was infected with the AIDS virus at the start. Half the participants received ARVs immediately, while the other half waited until their infections caused serious immune damage.

An analysis 6 years into the study, which was planned to last 10 years, found that 39 people had become infected, 28 from their regular partners. Of those 28, all but one had a partner in the group that waited to start treatment.

The dramatic result mirrors findings from less-rigorous earlier studies. Still, says Michel Sidibé, who heads the Joint United Nations Programme on HIV/AIDS, "it's a game-changer in the AIDS response." Some HIV/AIDS advocates caution that the good news will have an impact only if the world massively scales up distribution of ARVs to people who can't afford them, which there are no plans to do.

http://scim.ag/NIAID-study

Lizard Lairs Are All in the Family

The great desert skink is the homebody of the lizard world. The Australian reptiles (*Liopholis kintorei*) dig elaborate burrows, which, scientists have now discovered, shelter closely related family members and can be occupied for up to seven consecutive years.

By trapping lizards and snipping off a tiny portion of their tails for DNA analysis, Steve McAlpin and his colleagues at Macquarie University in Sydney, Australia, found that adult desert skinks live in the same burrow with multiple generations of their children. Both parents and siblings

CREDITS (TOP TO BOTTOM): NICK RISINGER, SKYSURVEY.ORG; YANG XU/UC SAN DIEGO

BY THE NUMBERS

<10 Stars in the constellation Orion visible to 59% of 2188 participants in a U.K. assessment of light pollution. Just 1% of star watchers had skies dark enough to make out more than 30 stars.

$796 billion The economic impact of the Human Genome Project on the U.S. economy over the past decade, according to a report commissioned by the Life Technologies Foundation. The Human Genome Project cost the U.S. government $3.8 billion.

$225 million Donation to the University of Pennsylvania School of Medicine by Philadelphia philanthropists Raymond and Ruth Perelman, one of the largest gifts ever given to a medical school.

Desert skinks build elaborate nests that house multiple generations.

CREDITS (TOP TO BOTTOM): COURTESY OF VALERIE WEISS; ADAM STOW/MACQUARIE UNIVERSITY; SHANNON P. GERRY AND DAVID J. ELLERBY

pitch in to build and maintain their home, the team reported online 11 May in the journal *PLoS ONE*. These complex tunnel networks, which measure up to 13 meters across, feature multiple entrances and designated outside latrine areas where the lizards go to defecate.

Although many species of birds and mammals exhibit such cooperative behavior, this is the first report of lizards constructing a family house. Desert skinks are fairly faithful lovers, which could help explain why families stick together. The finding may bolster the hypothesis that cooperation evolved in groups of genetically related individuals.

Random Sample

From Bench to Big Screen

You think your Ph.D. was tough? Harvard Medical School grad student Samantha Bazarick's cell biology project has been stuck for a whole year. Meanwhile, her lab is populated by petulant postdocs and abusive professors, and her love life is in shambles. Her carefully planned ascent to scientific glory is in a tailspin.

But don't worry—Samantha is fictional. She's the main character in *Losing Control*, a new film by former biophysicist Valerie Weiss. (Spoiler alert: The plot echoes recent intrigues involving scientists at Harvard Medical School.) The film is now on the festival circuit and will make a stop at the National Academy of Sciences in Washington, D.C., in October (www.losingcontrolmovie.com).

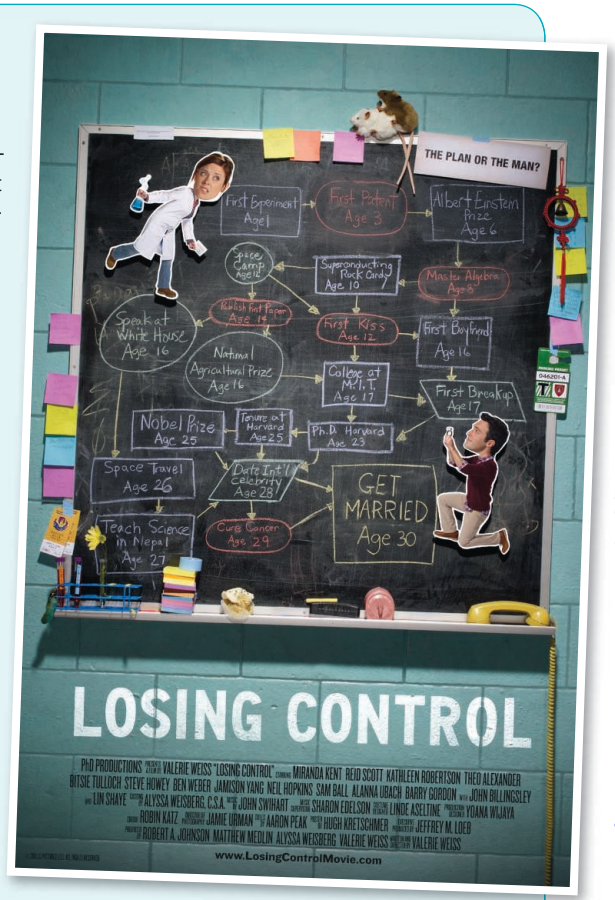

Weiss herself finished a Ph.D. at Harvard in 2001, but she says the film is not based on her own experience. "I actually had a wonderful Ph.D.," she says. "It's supposed to be a screwball comedy." Nonetheless, Samantha's nightmare scenario will resonate with many suffering scientists.

Science and Hollywood aren't so different, Weiss says. "The motivations are the same: stories that are new and fresh." And getting funding for your work is just as great a preoccupation and time drain. But there are advantages to her new profession. "In science you have to come back to the hard data," she says. "But as an independent filmmaker, I can follow my imagination anywhere."

Swimming on a Full Stomach

If you've ever been too full to move after a large meal, envy the leech, which can squirm away even when bloated up to 10 times its normal size on a bloody feast. Now it appears that the signaling molecule serotonin is behind the talent.

When leeches swell up, they stretch their muscles to their limit. This should prevent the muscles from expanding and contracting. Yet leeches wriggle around just fine, says Shannon Gerry, a biomechanist at Wellesley College in Massachusetts.

To find out why, Gerry and fellow Wellesley biomechanist David Ellerby chopped leeches into segments and soaked the chunks in a solution containing serotonin, which stimulates feeding in leeches, or in saline. After stretching the segments to lengths that would simulate swimming after feeding, they used electricity to make them contract. Segments exposed to serotonin exerted more force than did the control segments, no matter how strained they were.

Serotonin, it seems, allows the taxed muscles to push past the strain, the researchers reported online in *Biology Letters* last week. They suggest that serotonin might relax molecules that crosslink muscle fibers so that the muscles can move more easily.

http://scim.ag/leech-swim

Published by AAAS

THEY SAID IT

"Climate change is occurring, is very likely caused primarily by the emission of greenhouse gases from human activities, and poses significant risks for a range of human and natural systems. Each additional ton of greenhouse gases emitted commits us to further change and greater risks."

—The National Research Council Committee on America's Climate Choices, in its fifth and final report to the United States Congress on climate change.

Although science in general was relatively well protected from severe government spending cuts announced last year, astronomy and particle physics took a big hit. A report released last week by the House of Commons Science and Technology Committee says the two fields will have 50% less funding in 2014–15 than they did in 2005.

The committee was particularly scathing about the decision to withdraw support from all ground-based optical and infrared telescopes in the Northern Hemisphere, noting that British astronomers will lose access to cutting-edge instruments and the country's reputation as an international partner could suffer. "The idea that subjects like astronomy and particle physics do not provide immediate economic returns and therefore can be sacrificed at the altar of cutbacks is nonsense," says committee chair Andrew Miller. Welcome words for Britain's big-science supporters, but the impact will be limited: the committee has no direct legislative power. **http://scim.ag/UKastro**

Paris **6**

Goodbye, Rinderpest

Animal health officials are about to report that rinderpest, which has decimated cattle herds for millennia, has been eradicated worldwide after a 17-year vaccination effort. On 25 May in Paris, the World Organization for Animal Health will certify the last eight countries, which include Micronesia, Sri Lanka, and Kazakhstan, as free of the disease. Then on 28 June in Rome, the governing body of the United Nations' Food and Agriculture Organization is expected to issue a declaration of global eradication. Rinderpest, a viral disease, was once endemic across Eurasia and Africa with periodic outbreaks killing calves and devastating herders. The virus was last detected in 2001 in Kenya. It will be the first animal disease to be eradicated and only the second disease in human history after smallpox.

FINDINGS

Is That Fish Worth Chasing?

Harbor seals in the murky North Sea rely on their whiskers to follow the wake a fish leaves behind. A new study reveals that whiskers can also gather detailed information about what the seal is hunting.

Biologist Wolf Hanke of the University of Rostock in Germany and colleagues worked with a harbor seal named Henry, a veteran research participant. First, they created wakes in a box of still water at the bottom of a pool using motorized paddles of different sizes; Henry waited outside the box wearing noise-blocking headphones and a blindfold. Once the paddle stopped, Henry dunked his front half inside and let the eddies swirl around his whiskers. He then pressed one of two buttons with his nose, indicating whether the wake had been made by one of three paddle sizes he'd been trained to recognize or by an unfamiliar one.

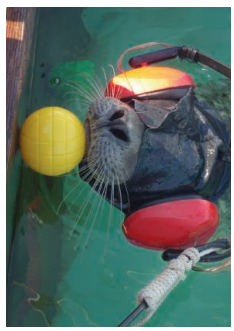

Henry chose correctly more than 90% of the time, as long as the familiar and unfamiliar paddles differed in width >>

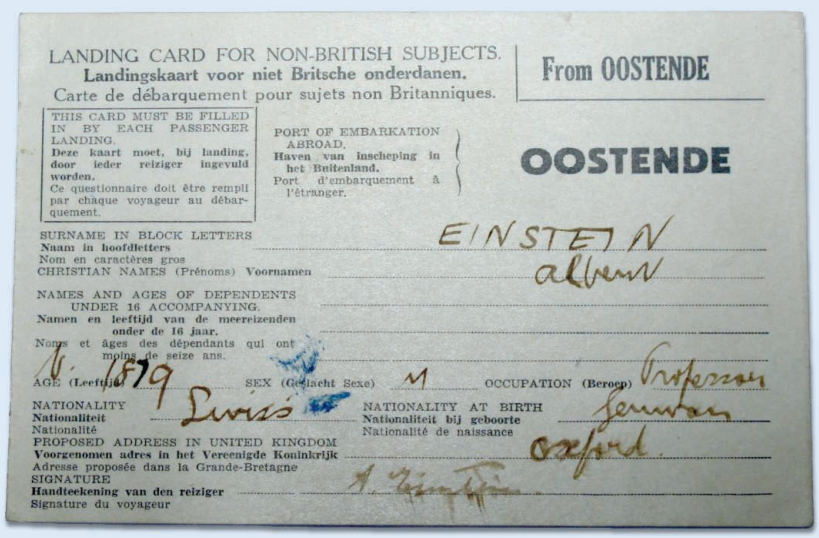
LANDING CARD FOR NON-BRITISH SUBJECTS.
Landingskaart voor niet Britsche onderdanen.
Carte de débarquement pour sujets non Britanniques.

From OOSTENDE

THIS CARD MUST BE FILLED IN BY EACH PASSENGER LANDING.
Deze kaart moet, bij landing, door ieder reiziger ingevuld worden.
Ce questionnaire doit être rempli par chaque voyageur au débarquement.

PORT OF EMBARKATION ABROAD, Haven van inscheping in het Buitenland, Port d'embarquement à l'étranger.
OOSTENDE

SURNAME IN BLOCK LETTERS
Naam in hoofdletters
Nom en caractères gros
EINSTEIN

CHRISTIAN NAMES (Prénoms) Voornamen
albert

NAMES AND AGES OF DEPENDENTS UNDER 16 ACCOMPANYING.
Namen en leeftijd van de meereizenden onder de 16 jaar.
Noms et âges des dépendants qui ont moins de seize ans.

AGE (Leeftijd) 1879
SEX (Geslacht Sexe) M
OCCUPATION (Beroep) Professor

NATIONALITY
Nationaliteit
Nationalité
Swiss

NATIONALITY AT BIRTH
Nationaliteit bij geboorte
Nationalité de naissance
German

PROPOSED ADDRESS IN UNITED KINGDOM
Voorgenomen adres in het Vereenigde Koninkrijk
Adresse proposée dans la Grande-Bretagne
Oxford

SIGNATURE
Handteekening van den reiziger
Signature du voyageur
A Einstein

Spacetime Souvenir

On 26 May 1933, a wild-haired German physics professor stepped off a ferry from Oostende, Belgium, and handed this landing card to border authorities in Dover, England. This year, museum curators on an artifact-hunting trip to a border agency office near Heathrow Airport found the card, signed by Albert Einstein, among the personal collections of immigration officers.

Einstein "already had his Nobel Prize," so the border agent who stamped it "might have thought, 'Ooh, I'll keep this,' " says Lucy Gardner, assistant curator at the Merseyside Maritime Museum in Liverpool, where the card went on display 10 May. On the card, Einstein records his nationality as Swiss; he had left Germany, where the Nazis had denounced his theory of relativity and burned his books, in 1932. He lists Oxford, where he would give a series of lectures, as his expected address. Later that year, Einstein immigrated to the United States, never to return to Germany.

CREDITS (TOP TO BOTTOM): MARINE SCIENCE CENTER, ROSTOCK; NATIONAL MUSEUMS LIVERPOOL

Published by AAAS

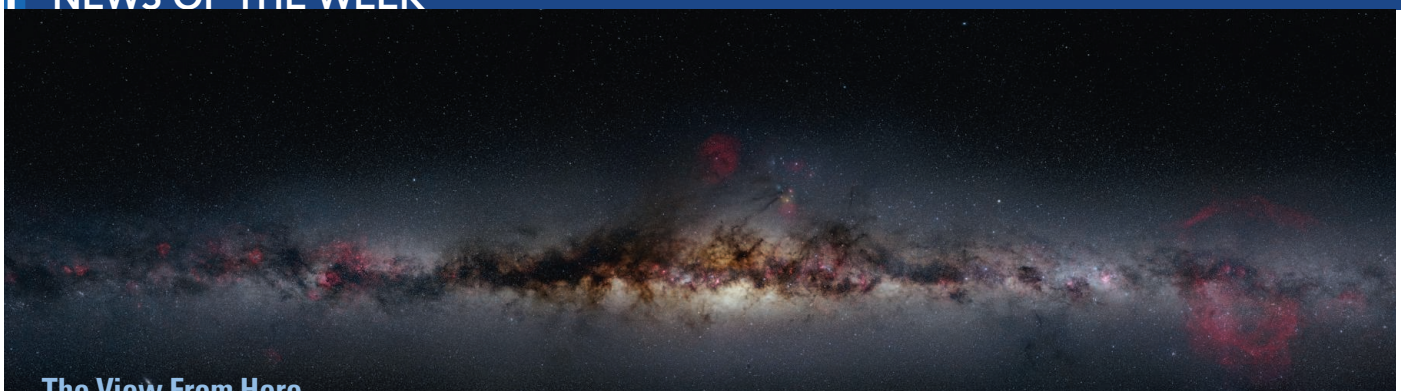

The View From Here

Ever wonder what the night sky would look like if all the stars grew thousands of times brighter? Go see for yourself at www.skysurvey.org.

The Photopic Sky Survey is the labor of love of amateur astronomer Nick Risinger, who quit his job as a marketing director in Seattle, Washington, and spent a year lugging sensitive cameras almost 100,000 kilometers around the United States and to South Africa. He then stitched together the 37,440 images to create the largest ever true-color sky survey—a zoomable, 360° panorama of the universe from Earth's point of view.

"Its main value is as an educational tool," Risinger says. But Jonathan McDowell, an astrophysicist at Harvard University, says astronomers could use the survey's 5000 megapixels to identify objects to observe. "The human eye is very good at spotting things that are unusual in shape or color," he says. "And of course, it's very pretty."

>>FINDINGS

by at least 4 cm, the team reported last week in *The Journal of Experimental Biology*. Laser-aided analysis of the eddies revealed that he could "read" information such as the width of the wake and its velocity—clues to the size of a passing fish, Hanke says, and whether it's worth chasing.

http://scim.ag/chase-fish

Mice Reject Reprogrammed Cells

Scientists have high hopes that stem cells called induced pluripotent stem (iPS) cells can be turned into replacement tissues for patients with injury or disease. Derived from a patient's own cells, scientists had assumed they wouldn't be rejected—a common problem with organ transplants. But a new study suggests otherwise.

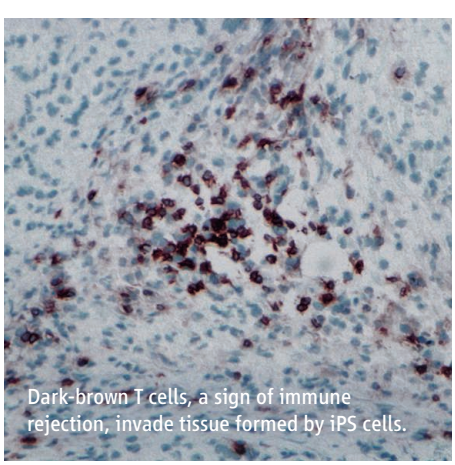

Dark-brown T cells, a sign of immune rejection, invade tissue formed by iPS cells.

Immunologist Yang Xu of the University of California, San Diego, and his colleagues implanted iPS cells, which are reprogrammed from adult cells, into mice that were genetically identical to the iPS cell donor. To the scientists' surprise, the cells were attacked by the recipients' immune systems and were rejected, the team reported online last week in *Nature*. The culprit seems to be incomplete reprogramming that leaves some genes in iPS cells misexpressed, Xu says.

The results add to a series of findings that iPS cells differ in subtle but potentially important ways from more controversial embryonic stem cells. Meanwhile, dozens of labs are working on ways to improve the reprogramming process so that the stray gene expression is eliminated.

http://scim.ag/iPSC-problems

HIV Treatment Prevents Heterosexual Transmission

HIV-infected people who start antiretroviral (ARV) treatment at earlier stages of the disease lowered their risk of transmitting the virus to their sexual partners by 96%, according to a multicountry study that ended abruptly last week.

The $73 million study by the U.S. National Institute of Allergy and Infectious Diseases recruited 1763 couples (97% heterosexual) in which only one partner was infected with the AIDS virus at the start. Half the participants received ARVs immediately, while the other half waited until their infections caused serious immune damage.

An analysis 6 years into the study, which was planned to last 10 years, found that 39 people had become infected, 28 from their regular partners. Of those 28, all but one had a partner in the group that waited to start treatment.

The dramatic result mirrors findings from less-rigorous earlier studies. Still, says Michel Sidibé, who heads the Joint United Nations Programme on HIV/AIDS, "it's a game-changer in the AIDS response." Some HIV/AIDS advocates caution that the good news will have an impact only if the world massively scales up distribution of ARVs to people who can't afford them, which there are no plans to do.

http://scim.ag/NIAID-study

Lizard Lairs Are All in the Family

The great desert skink is the homebody of the lizard world. The Australian reptiles (*Liopholis kintorei*) dig elaborate burrows, which, scientists have now discovered, shelter closely related family members and can be occupied for up to seven consecutive years.

By trapping lizards and snipping off a tiny portion of their tails for DNA analysis, Steve McAlpin and his colleagues at Macquarie University in Sydney, Australia, found that adult desert skinks live in the same burrow with multiple generations of their children. Both parents and siblings

CREDITS (TOP TO BOTTOM): NICK RISINGER, SKYSURVEY.ORG; YANG XU/UC SAN DIEGO

BY THE NUMBERS

<10 Stars in the constellation Orion visible to 59% of 2188 participants in a U.K. assessment of light pollution. Just 1% of star watchers had skies dark enough to make out more than 30 stars.

$796 billion The economic impact of the Human Genome Project on the U.S. economy over the past decade, according to a report commissioned by the Life Technologies Foundation. The Human Genome Project cost the U.S. government $3.8 billion.

$225 million Donation to the University of Pennsylvania School of Medicine by Philadelphia philanthropists Raymond and Ruth Perelman, one of the largest gifts ever given to a medical school.

Desert skinks build elaborate nests that house multiple generations.

CREDITS (TOP TO BOTTOM): COURTESY OF VALERIE WEISS; ADAM STOW/MACQUARIE UNIVERSITY; SHANNON P. GERRY AND DAVID J. ELLERBY

pitch in to build and maintain their home, the team reported online 11 May in the journal *PLoS ONE*. These complex tunnel networks, which measure up to 13 meters across, feature multiple entrances and designated outside latrine areas where the lizards go to defecate.

Although many species of birds and mammals exhibit such cooperative behavior, this is the first report of lizards constructing a family house. Desert skinks are fairly faithful lovers, which could help explain why families stick together. The finding may bolster the hypothesis that cooperation evolved in groups of genetically related individuals.

Random Sample

From Bench to Big Screen

You think your Ph.D. was tough? Harvard Medical School grad student Samantha Bazarick's cell biology project has been stuck for a whole year. Meanwhile, her lab is populated by petulant postdocs and abusive professors, and her love life is in shambles. Her carefully planned ascent to scientific glory is in a tailspin.

But don't worry—Samantha is fictional. She's the main character in *Losing Control*, a new film by former biophysicist Valerie Weiss. (Spoiler alert: The plot echoes recent intrigues involving scientists at Harvard Medical School.) The film is now on the festival circuit and will make a stop at the National Academy of Sciences in Washington, D.C., in October (www.losingcontrolmovie.com).

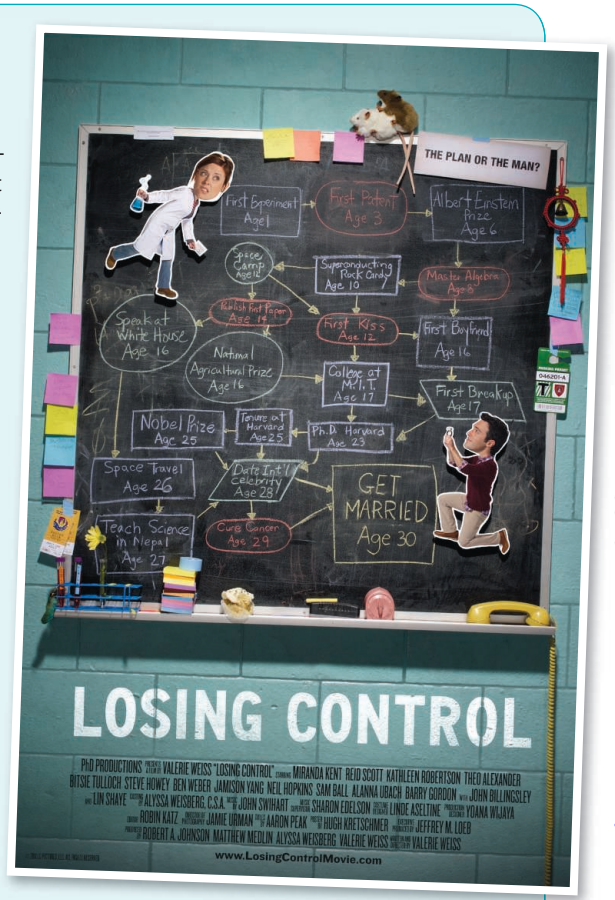

Weiss herself finished a Ph.D. at Harvard in 2001, but she says the film is not based on her own experience. "I actually had a wonderful Ph.D.," she says. "It's supposed to be a screwball comedy." Nonetheless, Samantha's nightmare scenario will resonate with many suffering scientists.

Science and Hollywood aren't so different, Weiss says. "The motivations are the same: stories that are new and fresh." And getting funding for your work is just as great a preoccupation and time drain. But there are advantages to her new profession. "In science you have to come back to the hard data," she says. "But as an independent filmmaker, I can follow my imagination anywhere."

Swimming on a Full Stomach

If you've ever been too full to move after a large meal, envy the leech, which can squirm away even when bloated up to 10 times its normal size on a bloody feast. Now it appears that the signaling molecule serotonin is behind the talent.

When leeches swell up, they stretch their muscles to their limit. This should prevent the muscles from expanding and contracting. Yet leeches wriggle around just fine, says Shannon Gerry, a biomechanist at Wellesley College in Massachusetts.

To find out why, Gerry and fellow Wellesley biomechanist David Ellerby chopped leeches into segments and soaked the chunks in a solution containing serotonin, which stimulates feeding in leeches, or in saline. After stretching the segments to lengths that would simulate swimming after feeding, they used electricity to make them contract. Segments exposed to serotonin exerted more force than did the control segments, no matter how strained they were.

Serotonin, it seems, allows the taxed muscles to push past the strain, the researchers reported online in *Biology Letters* last week. They suggest that serotonin might relax molecules that crosslink muscle fibers so that the muscles can move more easily.

http://scim.ag/leech-swim

Published by AAAS

SPACE SCIENCE

Chinese Academy Takes Space Under Its Wing

BEIJING—In 1993, Li Tipei envisioned a novel space telescope that would use a simple design but sophisticated math to reconstruct images of far-flung objects from the hard x-rays and gamma rays they emit. After years of delays, Li's dream is about to come true. On 3 May, Wu Ji, director of the Center for Space Science and Applied Research of the Chinese Academy of Sciences here, told Chinese media that the Hard X-ray Modulation Telescope (HXMT) is the first of five space science missions slated for launch in CAS's decadal plan, which began this year.

The bevy of missions marks a turning point for Chinese space science. China has sent more than 100 satellites into space, but only one, Wu told *Science*, had a dedicated science mission: Double Star, a project with Europe in which two satellites carried out research on magnetic storms from 2004 to 2007. All other satellites have served purposes such as telecommunications, surveillance, remote sensing, and weather forecasting. Even China's two lunar missions—Chang'e-1 and -2—were driven primarily by engineering goals and science came second, Wu says.

Now space science, a poor stepchild under the China National Space Administration (CNSA), has found in CAS a new parent keen to boost its development. Under CAS's new Innovation 2020 program, space science is slated to receive 3.6 billion RMB ($554 million) over the next 5 years. During this period, the academy plans to establish a National Space Science Center with a stable budget to oversee space research projects.

For years, China's space science enterprise has been held back because its erstwhile overseer, CNSA, is a space agency in name only: It has no budget, no personnel, and no mandate other than to represent China in the international space arena. The real power resides with the State Administration for Science, Technology and Industry for National Defense (SASTIND), whose director doubles as CNSA head. But SASTIND is a weakened descendant of an agency that spun off a military department in the late 1990s that now controls rocket launches and the manned space program. That left SASTIND, nominally a civilian agency, to run a utilitarian unmanned program. SASTIND's culture of secrecy runs counter to the openness required for science, say Chinese researchers, who welcome CAS's taking the lead.

LOFTY AMBITIONS

Mission	Chief scientist	Goals	Estimated launch
HXMT	Li Tipei, CAS Institute of High Energy Physics and Tsinghua University	Survey of x-ray sources; detailed observations of known objects	2014
Shijian-10	Hu Wenrui, CAS Institute of Mechanics	Study physical and biological systems in microgravity and strong radiation environment	Early 2015
KuaFu Project	William Liu, Canadian Space Agency and CAS Center for Space Science and Applied Research	Study solar influence on space weather	Mid-2015
Dark Matter Satellite	Chang Jin, CAS Purple Mountain Observatory	Search for dark matter; study cosmic ray acceleration	Late 2015
Quantum Science Satellite	Pan Jianwei, University of Science and Technology of China	Quantum key distribution for secure communication; long-distance quantum entanglement	2016

HXMT is not the only mission being thrown a lifeline. Another is KuaFu, a Sino-Canadian mission to study the sun's influence on space weather (*Science*, 4 August 2006, p. 607). China will contribute $154 million to the project and plans to send a satellite in early 2015 to a patch of space where the solar wind and Earth's magnetosphere are roughly equal in force, creating a kind of eddy where the craft will hover and train its gaze on the sun. Canada would put two complementary satellites into polar Earth orbit in 2016 or 2017.

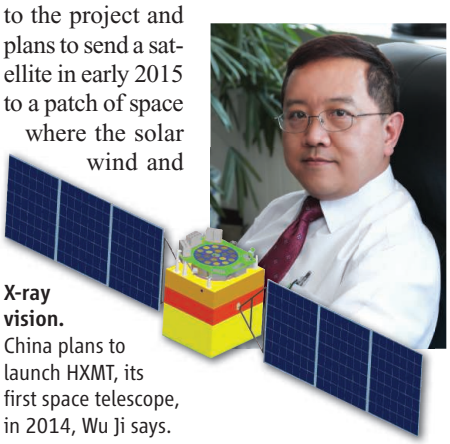

X-ray vision. China plans to launch HXMT, its first space telescope, in 2014, Wu Ji says.

CREDITS (TOP TO BOTTOM): COURTESY WU JI; COURTSEY OF IHEP, CAS (INSET)

CAS will also fund research and design work on two new missions that are aiming for launch in the second half of the decade. One satellite would be on the lookout for gamma rays produced when dark matter particles annihilate each other. The craft would also tune in to a high-energy electron spectrum that may shed light on the mysterious propagation and acceleration of cosmic rays.

A second satellite in development intends to make a quantum leap in space science. One goal is to implement high-speed quantum key distribution between the satellite and Earth stations as a test bed for secure intercontinental quantum communication, says the mission's chief scientist, physicist Pan Jianwei of the University of Science and Technology of China in Hefei. A second aim is to install a source on the satellite that would generate photon pairs whose quantum states are highly correlated. Such entangled photon pairs can be used to investigate long-distance distribution of entanglement, experiment with quantum teleportation—instantly transporting quantum information to another location—and test principles of quantum mechanics.

To realize these aspirations, CAS is counting on HXMT—China's first space telescope—to pave the way. From its low Earth orbit, HXMT would operate in a wide-field mode, cataloging objects such as x-ray binary systems and supermassive black holes, or in a pointing mode to zero in on known sources. The finance ministry has allocated $123 million toward the satellite's construction. CAS and SASTIND will split the $30.6 million cost of building the telescope.

HXMT and other science missions will not be entirely independent of the military, which builds China's rockets and puts them in orbit. For SASTIND missions, the army customarily waives the $15.3 million launch fee, sources say. Whether CAS can persuade the military to foot the bill for launching other satellites on its roster of upcoming missions may be a critical test of its ability to get the country's space science truly off the ground.

–HAO XIN

Published by AAAS

ECOLOGY

Pioneering Center Ponders Future as NSF Pulls Out

Part think tank, part conference and computing facility, the National Center for Ecological Analysis and Synthesis (NCEAS) in Santa Barbara, California, tends to elicit superlatives about its work over the past 15 years. "It's the most successful undertaking in ecology ever," says marine ecologist Boris Worm of Dalhousie University in Halifax, Canada. The center has fostered collaborations that have gathered rich data sets, yielding some of the most widely cited work in the field.

But the future of NCEAS is in question as it faces the end of its core funding from the U.S. National Science Foundation (NSF). The support was always time-limited—NSF-funded centers are expected to support themselves or close, regardless of their success—but supporters say the policy is a mistake in this case. "I think NSF underestimates how much value was added to the scientific enterprise by the unique way NCEAS has been set up," says Peter Kareiva, vice president and chief scientist at The Nature Conservancy in Arlington, Virginia.

NCEAS continues to look for new money, but in the current financial squeeze, the center post-NSF will likely be a smaller, different place, with an emphasis more on applied problems than fundamental ecological questions. "I'm pretty sad" about the impending shrinkage, says marine ecologist Larry Crowder of Duke University in Durham, North Carolina. Complicating matters, the director who was brought in to help plan the center's future direction last week announced he is leaving after 16 months on the job.

NCEAS was born of discussions in the late 1980s among ecologists. Many wanted more big-picture analysis, with large patterns and principles gleaned from disparate sources of data. Another hope was for more collaboration between ecology and other disciplines to generate advice for policymakers. NSF requested proposals for a center to do just that. The University of California, Santa Barbara (UCSB), won the competition in 1995.

Ever since, NCEAS has solicited ideas twice a year with remarkably open-ended requests for proposals. "We just ask the community of ecologists: 'What's hot right now? What do you want to do?' " says Deputy Director Stephanie Hampton. Recent subjects include jellyfish blooms and global patterns of wildfires.

In each project, researchers analyze and integrate various data sets to answer a pressing question, for instance, why fisheries scientists and marine ecologists could have such different views of the health of the oceans (*Science*, 10 April 2009, p. 170). Working groups of a dozen or so ecologists visit the facility several times over a year or two. During days-long brainstorming sessions, they explore the data. The interactions often include a resident group of roughly two dozen postdocs and scientists on sabbaticals, as well as staff experts in data mining.

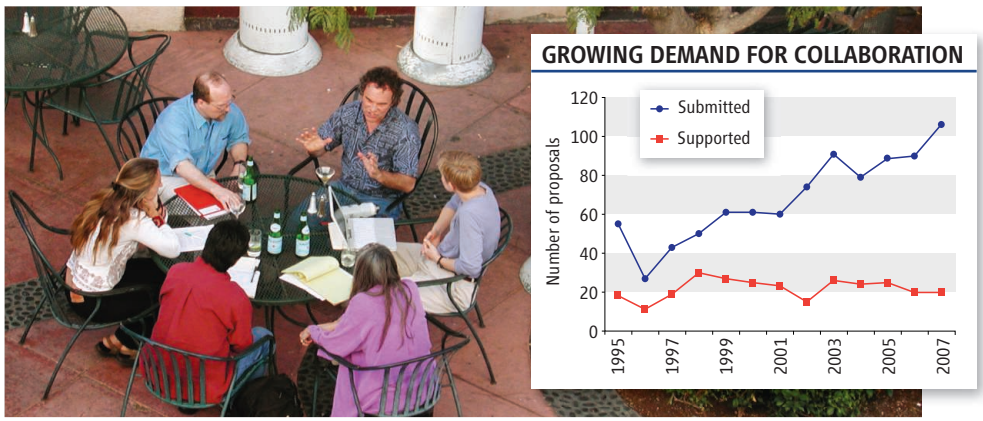

Coming together. Brainstorming sessions in Santa Barbara have combined many data sets and yielded high-impact papers. The facility's popularity has risen, but its capacity may have to be scaled back.

Numerous high-profile papers have resulted—identifying better ways to predict the distribution of species, for example—and a 2005 analysis of citations put NCEAS in the top 1% of institutions in ecology and environment worldwide for impact factor. "Its success is breathtaking," says Taylor Ricketts of the World Wildlife Fund, who chairs the NCEAS Science Advisory Board. The approach has been replicated in more than 18 places, such as the National Evolutionary Synthesis Center in Durham.

In fiscal year 2010, the NSF grant provided $3.7 million for postdocs, sabbaticals, and working groups. On average, NSF support has covered about half of the NCEAS budget. The rest comes from UCSB and from customers—philanthropies and state and federal agencies—that the commission studies. After two NSF grants, NCEAS received a rare third in 2006, which NSF made clear was the last. "We've worked on the [funding] problem since then," says Michael Witherell, UCSB's vice chancellor for research, who says the university is committed to supporting NCEAS. "We will do everything we can to continue providing this service to the community."

After longtime director James Reichman retired, population ecologist Edward McCauley was eventually recruited from the University of Calgary in Canada to help create a vision for NCEAS. Arriving in January 2010, McCauley hoped to get NSF funding for a new type of center, a "synthesis" center that will focus on environmental problems and include geoscientists and a broader array of social sciences. Last September, NSF rejected NCEAS's proposal.

McCauley says existing customers remain interested in working with NCEAS, but that may not sustain the current size of operations. "Sometimes you have to get smaller before you can get bigger," he says. McCauley, who will return to the University of Calgary in July to be vice president for research, says he is departing for personal reasons. "Ed McCauley leaving is a blow," Kareiva says, but he is optimistic about NCEAS finding a talented replacement. The remaining NSF funds can be stretched out until July 2012 to complete existing projects and allow postdocs to finish.

Worm worries that without NSF funding, NCEAS will shift toward supporting applied questions that aren't coming directly from the scientific community, an approach that he says "doesn't sound as high-risk or academically interesting." But Stephen Carpenter of the University of Wisconsin, Madison, says thanks to the inspiration of NCEAS, more such big-picture collaboration is now happening on campuses and at field stations. "People are accustomed to sharing data," he says. "The culture has changed." **–ERIK STOKSTAD**

CREDITS: NCEAS

Published by AAAS

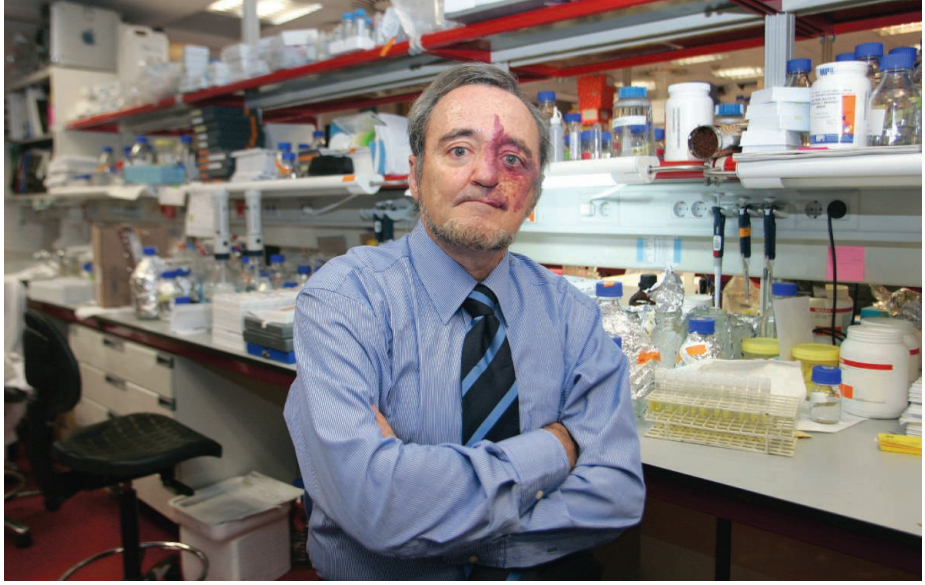

CREDIT: EL PAIS PHOTOS/NEWSCOM

Back to the bench. Mariano Barbacid says he wants to spend more time on research.

CANCER RESEARCH

Spain's 'Lonely Fighter' Steps Down Amid a Highly Public Spat

BARCELONA—Mariano Barbacid is leaving the helm of Spain's flagship cancer center the way he has spent much of his time there: fighting fiercely. Since the Spanish government lured the Madrid-born scientist back from the United States 13 years ago to create the National Cancer Research Centre (CNIO) in his hometown, Barbacid has been involved in a series of conflicts with the government and his staff members. Just as he is about to give up his post, another ugly spat has erupted.

At stake this time is Barbacid's plan to raise private money to work on a potential cancer drug target his team recently discovered, a plan the government has called "illegal." So far, neither side has budged. Meanwhile, the search for a new CNIO director was halted this weekend when an international panel of experts, dismayed by a series of leaks about potential candidates, decided to pull out of the selection process. Barbacid plans to stay on as a group leader after he gives up the director's post, which could complicate any successor's job.

The clash became public on 3 May, when CNIO issued a press release to announce that Barbacid and his Experimental Oncology Group had identified a cell signaling protein, called c-Raf kinase, that could serve as a potential target for drugs against non–small cell lung cancer. (Their finding was published online in *Cancer Cell* on 21 April.) The press release said that CNIO would not be able to search for inhibitors of the protein, however, because the Ministry of Science and Innovation had refused to give the institute additional funds or let it use outside money.

Barbacid says two private funders, whose names he declines to reveal, are ready to provide €10 million per year for 5 years for drug discovery at CNIO. To make that possible, he last year proposed setting up a so-called economic interest grouping (EIG). But the ministry argues that CNIO, as a public foundation, cannot participate in an EIG, because it would make the institute liable for any of the partnership's debts and therefore put its assets at risk.

The day after CNIO's press release, the ministry shot back, saying that CNIO has accumulated €58.6 million from its annual government funding allocations, and that there is financial room to start new projects. The statement also attacked Barbacid's professional ethics, claiming he overplayed the potential value of c-Raf kinase and raised "false expectations" among patients.

Barbacid calls the statement "an abuse of power" on the part of Spain's science and innovation minister, Cristina Garmendia. He also disputes the government's numbers. Since its creation in 2005, CNIO's Experimental Therapeutics Programme has been run separately from the rest of CNIO with government loans amounting to €31.2 million, he says. Only €4.7 million of that is left, just enough to finish two ongoing drug-discovery projects, according to Barbacid. He adds that opinions by two "prestigious lawyers" support his case for an EIG, and that other foundations have created them as well.

The discovery that started the row could help solve a long-standing problem in cancer therapy. Scientists know that a protein called K-Ras promotes lung cancer, but they had not been able to develop drugs that inhibit it. Barbacid's team has shown that K-Ras needs c-Raf kinase to promote cancer, and that knocking out c-Raf kinase genes prevented the development of cancer with no apparent side effects, at least in mice. That makes c-Raf kinase an important new drug target, says David Tuveson of Cancer Research UK's Cambridge Research Institute, who published similar results online 11 May in *Cancer Discovery*.

Several Spanish scientists told *Science* that it's clear their country's research centers need to be given more flexibility in how to access private funding. But most of all, they want the quarrel to stop. "Both parties should put aside personal differences to find common ground … for the benefit of patients," says Manel Esteller, a cancer scientist at the Bellvitge Institute for Biomedical Research here who worked at CNIO between 2001 and 2008. "Obviously this conflict is threatening the future of the CNIO as a leading cancer centre," says Miguel Ángel Piris, who recently left CNIO for the Hospital Universitario Marqués de Valdecilla in Santander.

A well-known figure in Spain, Barbacid spent half his career in the United States, first at the National Cancer Institute—where he was one of the first to discover a human oncogene—and later at the Bristol-Myers Squibb Pharmaceutical Research Institute in Princeton, New Jersey. He returned to Spain in 1998, when the government offered him the money and freedom to set up a new institute. Tuveson says Barbacid "single-handedly has taken the CNIO from a concept to a leading center in the world."

But his stint hasn't been peaceful. Between 2000 and 2002, he publicly battled the government over CNIO's budget. Several high-profile researchers have left CNIO because of what they said was his authoritarian leadership style. Barbacid is a "lonely fighter" and "hard-nosed," says CNIO Vice Director Erwin Wagner. "If he had been a better communicator, some of the problems would probably not have arisen," Wagner adds.

The search for a successor has been on since Barbacid announced in 2009 that he wanted to spend more time on research. In the past few weeks, the names of the four candidates or former candidates under consideration have leaked to the press, leading the international selection panel to resign. On Monday, the ministry said that a decision had been postponed until 22 June.

–ELISABETH PAIN

Elisabeth Pain is a contributing editor for ScienceCareers.org.

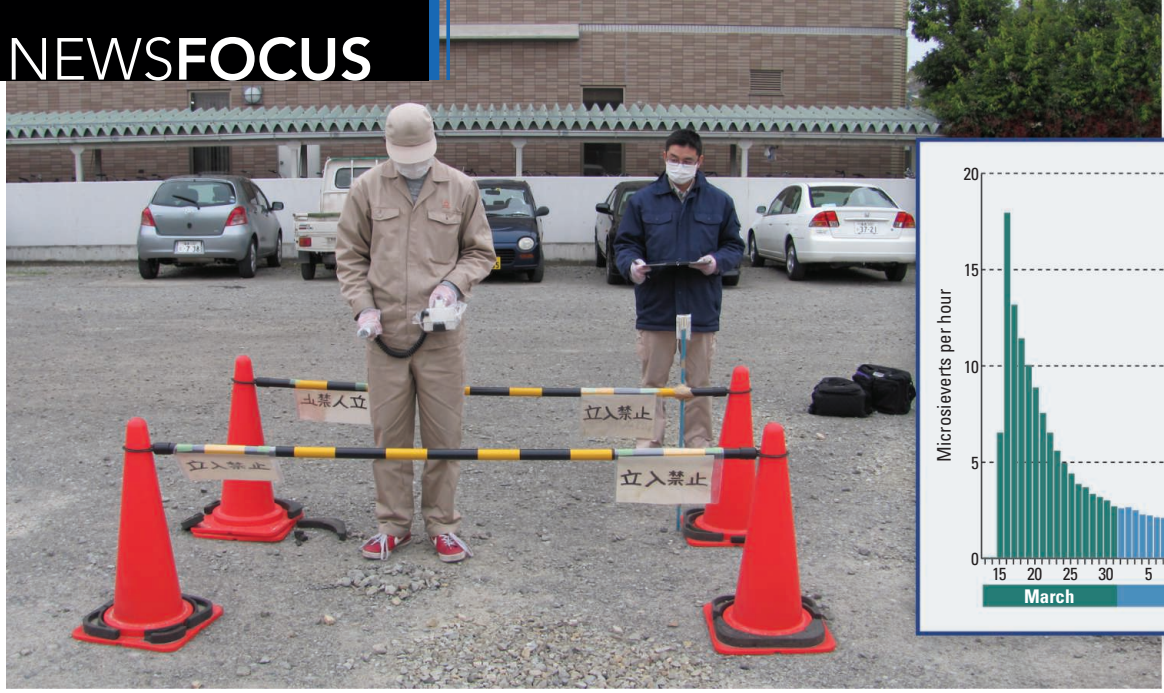

Fukushima Revives The Low-Dose Debate

The general public avoided exposure to high levels of radioactivity, but questions linger about the long-term effects of contamination

FUKUSHIMA, JAPAN—At 5 p.m. sharp, Mitsuru Itou watches as a technician steps inside a quartet of orange traffic cones and black-and-yellow traffic bars marking a "keep out" area in a gravel lot. Holding a radiation meter at his waist, the technician waits for the instrument to stabilize. Then every 30 seconds for the next 2½ minutes he recites the count. Itou, a supervisor with the Public Health and Welfare Office of Fukushima Prefecture, correctly predicts that the readings will average 1.6 microsieverts per hour. "That's what [the radiation] has come down to for some time now," he says. The results are phoned in to a disaster center, which posts them to its Web site. This ritual is repeated every hour at seven locations across the prefecture to track environmental radiation from the Fukushima Daiichi nuclear power plant, 63 kilometers southeast of Fukushima city. The measured levels range from two to 1000 times normal background radiation—and residents, officials, and scientists wonder what that may mean for public health.

The magnitude-9.0 earthquake and tsunami on 11 March knocked out nuclear fuel cooling systems at the power plant. In the days that followed, overheating triggered hydrogen explosions that spewed radioisotopes into the air. Radiation spiked 4 days after the first explosion, according to measurements here and at other ground-monitoring sites hastily set up after the earthquake. Since then, radiation levels have ebbed as short-lived radionuclides, such as iodine-131 with a half-life of 8 days, decay into stable isotopes.

Across Fukushima and neighboring prefectures, small amounts of cesium-134 and cesium-137, isotopes with half-lives of 2 and 30 years respectively, lie on the ground. Cleanup workers have stripped contaminated topsoil from some schoolyards, and remediation or permanent evacuation is likely for the worst areas. But for much of the prefecture, "we're stuck, there are no practical countermeasures," says Hisashi Katayose, a Fukushima official in charge of radiation monitoring.

As a result, several thousand of Fukushima's 2 million residents have been thrust into the middle of a vigorous scientific debate about the health effects of long-term exposure to low levels of radiation. "We're all guinea pigs," says Akira Watanabe, a meteorologist who is vice president of Fukushima University here. A central question is whether there's a threshold below which radiation has no ill effect. "Dose threshold is a very contentious issue in the radiation community," says radiation epidemiologist Roy Shore, research head at the Radiation Effects Research Foundation in Hiroshima. Some researchers believe even unavoidable background radiation can be a factor in causing cancer. Others argue that tiny doses of radiation are not harmful. Some scientists even claim that low doses, by stimulating DNA repair, make you healthier—an effect known as hormesis.

Studies in Fukushima could help clarify the picture. But getting answers will not be easy. Radiation exposure levels for most people were elevated so minutely above background that it may be impossible to tease out carcinogenic effects from other risk factors, such as smoking or diet. "In order to detect an elevation in risk, one needs to study much larger numbers of people," Shore says, especially given that 40% of all Japanese develop cancer.

That has experts wondering whether and how to carry out such studies. "It is difficult to say at this point, especially since the crisis is not over," says Shunichi Yamashita, a radiation health expert at Nagasaki University who is advising the Fukushima prefectural government. Forging ahead with a population study, as daunting as it may be, could nevertheless have a scientific payoff. "If you do the study and don't find anything, that should be an important message," says Dale Preston, a biostatistician specializing in radiation health effects at Hirosoft International in Eureka, California.

Where to draw the line?

Perhaps the sole point on which scientists agree is that radiation damages DNA in ways that can cause cancer many years after exposure. When radioisotopes lodge in cer-

PHOTO CREDIT: D. NORMILE/*SCIENCE*; GRAPH SOURCE: FUKUSHIMA PREFECTURE

Published by AAAS

Hot job. Technicians check radiation hourly in a gravel lot in Fukushima City. Exposure has dropped but remains 35 times above background.

CREDIT: KYODO/LANDOV

tain organs—such as iodine-131 in the thyroid gland—the constant bombardment of surrounding tissue can overwhelm repair mechanisms and trigger cancer.

The clearest insights come from decades of follow up on survivors of the atomic bombings of Hiroshima and Nagasaki. These studies have linked an acute dose of 100 millisieverts (mSv) of radiation—16 times the amount that an individual receives on average from all sources over the course of a year—to a 1.05 times increase in the chance of developing some form of cancer. Children with similar exposures appeared to have a higher risk of developing cancer later. These risks scaled linearly as exposures increased.

But the health effects of chronic low-level radiation exposure over years or decades are far from clear. Several large cohort studies of medical x-ray technicians and nuclear industry workers suggest a slight increase in cancer risk at exposures below 100 mSv, Shore says. To err on the safe side, most radiation protection agencies follow the linear no-threshold model, which posits that risk diminishes with decreasing exposure but that any increase above background poses a cancer risk. Extrapolating from this model to estimate health effects in a population "is not wise because of the uncertainties," Shore says.

Opportunities to narrow uncertainties have been missed. In the aftermath of the Soviet Union's April 1986 Chernobyl nuclear accident, which spewed radionuclides over a swath of Europe, "there was no continuity, no overarching panel looking at how science should be done," says Ronald Chesser, a radiation biologist at Texas Tech University in Lubbock. The subsequent Soviet collapse, scarce funding, imprecise dosimetry, and difficulties tracking people over the years have limited the number of studies and their reliability, he says. The United Nations Scientific Committee on the Effects of Atomic Radiation (UNSCEAR) concluded in a 2008 report that over 6000 cases of thyroid cancer in young people could be linked to Chernobyl but that evidence for other cancers was inconclusive. To resolve outstanding questions, on 26 April the World Health Organization's International Agency for Research on Cancer in Lyon, France, asked the international community to support a Chernobyl Health Effects Research Foundation to conduct life-span studies, similar to those following A-bomb survivors in Japan.

Animal studies have yielded conflicting data. Laboratory experiments on animals indicate that as doses decrease, less and less damage escapes DNA-repair mechanisms, says Yoshihisa Matsumoto, a radiation biologist at the Tokyo Institute of Technology. "There must be some threshold below which the damage is completely repaired," he says. Chesser says some of his group's studies of mice exposed to radioactivity around Chernobyl hint at hormesis: Small exposures over 10 to 45 days, they found, appeared to temper damage from an acute radiation dose delivered in the lab later. He thinks the reaction to low doses could be quite complex. "There's not going to be a uniform response of all biological functions to low levels of radiation," Chesser predicts.

Patchy contamination

Japan's experience tracking A-bomb survivors, an early start gathering data on environmental exposures in Fukushima, and a family registry system that tracks virtually all individuals all offer "great advantages" in devising more definitive low-dose studies, says Preston, who believes such a study would be well worth the cost. "I think we will learn something important," he says.

The 800 or so workers who have helped bring the Fukushima reactors under control will be included in an ongoing study of nuclear industry workers by the Tokyo-based Radiation Effects Association. Many workers are getting higher doses in weeks than they would have received on the job over a year. Fukushima residents facing higher than background exposure can blame an unfortu-

Schoolyard Radiation Policy Brings a Backlash

TOKYO—The Japanese government has made a number of missteps during the 2-month-long Fukushima nuclear power plant crisis. But the most controversial may have been the release of guidelines from the education ministry on allowable radiological contamination in schoolyards. They seem to allow children to accumulate radiation exposures of 20 millisieverts (mSv) over the course of a year. By comparison, nuclear industry workers in Japan can absorb no more than 100 mSv per year; the limit for U.S. nuclear personnel is 50 mSv per year.

The 19 April announcement unleashed a torrent of criticism from civic groups and experts. "Setting [such radiation limits] for elementary schools is inexcusable," Toshiso Kosako, a radiation health expert at the University of Tokyo, said on 30 April, when he resigned as an adviser to Prime Minister Naoto Kan on the nuclear crisis. Because children are known to be more susceptible than adults to risks of cancer from radiation, Physicians for Social Responsibility, a U.S. antinuclear proliferation group, condemned the exposure limit as "unconscionable."

Dirty dirt. Fukushima schools are stripping contaminated topsoil from playgrounds.

The ministry has backpedaled—but not fully retreated. On 11 May, it released suggestions for removing contaminated topsoil from schoolyards to reduce radiation exposures. But it did not change or retract the exposure guidelines.

In its "provisional idea" for acceptable levels of radiation in schoolyards, the education ministry cited a 2009 recommendation from the International Commission on Radiological Protection (ICRP), an Ottawa-based nongovernmental organization. During emergencies, ICRP Publication 109 states, populations can be exposed to 20 to 100 mSv per year. The education ministry calculated that children could spend 8 hours a day in a schoolyard exposed to as much as 3.8 microsieverts per hour, and 16 hours a day indoors exposed to 1.52 microsieverts per hour, and not exceed the 20-mSv limit. Civic groups contend that the education ministry should follow another ICRP recommendation, which states that exposure limits for long-term residence in contaminated areas after an accident should be kept "in the lower part of the 1-20 mSv/year" range.

In the past few weeks, several schools took matters into their own hands and stripped topsoil from their grounds. On 11 May, the ministry jumped on that bandwagon, announcing test results showing that swapping the top 10 centimeters of topsoil with dirt from deeper down cut surface radiation 90%. Stripping and burying the topsoil in a deep hole reduces surface radiation 99%. The ministry is leaving final decisions on what to do in the hands of local officials. **–D.N.**

Published by AAAS

nate shift in the prevailing winds. Just after the 11 March disaster, much of the radioactive contamination from the reactor complex was swept out to sea. But on 15 March, a counterclockwise wind carried contamination back over the prefecture, Watanabe says. "And then it rained."

Authorities are keeping a close vigil on the patchy contamination. In addition to the sampling by Fukushima Prefecture, the education ministry is monitoring radiation levels nationwide, including at 100 locations in the prefecture. A team from Fukushima University recently mapped radiation levels at 370 spots in the prefecture and, using weather balloons, confirmed that atmospheric radiation levels have dropped to near background levels.

That broad-brush impression of radioactive contamination of the landscape isn't sufficient for population studies. Shore says it will be important to reconstruct exposures to identify a cohort with the highest exposures. Researchers also need to ascertain where people were during the peak exposure period and where they obtained food and drinking water. Any robust study would also include detailed medical histories and information on smoking habits, diet, and possible exposure to other toxicants, as well as matched controls with little or no exposure. That information "would make possible an informed long-term cohort study," Shore says.

Aloft. Fukushima University's Akira Watanabe is leading an effort to map radiation in the air and on the ground.

Estimating individual doses from environmental data is neither easy nor precise. An alternative technique was developed by a team led by David Brenner, a radiation biophysicist at Columbia University Medical Center in New York City, to plan a response to a radiation release by terrorists. The method rapidly screens blood samples for fragments of DNA and DNA-repair complexes; exposures are calculated based on the number of fragments.

Scientists hope a respected entity will organize a high-quality research plan involving all levels of government. Fukushima Medical University is bidding for that role. A spokesperson has confirmed that the university will establish a research initiative with support from radiation health experts at Nagasaki and Hiroshima universities. Details may be released next month.

Some researchers doubt that any study in Fukushima, no matter how well devised, will reveal much. The radiation exposure of the general population "is too small to give a statistically significant increase in stochastic effects such as cancer," argues Ohtsura Niwa, professor emeritus of radiation biology at Kyoto University. But even negative data would complement UNSCEAR's conclusions on Chernobyl, Niwa says, "and, in this sense, have global implications." As for the linear no-threshold model, Preston says, "I don't think anything [done in Fukushima] is going to resolve that debate."

One real effect of the radioactive contamination is the gnawing fear—groundless or not—that low levels of radiation could harm their children. For that reason alone, Yamashita says, "a center or some sort of system to support long-term health follow-ups is definitely necessary." **–DENNIS NORMILE**

Crippled Reactors to Get Cooled and Wrapped

TOKYO—The crisis at the stricken Fukushima Daiichi nuclear power plant may have faded from the headlines, but it's far from over. To cope with the loss of reactor cooling systems knocked out by the 11 March earthquake and tsunami, the plant's owner, Tokyo Electric Power Co., has installed jury-rigged cooling setups that have cut radiation emissions dramatically. But some 100,000 residents who were evacuated will not return home until the reactors are firmly under control. Last month, Tokyo Electric unveiled a two-stage plan to build more robust cooling systems and reduce radiation leaks within 3 months, then, 3 to 6 months later, achieve a cold shutdown in which fuel is cooled by water below the boiling point at atmospheric pressure.

Nuclear fuel in four of the plant's six reactors overheated, with extensive core damage in three units. Last week, a robotic inspection increased suspicions that the fuel in unit 1 may have melted through the bottom of the pressure vessel and pooled at the base of the containment structure. Hydrogen explosions completely blew the upper walls and roofs off two units and severely damaged a third; vessels and piping are leaking contaminated water. "There are many challenging tasks ahead," says Tony Irwin, a nuclear technology expert at Australian National University and the University of Sydney. Workers must reduce radiation levels, plug leaks, and decontaminate water—all while the threat of aftershocks persists.

In the early days, Tokyo Electric hoped to restart Fukushima's original cooling systems. But the company was forced to explore alternatives, says Hidehiko Nishiyama, deputy director of Japan's Nuclear and Industrial Safety Agency. The utility is now planning to build heat exchangers that will circulate fresh water through the reactors to cool the fuel. To seal off reactor buildings, engineers are planning to wrap them in polyester sheets stretched over steel frames.

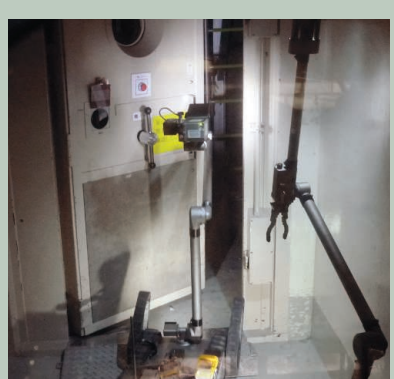

Off limits. Robots are finding radiation too high for humans.

The biggest challenge, Nishiyama says, is protecting workers. Some have been entering the unit 1 building to prepare for construction. But so far, only robots have entered the unit 2 and 3 reactor buildings, where radiation levels top 50 millisieverts per hour. Tokyo Electric may expand the use of robots, which so far have been limited to taking radiation measurements and videos. Because integrated circuits can be affected by radiation, these probes must be primarily mechanical or have hardened electronics. Once new cooling systems and enclosures are in place, work could start on the semipermanent buildings needed for recovering nuclear fuel and decommissioning the reactors, a process that could take a decade or longer. **–D.N.**

CREDITS (TOP TO BOTTOM): D. NORMILE/*SCIENCE*; TOKYO ELECTRIC POWER CO.

Published by AAAS

Hot job. Technicians check radiation hourly in a gravel lot in Fukushima City. Exposure has dropped but remains 35 times above background.

CREDIT: KYODO/LANDOV

tain organs—such as iodine-131 in the thyroid gland—the constant bombardment of surrounding tissue can overwhelm repair mechanisms and trigger cancer.

The clearest insights come from decades of follow up on survivors of the atomic bombings of Hiroshima and Nagasaki. These studies have linked an acute dose of 100 millisieverts (mSv) of radiation—16 times the amount that an individual receives on average from all sources over the course of a year—to a 1.05 times increase in the chance of developing some form of cancer. Children with similar exposures appeared to have a higher risk of developing cancer later. These risks scaled linearly as exposures increased.

But the health effects of chronic low-level radiation exposure over years or decades are far from clear. Several large cohort studies of medical x-ray technicians and nuclear industry workers suggest a slight increase in cancer risk at exposures below 100 mSv, Shore says. To err on the safe side, most radiation protection agencies follow the linear no-threshold model, which posits that risk diminishes with decreasing exposure but that any increase above background poses a cancer risk. Extrapolating from this model to estimate health effects in a population "is not wise because of the uncertainties," Shore says.

Opportunities to narrow uncertainties have been missed. In the aftermath of the Soviet Union's April 1986 Chernobyl nuclear accident, which spewed radionuclides over a swath of Europe, "there was no continuity, no overarching panel looking at how science should be done," says Ronald Chesser, a radiation biologist at Texas Tech University in Lubbock. The subsequent Soviet collapse, scarce funding, imprecise dosimetry, and difficulties tracking people over the years have limited the number of studies and their reliability, he says. The United Nations Scientific Committee on the Effects of Atomic Radiation (UNSCEAR) concluded in a 2008 report that over 6000 cases of thyroid cancer in young people could be linked to Chernobyl but that evidence for other cancers was inconclusive. To resolve outstanding questions, on 26 April the World Health Organization's International Agency for Research on Cancer in Lyon, France, asked the international community to support a Chernobyl Health Effects Research Foundation to conduct life-span studies, similar to those following A-bomb survivors in Japan.

Animal studies have yielded conflicting data. Laboratory experiments on animals indicate that as doses decrease, less and less damage escapes DNA-repair mechanisms, says Yoshihisa Matsumoto, a radiation biologist at the Tokyo Institute of Technology. "There must be some threshold below which the damage is completely repaired," he says. Chesser says some of his group's studies of mice exposed to radioactivity around Chernobyl hint at hormesis: Small exposures over 10 to 45 days, they found, appeared to temper damage from an acute radiation dose delivered in the lab later. He thinks the reaction to low doses could be quite complex. "There's not going to be a uniform response of all biological functions to low levels of radiation," Chesser predicts.

Patchy contamination

Japan's experience tracking A-bomb survivors, an early start gathering data on environmental exposures in Fukushima, and a family registry system that tracks virtually all individuals all offer "great advantages" in devising more definitive low-dose studies, says Preston, who believes such a study would be well worth the cost. "I think we will learn something important," he says.

The 800 or so workers who have helped bring the Fukushima reactors under control will be included in an ongoing study of nuclear industry workers by the Tokyo-based Radiation Effects Association. Many workers are getting higher doses in weeks than they would have received on the job over a year. Fukushima residents facing higher than background exposure can blame an unfortu-

Schoolyard Radiation Policy Brings a Backlash

TOKYO—The Japanese government has made a number of missteps during the 2-month-long Fukushima nuclear power plant crisis. But the most controversial may have been the release of guidelines from the education ministry on allowable radiological contamination in schoolyards. They seem to allow children to accumulate radiation exposures of 20 millisieverts (mSv) over the course of a year. By comparison, nuclear industry workers in Japan can absorb no more than 100 mSv per year; the limit for U.S. nuclear personnel is 50 mSv per year.

The 19 April announcement unleashed a torrent of criticism from civic groups and experts. "Setting [such radiation limits] for elementary schools is inexcusable," Toshiso Kosako, a radiation health expert at the University of Tokyo, said on 30 April, when he resigned as an adviser to Prime Minister Naoto Kan on the nuclear crisis. Because children are known to be more susceptible than adults to risks of cancer from radiation, Physicians for Social Responsibility, a U.S. antinuclear proliferation group, condemned the exposure limit as "unconscionable."

Dirty dirt. Fukushima schools are stripping contaminated topsoil from playgrounds.

The ministry has backpedaled—but not fully retreated. On 11 May, it released suggestions for removing contaminated topsoil from schoolyards to reduce radiation exposures. But it did not change or retract the exposure guidelines.

In its "provisional idea" for acceptable levels of radiation in schoolyards, the education ministry cited a 2009 recommendation from the International Commission on Radiological Protection (ICRP), an Ottawa-based nongovernmental organization. During emergencies, ICRP Publication 109 states, populations can be exposed to 20 to 100 mSv per year. The education ministry calculated that children could spend 8 hours a day in a schoolyard exposed to as much as 3.8 microsieverts per hour, and 16 hours a day indoors exposed to 1.52 microsieverts per hour, and not exceed the 20-mSv limit. Civic groups contend that the education ministry should follow another ICRP recommendation, which states that exposure limits for long-term residence in contaminated areas after an accident should be kept "in the lower part of the 1-20 mSv/year" range.

In the past few weeks, several schools took matters into their own hands and stripped topsoil from their grounds. On 11 May, the ministry jumped on that bandwagon, announcing test results showing that swapping the top 10 centimeters of topsoil with dirt from deeper down cut surface radiation 90%. Stripping and burying the topsoil in a deep hole reduces surface radiation 99%. The ministry is leaving final decisions on what to do in the hands of local officials. **–D.N.**

Published by AAAS

nate shift in the prevailing winds. Just after the 11 March disaster, much of the radioactive contamination from the reactor complex was swept out to sea. But on 15 March, a counterclockwise wind carried contamination back over the prefecture, Watanabe says. "And then it rained."

Authorities are keeping a close vigil on the patchy contamination. In addition to the sampling by Fukushima Prefecture, the education ministry is monitoring radiation levels nationwide, including at 100 locations in the prefecture. A team from Fukushima University recently mapped radiation levels at 370 spots in the prefecture and, using weather balloons, confirmed that atmospheric radiation levels have dropped to near background levels.

That broad-brush impression of radioactive contamination of the landscape isn't sufficient for population studies. Shore says it will be important to reconstruct exposures to identify a cohort with the highest exposures. Researchers also need to ascertain where people were during the peak exposure period and where they obtained food and drinking water. Any robust study would also include detailed medical histories and information on smoking habits, diet, and possible exposure to other toxicants, as well as matched controls with little or no exposure. That information "would make possible an informed long-term cohort study," Shore says.

Aloft. Fukushima University's Akira Watanabe is leading an effort to map radiation in the air and on the ground.

Estimating individual doses from environmental data is neither easy nor precise. An alternative technique was developed by a team led by David Brenner, a radiation biophysicist at Columbia University Medical Center in New York City, to plan a response to a radiation release by terrorists. The method rapidly screens blood samples for fragments of DNA and DNA-repair complexes; exposures are calculated based on the number of fragments.

Scientists hope a respected entity will organize a high-quality research plan involving all levels of government. Fukushima Medical University is bidding for that role. A spokesperson has confirmed that the university will establish a research initiative with support from radiation health experts at Nagasaki and Hiroshima universities. Details may be released next month.

Some researchers doubt that any study in Fukushima, no matter how well devised, will reveal much. The radiation exposure of the general population "is too small to give a statistically significant increase in stochastic effects such as cancer," argues Ohtsura Niwa, professor emeritus of radiation biology at Kyoto University. But even negative data would complement UNSCEAR's conclusions on Chernobyl, Niwa says, "and, in this sense, have global implications." As for the linear no-threshold model, Preston says, "I don't think anything [done in Fukushima] is going to resolve that debate."

One real effect of the radioactive contamination is the gnawing fear—groundless or not—that low levels of radiation could harm their children. For that reason alone, Yamashita says, "a center or some sort of system to support long-term health follow-ups is definitely necessary." **–DENNIS NORMILE**

Crippled Reactors to Get Cooled and Wrapped

TOKYO—The crisis at the stricken Fukushima Daiichi nuclear power plant may have faded from the headlines, but it's far from over. To cope with the loss of reactor cooling systems knocked out by the 11 March earthquake and tsunami, the plant's owner, Tokyo Electric Power Co., has installed jury-rigged cooling setups that have cut radiation emissions dramatically. But some 100,000 residents who were evacuated will not return home until the reactors are firmly under control. Last month, Tokyo Electric unveiled a two-stage plan to build more robust cooling systems and reduce radiation leaks within 3 months, then, 3 to 6 months later, achieve a cold shutdown in which fuel is cooled by water below the boiling point at atmospheric pressure.

Nuclear fuel in four of the plant's six reactors overheated, with extensive core damage in three units. Last week, a robotic inspection increased suspicions that the fuel in unit 1 may have melted through the bottom of the pressure vessel and pooled at the base of the containment structure. Hydrogen explosions completely blew the upper walls and roofs off two units and severely damaged a third; vessels and piping are leaking contaminated water. "There are many challenging tasks ahead," says Tony Irwin, a nuclear technology expert at Australian National University and the University of Sydney. Workers must reduce radiation levels, plug leaks, and decontaminate water—all while the threat of aftershocks persists.

In the early days, Tokyo Electric hoped to restart Fukushima's original cooling systems. But the company was forced to explore alternatives, says Hidehiko Nishiyama, deputy director of Japan's Nuclear and Industrial Safety Agency. The utility is now planning to build heat exchangers that will circulate fresh water through the reactors to cool the fuel. To seal off reactor buildings, engineers are planning to wrap them in polyester sheets stretched over steel frames.

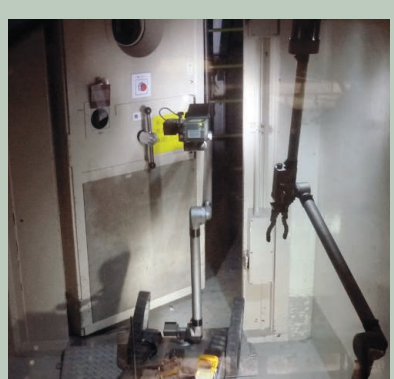

Off limits. Robots are finding radiation too high for humans.

The biggest challenge, Nishiyama says, is protecting workers. Some have been entering the unit 1 building to prepare for construction. But so far, only robots have entered the unit 2 and 3 reactor buildings, where radiation levels top 50 millisieverts per hour. Tokyo Electric may expand the use of robots, which so far have been limited to taking radiation measurements and videos. Because integrated circuits can be affected by radiation, these probes must be primarily mechanical or have hardened electronics. Once new cooling systems and enclosures are in place, work could start on the semipermanent buildings needed for recovering nuclear fuel and decommissioning the reactors, a process that could take a decade or longer. **–D.N.**

CREDITS (TOP TO BOTTOM): D. NORMILE/*SCIENCE*; TOKYO ELECTRIC POWER CO.

Published by AAAS

SEISMOLOGY

New Work Reinforces Megaquake's Harsh Lessons in Geoscience

High-tech analyses of Japan's March earthquake overturn long-held views of fault behavior and warn that another disaster may be looming

The moment the Tohoku-Oki earthquake struck off northern Japan on 11 March, many researchers knew their expectations had been shattered. The great offshore fault could not be counted on to behave at all predictably. And using onshore observations to gauge whether an offshore fault is building toward failure has grave limitations.

Now three papers (http://scim.ag/M-Simons, http://scim.ag/S-Ide, and http://scim.ag/M-Sato) published online this week in *Science* help show why the inevitable release of seismic energy failed to play out as expected and why monitoring from afar fell short. The papers also point to a possible huge quake to the south, closer to Tokyo. Seismologists are concerned, says Mark Simons of the California Institute of Technology in Pasadena, but they are also now acutely aware of their limitations. "We have no idea what's going on" to the south, he says, but they're anxious to find out.

Many seismologists had thought that the offshore fault north of Tokyo was fairly simple and uniform. The ocean plate diving beneath Japan, the thinking went, should stick and slowly build up enough stress to rupture the fault. And the fault should fail segment by segment in large but not huge earthquakes. That's how the fault seemed to have behaved in recent centuries, with quakes of magnitude 7 to 8 or so popping off on any one segment every few decades or few centuries.

But it turns out that the fault has more than one mode of operation. The three *Science* papers gauge where and by how much the fault slipped in the 11 March magnitude-9.0 quake. Simons and his colleagues combined seismic data recorded around the world, crustal movements on Japan recorded by GPS, and tsunami waves recorded at buoys at sea. Satoshi Ide of the University of Tokyo and colleagues compared the seismic signature of the magnitude 9 with that of its largest foreshock, a magnitude 7.3. And Mariko Sato of the Japan Coast Guard in Tokyo and colleagues actually measured the motion of the sea floor before and after subsea GPS observations. "You can't have a better recorded earthquake," says David Wald of the U.S. Geological Survey in Golden, Colorado, who was not involved in any of the studies.

The three studies and unpublished estimates by other groups suggest that during the quake, the descending ocean plate and the overlying plate carrying Japan slipped past each other by as much as 50 to 60 meters. "Those are enormous slips," Wald says, running about two to three times the maximum slip reported for the magnitude-8.8 Maule, Chile, quake of last year. But the pattern of slip is equally striking. Five contiguous segments of the fault spanning more than 600 kilometers broke at once in the quake, rather than one or at most two, as scientists had assumed. But only two central segments experienced extreme slip, and that high slip was concentrated far offshore on the shallower part of the fault (within the figure's yellow contours). Historic quakes had broken short segments of the deeper part of the fault nearer land (the loops of various colors).

Obviously, the fault is more complicated than most researchers had assumed. Simons and his colleagues suggest that some irregularity on the fault is to blame. Something—perhaps a seamount on the sinking plate—pinned the high-slip patch of fault in place for 500 or 1000 years, they argue, while patches around it failed repeatedly in smaller quakes. The apparent absence of quakes in the stuck patch led many seismologists to assume that the fault there could be slowly but steadily slipping without building up any strain. And their only means of monitoring the buildup of strain on the fault—GPS measurements of slow ground movement on land—was greatly handicapped by having the stuck patch 150 kilometers offshore. With such a limited perspective on the past release and the current buildup of strain, a magnitude-9 quake caught researchers by surprise.

Learning that most of the March megaquake's slip was concentrated on two segments makes scientists more worried about other faults around the Pacific. "If you can get a 9 that is this compact," Wald says, "it increases the number of places you can [fit in] a 9 where you may not have expected one."

All eyes are now on the southern portion of the length of fault that broke in the Tohoku quake. Neither historical quakes nor the Tohoku quake has broken the offshore, shallow portion of the fault there. And the Tohoku rupture transferred stress southward along the fault, abruptly increasing the stress there. As had been the case to the north, researchers can't say for sure whether that portion of the fault (marked by the question mark) has been freely slipping without generating quakes or locked and building strain toward a quake.

If the offshore southern portion is indeed stuck, Simons and colleagues see "the possibility of a sibling to the 2011 event" that could be "similar to what just occurred offshore," but half as far from Tokyo. So researchers are anxious to find out whether the stress transferred southward from the 9 has accelerated slow slip on the fault and thus defused the threat of a quake. If the fault isn't slipping, another quake would be in the works. Speed is of the essence: A magnitude-8.7 sibling quake followed the 2004 Indian Ocean megaquake by 3 months. **–RICHARD A. KERR**

EARTHQUAKES OF THE JAPAN TRENCH

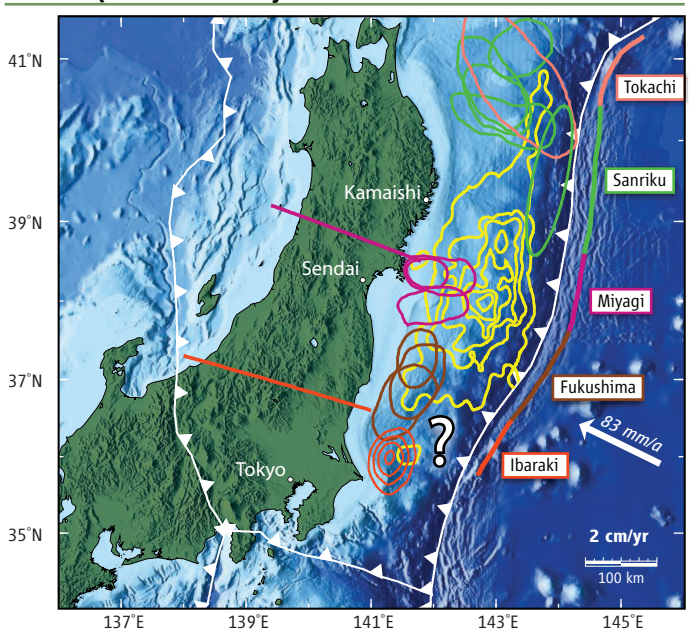

A game of ring toss. March's huge quake (yellow contours) and past smaller quakes (colored loops) have left a patch of threatening fault (question mark).

CREDIT: ADAPTED FROM MARK SIMONS *ET AL.*, *SCIENCE* (2011)

Published by AAAS

Out of the blue. Students at California State University, Northridge, ponder the destruction wrought by a quake on an unrecognized fault.

SEISMOLOGY

Seismic Crystal Ball Proving Mostly Cloudy Around the World

Failing at quake prediction, seismologists tried making fuzzier forecasts, but Japan's megaquake is only the latest reminder of the method's shortcomings

When a devastating megaquake rocked the region north of Tokyo in March, nobody saw such a huge quake coming. "Japanese scientists are among the world's best, and they have the best monitoring networks," notes geophysicist Ross Stein of the U.S. Geological Survey (USGS) in Menlo Park, California. "It's hard to imagine others are going to do forecasting better. No one group is doing it in a way we'd all be satisfied with."

In China, New Zealand, and California as well, recent earthquakes have underscored scientists' problems forecasting the future. A surprisingly big quake arrives where smaller ones were expected, as in Japan; an unseen fault breaks far from obviously dangerous faults, as in New Zealand. And, most disconcerting, after more than 2 decades of official forecasting, geoscientists still don't know how much confidence to place in their own warnings. "We can't really tell good forecasts from the bad ones" until the surprises arrive, Stein says. But improvements are in the works.

Simple beginnings

The current focus of earthquake prognostication research represents a retreat from its ambitious aims of a few decades ago. In the 1960s and '70s, seismologists worked on *prediction*: specifying the precise time, place, and magnitude of a coming quake. To do that, scientists needed to identify reliable signals that a fault was about to fail: a distinctive flurry of small quakes, a whiff of radon gas oozing from the ground, some oddly perturbed wildlife. Unfortunately, no one has yet found a bona fide earthquake precursor. By the time the 2004 magnitude-6.0 Parkfield earthquake—the most closely monitored quake of all time—struck the central San Andreas fault without so much as a hint of a precursor (*Science*, 8 October 2004, p. 206), most researchers had abandoned attempts at precise prediction.

PROBABILISTIC SEISMIC HAZARD MAP

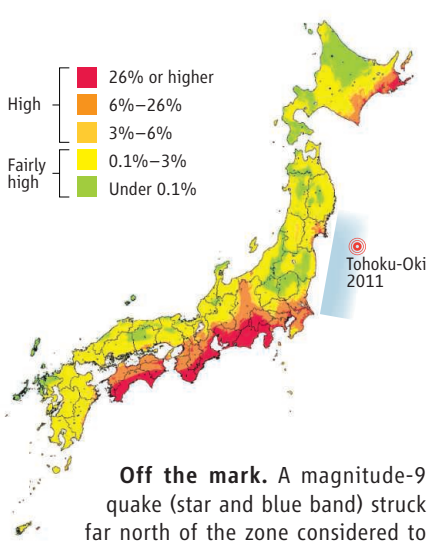

Off the mark. A magnitude-9 quake (star and blue band) struck far north of the zone considered to have the greatest seismic hazard (red).

Parkfield did mark an early success of a new strategy: quake *forecasting*. Rather than waiting for a warning sign, forecasters look to the past behavior of a fault to gauge future behavior. They assume that strain on a fault is building steadily and that the same segment of fault that broke in the past will produce a similar break again in the future, once it reaches the same breaking point. Instead of giving the year or range of years when the next quake will strike a particular segment of fault, they express it as a probability.

USGS issued its first official earthquake forecast for the San Andreas in 1988 (*Science*, 22 July 1988, p. 413). Parkfield, which had a long record of similar quakes at roughly 22-year intervals, rated a 99% probability of repeating in the next 30 years. That turned out to be a success for the 1988 forecast. And the southern Santa Cruz Mountains segment, which last slipped in the 1906 San Francisco quake, was given a 30% chance of failing again within 30 years, which it did in 1989.

Since then, the 1988 San Andreas forecast has had no more hits, but it has missed plenty of serious California seismic activity. The reason: lack of data. Quake forecasting "is highly conditioned on the information available," says William Ellsworth, a seismologist at USGS's office in Menlo Park. Ellsworth served on USGS's Working Group on California Earthquake Probabilities (WGCEP) that issued the 1988 forecast. Given the sorely limited knowledge of California fault history, WGCEP limited itself to the best-known fault segments, mainly on the San Andreas fault. It ignored not only a plethora of unrelated faults but also most branches of the San Andreas that slice through populated regions such as the San Francisco Bay area.

The limitations of that narrow focus became clear while the group was still reaching its conclusions. At its 23 November 1987 meeting, members decided that the particularly skimpy information on one fault, the Superstition Hills fault in far Southern Cali-

CREDITS (TOP TO BOTTOM): MARK J. TERRILL/AP IMAGES; ADAPTED FROM THE EARTHQUAKE RESEARCH COMMITTEE, NATIONAL SEISMIC HAZARD MAPS FOR JAPAN (2010), HEADQUARTERS FOR EARTHQUAKE RESEARCH PROMOTION

Published by AAAS

fornia, prevented them from making a forecast. Within hours, a magnitude-6.5 quake struck that fault, followed 11 hours later by a magnitude-6.7 quake on a previously unknown, intersecting fault. There would be other surprises on little-known faults: the 1992 magnitude-7.3 Landers quake off the southern San Andreas (1 killed, $92 million in damage); the 1994 magnitude-6.7 Northridge earthquake on a previously unknown, buried fault (60 killed, $20 billion in damage); and the 1999 Hector Mine quake, magnitude 7.1, in the remoteness of the Mojave Desert.

Modern prognostication

But earthquake forecasting "has hardly stood still over 20-plus years," Ellsworth notes. Scientists now have much more information about faults both major and minor; just as significant, they have developed a much keener sense of how to proceed when data are lacking. "To do seismic hazard right, we have to acknowledge we don't know how Earth works," says seismologist Edward Field of USGS in Golden, Colorado, who is leading the next official forecast for California, due in 2012.

In the past, Field notes, official forecasters would take their best guess at how a fault works—for example, what length of fault will break and how fast the fault slips over geologic time—and feed it into a single forecast model, which would spit out a probability that a particular quake would occur in the next 30 years. WGCEP followed that approach for its 1988 and 1995 forecasts.

In the late 1990s, however, it became clear that a single model wasn't enough. "There's no agreement on how to build one model," Field says, "so we have to build more than one to allow for the range of possible models." Forecasters merged 480 different models for the 2007 California forecast to produce a single forecast with more clearly defined uncertainties. They aren't done yet. Current models cannot produce some sorts of quakes that have actually occurred, Field says, including the sorts that struck New Zealand and Japan.

Those two quakes are "perfect examples of what we need to fix," Field says. In New Zealand, last September's magnitude-7.1 Darfield quake struck a previously unknown fault that probably hadn't ruptured for the past 15,000 years. Scientists were aware that a quake of that size was possible in the region. New Zealand's official forecast estimated that "background" seismicity would give rise somewhere to one about once in 10,000 years. The New Zealand forecast "is doing its job," says seismologist Mark Stirling of New Zealand's GNS Science in Lower Hutt—but in this case, the information was too vague to be of much use. (Once the quake had occurred, statistical forecasting based on the size of the main shock did anticipate the possibility of its largest aftershock: a magnitude-6.3 quake in February that heavily damaged older structures in Christchurch.)

In the case of the Tohoku earthquake, the culprit was an "unknown unknown." Japanese seismologists preparing official Japan forecasts have assumed that the offshore fault running the length of the main island north of Tokyo had largely revealed its true nature. "I thought we really understood the Tohoku area," says seismologist James Mori of Kyoto University in Japan. "Five hundred years seemed to be a long enough quake history given the [large] number of earthquakes."

Drawing on a centuries-long history of quakes of magnitude 7 to 8 rupturing various parts of the fault, members of the official Earthquake Research Committee had divided the offshore fault into six segments, each roughly 150 kilometers long, that they expected to rupture again. They assigned each segment a probability of rupturing again in the next 30 years; the probabilities ranged from a few percent to 99% in recent official forecasts.

Official forecasters had not included the possibility of more than two segments rupturing at once. They knew that two adjacent segments seemed to have broken together in 1793 to produce a magnitude-8.0 quake. And at their meeting in February, they also considered geologic evidence that a big tsunami in 869 C.E. had swept several kilometers inland across the same coastal plain inundated in March. But they concluded they had too little data to consider what sort of earthquake would result if more than two segments failed at once, says seismologist Kenji Satake of the University of Tokyo, who served on the committee. "I don't think anyone anticipated a 9.0," Satake says.

In the event, five fault segments failed in one magnitude-9.0 quake (see p. 911). (The disastrous 2008 Wenchuan quake in China also grew to an unimagined size by breaking multiple fault segments.) In Japan, "what happened was a very improbable, 1000-year event," Ellsworth says. The most dangerous earthquakes tend to be rare, and their very rarity, unfortunately, makes them hard to study.

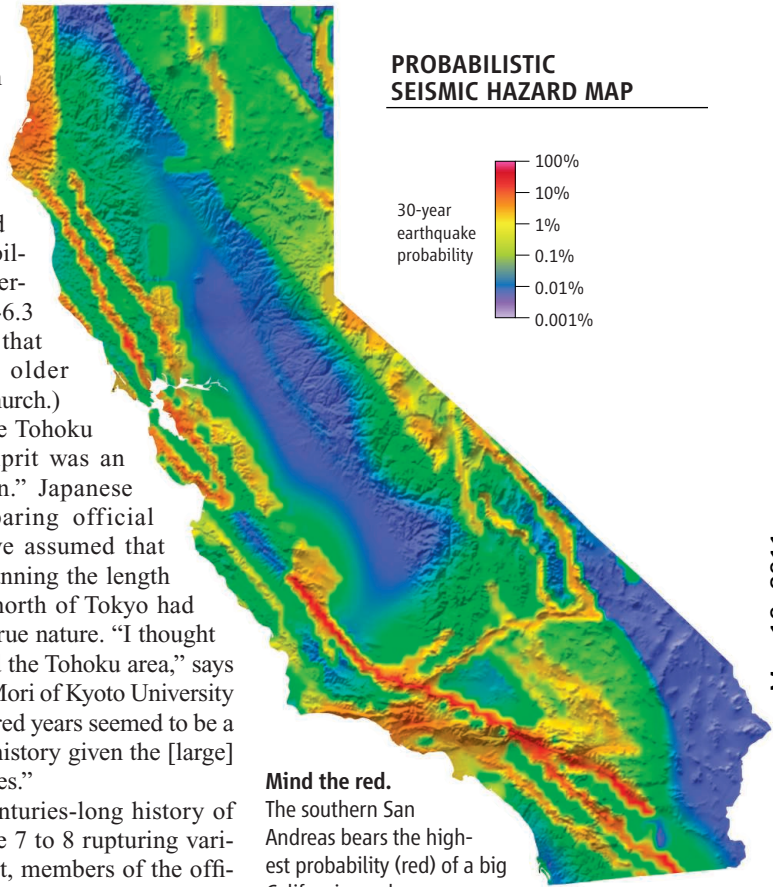

Mind the red. The southern San Andreas bears the highest probability (red) of a big California quake.

CREDIT: ADAPTED FROM THE SOUTHERN CALIFORNIA EARTHQUAKE CENTER/NSF/USGS

In spite of the obstacles, improvements are on the way. Previous official forecasts for California considered each fault segment in isolation, and they ignored aftershocks such as those that caused so much damage in New Zealand. By contrast, Field says, the next forecast, due in 2012, will allow the possibility of ruptures breaking through onto adjacent segments, such as a rupture on a side fault breaking onto the San Andreas itself. And it will also accommodate aftershocks.

Seismologists are also beginning to test their models against new earthquakes as they occur. Because larger quakes are rarer than smaller ones, their forecasts take longer to test. (Testing on California quakes for the past 5 years, for example, gets you only up to magnitude 5.) So it pays to cast as wide a net as possible. "The best strategy is testing around the globe," Stein says. He is chair of the scientific board of the GEM Foundation, a nonprofit based in Pavia, Italy, which is developing a global earthquake model to make worldwide forecasts. By including the whole world, Stein says, the model should enable scientists to test forecasts of big, damaging earthquakes in a practical amount of time.

–RICHARD A. KERR

Published by AAAS

Exploded myth? Revisionist historians hope to change alchemists' image as delusional buffoons.

HISTORY OF SCIENCE

The Alchemical Revolution

As cryptic manuscripts and centuries-old labware yield their secrets, scholars are coming to realize that medieval "chymists" were real scientists after all

For possibly the first time in 2 millennia, a chemist has used an ancient formula to transmute silver into gold. The secret, a solution called "divine water," was in an ancient Greco-Egyptian metalworking manuscript originally written on papyrus and preserved in a mummy wrapping. Following the recipe exactly (lime, sulfur, and the "urine of a youth" combined and heated "until the liquid looks like blood"), Lawrence Principe mixed chemicals under a fume hood, heated the solution over a Bunsen burner, dropped in a silver Canadian Maple Leaf coin, and watched, pleased, as the coin turned yellow.

It wasn't real gold, of course. Principe, who holds dual Ph.D.s in organic chemistry and history of science, says the layer of gold-tinted oxidation on the coin's surface might be useful for making metal ornaments look more expensive. But if the metal's color could be changed, a 3rd century thinker might have surmised, then why not its other properties? Could any base metal be transmuted entirely into gold?

Those were reasonable questions for the time, Principe believes. "Science doesn't progress ever forward in one grand, royal road," he says. "It's a twisted, thorny labyrinth with multiple pathways." Yet alchemy is certainly a thorn in the side of historians: an unwelcome reminder of science's foray into magic.

Principe and a growing number of other science historians, however, hold that alchemists—"chymists" is their preferred, less-loaded term—were serious scientists who kept careful lab notes and followed the scientific method as well as any modern researcher. He tests that hypothesis by recreating their experiments in a sunny storage closet repurposed as a small lab at Johns Hopkins University in Baltimore, Maryland. If the alchemists saw what they claimed, he says, then it's high time for an "alchemical revolution" to restore them to scientific respectability.

Garage alchemy. Working at home, William Newman replicated a chymist's possible glimpse of atomic theory.

In the view of these advocates, alchemists have been unjustly ranked with witches and mountebank performers, when in fact they were educated men with limited tools for inquiring into the nature of the universe. The mystical stories that shroud their writings suggest that they were busy recording spiritual visions. But the truth is more complex: As concerned as modern patent applicants about having their secrets stolen, chymists often coded their protocols behind a tapestry of arcane metaphors, allegories, and drawings. Their royal patrons encouraged such obscurity, worrying that successful transmutation of metal into gold would devalue their currency. And too much clarity could prove fatal at a time when falsely claiming success at transmutation might be punishable by death.

If the lives of the chymists weren't hard enough, in the late 17th century as the European Enlightenment took the stage, a rising class of scientific professionals began a deliberate campaign to smear the entire discipline. In a talk to Leiden University professors in 1718, the Dutch physician Herman Boerhaave apologized in advance about his topic. "I must talk about chemistry!" he said. "About chemistry! A subject disagreeable, vulgar, laborious, [and] far from the affairs of intelligent people." Well-known scientists such as Isaac Newton and Robert Boyle dabbled in chymistry at their peril; their work was often hidden from other scholars or suppressed, only to resurface in the 20th century. While chemistry eventually regained its good name, alchemy remained a bête noire among historians of science for centuries. Until recently, peer-reviewed journals refused to publish papers on the topic.

"The way alchemy was presented in the early 1980s was a parody, partially created in the 18th century and added to by people who didn't read the sources and tried to recraft the sources into their own ideas," Principe says. "But what was the daily activity of an alchemist? When he got up each morning and went into his workshop, what was actually in the flasks that he held? What was he thinking

CREDITS (TOP TO BOTTOM): *THE ALCHEMIST'S EXPERIMENT TAKES FIRE*, 1687/HENDRICK HEERSCHOP; DUTCH/OIL ON CANVAS LAID DOWN ON BOARD/GIFT OF FISHER SCIENTIFIC INTERNATIONAL/COURTESY OF THE CHEMICAL HERITAGE FOUNDATION COLLECTIONS/PHOTOGRAPH BY GREGORY TOBIAS; ISTOCKPHOTO; COURTESY OF BILL NEWMAN

Published by AAAS

about?" That's the question Principe says he's been working on for 30 years, "and I'm still trying to answer it. It's maybe a bit obsessive."

Obsession is what it takes: Even after cutting through all the symbolic coding, recreating experiments is difficult. "We talk about lots of these processes as though they were easy, while they actually involve a lot of tacit knowledge," says William Newman, a historian at Indiana University, Bloomington, who also works on chymistry re-creations—some of them with a furnace in his own garage. Considering that even the best post-Renaissance experimenters distilled phosphorus from urine, melted silver from whatever coins they might be carrying, and used inexact heat sources, their results were difficult, if not impossible, for them to reproduce. "You have to back-engineer to understand how the theory integrates with the practice," Newman says. "There's no better way to do that than to do the experiments themselves."

Online
sciencemag.org
Podcast interview with author Sara Reardon.

Principe's current pet project is to understand the glow of the Bologna stone: a legendary rock that, when placed in a fire, was one of the first recorded examples of natural phosphorescence. By chance, a 17th century cobbler who had put a piece of barite in his fire stumbled upon the perfect combination of factors to light it, but re-creating the process stumped centuries of chymists. Following clues from a manuscript by the 17th century natural philosopher (and alchemist) Wilhelm Homberg, Principe went to Italy and retrieved bits of barite from a field that is now a skeet-shooting range outside Bologna. In a replica he built of Homberg's oven, and measuring parameters such as temperature, pressure, and gas exchange, he's gotten them to glow faintly—just as described 300 years ago. "As I read Homberg's description, both of the stones and how you work with them, I never understood it at a really deep level until I had done it myself," Principe says.

Re-creating experiments, the historians say, helps describe how the mysteries that teased early chymists gave rise to modern science. For example, Newman traces atomic theory directly back to the early 17th century German chymist Daniel Sennert. The existence of atoms had been proposed on metaphysical grounds centuries earlier, but Sennert was the first to infer it experimentally. While researching transmutation, he found that silver could be re-isolated after being dissolved in nitric acid—evidence, Sennert concluded, that metals are made up of irreducible "corpuscles."

"A lot of scientific laws that were formulated as late as the 19th century were actually in play much earlier than we had imagined," says archaeologist Marcos Martinón-Torres of University College London. "We easily dismiss things chymists did as superstitious, but when you look further into it, they have a lot more ingenuity than we credit them for."

For instance, as early as the 14th century, many alchemists believed that their experiments would work only if their crucibles were made in the Hesse region of Germany. While excavating labs in Austria, Martinón-Torres dug up broken shards of such crucibles and analyzed their chemical makeup using scanning electron microscopy, x-ray diffraction, and other imaging techniques. It turned out there was truth behind the lore: In a 2006 paper in *Nature*, Martinón-Torres revealed that Hessian potters in the 15th century knew how to make a highly heat-resistant ceramic component now called mullite. The secret, later lost and not rediscovered until the 1920s, enabled chymists to conduct technically demanding experiments.

Martinón-Torres also analyzed traces of the chemicals the crucibles had held. For the most part, he says, the results agree with the chymists' notes. "They never discovered transmutation, but they discovered modern experimental science instead," he says—and with it tangible byproducts such as cosmetics, pigments, and medicines.

These new realizations have brought a swarm of students to the field and inspired a growing number of international conferences on alchemy. "I can't even keep up with the literature now," Principe says. History is being rewritten as scholars unearth neglected manuscripts, outing a growing number of early scientists as closet alchemists.

On one such foray, Principe recently struck a glimmer of gold. He found buried in a Russian military archive an unpublished chymistry textbook by Homberg, the official chemist of the French Royal Academy. The manuscript had been hidden since 1716; Principe spent 7 years tracking it down. In it, Homberg claimed to have discovered the philosopher's stone: the fabled element that would transmute base metals into gold.

Alchemist nouveau. Ancient manuscripts gave Lawrence Principe the recipe for "divine water" that can turn a silver coin into faux gold.

"He was an alchemist!" Principe says with glee. Homberg had covertly searched for the secret of transmutation with the Duc d'Orleans and described his successful method in his textbook, much to the chagrin of the nascent academy. "The academy is funded by the crown; they're publicly the most visible intellectuals in France. You don't want them dealing with something that has this bad reputation," says Principe, who is currently writing a biography of Homberg. "That's probably why his final manuscript was never published."

So what happens if Principe manages to re-create Homberg's last protocol right down to the pièce de résistance? "If I do, you can visit me in my lavish villa somewhere and ask me about it," he told an audience at the 2011 meeting of AAAS (publisher of *Science*). "I won't tell you about it, but I can offer you a glass of wine and we can talk about something else."

–SARA REARDON

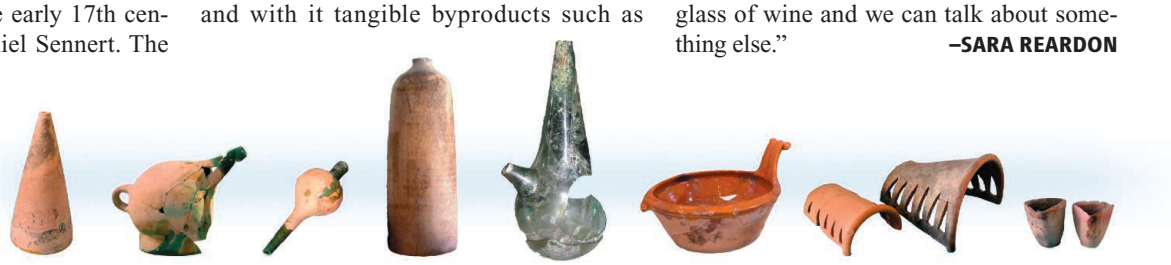

Relics of science. Flasks and beakers from 16th century labs in Austria's Oberstockstall monastery reveal what alchemists were brewing.

CREDITS (TOP TO BOTTOM): K. D. KUNTZ; COURTESY LAWRENCE PRINCIPE; MARCOS MARTINÓN-TORRES

Published by AAAS

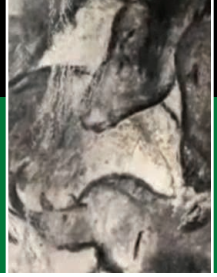

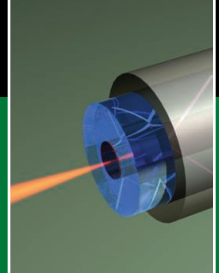

LETTERS

edited by Jennifer Sills

Unexamined Bodies of Evidence

IN HIS NEWS & ANALYSIS STORY "DO ISLAND SITES SUGGEST A COASTAL ROUTE TO THE AMERICAS?" (4 March, p. 1122), M. Balter discusses the implications of evidence that more than 10,000 years ago, people used marine resources and specialized technology on California's Channel Islands. He mentions that some archaeologists, citing Spanish ethnohistorical observations, argue against interpreting the evidence as support for a coastal route from Alaska, suggesting instead that mainlanders used the islands seasonally. Later in the story, Daniel Sandweiss notes the need for DNA studies and states, "we need to find where the bodies are."

Two such bodies, a rare double burial, were recovered during archaeological excavations at the University of California, San Diego, chancellor's residence in 1976 (*1*). Radiocarbon dating carried out in 1977 gave dates of 8730 to 9350 years before present, slightly younger than the material found at the Channel Island sites, but still very old by North American osteological standards and similar to the age of the skeleton found in Kennewick in 1996 (8340 to 9200 years before present). Stable carbon and nitrogen isotope analyses made almost 30 years ago on bone collagen extracted from the skeletons indicates year-round, not seasonal, dependence on marine mammals and subsistence on high–trophic-level fish, possibly indicative of early open-ocean fishing (*2*). Low levels of aspartic acid racemization in the bones suggest that it might be possible to retrieve endogenous DNA (*3*). With state-of-the-art ancient DNA (aDNA) extraction, amplification, and sequencing methods (*3*, *4*), there is a strong possibility that aDNA sequences will be obtained for these skeletal remains. Such information could be used to assess their genetic affiliation, if any, with modern American Indian groups.

California's Channel Islands

Unfortunately, the University of California administration has failed to honor research requests for the study of these unique skeletons. Instead, the University of California favors the ideology [see also (*5*)] of a local American Indian group over the legitimacy of science. In contrast, the 2004 Kennewick case verdict stated that there was insufficient evidence to establish that the skeleton was Native American or related to any living American Indian group (*6*). The potential loss of the La Jolla skeletons would have a profoundly negative impact on our knowledge of the peopling of the Americas and the antiquity of coastal adaptations (*7*, *8*).

MARGARET J. SCHOENINGER,[1]* JEFFREY L. BADA,[2] PATRICIA M. MASTERS,[3] ROBERT L. BETTINGER,[4] TIM D. WHITE[5]

[1]Department of Anthropology, University of California, San Diego, La Jolla, CA 92093–0532, USA. [2]Scripps Institution of Oceanography, University of California, San Diego, La Jolla, CA 92093–0212, USA. [3]Inman and Masters Consultants, 2604 Ellentown Road, La Jolla, CA 92037, USA. [4]University of California, Davis, Davis, CA 95616–8522, USA. [5]University of California, Berkeley, Berkeley, CA 94720–3140, USA.

*To whom correspondence should be addressed. E-mail: mjschoen@ucsd.edu

References

1. G. E. Kennedy, *J. New World Archaeol.* **5**, 4 (1983).
2. M. J. Schoeninger *et al.*, *Am. J. Phys. Anthropol.* **138** (suppl.), 231 (2009).
3. C. Schwarz *et al.*, *Nucleic Acids Res.* **37**, 3215 (2009).
4. H. A. Burbano *et al.*, *Science* **328**, 723 (2010).
5. A. Lawler, *Science* **330**, 166 (2010).
6. Bonnichsen v. United States, 367 F.3d 864, 876 (9th Cir. 2004).
7. R. Dalton, *Nature* **458**, 265 (2009).
8. C. Holden, *Science* **324**, 317 (2009).

Primary Prevention of Cancer

THE SPECIAL ISSUE "CANCER CRUSADE AT 40" (25 March, pp. 1539–1570) overlooked the importance of primary prevention through the identification of environmental and occupational carcinogens.

The IARC Monographs Program on the Evaluation of Carcinogenic Risks to Humans has evaluated ~1000 chemicals and exposures, finding 107 that are carcinogenic to humans, 59 that are probably carcinogenic, and 266 that are possibly carcinogenic (*1*). The National Toxicology Program (NTP) tested nearly 600 chemicals in two species of rodents, with more than half causing cancer in at least one sex of one species (*2*). The congressionally mandated National Toxicology Program Report on Carcinogens (*3*) lists 246 agents that are known (58) or reasonably anticipated (188) to be human carcinogens. Other programs, such as the Cesare Maltoni Cancer Research Center (*4*) and the California Environmental Protection Agency (EPA) (*5*), have also worked to identify risks and have found about 600 chemicals to be

Letters to the Editor

Letters (~300 words) discuss material published in *Science* in the past 3 months or matters of general interest. Letters are not acknowledged upon receipt. Whether published in full or in part, Letters are subject to editing for clarity and space. Letters submitted, published, or posted elsewhere, in print or online, will be disqualified. To submit a Letter, go to www.submit2science.org.

Published by AAAS

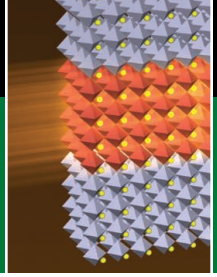

Oxides as thin slices

922

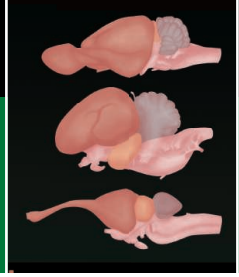

Ancestral brains

926

carcinogenic. These lists are not additive or mutually exclusive. Despite these efforts, most of the ~80,000 chemicals in commerce have not been tested for carcinogenicity.

Once a chemical has been classified as carcinogenic, regulatory agencies evaluate the information and decide how to proceed. Responses range from taking no action to banning the chemical. In the case of 1,3-butadiene (classified as a human carcinogen by IARC, EPA, and NTP), the occupational exposure standard was reduced from 1000 parts per million to 1 part per million (*6*). In another case, phenolphthalein (classified as possibly carcinogenic to humans by IARC and as reasonably anticipated to be a human carcinogen by NTP) was banned from over-the-counter pharmaceutical products based on bioassay findings. Unfortunately, any decision takes substantial time to formulate, and no action has yet been taken in the case of many identified carcinogens. Furthermore, human carcinogens that are economically important chemicals or those without easily available substitutes are rarely banned (examples of those still in use include benzene, 1,3-butadiene, and vinyl chloride monomer).

It is time to apply the knowledge we have gained through cancer bioassay results by making renewed efforts to avoid, reduce, and eliminate exposures to chemicals and agents identified as carcinogens (*7*–*10*). Using these strategies would go a long way toward primary prevention of human cancers (*11*).

JAMES HUFF

National Institute of Environmental Health Sciences, Research Triangle Park, NC 27709, USA. E-mail: huff1@niehs.nih.gov

References

1. International Agency for Research on Cancer Monographs (http://monographs.iarc.fr/).
2. National Toxicology Program, Long-Term Study Reports (http://ntp.niehs.nih.gov/index.cfm?objectid=0847DDA0-F261-59BF-FAA04EB1EC032B61).
3. U.S. Department of Health and Human Services, Public Health Service, National Toxicology Program "Report on Carcinogens, 11th Edition" (2004); http://ntp.niehs.nih.gov/?objectid=035E5806-F735-FE81-FF769DFE5509AF0A.
4. Istituto Ramazzini, CMCRC bioassay listing (www.ramazzini.it/ricerca/publications.asp).
5. State of California Environmental Protection Agency, Office of Environmental Health Hazard Assessment, "Chemicals known to the state to cause cancer or reproductive toxicity" (2011); http://oehha.ca.gov/prop65/prop65_list/files/P65List031811links.pdf.
6. Occupational Safety and Health Administration, "Final rule: Occupational exposure to 1,3-butadiene" (Department of Labor, 1997); www.osha.gov/pls/oshaweb/owadisp.show_document?p_table=PREAMBLES&p_id=740.
7. L. Tomatis *et al*., *Carcinogenesis* **18**, 97 (1997).
8. D. P. Rall, *Drug Metab. Rev.* **32**, 119 (2000).
9. L. Tomatis, R. L. Melnick, J. Haseman, J. C. Barrett, J. Huff, *FASEB J*. **15**, 195 (2001).
10. J. Huff, *Occup. Environ. Med*. **67**, 720 (2010).
11. R. L. Melnick, J. Huff, *Environ. Health* **10** (suppl. 1), S14 (2011).

TECHNICAL COMMENT ABSTRACTS

Comment on "Positive Selection of Tyrosine Loss in Metazoan Evolution"

Zhixi Su, Wei Huang, Xun Gu

Tan *et al*. (Reports, 25 September 2009, p. 1686) argued that loss of tyrosine residues from proteins in metazoans was driven by positive selection to remove potentially deleterious phosphorylation sites. We challenge this hypothesis, providing evidence that the high guanine-cytosine (GC) content of metazoan genomes was the primary driver in the loss of tyrosine residues.

Full text at www.sciencemag.org/cgi/content/full/332/6032/917-a

Response to Comment on "Positive Selection of Tyrosine Loss in Metazoan Evolution"

Chris Soon Heng Tan, Erwin Schoof, Pau Creixell, Adrian Pasculescu, Wendell A. Lim, Tony Pawson, Gary D. Bader, Rune Linding

Su *et al*. claim guanine-cytosine (GC) content variation can largely explain the observed tyrosine frequency variation independent of adaptive evolution of cell-signaling complexity. We found that GC content variation, in the absence of selection for amino acid changes, can only maximally account for 38% of the observed tyrosine frequency variation. We also uncovered other mechanisms acting to reduce tyrosine phosphorylation that further support our previous proposal.

Full text at www.sciencemag.org/cgi/content/full/332/6032/917-b

Rights for Sentient Animals

IN THE NEWS FOCUS STORY "THE RISE OF ANIMAL law" (1 April, p. 28), G. Miller reiterates the view of animal rights advocates that intelligent animals such as chimpanzees and dolphins meet the criteria of personhood and should therefore have basic rights similar to human babies or coma patients. Although there is no universal definition of personhood, it generally refers to "a thinking intelligent being that has reason and reflection, and can consider itself as itself, the same thinking thing in different times and places" (*1*). These features reflect cognitive capacities such as fast mapping, self-awareness, and episodic memory that have indeed been demonstrated in various mammals and birds (*2*–*4*). However, they are absent in human babies and coma patients, who nevertheless have basic human rights. This suggests that human rights do not depend on cognitive capacities but on membership in the human species. Therefore, neither cognitive capacities nor babies and coma patients help in making a case for extending human rights to animals.

Sentience, in contrast, is both a necessary and sufficient condition for the moral significance of animals (*5*). If applied to all sentient animals (which may include all vertebrates and possibly even some invertebrates), the abolitionist nature of animal rights would have serious consequences for our use of animals in research, in food production, and as companion animals. Restricting animal rights to intelligent animals such as chimpanzees and dolphins may have majority appeal, but it is a poor compromise. Introducing a double standard among sentient animals on the basis of cognitive capacities would likely result in fruitless controversy over which cognitive capacities are relevant, and in arbitrary discrimination against animals that may be sentient but do not possess these capacities. At least, I would expect some evidence for a positive correlation between cognitive capacity and suffering (or well-being) before promoting such a double standard, given that the correlation might in fact be negative.

HANNO WÜRBEL

Division of Animal Welfare and Ethology, Justus-Liebig-University of Giessen, Giessen, D-35392, Germany. E-mail: Hanno.Wuerbel@vetmed.uni-giessen.de

References

1. J. Locke, *An Essay Concerning Human Understanding* (1690).
2. J. Kaminski, J. Call, J. Fischer, *Science* **304**, 1682 (2004).
3. H. Prior, A. Schwarz, O. Güntürkün, *PLoS Biol*. **6**, e202 (2008).
4. N. S. Clayton, A. Dickinson, *Nature* **395**, 272 (1998).
5. G. L. Francione, *Animals as Persons: Essays on the Abolition of Animal Exploitation* (Columbia Univ. Press, New York, 2008).

Comment on "Positive Selection of Tyrosine Loss in Metazoan Evolution"

Zhixi Su,[1] Wei Huang,[1] Xun Gu[1,2]*

Tan *et al.* (Reports, 25 September 2009, p. 1686) argued that loss of tyrosine residues from proteins in metazoans was driven by positive selection to remove potentially deleterious phosphorylation sites. We challenge this hypothesis, providing evidence that the high guanine-cytosine (GC) content of metazoan genomes was the primary driver in the loss of tyrosine residues.

Tan *et al.* (*1*) reported that the genome-wide frequency of the amino acid tyrosine (Y) is inversely associated with the number of cell types and the number of tyrosine kinases in budding yeast and 15 metazoan model organisms. To explain this observation, they argued that the evolutionary process of tyrosine loss must have been driven by positive selection that removed deleterious phosphorylation sites, an adaptive mechanism to allow an increase in the number of tyrosine kinases, which in turn facilitated an increase in the number of cell types in metazoans. We present strong evidence that the increased GC content in coding and flanking regions caused by directional mutational pressure or natural selection (*2*–*5*), as well as GC isochors in warm-blooded animals (*6*), is the main driver for the reduction in tyrosine content over metazoan evolution. This is simply because tyrosine is encoded by two AU(T)-rich codons (UAU and UAC) that are underrepresented in genomes having high GC content. Hence, a more plausible evolutionary scenario is that in metazoans biased nucleotide substitutions (A/T → G/C) removed spurious tyrosine phosphorylation sites, a random genomic dynamics independent of the adaptive evolution of cell-signaling complexity.

As recognized by Tan *et al.* (*1*) and shown here in Fig. 1A, the inverse relationship between the number of cell types and tyrosine frequency collapses in the choanoflagellate *Monosiga brevicollis*, a unicellular species (with five to seven cell subtypes) (*7*) close to the metazoan lineage that contains a large number of tyrosine kinases (*8*). We note that at 54%, the GC content of the choanoflagellate genome (*9*) is much higher than that of the budding yeast (38%) and most metazoans (35% to 47%). Therefore, the low frequency of tyrosines in the choanoflagellate could be simply a consequence of its high GC content. To determine whether this is a general pattern, we conducted the following analysis on the genomes of budding yeast, metazoans, and choanoflagellate (*9*). We controlled for the GC isochores that exist in warm-blooded animals (*6*) by calculating the GC content in each species based only on the genomic regions that flank protein-coding genes (see the legend of Fig. 1B). It has been shown that the GC content of coding and contiguous noncoding sequences are highly correlated in vertebrate genomes (*10*). Impressively, Fig. 1B shows a high negative correlation between GC content and tyrosine frequency (Spearman's $R = -0.85$, $P < 1 \times 10^{-4}$; Pearson's $R = -0.81$, $P < 1 \times 10^{-4}$). We therefore conclude that GC content can explain most of the variation in tyrosine frequency among the genomes of budding yeast, metazoans, and choanoflagellate (see table S1).

The above regression analysis, which is also presented by Tan *et al.* (*1*), fails to correct for the topology of the phylogenetic tree that may inflate the significance level (*11*). Even after this potential bias is corrected (*11*, *12*), the negative re-

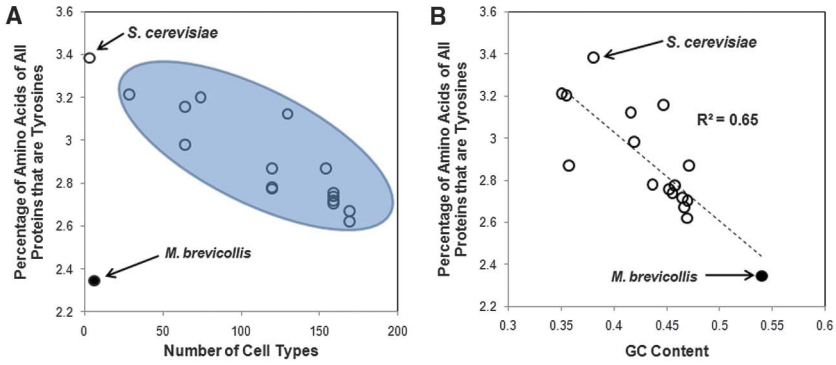

Fig. 1. Genomic GC-content bias and evolution of tyrosine kinase–related cell signaling. (**A**) Relationship between the frequency of tyrosine (Y) and the number of cell types in budding yeast (*Saccharomyces cerevisiae*) and 15 metazoans (*1*), plus a choanoflagellate (*M. brevicollis*). The number of cell types in each species was obtained from the literature (*1*, *7*). Tyrosine frequencies were calculated on all protein-coding genes; only the longest protein isoform was used. (**B**) Relationship between the frequency of tyrosine and the GC content. For each species, the GC content was calculated from upstream 2 kb and downstream 2 kb noncoding sequences surrounding all protein-coding genes. Different technical treatments, for example, analysis-based different cutoffs (such as 5 kb) in defining surrounding noncoding regions, or based on the GC content at the four-fold degenerate sites of genes (GC4) (Pearson's $R = -0.59$), GC content at third codon positions of codons (GC3) ($R = -0.62$), or GC content of all coding sequences ($R = -0.74$) (see SOM Text and table S1 for details).

Table 1. Correlations of amino acid frequency with GC content.

Amino acid	Genetic codons	Spearman's *R*†
	Encoded by GC-rich codons	
Proline (P)	CCU,CCC,CCA,CCG	0.78***
Alanine (A)	GCU,GCC,GCA,GCG	0.69**
Glycine (G)	GGU,GGC,GGA,GGG	0.73***
Tryptophan (W)	UGG	0.60*
	Encoded by AU-rich codons	
Phenylalanine (F)	UUU,UUC	−0.70**
Tyrosine (Y)	UAU,UAC	−0.85***
Asparagine (N)	AAU,AAC	−0.82***
Lysine (K)	AAA,AAG	−0.52*
Isoleucine (I)	AUU,AUC,AUA	−0.83***
Methionine (M)	AUG	−0.69**

†Conventional regression analysis: *$P < 0.05$ **$P < 0.01$ ***$P < 0.001$. After correcting the effect of phylogenetic topology (see SOM), all remain statistically significant ($P < 0.05$) except for lysine and tryptophan, although the trend is the same, probably due to the small sample size used in this study.

[1]MOE Key Laboratory of Contemporary Anthropology and Center for Evolutionary Biology, School of Life Sciences, Institutes of Biomedical Sciences, Fudan University, Shanghai 200433, China. [2]Department of Genetics, Developmental and Cell Biology, Iowa State University, Ames, IA 50011, USA.

*To whom correspondence should be addressed. E-mail: xgu@iastate.edu

lationship between the GC content and tyrosine frequency remains significant [$P < 1 \times 10^{-3}$; see Supporting Online Material (SOM) text]. Moreover, the GC-content hypothesis predicts a similar trend in other amino acids encoded by AU(T)-rich codons, such as phenylalanine (F), asparagine (N), lysine (K), isoleucine (I), and methionine (M), and an opposite trend for those amino acids encoded by GC-rich codons, such as proline (P), alanine (A), glycine (G), and tryptophan (W). Table 1 shows these two patterns as predicted, which is consistent with what is observed in bacteria (*12*). For most amino acids encoded by GC-intermediate codons (*12*), the effects of GC content are weak. These pervasive correlations suggest that it is not necessary to assume a unique adaptive mechanism to explain the variation in tyrosine frequencies among these organisms.

Our analysis provides insight into the evolution of tyrosine kinases in metazoans and choanoflagellates. Subsequent to the time these lineages split more than ~1 billion years ago, the GC content increased independently in both lineages. These increases in GC content would be expected to have resulted in losses of tyrosine sites. As suggested by Tan *et al*. (*1*), removing deleterious tyrosine phosphorylation sites may have facilitated the expansion of tyrosine kinases by gene duplications, which occurred independently in metazoans and choanoflagellates. In any case, the inverse relationship between the number of tyrosine kinases and tyrosine frequency holds in both lineages (*1*). Probably driven by natural selection, the metazoan ancestor used the increasing numbers of tyrosine kinases to enhance the evolutionary capability toward the stage of multicellularity. In choanoflagellates, the exact role of these species-specific tyrosine kinases during the process of adaptation at the organismal level remains unknown.

In conclusion, Tan *et al*. (*1*) suggested that expansion of tyrosine kinases drove the conversion of tyrosine to other amino acids. The difficulty with this argument, however, is that the frequencies of amino acids unrelated to phosphorylation are also highly correlated with the number of protein kinases, or cell types. In contrast, our hypothesis easily explains this observation. The observed changes (reductions and increases) in amino acid frequencies are simply secondary correlations due to changes in GC content (Table 1). Although tyrosine loss was clearly a by-product of GC content variation, it remains unknown exactly how it participated in the emergence in metazoans of potentially adaptive tyrosine signaling networks (*13*).

References and Notes

1. C. S. H. Tan *et al*., *Science* **325**, 1686 (2009).
2. N. Sueoka, *Proc. Natl. Acad. Sci. U.S.A.* **85**, 2653 (1988).
3. G. Bernardi, G. Bernardi, *J. Mol. Evol.* **24**, 1 (1986).
4. M. Lynch, *Proc. Natl. Acad. Sci. U.S.A.* **104** (suppl. 1), 8597 (2007).
5. L. Duret, N. Galtier, *Annu. Rev. Genomics Hum. Genet.* **10**, 285 (2009).
6. G. Bernardi *et al*., *Science* **228**, 953 (1985).
7. S. B. Hedges, J. E. Blair, M. L. Venturi, J. L. Shoe, *BMC Evol. Biol.* **4**, 2 (2004).
8. G. Manning, S. L. Young, W. T. Miller, Y. Zhai, *Proc. Natl. Acad. Sci. U.S.A.* **105**, 9674 (2008).
9. N. King *et al*., *Nature* **451**, 783 (2008).
10. M. Costantini, G. Bernardi, *Gene* **410**, 241 (2008).
11. J. Felsenstein, *Am. Nat.* **125**, 1 (1985).
12. X. Gu, D. Hewett-Emmett, W. H. Li, *Genetica* **102-103**, 383 (1998).
13. X. Gu, *J. Exp. Zool. Mol. Dev. Evol.* **312B**, 75 (2009).

Acknowledgments: This work was supported by the Shanghai Rising-Star Program (09QA1400200) to Z.S. We are grateful to P. Schnable and two anonymous referees for their insightful comments and suggestions that have improved the manuscript substantially. We also thank Tan *et al*. for pointing out erroneously computed GC4 correlations with tyrosine frequency and other discrepancies in earlier versions of this manuscript, which have now been corrected.

Supporting Online Material

www.sciencemag.org/cgi/content/full/332/6032/917-a/DC1
SOM Text
Figs. S1 to S3
Table S1
References

21 January 2010; accepted 11 April 2011
10.1126/science.1187374

Response to Comment on "Positive Selection of Tyrosine Loss in Metazoan Evolution"

Chris Soon Heng Tan,[1,2,3] Erwin M. Schoof,[4,5]* Pau Creixell,[4,5]* Adrian Pasculescu,[1] Wendell A. Lim,[6] Tony Pawson,[1,2] Gary D. Bader,[1,2,3] Rune Linding[4,5]†

Su *et al*. claim guanine-cytosine (GC) content variation can largely explain the observed tyrosine frequency variation, independent of adaptive evolution of cell-signaling complexity. We found that GC content variation, in the absence of selection for amino acid changes, can only maximally account for 38% of the observed tyrosine frequency variation. We also uncovered other mechanisms acting to reduce tyrosine phosphorylation that further support our previous proposal.

The expression of Src tyrosine kinase in the unicellular yeast *Schizosaccharomyces pombe* and *Saccharomyces cerevisiae*, whose genomes encode no tyrosine kinase, is toxic due to deleterious tyrosine phosphorylation (*1*, *2*). This raises the question of how metazoans have evolved to accommodate the numerous tyrosine kinases encoded in their genomes (e.g., 90 tyrosine kinases in humans). We proposed that an observed tyrosine depletion (OTD) in metazoan proteins—in addition to tyrosine phosphatase and spatiotemporal/contextual regulation of tyrosine kinases—helps reduce deleterious tyrosine phosphorylation (*3*, *4*). We further proposed that this accounts, at least in part, for the observed negative correlation of genomic tyrosine frequency ($Freq_{Tyr}$) with cell type number and tyrosine kinase number (Num_{TyrKin}) across different species (*3*). The mutational forces changing GC content, briefly mentioned in our original paper and highlighted by Su *et al*. (*5*), might have facilitated the OTD. However, we disagree with Su *et al*. that "biased nucleotide substitutions (A/T → G/C) removed spurious tyrosine phosphorylation sites, a random genomic dynamics independent of the adaptive evolution of cell-signaling complexity" and that GC content variation can explain most of the observed variation in $Freq_{Tyr}$.

Genetic mutations generate phenotypic variation for selection forces to act upon. Hence, the observed high GC content in metazoans does not nullify our proposal. The concern is whether the OTD has been passively driven, in the absence of selection for amino acid changes, by (i) the mutational forces behind high GC content and (ii) the selection for their effects at the nucleotide level (e.g., transcription and translation) that we collectively termed GC directional force (GC force). We computed a GC-content measure minimally influenced by amino acid selection: GC content at the third position of all four-fold degenerate codons (GC4). We correlated $Freq_{Tyr}$ with GC4 content to quantify how much OTD could be passively driven by GC force on protein-coding regions that can directly affect amino acid changes, in contrast to Su *et al*. who focus on GC content in noncoding regions. There are eight amino acids encoded by four-fold degenerate codons. The GC content at the third position for each of them (GC3) and the computed GC4 showed strong correlation with each other (see Fig. 1A). Thus, we conclude that GC4 content is a robust readout of global GC directional forces minimally influenced by amino acid selection. We also computed GC content at all codon positions (GC_{123}) for comparison.

We found that variation in GC4, GC_{123}, and Num_{TyrKin} can individually account for up to 37.6, 56.2, and 73.4% of variation in $Freq_{Tyr}$, respectively (R^2) (Fig. 1B). Adopting the approach by Su *et al*. to correct for phylogenetic relationship of species analyzed (gradual Brownian model), the statistical significance for the negative correlation of $Freq_{Tyr}$ with GC4, GC_{123}, and Num_{TyrKin} is $P = 8.5 \times 10^{-3}$, 1.6×10^{-3}, and 1.8×10^{-4} (subroutine test in R software), respectively (*6*). The GC4 content of a subset of species does correlate negatively with $Freq_{Tyr}$ (Fig. 1B, yellow ellipse), but the trend is reversed in several other lineages (Fig. 1B, blue ellipse). In contrast, $Freq_{Tyr}$ covaries more consistently with Num_{TyrKin} across different lineages (Fig. 1B). Performing an orthogonal analysis using a generalized additive linear model (*7*, *8*), which models the effects of multiple parameters on a variable simultaneously, we also observed that $Freq_{Tyr}$ correlates better with Num_{TyrKin} than with GC4 (Table 1). These results invalidate Su *et al*.'s claim that GC content variation alone can explain most of the observed variation in $Freq_{Tyr}$. As GC directional forces on coding regions directly influence amino acid frequency in the absence of selection forces, we question why Su *et al*. chose to emphasize the correlation of $Freq_{Tyr}$ with GC content variation in noncoding regions while not commenting on the results of GC4 variation in coding regions. As we are studying protein evolution, it is more relevant to focus on protein-coding DNA regions.

Although we previously acknowledged that other mechanisms may have contributed to the OTD, we supported our proposal with empirical data that human proteins with no detectable phosphotyrosines (non-pTyr proteins) have lost considerably more tyrosines than known tyrosine-phosphorylated proteins (pTyr proteins), as compared with their *S. cerevisiae* orthologs (*3*). Here, we extended this analysis to *S. pombe* and reached the same conclusion (Fig. 2A). Yeasts are compared because they are the known eukaryotes phylogenetically closest to human that lack a dedicated phosphotyrosine signaling system, and we implicitly assume both species are informative of the ancestral tyrosine frequency. Our conclusion is supported by the observation that phenylalanine is not lost preferentially in either protein group (Fig. 2A). This is crucial because phenylalanine and tyrosine are structurally identical except for a phosphorylatable hydroxyl group on tyrosine, and are each encoded by two AT-rich codons (Phe: TTT and TTC; Tyr: TAT and TAC), and thus should be subjected to a similar degree of GC force. Hence, the observed preferential loss of tyrosine is due to the presence of its hydroxyl group and strongly supports the argument that signaling fidelity is a driving force behind OTD.

During evolution, phenylalanine and tyrosine are commonly substituted for each other because of their similar physicochemical properties and encoding codons [see BLOSUM matrices, for example (*9*)]. We investigated their substitution pattern from yeast to human. As expected, tyrosines in yeast are most frequently substituted with phenylalanine (~35%) in human, whereas phenylalanine and tryptophan in yeast are frequently substituted with tyrosine in human (Fig. 2B). However, we observe that the substitution of phenylalanine and tryptophan in yeast by tyrosine in human is significantly underrepresented in non-pTyr proteins compared with pTyr proteins (Fig. 2B) ($P < 10^{-7}$, Fisher's exact test, one-tailed). This phenomenon is minimally influenced by GC force because only T ↔ A substitution is required to directly switch between phenylalanine and tyrosine. We detected no statistical difference ($P < 0.01$, Fisher's exact test, two-tailed) in the substitution of tyrosine in yeast with phenylalanine and tryptophan in human between the two protein groups. Thus, constrained substitution of phenylalanine and tryptophan with tyrosine is possibly another mechanism contributing to OTD and supports our observation that there is selection pressure to remove tyrosines for signaling fidelity.

[1]Samuel Lunenfeld Research Institute, Mount Sinai Hospital, Toronto, Canada. [2]Department of Molecular Genetics, University of Toronto, Toronto, Canada. [3]The Donnelly Centre, University of Toronto, Toronto, Canada. [4]The Institute of Cancer Research (ICR), London, UK. [5]Cellular Signal Integration Group (C-SIG), Center for Biological Sequence Analysis (CBS), Department of Systems Biology, Technical University of Denmark (DTU), DK-2800 Lyngby, Denmark. [6]Howard Hughes Medical Institute and Department of Cellular and Molecular Pharmacology, University of California, San Francisco, USA.

*These authors contributed equally to this work.
†To whom correspondence should be addressed. E-mail: linding@cbs.dtu.dk

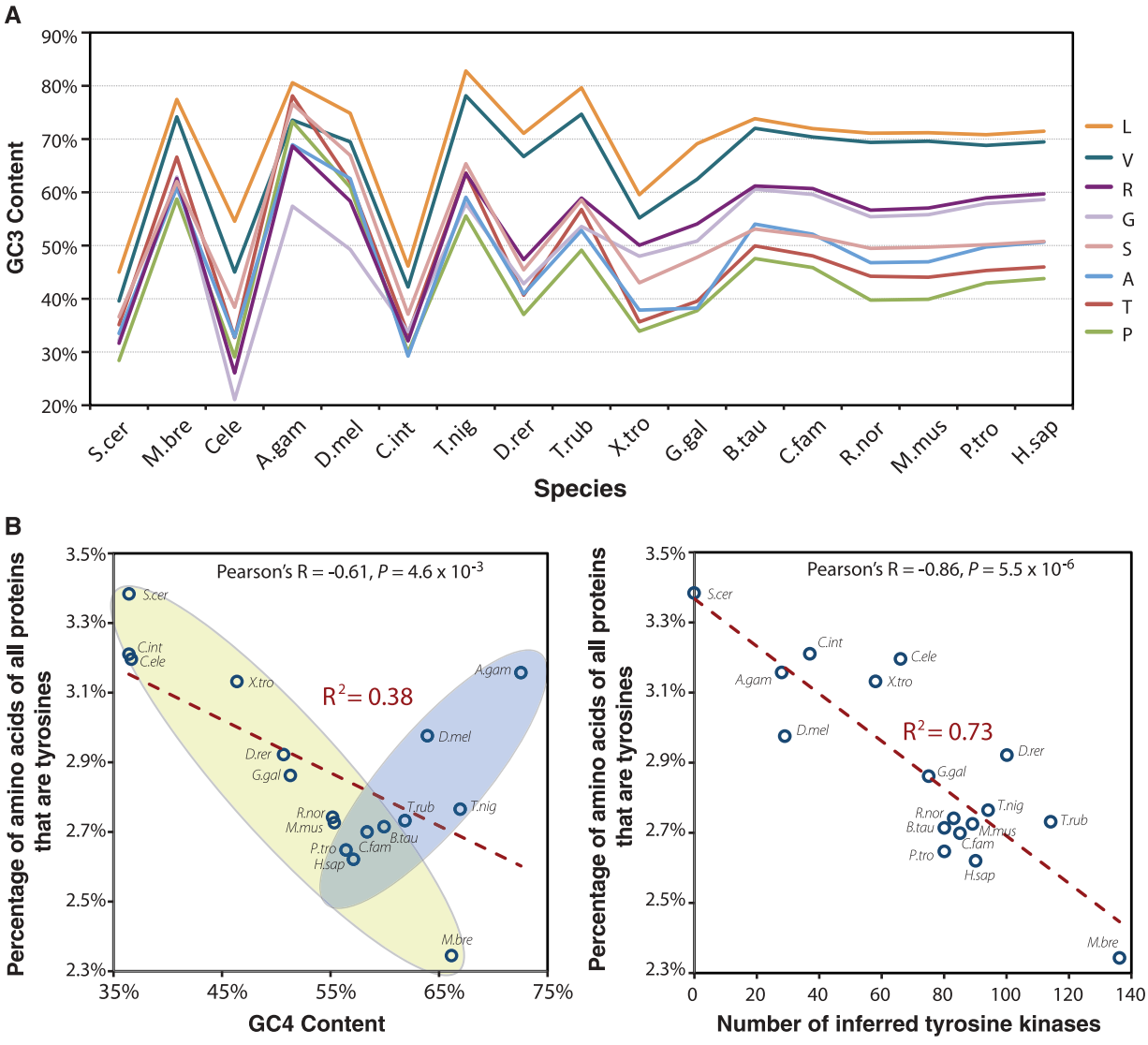

Fig. 1. (**A**) GC content at the third codon position (GC3) for each set of four-fold degenerate codons in all coding sequences in different species. The four-fold degenerate codon set of each amino acid are GCN (alanine), CGN (arginine), GGN (glycine), CTN (leucine), CCN (proline), TCN (serine), ACN (threonine), and GTN (valine). The species are sorted with decreasing evolutionary distance from human. The GC3 content for these eight amino acids are highly correlated with each other (average Pearson's correlation = 0.85, SD = 0.11). GC3 content for all sets of four-fold degenerate codons are summed to derive the GC4 content for each species. The GC4 content is strongly correlated with GC3 content of these eight amino acids across the species analyzed (average Pearson's correlation = 0.96, SD = 0.036). (**B**) Correlation of genomic tyrosine frequency ($Freq_{Tyr}$) with GC4 content and inferred number of tyrosine kinases (Num_{TyrKin}) in species analyzed. Num_{TyrKin} are inferred as previously described (*3*) except for *Monosiga brevicollis*, which is based on (*14*). The low $Freq_{Tyr}$ and high Num_{TyrKin} observed in *M. brevicollis* is consistent with our proposed evolutionary model (*3*). The species analyzed are budding yeast (*S. cerevisiae*), choanoflagellate (*M. brevicollis*), worm (*Caenorhabditis elegans*), sea squirt (*Ciona intestinalis*), fly (*Drosophila melanogaster*), mosquito (*Anopheles gambiae*), zebrafish (*Danio rerio*), tetraodon pufferfish (*Tetraodon nigroviridis*), Japanese pufferfish (*Takifugu rubripes*), frog (*Xenopus tropicalis*), chicken (*Gallus gallus*), dog (*Canis familiaris*), cow (*Bos taurus*), mouse (*Mus musculus*), rat (*Rattus norvegicus*), chimpanzee (*Pan troglodytes*), and human (*Homo sapiens*). Looking at the closest pairs of species in five lineages (*R.nor/M.mus*, *P.tro/H.sap*, *C.fam/B.tau*, *T.rub/T.nig*, and *D.mel/A.gam*), a negative relationship between $Freq_{Tyr}$ and Num_{TyrKin} is observed for all five species pairs. Contradicting Su *et al.*'s claim, a positive correlation between $Freq_{Tyr}$ and GC4 is observed for three species pairs (*C.fam/B.tau*, *T.rub/T.nig*, and *D.mel/A.gam*).

Next, for the set of tyrosines that are conserved between human and *S. cerevisiae* as identified from sequence alignments, we applied the NetPhorest algorithm (*10*) to investigate their propensity to be phosphorylated by human tyrosine kinases that are influenced by residues flanking the tyrosines on primary sequences. In general, we found that tyrosines from human are less phosphorylatable by human tyrosine kinases than the corresponding tyrosines from *S. cerevisiae* (Fig. 2C) ($P = 5.34 \times 10^{-5}$, Wilcoxon Test). This suggests that there are selection forces favoring mutations flanking tyrosines that reduce tyrosine phosphorylation.

In summary, we contend that our analysis invalidates Su *et al.*'s claims. Furthermore, we uncovered multiple plausible mechanisms acting to reduce tyrosine phosphorylation. Hence, we suggest that using GC content variation as an Occam's Razor, without considering the physicochemical properties of amino acids in relation to the study of biological systems, can compromise our understanding of similar phenomena. Su *et al.* concur with us that low $Freq_{Tyr}$ permitted the expansion of tyrosine kinases through reducing deleterious phosphotyrosines. Reciprocally, an increased Num_{TyrKin}, other than promoting

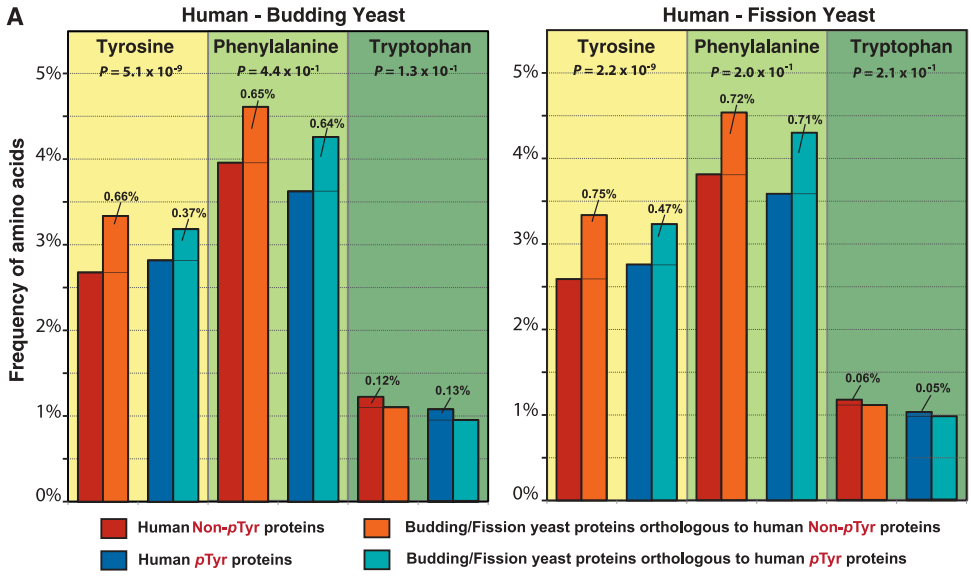

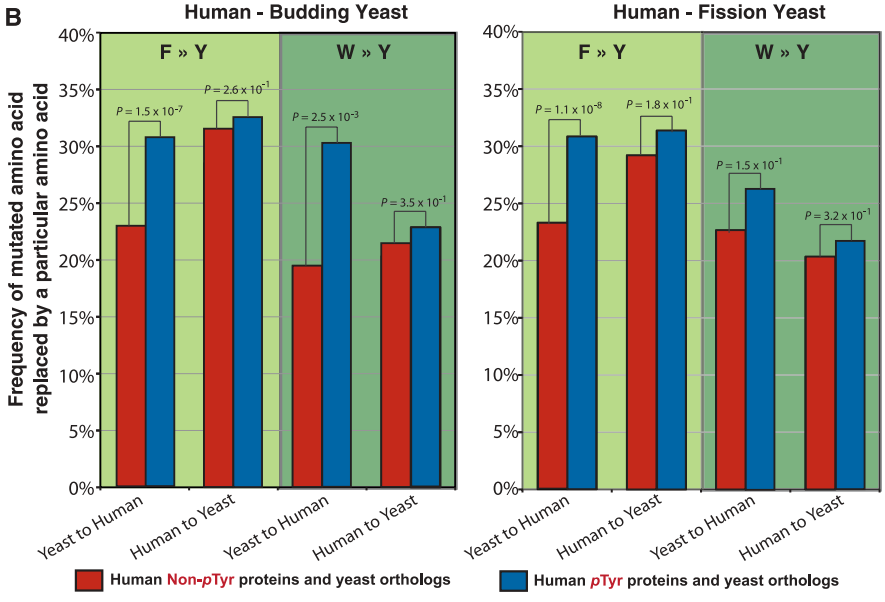

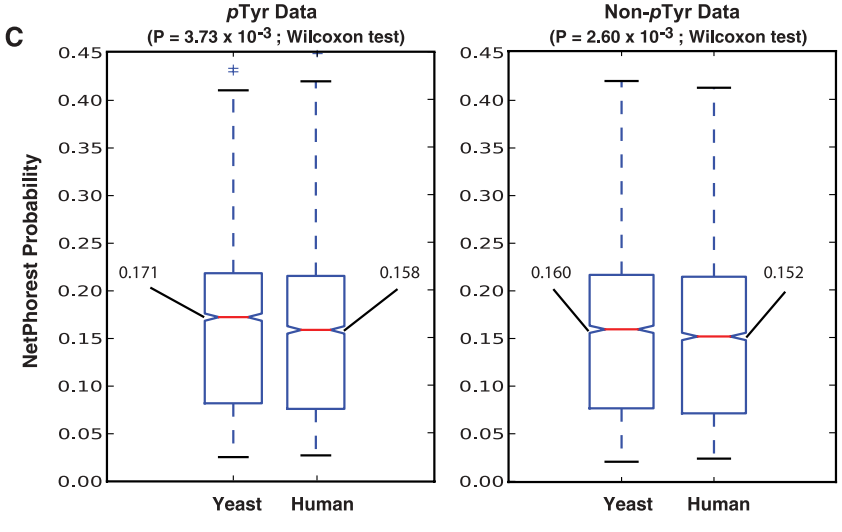

Fig. 2. (**A**) Frequency of tyrosine, phenylalanine, and tryptophan in human tyrosine-phosphorylated (pTyr) proteins, human non–tyrosine-phosphorylated (non-pTyr) proteins, and their protein orthologs in budding yeast (*S. cerevisiae*) and fission yeast (*S. pombe*). Tyrosine, but not phenylalanine and tryptophan, is preferentially depleted in non-pTyr proteins over pTyr proteins. Classification of pTyr and non-pTyr human proteins is based on empirical data [as previously described (*3*)], which are available in (*15*). Human protein orthologs in budding yeast and fission yeast are inferred using Inparanoid as described in (*3*), and only proteins with an inferred one-to-one orthologous relationship are used. Phenylalanine and tyrosine are structurally identical except for the hydroxyl group on tyrosine that renders the residue phosphorylatable. Tryptophan is also included for comparison because it is physicochemically similar to phenylalanine and tyrosine. Statistical significance indicated is for differences in the distribution between pTyr and Non-pTyr protein sets for observed differences in amino acid frequency of human-yeast orthologous protein pairs, computed with Mann-Whitney test (one-tailed) as previously described (*3*) using R (*16*). (**B**) Observed substitution of phenylalanine and tryptophan by tyrosine between human and yeasts. Pairwise sequence alignments between orthologous protein pairs are performed using MAFFT with default parameters (*17*). We then computed the frequency of mutated phenylalanine and tryptophan being substituted with tyrosine from yeast to human and vice versa. To reduce error due to faulty alignments, residues with fewer than five identical aligned flanking residues out of 10 positions (five on each side) are excluded. We observed that the substitution rate of phenylalanine by tyrosine from yeast to human for pTyr proteins is similar to the rate for human to yeast. However, the rate is significantly lower for non-pTyr from yeast to human. Statistical significance of observed differences is computed with Fisher's exact test (one-tailed) using R. (**C**) Lower phosphorylation propensity of tyrosines in human compared to *S. cerevisiae*. Tyrosines conserved between human and *S. cerevisiae*, as identified from pairwise sequence alignments, are tested for their phosphorylation propensity by human tyrosine kinases using the NetPhorest algorithm (*10*). Proteins with experimentally observed phospho-tyrosines (pTyr) are tested separately from proteins that have no experimentally observed phospho-tyrosines (non-pTyr). The median probabilities are labeled for each data set, and the indicated *P* values were calculated using the Wilcoxon test.

Table 1. Statistical linear models for correlation between tyrosine frequency ($Freq_{Tyr}$) and one or more of the variables GC4 content (GC4) and tyrosine kinase number (Num_{TyrKin}). Results are produced with R (*16*). AIC, Akaike information criterion (lower values indicate a better model). Pr, probability. The last column is a visual indicator of the significance of the estimated parameters: ***$P < 0.001$; **$P < 0.01$; *$P < 0.05$.

Statistical linear model	AIC	R^2	R^2 adjusted	Variables	Estimate	Std. Error	t	Pr (>|t|)	P
$Freq_{Tyr}$ ~ GC4	0.80	0.363	0.32	(Intercept)	3.63	0.265	13.71	6.83×10^{-10}	***
				GC4	−0.0147	0.00505	−2.92	1.05×10^{-2}	*
$Freq_{Tyr}$ ~ Num_{TyrKin}	−14.13	0.735	0.72	(Intercept)	3.37	0.0840	40.11	$<2 \times 10^{-16}$	***
				Num_{TyrKin}	−0.00675	0.00105	−6.45	1.09×10^{-5}	***
$Freq_{Tyr}$ ~ GC4 + Num_{TyrKin}	−19.58	0.829	0.80	(Intercept)	3.71	0.143	26.05	2.92×10^{-13}	***
				GC4	−0.00808	0.00291	−2.78	1.49×10^{-2}	*
				Num_{TyrKin}	−0.00579	0.00094	−6.18	2.39×10^{-5}	***

tyrosine-removing mutations, could also constrain new tyrosine appearance to favor $Freq_{Tyr}$ change unidirectionally. We found it interesting, based on Su *et al*.'s result, that $Freq_{Tyr}$ negatively correlates better with GC content in flanking noncoding regions than with GC4 content and wonder whether CpG dinucleotide site and transcription initiation are attributing factors. If increased GC content does associate with increased gene and protein expression (e.g., abundance and multitissue expression) reported in studies (*11*–*13*), we speculate that it helps to remove more tyrosines to counter increased encounters of cellular proteins with tyrosine kinases.

References and Notes

1. G. Superti-Furga, S. Fumagalli, M. Koegl, S. A. Courtneidge, G. Draetta, *EMBO J.* **12**, 2625 (1993).
2. G. Superti-Furga, K. Jönsson, S. A. Courtneidge, *Nat. Biotechnol.* **14**, 600 (1996).
3. C. S. H. Tan *et al*., *Science* **325**, 1686 (2009).
4. R. Linding *et al*., *Cell* **129**, 1415 (2007).
5. Z. Su, W. Huang, X. Gu, *Science* **332**, 917 (2011); www.sciencemag.org/cgi/content/full/332/6032/917-a.
6. To address Su *et al*.'s criticism directly, we applied the gradual Brownian model as described in the supporting online material (SOM) of Su *et al*., using the species tree inferred by them. The contrast program in PHYLIP software suite computed $R = -0.66$ and $R = -0.83$ for the correlation of $Freq_{Tyr}$ with GC4 and Num_{TyrKin}, respectively. Even without this sophisticated analysis, we already observed that $Freq_{Tyr}$ shows a stronger covariance with Num_{TyrKin} than with GC4 among pairs of closely related species in a phylogenetic-aware manner (see Fig. 1B). The computed contrast values are in the SOM for this paper.
7. S. N. Wood, *Generalized Additive Models: An Introduction with R* (Chapman & Hall/CRC, Boca Raton, FL, 2006).
8. J. J. Faraway, *Linear Models with R* (Chapman & Hall/CRC, Boca Raton, FL, 2004).
9. S. Henikoff, J. G. Henikoff, *Proc. Natl. Acad. Sci. U.S.A.* **89**, 10915 (1992).
10. M. L. Miller *et al*., *Sci. Signal.* **1**, ra2 (2008).
11. A. E. Vinogradov, *Trends Genet.* **21**, 639 (2005).
12. G. Kudla, L. Lipinski, F. Caffin, A. Helwak, M. Zylicz, *PLoS Biol.* **4**, e180 (2006).
13. J. M. Landolin *et al*., *Genome Res.* **20**, 890 (2010).
14. G. Manning, S. L. Young, W. T. Miller, Y. Zhai, *Proc. Natl. Acad. Sci. U.S.A.* **105**, 9674 (2008).
15. C. S. H. Tan *et al*., *Sci. Signal.* **2**, ra39 (2009).
16. R Foundation for Statistical Computing, www.R-project.org.
17. K. Katoh, H. Toh, *Brief. Bioinform.* **9**, 286 (2008).

Acknowledgments: We thank B. Liu for reference assistance, reviewers for their critical comments, and all our colleagues for their feedback on the initial finding that has greatly improved the present work. R.L. and this work are supported by a Human Frontier Science Program (HFSP) Career Development Award.

Supporting Online Material

www.sciencemag.org/cgi/content/full/332/6032/917-b/DC1
SOM Text
References

19 March 2010; accepted 26 April 2011
10.1126/science.1188535

SCIENCE IN FILM

Truly Multidimensional

The nexus of art and science is nowhere as tantalizing as in places like Grotte Chauvet. Discovered in December 1994 by three speleologists, the cave in southern France is generally thought to contain the world's earliest known cave paintings. Dated to as old as 30,000 to 32,000 radiocarbon years ago, the Chauvet paintings speak directly to archaeologists, paleontologists, and geologists—as well as art historians, painters, and writers—about the roots of our species' obsession to create.

Cave of Forgotten Dreams
Werner Herzog, Director
Creative Differences Productions and History Films, France/Canada/USA/UK/Germany, 2010.
90 minutes.
www.caveofforgottendreams.co.uk

Werner Herzog, one of cinema's ablest chroniclers of various kinds of human obsession, delivers his own perspective on the Chauvet Pont-d'Arc cave in *Cave of Forgotten Dreams*. The documentary premiered at the Toronto International Film Festival in September 2010 and has been released commercially in the United States and the United Kingdom this spring. To prevent deterioration of the paintings, the French Ministry of Culture carefully controls access to the cave. The ministry granted Herzog special permission to descend into the cave but required the filmmaker and his three-person team to wear sterile boots, use only special heat-free lamps to illuminate the cave walls, and complete their shooting in six brief, four-hour visits. The result is a film that feels roughhewn and sometimes frustratingly incomplete—but that should still be seen, and seen on a big screen, by anyone with an interest in what makes humans human.

Herzog, who wrote and narrates the film, is plainly fascinated by the site's science and by the researchers who are exploring the cave's archaeology and geology. He effectively uses meticulous laser-scanning data compiled by scientists to convey the cave's scale and shape. A particularly successful segment presents an interview with cave art specialists Carole Fritz and Gilles Tosello, who have painstakingly used photographs, drawings, and arguments based on superposition to reconstruct the creative steps that led to the cave's celebrated Horse Panel (which comprises two rhinoceroses locking horns, the heads and upper bodies of three wild cattle, and four horse heads). They conclude that much of the panel was the work of a single, supremely gifted artist—a Rembrandt among the small, talented group that descended into the cave to make its mark.

Yet those seeking a complete, or conventional, documentary treatment should look elsewhere. Nowhere, for example, does Herzog mention the doubts that some academics outside of the core French team have raised regarding the extreme antiquity of the paintings, claimed to predate the archetypal cave art at Lascaux by as much as 15,000 years (*1*). Instead, Herzog's project clearly reflects his own career as a filmmaker and the idiosyncratic vision he has carved out in some 50 films since 1968. He seems, indeed, interested not so much in what science tells us about the cave and its artists as in what it cannot tell us across what he refers to as the "abyss of time." At one point, during an otherwise engaging conversation with a young researcher (and former circus performer) working on the laser-mapping project, Herzog compares the undertaking to assembling the thousands and thousands of names and numbers in the Manhattan telephone directory—an impressive data set, but one that, according to Herzog, can say little about the people's daily lives, their families, and their dreams.

Much of the film's publicity has dwelt on the fact that it was shot in 3D format. While sometimes distracting in the exterior sequences, the technique works marvelously within Grotte Chauvet itself, documenting the tunnels and constricted passages, the calcite stalagmites thrust up like immense fingers from the cave floor, and especially the curves and contours of the rock walls themselves. Those contours, Herzog aptly notes, form an integral part of the artwork, accent the play of torchlight and shadow, and even impart a sense of motion that, from his perspective, makes the Chauvet art a sort of "proto-cinema."

The film is at its most effective, however, when Herzog ceases his narration entirely and lets the art speak for itself. The most impressive and moving sequence comes near the end, when—amid vocal and flute music of unearthly beauty, composed by Ernst Reijseger—the camera moves serenely among the paintings on the carefully lit cave wall. Here, Herzog's instincts as a master of arresting imagery take over, and he finally provides a true sense of the accomplishment of Chauvet—and the human drive and mystery behind it—that the film previously articulated only imperfectly.

Regrettably, Herzog undermines his own achievement though a bizarre "postscript" involving a nearby nuclear power plant, an artificial biosphere, and a pair of albino crocodiles, all of which he attempts, with limited success, to tie back to the human experience of the cave. Yet, fortunately, after the film, it is the art itself to which the mind returns. And all of us who will never set foot inside Grotte Chauvet should be thankful that Herzog has made the journey for us and given us a record of it in this unique and visionary film.

–Stewart Wills

References
1. M. Balter, *Science* **321**, 904 (2008).

10.1126/science.1207841

CREDIT: CREATIVE DIFFERENCES PRODUCTIONS

Published by AAAS

SCIENCE EDUCATION

Inquiry-Based Writing in the Laboratory Course

Writing lab reports in science classes can be more productive and engaging if the experience is structured well.

Cary Moskovitz[1]* and David Kellogg[2,3]

Scientific writing is increasingly recognized as a key component of an undergraduate scientific education. As an integral part of scientific practice, scientific writing is best learned in the context of doing science (*1*, *2*). Because students "do" science (as opposed to "learn about" science) almost exclusively in laboratory courses (*3*, *4*), they need to learn the skills of scientific writing there.

The inadequacies of the traditional lab, in which students go through the motions of laboratory work in a series of "cookbook" activities, have been widely recognized. Inquiry-based approaches to lab instruction are transforming the undergraduate lab by having students undertake actual experiments designed to help them learn to think scientifically (*5*–*7*). However, educational reform has yet to overcome the inertia of the traditional school "lab report." Even in inquiry-based settings, such lab reports remain largely inauthentic and make-work affairs, involving little actual communication beyond the implicit argument for a good grade. Real scientific writing, on the other hand, involves a variety of rhetorical functions including persuading skeptical audiences, constructing interpretive frameworks, refuting the work of others, and so forth.

In short, the inquiry philosophy has not yet been extended to include what might be called "inquiry-based writing." In our view, successful inquiry-based writing requires three modifications to the inquiry lab. First, lab courses should give students practice in forms of writing actually used by scientists. Second, writing tasks must be aligned with the activity of the lab so that students have something meaningful to say. And third, student writing must have a real audience (see the chart).

Forms of Writing in the Lab Course

Broadly speaking, recent reforms to writing in the lab course can be classified as either "writing to learn" (WTL) or "writing as professionalization" (WAP). Much of this work has taken place in chemistry education (*8*). In the WTL approach, writing tasks are designed to help students engage with the scientific method and learn scientific ideas by reflecting on their experience. An exemplary version is the Science Writing Heuristic (SWH), which reframes the traditional school lab report as guided questions, providing opportunities for personal reflection about both the science and the scientific process (*9*). For example, in contrast with traditional lab reports—in which students insert content into boxes labeled "Methods," "Results," and so on—the SWH asks students to address thought-provoking questions such as "What can I claim?" and "How do I know?" (*10*).

In WTL, writing is primarily a tool to enhance scientific learning; it treats writing as a means rather than an end. When scientific writing is taught without regard to rhetorical function, expectations set for student reports are likely to be at odds with those of professional scientific discourse. SWH instructors, for example, are expected to check whether each student "lists all data" (*11*). Yet a key skill in communicating science is selecting which data to present.

The first step toward inquiry-based lab writing is to assign forms of writing that working scientists use. This step has been taken by the WAP approach (*12*). Students in WAP classes produce professional forms such as the conference poster; the research proposal; the review article; and, in the lab course especially, the experimental research report (*13*–*15*).

But because lab courses do not generally replicate the professional research settings that produce actual journal articles, assigning the experimental report brings its own pedagogical challenges. Consider what happens in the introductory sections of the typical research report: Researchers describe a knowledge gap in the literature and then explain how their current research fills that gap (*16*). But even in an inquiry-based lab, students have no research agenda and lack the breadth of knowledge needed to discuss their experiments in the context of the primary literature. Writing standard introductions for such labs can only be a sham. Students are not positioned to learn how to write such introductions until they have a scientific idea of their own to advance and at least a cursory knowledge of the related literature, probably late in their undergraduate studies.

The same problem exists with the teaching of the Methods (or Experimental) section. Because teaching the entire scientific paper at once is inherently problematic, one described strategy is to begin with the part that seems easiest on the surface: the Methods (*14*). Yet asking students to write Methods for experiments where the procedure is specified in detail in a lab manual, a common practice in WAP-style courses, requires that they engage in yet another kind of sham, because there is little for them to do but parrot back selected details from the manual. As students well know, those

Designing effective inquiry-based writing assignments

Give students practice in authentic forms of scientific writing

Consider a wide variety of professional genres, including experimental reports, methods papers, proposals, and peer reviews.

Consider only part of a genre as a whole assignment

Ensure that students have something meaningful to say

Design assignments for the curriculum rather than the individual course.

Assign only those parts of a genre that match the realities of the lab setting.

Abandon any part of an assignment that lacks an authentic communicative function.

Create a real communication scenario

Position students as apprentice scientists.

Position instructors as scientific readers.

Assign only as much writing as instructors can read and respond to thoughtfully.

[1]Thompson Writing Program, Duke University, Durham, NC 27708, USA. [2]Department of English, Coastal Carolina University, Conway, SC 29528, USA. [3]Department of Biological Sciences, National University of Singapore, Singapore 117543.

*Author for correspondence. E-mail: cmosk@duke.edu

Published by AAAS

who will actually read these reports already know what was done. Devoid of an authentic communicative purpose, students have no basis for deciding which details should be included. Students should learn to write Methods in more advanced lab courses when they are designing their own experiments or at least substantially altering standard protocols.

Alignment and Audience

The second step toward inquiry-based lab writing is aligning student writing with lab activity. Short of the independent research project, no undergraduate course can replicate the total context of the research environment necessary to produce experimental reports in full. But if we relax the assumption that students must produce entire experimental reports for every lab or even in every course, we can design tasks that give students something to say: Introductions are written by advanced students undertaking original research; methods, by intermediate students who design experiments. In most lower-level labs, students have no research agenda nor do they design experiments. They do, however, generate and evaluate data; thus students at this stage can present and discuss results.

Yet to fully engage in laboratory writing, student authors need not only something to say, but also someone to say it to. Of the methods common approaches to laboratory writing considered here, WTL is not particularly concerned with the reader, and WAP assignments typically ask students to imagine that they are addressing, broadly, scientists in the field, an abstraction that means little and provides little useful guidance to novices. Therefore, the third and final step toward inquiry-based writing is to provide students a tangible audience for their written work.

Picture the standard introductory-level titration lab. Now imagine that some students receive contaminated reagents, but they do not know who received which. Now, imagine that students are given, at random, either contaminated or uncontaminated reagents, but they do not know who received which. This inquiry-based version engages students in meaningful scientific inquiry, and yet the instructor still operates primarily as a grader. But if the instructors, too, are kept ignorant of the distribution of reagents, they cannot know what the results should be. Instead of grading a product in which claims match expected outcomes (*11*), they must read student writing as scientists, evaluating how clearly and convincingly each case is made. And once instructors shift from mere graders to readers, students cannot merely reproduce the form of scientific argument but must actually make scientific arguments (*17*).

What would inquiry-based writing in this lab look like? No longer compelled to have students write an introduction or describe methods, we might ask them to write only a single, well-designed page. This page would include a main claim supported by key results, appropriate visual displays, analysis of error, and so forth. Although considerably shorter than the typical lab report, this assignment makes authentic rhetorical demands, requiring students to argue for an interpretation of their data under constraints typically faced by the writing scientist. Similar to the body of a "letter" or "short communication," this highly condensed writing can help students learn to construct a representation of their data that is both selective and compelling (does not ignore results that challenge the hypotheses).

The Inquiry-Based Writing Lab

When writing tasks are integral to lab activity and when student writing has a real audience, students are more likely to find such tasks meaningful and engaging, and instructors can respond to such writing as the scientists they are, rather than as evaluators of standardized work or grammarians. Further, eliminating unproductive writing tasks allows both student and instructor to spend more time doing important work. Students can concentrate on a limited number of skills that are essential for writing science but rarely the subject of extended instruction: how to decide which data to present; how to use graphs, tables, and other visual displays effectively; and how to discuss those graphic supports in the accompanying prose. Instructors in turn can demand higher-quality work and provide more-useful feedback.

Some may worry that under our proposal students will not learn how to write a complete research report. Although undergraduate science majors should have the opportunity to design their own experiments and take on a scientific research project of their own (*5*), this is unlikely before the senior year. The senior-year research project therefore provides the proper occasion for learning to write the research report in its entirety.

Those who oversee undergraduate science labs may have pragmatic concerns about the cost of change: the time involved in redesigning assignments, the need to train teaching assistants differently, the need to rethink evaluation, and so forth. All serious pedagogical reform has costs, especially reform involving deep changes in mindset and practice. But there are long-term savings as well, when we consider the reductions in the amount of writing students produce.

Many institutions may find it impractical to implement all three proposed modifications at once. Thus, we suggest implementing change in the order we have described, as each modification is a precondition for the next. Finally, some instructors and students will find the transformation uncomfortable. But just as with inquiry-based labs, transitional discomfort is necessary to gain the advantages provided by a more realistic approach.

What is required of inquiry-based writing is precisely what is evaluated in day-to-day communication among scientists: care and integrity in handling data, clarity and persuasiveness of communication, relevant and compelling results. If we are serious about improving students' abilities as scientific communicators, we must take them seriously both as apprentice scientists and as apprentice writers of science.

References and Notes

1. D. Russell, in *Reconceiving Writing, Rethinking Writing Instruction*, J. Petraglia, Ed. (Erlbaum, Hillsdale, NJ, 1995), pp. 51–78.
2. N. Lerner, *Writ. Commun.* **24**, 191 (2007).
3. L. Jackson, W. Meyer, J. Parkinson, *Engl. Specif. Purposes* **25**, 260 (2006).
4. G. Braine, *Engl. Specif. Purposes* **8**, 3 (1989).
5. National Research Council, *Transforming Undergraduate Education in Science, Mathematics, Engineering, and Technology* (National Academies Press, Washington, DC, 1999).
6. National Research Council, *Inquiry and the National Science Education Standards: A Guide for Teaching and Learning* (National Academy Press, Washington, DC, 1997).
7. D. J. Adams, *Bioscience Educ.* **13**(3), 1 (2009); (www.bioscience.heacademy.ac.uk/journal/vol13/beej-13-3.pdf).
8. M. J. Elliott, K. K. Stewart, J. J. J. Lagowski, *Chem. Educ.* **85**, 145 (2008).
9. T. J. Greenbowe, J. R. Poock, K. A. Burke, B. M. Hand, *J. Chem. Educ.* **84**, 1371 (2007).
10. K. A. Burke, T. J. Greenbowe, B. M. Hand, *J. Chem. Educ.* **83**, 1032 (2006).
11. K. A. Burke, T. J. Greenbowe, B. M. Hand, excerpts from "The process of using inquiry and the science writing heuristic," prepared for the Middle Atlantic Discovery Chemistry Program, Moravian College, Bethlehem, PA, 5 and 6 June 2005; http://avogadro.chem.iastate.edu/SWH/swhwkshpmanual.pdf.
12. Asking students to write professional forms in the lab is not itself a new idea (*18*).
13. D. E. Gragson, J. P. Hagen, *J. Chem. Educ.* **87**, 62 (2010).
14. P. J. Alaimo, J. C. Bean, J. M. Langenhan, L. Nichols, *Writing Across Curric. J.* **20**, 17 (2009).
15. M. Dunstan, P. Bassinger, *J. Chem. Educ.* **74**, 1067 (1997).
16. J. Swales, in *Genre Analysis: English in Academic and Research Settings*, M. H. Long and J. C. Richards, Eds. (Cambridge Applied Linguistics, Cambridge Univ. Press, Cambridge, 1990), pp. 137–166.
17. J. Osborne, *Science* **328**, 463 (2010).
18. V. D. Sarkis, *J. Chem. Educ.* **51**, 745 (1974).

10.1126/science.1200353

PHYSICS

High-Power Fiber Lasers

The brightness, robustness, and flexibility of high-power fiber laser sources provide an enabling technology for science and industry.

Johan Nilsson and David N. Payne

Lasers are used in a wide range of applications that benefit from the pin-sharp (spatially coherent) beam and immense pulse peak power they can provide. In many cases, notably manufacturing, high average power is essential for cutting, welding, and drilling. The low-power optical fiber amplifier (*1*), acclaimed as the mainstay of the fiber-based Internet, can be massively scaled to emerge as an industrial laser frontrunner, reaching an output power of >1 kW (*2*) and, more recently, an astounding 10 kW (*3*). These results were obtained with (nearly) diffraction-limited beam quality, which determines the ability to focus to a tight spot. Together with the power and wavelength, it determines the spatial brightness, or radiance. The brightness is exceptionally high for these fiber lasers, and this, rather than the power itself, determines the power density achievable on a target.

There are several "secrets" behind the success of high-power fiber lasers. One is cladding-pumping (*4*–*6*), which uses a more sophisticated fiber structure than that of a conventional optical fiber (see the figure). In addition to the usual few-micrometer-sized core for guiding the light, these double-clad fibers include a second, coaxial, waveguide that surrounds the core. Most fiber lasers are optically pumped by semiconductor laser diodes, and the large size of this second waveguide allows pumping with numerous pump diodes that provide several kilowatts of low-cost, low-brightness optical power.

Then there is the incorporation into the core of ytterbium as the laser-active (amplifying) dopant. Ytterbium is a very efficient laser ion, partly due to the proximity of the wavelength of the amplified light (typically 1040 to 1100 nm) to that of the pump (typically 910 to 980 nm) (*7*, *8*). The difference is called the "quantum defect" and determines the amount of surplus heat a laser will produce; to minimize this, a pump wavelength of 1020 nm was used for the 10-kW demonstration (*3*). The optical conversion efficiency of a fiber laser can exceed 80%, at an electrical-to-optical conversion of 40%. Furthermore, ytterbium can be incorporated in concentrations as high as several percent so that practical fiber laser lengths of a few meters can absorb the pump light. An early enabling commercial breakthrough was the development of new silica-based glass hosts that allow for high ytterbium concentrations without the photodarkening from which many silica hosts suffer. Beside ytterbium, erbium and thulium are used for wavelengths around 1.6 and 2 μm, respectively, reaching powers of about 0.3 and 1 kW

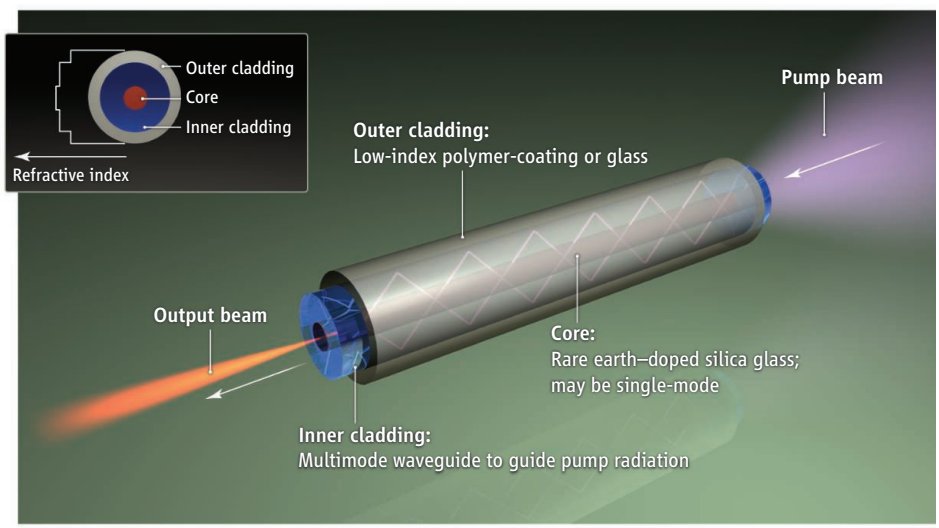

Fiber lasing. Schematic of a double-clad fiber laser in an end-pumped configuration (not to scale).

A prime attraction of fiber waveguiding lasers over their conventional optically pumped "bulk" laser cousins is thermal management. A host of thermal gremlins have plagued bulk lasers over the years, from catastrophic fracture to thermal beam distortions that degrade the beam quality, thus limiting the brightness. By contrast, the long fiber laser is made from refractory silica and has a hair-thin active region from which it is easy to extract heat. The reduced thermal load per unit length lowers the thermally induced refractive-index distortions and, furthermore, a guided laser mode can maintain an unperturbed, flat wavefront even in the presence of such distortions.

There is, however, a drawback in having a long and thin gain medium—nonlinear optical degradation. There is an optimal ratio of the length of the gain medium to the cross-sectional area that best balances thermal and nonlinear degradation (*8*). Waveguiding makes it possible to reach this optimal ratio, whereas in a bulk laser the inevitable diffraction can make the ratio orders of magnitudes smaller than optimal. The right ratio is, however, not sufficient. It is also necessary to have a large core to keep the power density below the damage threshold and improve the energy storage, in case of high-energy pulses. There are limits to the core diameter in a fiber laser before the beam quality degrades and the guidance becomes too weak, which causes problems with bend loss and packaging. This occurs in the 50- to 100-μm region, although the cores in commerical single-mode devices are seldom larger than 30 μm.

Thanks to the trade-off between thermal and nonlinear limits, the impressive progress in core area scaling, and the superb properties of ytterbium-doped silica, fiber lasers excel as high-power, high-brightness laser sources. Equally important for their commercial success is the integration of all-fiber components to make a monolithic guided-wave laser that resists environmental abuse. However, fiber lasers are in their infancy, and this is only the beginning of the story. High-power fibers are often configured as amplifiers rather than as "pure" lasers (*8*). Fibers work very well as amplifiers with an unsurpassed ability to combine high gain, high power, and high efficiency. It is therefore possible to use a highly controlled, low-power laser (perhaps a semicon-

Optoelectronics Research Centre, University of Southampton, Southampton SO17 1BJ, UK. E-mail: jn@orc.soton.ac.uk

CREDIT: P. HUEY/*SCIENCE*

Published by AAAS

ductor diode) and boost its power with fiber amplifiers up to kilowatts.

The exquisite control offered by fiber at high power makes coherent beam combination an extremely exciting possibility for extending the power further, perhaps to the megawatt regime. There are a range of different methods through which the output beams of individual fiber sources can be combined (*8*, *9*), primarily to reach higher power and brightness than is possible from a single-fiber emitter. However, coherent combination in a phased-array laser configuration, rather like a radar antenna with active phase control of the individual beams, provides control of the spatial beam profile and a degree of beam steering and tracking (*10*). Digital holography is another version in which electronic means are used to control the beam profile (*11*). These are expensive systems, but costs can be reduced with simpler phase-control systems, provided that the laser phase noise is sufficiently low. Furthermore, although coherent beam combination has been restricted to continuous-wave systems, it is now being extended to the femtosecond pulsed regime (*12*).

Building on these results, the possibility of using coherently combined femtosecond fiber sources to drive wakefield accelerators for particle colliders is being explored (*13*). The multi-megawatt average power makes the efficiency levels that fibers offer a necessity. Although many thousands of fiber channels will have to be combined, the volume manufacturability, scalability, and reliability of active fiber technology makes this a tremendously exciting proposition for the next few decades.

References

1. R. J. Mears, L. Reekie, I. M. Jauncey, D. N. Payne, *Electron. Lett.* **23**, 1026 (1987).
2. Y. Jeong, J. K. Sahu, D. N. Payne, J. Nilsson, *Opt. Express* **12**, 6088 (2004).
3. E. Stiles, "New developments in IPG fiber laser technology," 5th International Workshop on Fiber Lasers, Dresden, Germany (2009).
4. R. D. Maurer, "Optical waveguide light source," U.S. Patent 3,808,549 (1974).
5. J. D. Kafka, "Laser diode pumped fiber laser with pump cavity," U.S. Patent 4,829,529 (1989).
6. E. Snitzer, H. Po, F. Hakimi, R. Tumminelli, B. C. McCollum, "Double-clad, offset core Nd fiber laser," in vol. 2 of *Optical Fiber Sensors*, OSA Technical Digest Series (Optical Society of America, Washington, DC, 1988), post-deadline paper PD5.
7. H. M. Pask *et al.*, *IEEE J. Sel. Top. Quantum Electron.* **1**, 2 (1995).
8. D. J. Richardson, J. Nilsson, W. A. Clarkson, *J. Opt. Soc. Am. B* **27**, B63 (2010).
9. T. Y. Fan, *IEEE J. Sel. Top. Quantum Electron.* **11**, 567 (2005).
10. T. M. Shay *et al.*, *Proc. SPIE* **7195**, 71951M (2009).
11. M. Paurisse *et al.*, *Opt. Express* **17**, 13000 (2009).
12. L. Daniault *et al.*, *Opt. Lett.* **36**, 621 (2011).
13. G. Mourou, D. Hulin, A. Galvanauskas, in *Super Strong Field in Plasmas*, D. Batani, M. Lontano, Eds. (American Institute of Physics, College Park, MD, 2006), pp. 152–163.

10.1126/science.1194863

PHYSICS

Shedding Light on Oxide Interfaces

The properties of a metallic oxide can be altered when it is confined as an ultrathin layer by layers of an insulating oxide.

German Hammerl[1] and Nicola Spaldin[2]

In the stable of solid-state materials, silicon is the workhorse. Its semiconductor properties are actually quite ordinary, but when other materials are harnessed to it to form interfaces, remarkable devices can be made that control the flow of electrical current with low applied voltages. In contrast, some transition metal oxides would be the stable's racehorses. Remarkable functional behaviors of this group include the ability to change from a metal to an insulator with a slight change in temperature, unusual magnetic properties, and even high-temperature superconductivity (*1*). Further novel properties are expected to emerge at interfaces created between transition metal oxides that already exhibit functional behavior, and these properties could be tuned through small changes in composition or by simply applying a bias voltage (*2*). However, like temperamental racehorses, the interfaces in these complex oxides can be more difficult to control than those formed by silicon. On page 937 of this issue, Boris *et al.* (*3*) report progress toward this goal by confining an ultrathin layer of lanthanum nickelate ($LaNiO_3$), normally a paramagnetic metal, between insulating lanthanum aluminate ($LaAlO_3$) layers, which leads to changes in its properties.

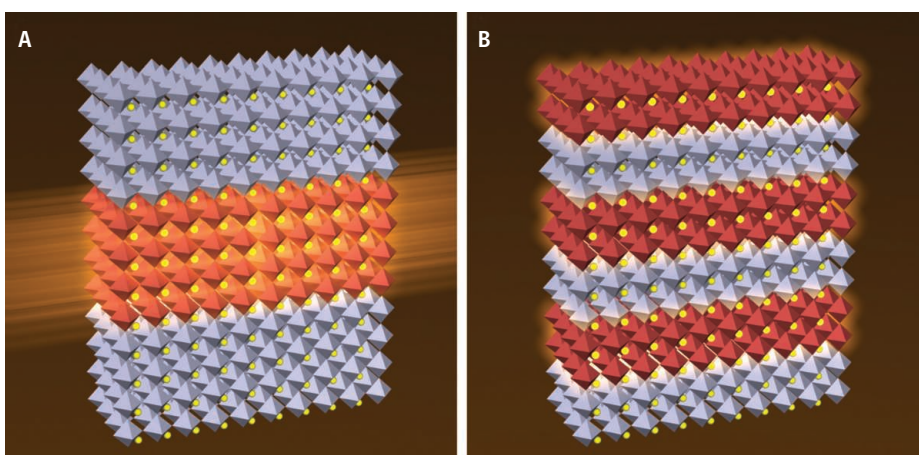

Thinner is different. Artistic illustration of two different electronic phases in heterostructures of $LaNiO_3$ (red), which is metallic as a bulk material, confined by $LaAlO_3$ (gray), which is a bulk insulator. (**A**) A confined $LaNiO_3$ layer that is four unit cells in thickness still shows metallic behavior. (**B**) When the thickness is reduced to two unit cells, a temperature-driven metal-insulator transition emerges.

CREDIT: COURTESY OF A. HERRNBERGER

The difference between semiconductors such as silicon and exotic transition metal oxides lies in the nature of the interactions between the constituent electrons. The electronic states of semiconductors are well described by conventional, single-particle band theory, in which individual electrons act independently. Contact between energy bands at interfaces can bend the bands or create energy barriers, which in turn can generate quasi-electric fields (which act on the charge carriers differently from true electric fields) or cause accumulation of charge carriers. In the complex oxides, however, there are strong correlations between the tightly

[1]Experimental Physics VI, Center for Electronic Correlations and Magnetism, University of Augsburg, Universitätsstr. 1, 86135 Augsburg, Germany. [2]Materials Theory, Department of Materials, ETH Zürich, Wolfgang-Pauli-Str. 27, 8093 Zürich, Switzerland. E-mail: german.hammerl@physik.uni-augsburg.de; nicola.spaldin@mat.ethz.ch

Published by AAAS

bound transition metal d electrons, and single electrons are no longer independent but influence the behavior of all other electrons in the crystal. The large electrical polarizability of oxygen also enhances the response of these materials to electric fields causing ferroelectric (a net electric dipole moment) or multiferroic (both ferroelectric and ferromagnetic) properties (*4*).

Boris *et al*. used pulsed laser deposition to grow superlattices—precise numbers of oxide layers with atomically sharp interfaces (see the figure). Samples with four-unit-cell thick $LaNiO_3$ layers grown between $LaAlO_3$ layers were metallic at temperatures from 8 to 300 K, just like bulk $LaNiO_3$. Samples with only two layers of $LaNiO_3$, in which each $LaNiO_3$ layer is next to a $LaAlO_3$ layer, showed a metal-to-insulator transition with subsequent magnetic ordering as the temperature was lowered.

Such effects might be mainly the result of strain in the layers, which can be induced by the substrate used for growth. To check whether this was the case, Boris *et al*. grew the same layer structures on strontium titanate ($SrTiO_3$), which has a larger lattice constant than the superlattice, and on lanthanum strontium aluminate ($LaSrAlO_4$), in which the lattice constant is smaller. The same behavior was seen in both cases, except for a shift of transition temperature (100 and 150 K, respectively), ruling out strain as the cause.

To demonstrate further that these effects were intrinsic to the superlattice structure, Boris *et al*. applied state-of-the-art surface probes. They used ellipsometry to measure the changes in the sample's electrical conductivity. Ellipsometry is not influenced by extrinsic impurities, particularly interdiffusion of ions between the layers, nor is it influenced by misfit dislocations resulting from inexact matching of the lattice constants at the interface, which can occur in oxide superlattices. They also used low-energy muon spin rotation to identify a change in the magnetic order accompanying the transition from the metallic to the insulating state. Here, spin-polarized muons with well-defined energies are implanted within the oxide heterostructure, where they align their magnetic moments parallel to those of the surrounding electrons. The measured directions of the subsequent positron decay products yield the local magnetic order of the electronic phase. The bilayered $LaNiO_3$ samples showed a clear magnetic transition, but the superlattices with thicker layers did not.

Deposition techniques such as pulsed laser deposition or molecular beam epitaxy are now well developed, so nearly defect-free superlattices with atomically sharp interfaces can be routinely grown. Unanticipated phenomena such as the metal-insulator transition described here, or conductivity at interfaces between the insulating oxides such as $LaAlO_3$ and $SrTiO_3$ (*5*) or interfacial superconductivity (*6*), are now regularly reported. However, there is still much work to be done before oxide materials reach the level of sophistication achieved in semiconductor heterostructures. Improved control and understanding of the role of defects is necessary, as well as systematic incorporation of multiple interfaces with different electronic properties (*2*).

From a practical point of view, demonstrations of integration with conventional semiconductors would be helpful, as would a detailed understanding of the behavior at interfaces with metallic electrodes (*7*). On the theoretical front, the aspects that make complex oxides desirable—in particular the strong correlations, the large polarizability, and the sensitive dependence on crystal chemistry and structure—also make them challenging to describe accurately. Improved techniques must combine many-body physics methods for describing strong correlations with computational materials methods, such as density functional theory, that can account for chemistry and structure. With these developments, which the community is poised to make over the next few years, true predictive capability and layer-by-layer construction of designer oxide superlattices should be achievable.

References

1. D. G. Schlom, L.-Q. Chen, X. Pan, A. Schmehl, M. A. Zurbuchen, *J. Am. Ceram. Soc.* **91**, 2429 (2008).
2. J. Mannhart, D. G. Schlom, *Science* **327**, 1607 (2010).
3. A. V. Boris *et al*., *Science* **332**, 937 (2011).
4. N. A. Spaldin, S. W. Cheong, R. Ramesh, *Phys. Today* **63**, 38 (2010).
5. A. Ohtomo, H. Y. Hwang, *Nature* **427**, 423 (2004).
6. A. Gozar *et al*., *Nature* **455**, 782 (2008).
7. M. Stengel, N. A. Spaldin, *Nature* **443**, 679 (2006).

10.1126/science.1206247

CELL BIOLOGY

The TASCC of Secretion

Roberto Zoncu[1,2,3] and David M. Sabatini[1,2,3,4]

Cells can spatially couple cellular degradation and protein synthesis to boost protein secretion.

The oncogene-induced activation of signaling pathways involving the tumor suppressor proteins p53 and retinoblastoma is likely an important mechanism for preventing the proliferation of potential cancer cells (*1*, *2*). This activation causes cells to exit the cell division cycle and enter a senescent state, which is characterized by major changes in chromatin structure that are thought to render senescence irreversible. Despite the absence of proliferation, senescent cells are not as quiescent as first thought, as they signal to their surrounding environment by activating a protein secretion program (*3*, *4*). On page 966 of this issue, Narita *et al*. (*5*) show that to enable this secretory state, a senescent cell profoundly reorganizes its endomembrane system.

[1]Whitehead Institute for Biomedical Research, 9 Cambridge Center, Cambridge, MA 02142, USA. [2]Department of Biology, Massachusetts Institute of Technology (MIT), Cambridge, MA 02139, USA. [3]The David H. Koch Institute for Integrative Cancer Research at MIT, 77 Massachusetts Avenue, Cambridge, MA 02139, USA. [4]Howard Hughes Medical Institute, Chevy Chase, MD 20815, USA. E-mail: sabatini@wi.mit.edu

The secretory program leads to the massive production of factors [collectively called the senescence-messaging secretome (SMS) or senescence-associated secretory phenotype (SASP)] that are released into the surrounding microenvironment (*3*, *4*). The composition of the SMS is heterogeneous. It includes growth factors, inflammatory cytokines, and modulators of the extracellular matrix, and its precise physiological role is highly controversial. For example, inflammation can modify the microenvironment in ways that favor cancer cell invasion and tumor growth (*6*, *7*); however, in the context of oncogene-induced cell senescence, inflammatory cytokines can also exert an autocrine, tumor-suppressive action (*8*–*11*).

Narita *et al*. found that expression of the oncogenic protein H-RasV12 in a senescent mammalian cell triggers a reorganization of its endomembrane system, which results in the formation of a membrane compartment that carries out the secretory program. They named this structure the TOR-autophagy spatial coupling compartment (TASCC). As the name suggests, the key components

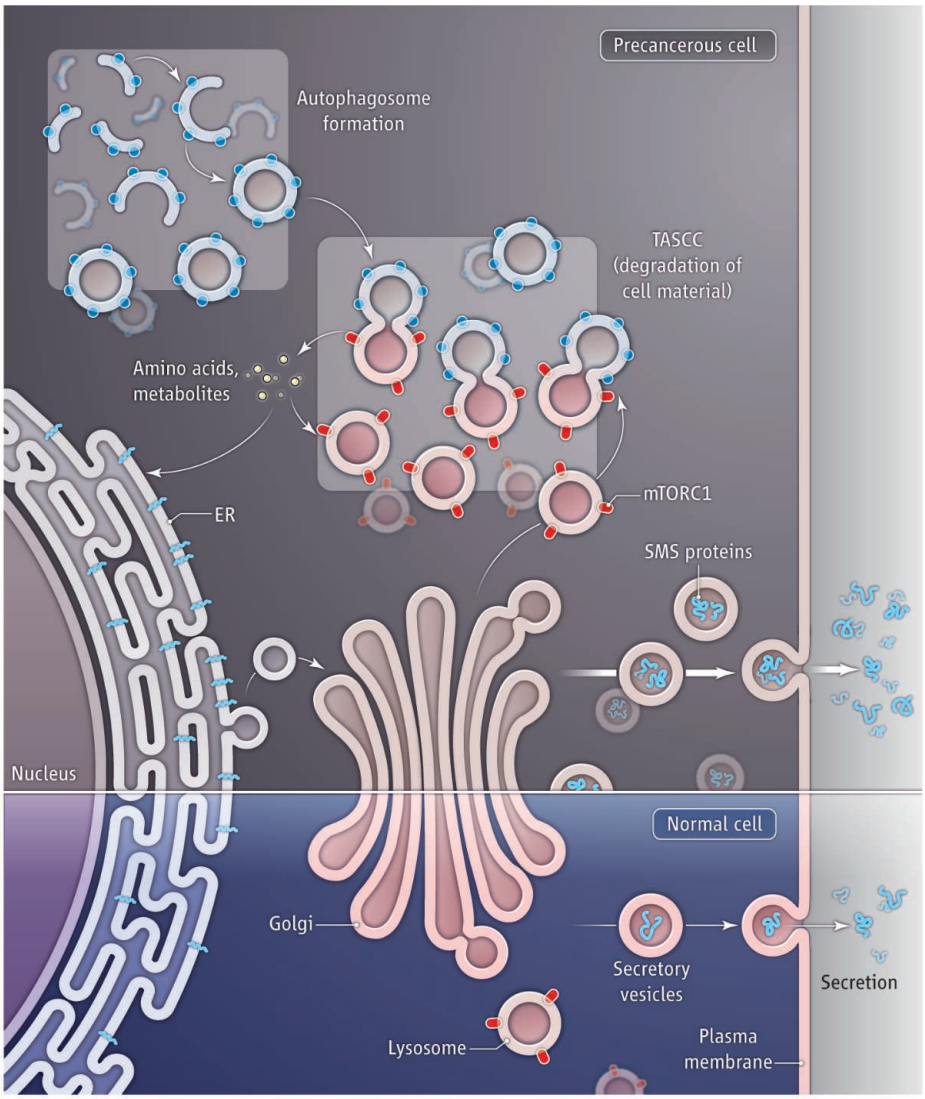

Reorganized to reinforce. In a normal mammalian cell (**bottom**), autophagy is suppressed by mTORC1. In a cell undergoing senescence (induced by the oncogene H-RasV12) (**top**), autophagosomes form at the cell periphery and as they mature, fuse with lysosomes that contain mTORC1, giving rise to the TASCC. Amino acids and other metabolites released from autophagolysosomes activate mTORC1 and boost protein synthesis. Newly synthesized proteins are secreted or rerouted to the TASCC for degradation to fuel further rounds of protein synthesis.

of this compartment are autophagosomes and the mammalian target of rapamycin (mTOR) complex 1 (mTORC1) kinase. In the proposed model, autophagosomes, which degrade aged organelles and proteins, generate a high flux of amino acids and other metabolites that provide building blocks for biosynthesis (*12*). mTORC1 promotes the utilization of these constituents for synthesizing SMS components. The key to this highly efficient process, according to the authors, is the tight spatial coupling of autophagy and mTORC1. In cells undergoing Ras-induced senescence, there is a large accumulation of mTORC1-studded lysosomes together with autophagosomes in a well-defined perinuclear location (see the figure). Blocking the localization of mTORC1 to the TASCC (*13*) reduced the synthesis and secretion of the SMS cytokines interleukin-6 (IL-6) and IL-8. Moreover, blocking autophagy, and thus cutting off the amino acid supply that activates mTORC1, caused the complete loss of mTORC1 from the TASCC.

Although bringing together autophagy and mTORC1 seems like a smart way to increase the secretory output of a cell, it also poses a logical problem: Activated mTORC1 phosphorylates autophagy initiators, including the serine-threonine kinase Unc-51–like kinase 1 (ULK1), thereby suppressing autophagy (*12*). Indeed, rapamycin, an inhibitor of mTORC1, induces autophagy even when cells are in a nutrient-rich environment. To explain this apparent paradox, Narita *et al*. analyzed the subcellular distribution of ULK1 and found it to be excluded from the TASCC. Moreover, they observed mature autophagosomes in the TASCC, whereas early autophagosomes were mostly outside the TASCC. Thus, in a senescent cell, autophagosomes form outside the TASCC, out of reach from the inhibitory action of mTORC1, but they progressively move inward as they mature. This finding has broad implications, because it suggests that spatial segregation of mTORC1 from autophagy-initiating factors may enable the maintenance of basal autophagy in actively growing cells.

Ultrastructural analyses revealed a close apposition of the TASCC with the endoplasmic reticulum (ER), Golgi apparatus, and trans-Golgi network. Moreover, Narita *et al*. found that newly synthesized proteins are enriched in the trans-Golgi network within 30 min of their synthesis, but accumulate in the TASCC shortly afterwards. Thus, a continuous flow of newly synthesized proteins traverses the secretory pathway and ends up in the TASCC. This extremely rapid protein turnover may be key in fueling the synthesis of SMS components.

A central question is whether senescence increases the activity of the secretory pathway as a whole, or whether it selectively boosts the synthesis and secretion of the SMS components alone. The high rate of protein turnover, together with the elevated autophagic activity, suggests a scenario in which the synthesis of many protein species may be nonselectively increased during Ras-induced senescence. However, most of these proteins would be destined for immediate degradation, whereas only SMS components would be selectively secreted. This seemingly wasteful mechanism may underlie a broader function for the TASCC in nonsenescent physiological settings. Indeed, Narita *et al*. identified TASCC-like structures in leukemia cells undergoing differentiation, as well as in renal glomerular cells in vivo. Thus, it is conceivable that multiple mechanisms could set up the TASCC and enhance general secretory activity, but the nature of the proteins being stabilized and secreted may be context-specific.

Narita *et al*. reveal the surprising ability of senescent cells to reorganize the morphology and the function of their endomembrane system. The findings provoke exciting questions about the mechanisms that lead to formation of the TASCC, including whether senescence-associated gene expression programs control membrane organization and dynamics, and whether H-RasV12 onco-

CREDIT: Y. HAMMOND/*SCIENCE*

Published by AAAS

gene and/or p53 are directly involved. Answers to these questions may clarify the role of the TASCC in maintaining the senescent state and in tumor suppression.

References and Notes

1. S. Courtois-Cox, S. L. Jones, K. Cichowski, *Oncogene* **27**, 2801 (2008).
2. F. d'Adda di Fagagna, *Nat. Rev. Cancer* **8**, 512 (2008).
3. T. Kuilman, D. S. Peeper, *Nat. Rev. Cancer* **9**, 81 (2009).
4. F. Rodier, J. Campisi, *J. Cell Biol.* **192**, 547 (2011).
5. M. Narita *et al., Science* **332**, 966 (2011); 10.1126/science.1205407.
6. J.-P. Coppé *et al., PLoS Biol.* **6**, e301 (2008).
7. D. Hanahan, R. A. Weinberg, *Cell* **144**, 646 (2011).
8. J. C. Acosta *et al., Cell* **133**, 1006 (2008).
9. R. M. Kortlever, P. J. Higgins, R. Bernards, *Nat. Cell Biol.* **8**, 877 (2006).
10. T. Kuilman *et al., Cell* **133**, 1019 (2008).
11. N. Wajapeyee, R. W. Serra, X. Zhu, M. Mahalingam, M. R. Green, *Cell* **132**, 363 (2008).
12. C. He, D. J. Klionsky, *Annu. Rev. Genet.* **43**, 67 (2009).
13. Y. Sancak *et al., Cell* **141**, 290 (2010).

10.1126/science.1207552

ATMOSPHERIC SCIENCE

Subtropical Rainfall and the Antarctic Ozone Hole

Simulations show that ozone depletion has had a large impact on Southern Hemisphere climate.

Steven B. Feldstein

For more than 100 years, researchers have understood that ozone in the stratosphere, the atmospheric layer between 10 and 50 km above Earth's surface, plays an important role in absorbing ultraviolet radiation and protecting life on Earth (*1*). In 1985, scientists and the public became alarmed when Farman *et al*. (*2*) reported that, during the Antarctic spring, stratospheric ozone concentrations over the continent were declining by as much as 50%, indicating the presence of a polar "ozone hole." Implementation of the 1987 Montreal protocol, an international agreement that phased out the use of some chlorofluorocarbons and other compounds that destroy stratospheric ozone, has led to the first stage of recovery (*3*). Researchers, however, had not widely recognized the ozone hole's impact on the climate of the troposphere (the lowest 10 km of the atmosphere) until recent observational (*4*) and state-of-the-art climate modeling studies (*5*–*8*). These studies showed that ozone depletion has a large influence during the Antarctic summer, when it drives a major air current called the mid-latitude westerly jet to a higher latitude, closer to Antarctica; this reduces sea level pressure over the continent, cooling much of the continental interior, coinciding with a warming of the Antarctic Peninsula. On page 951 of this issue, Kang *et al*. (*9*) expand our understanding of ozone depletion's impact on climate. Using a series of carefully designed climate model experiments, they show that ozone-induced climate change is not confined just to the vicinity of Antarctica but extends over much of the Southern Hemisphere, even reaching the tropics, where it appears to have resulted in increased summer precipitation in the subtropics.

To isolate the impact of reduced stratospheric ozone on tropospheric climate, recent studies have compared results from two types of climate model simulations: One specifies pre–ozone-hole concentrations of ozone; the other uses the more recent, ozone-depleted concentrations. Some studies also specify various concentrations of primary greenhouse gases in order to compare their influence on climate with that of depleted ozone. Together, such studies have provided climate modelers with strong support for the claim that stratospheric ozone depletion has been the dominant driver of climate change in the mid- and high-latitude Southern Hemisphere during the summer season. In particular, the pre-ozone-hole and depleted simulations produce differences in wind, temperature, and precipitation patterns that closely resemble changes observed in the atmosphere.

In their models, Kang *et al*. not only accounted for pre-ozone-hole and depleted ozone concentrations but also investigated the sensitivity of the model response to physical "parameterizations" (a key component of climate models that differs between models), and to the coupling of the atmosphere with the oceans and sea ice. All climate models use parameterization to represent important physical processes, such as those associated

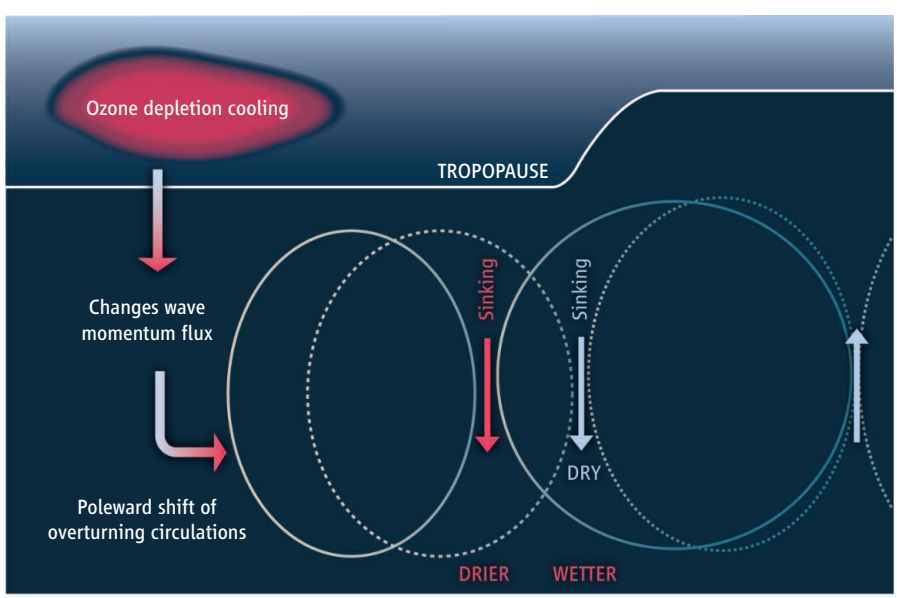

Catching a wave. In the Southern Hemisphere, cooling related to stratospheric ozone depletion over Antarctica alters atmospheric wave momentum fluxes, which causes circulation cells (solid and dotted circles) to shift poleward, altering precipitation patterns in the subtropics. Pre–ozone-hole circulation cells are illustrated with dotted lines and blue labels; depleted ozone cells are illustrated with solid lines and red labels.

CREDIT: S. LEE AND S.B. FELDSTEIN

The Pennsylvania State University, University Park, PA 16802, USA. E-mail: sbf1@meteo.psu.edu

Published by AAAS

with clouds, heat transport between the atmosphere and the Earth's surface, radiation and turbulence, that have a spatial scale smaller than the resolution of the model grid. There are important differences between the parameterizations used by various climate modeling groups. To evaluate these differences, the authors used two different climate models: the Canadian Middle Atmosphere Model (CMAM) and the National Center for Atmospheric Research/Community Atmospheric Model (CAM3). To investigate the possible impact of the ocean and sea ice, the researchers performed separate model runs in which the sea surface temperature and sea ice concentrations were either specified or allowed to vary with time through coupling with the atmosphere. All model experiments produced similar results, including increased summer precipitation in the subtropics that is very similar to the observed precipitation trend. The results indicate a lack of sensitivity to different climate models, and a limited role for the coupling of the atmosphere with the oceans and sea ice.

Kang *et al*. also addressed the question of what physical mechanism links ozone depletion with changes in tropical precipitation. Their model calculations show that the ozone decline is associated with a poleward expansion of the Hadley cell (a tropical circulation pattern characterized by air masses that rise near the equator, flow poleward in the upper troposphere, then descend in the subtropics and flow back toward the equator in the lower troposphere). What process drives the Hadley cell expansion? Previous studies have shown that an important driver of the Hadley cell is the momentum flux associated with synoptic-scale waves (the atmospheric waves that correspond to day-to-day weather) (*10*, *11*); indeed, Kang *et al*. find that the Hadley cell changes are linked to changes in wave momentum flux. This relationship between ozone depletion and wave momentum flux is tied to a fundamental question: What is the physical mechanism that connects wind and temperature change in the lower stratosphere to changes in these and other variables in the troposphere? This is an open question, and a number of researchers are actively pursuing an answer. One common factor underlying most proposed mechanisms involves changes to synoptic- and planetary-scale waves, particularly their instability (linear and nonlinear), propagation, breaking, and feedback features (*12*–*16*), all of which influence the wave momentum flux. Additional diagnostics studies with observational and model data could go a long way toward enhancing our understanding of both stratosphere/troposphere interaction in general and the linkage between the Antarctic ozone hole and tropical precipitation in particular.

References

1. S. Solomon, *Rev. Geophys.* **37**, 275 (1999).
2. J. C. Farman, B. G. Gardiner, J. D. Shanklin, *Nature* **315**, 207 (1985).
3. S.-W. Son *et al*., *Science* **320**, 1486 (2008).
4. D. W. J. Thompson, S. Solomon, *Science* **296**, 895 (2002).
5. J. M. Arblaster, G. A. Meehl, *J. Clim.* **19**, 2896 (2006).
6. N. P. Gillett, D. W. J. Thompson, *Science* **302**, 273 (2003).
7. L. M. Polvani, D. W. Waugh, G. J. P. Correa, S.-W. Son, *J. Clim.* **24**, 795 (2011).
8. S.-W. Son, N. F. Tandon, L. M. Polvani, D. W. Waugh, *Geophys. Res. Lett.* **36**, L15705 (2009).
9. S. M. Kang *et al*., *Science* **332**, 951 (2011).
10. H.-K. Kim, S. Lee, *J. Atmos. Sci.* **58**, 2859 (2001).
11. R. L. Pfeffer, *J. Atmos. Sci.* **38**, 1340 (1981).
12. G. Chen, I. M. Held, *Geophys. Res. Lett.* **34**, L21805 (2007).
13. P. J. Kushner, L. M. Polvani, *J. Clim.* **17**, 629 (2004).
14. Y. Song, W. A. Robinson, *J. Atmos. Sci.* **61**, 1711 (2004).
15. I. R. Simpson, M. Blackburn, J. D. Haigh, *J. Atmos. Sci.* **66**, 1347 (2009).
16. M. A. H. Wittman, A. J. Charlton, L. M. Polvani, *J. Atmos. Sci.* **64**, 479 (2007).

10.1126/science.1206834

PALEONTOLOGY

Evolving Large and Complex Brains

X-ray studies of two Early Jurassic fossils offer insight into the evolution of mammalian brains.

R. Glenn Northcutt

During the Mesozoic (~250 million to 65 million years ago), two distantly related groups of reptiles—the cynodont (or mammal-like) reptiles and the coelurosaurian theropod dinosaurs—gave rise to mammals and birds, respectively. Both mammals and birds evolved brains some 10 times as large, relative to a given body weight, as those of their ancestors (*1*). In both groups, these brains contributed to the evolution of the ability to control body temperature (endothermy) and complex social interactions, including parental care and a reliance on learning that even involves tool use (*2*, *3*). The size of most parts of the brain increased in birds and mammals, but the cerebral hemispheres and cerebellum, both of which are involved in sensory and motor integration, underwent particularly spectacular development (see the figure). Although mammals and birds evolved from distantly related groups of reptiles, the higher integrative centers and circuitry of their cerebral hemispheres are very similar, and comparative neurobiologists continue to vigorously debate whether these centers evolved from the same ancestral neural centers (*4*, *5*) or from different ones (*6*–*8*). Speculation about the evolutionary steps leading to large and complex mammalian and avian brains is equally contentious and unresolved, in part because of the rarity of fossil skulls and, until recently, the need to destroy such skulls in order to expose the endocasts (casts molded by the cranial cavity). Typically, endocasts are the only record of the brain's outward appearance in a transitional form, because brains themselves are rarely fossilized.

On page 955 of this issue, Rowe *et al*. (*9*) offer new insights into the early evolution of mammalian brains. Using high-resolution x-ray computed tomography, they reconstructed the endocasts of *Morganucodon* and *Hadrocodium*, two basal mammaliaforms from the Early Jurassic (~199 million to 175 million years ago). These data allow the authors to postulate that the evolution of these large and complex brains occurred in three major steps.

Triassic cynodont reptiles appear to have had relatively poor olfaction and vision, insensitive hearing, and a lack of fine motor coordination (*9*, *10*). Their brains were characterized by small olfactory bulbs, narrow and tubular cerebral hemispheres (exceeded in width by the cerebellum), and a dorsally exposed midbrain. The *Morganucodon* endocast reconstructed by Rowe *et al*. indicates that the brain was almost 50% larger than that of the earlier Triassic cynodonts, with the olfactory bulbs and cerebral hemispheres showing the greatest expansion, and the cerebral hemispheres now wider than the cerebellum and covering the midbrain. It is also likely that *Morganucodon* had body hair. The

Laboratory of Comparative Neurobiology, Scripps Institution of Oceanography and Department of Neurosciences, University of California, San Diego, La Jolla, CA 92093, USA. E-mail: rgnorthcutt@ucsd.edu

with clouds, heat transport between the atmosphere and the Earth's surface, radiation and turbulence, that have a spatial scale smaller than the resolution of the model grid. There are important differences between the parameterizations used by various climate modeling groups. To evaluate these differences, the authors used two different climate models: the Canadian Middle Atmosphere Model (CMAM) and the National Center for Atmospheric Research/Community Atmospheric Model (CAM3). To investigate the possible impact of the ocean and sea ice, the researchers performed separate model runs in which the sea surface temperature and sea ice concentrations were either specified or allowed to vary with time through coupling with the atmosphere. All model experiments produced similar results, including increased summer precipitation in the subtropics that is very similar to the observed precipitation trend. The results indicate a lack of sensitivity to different climate models, and a limited role for the coupling of the atmosphere with the oceans and sea ice.

Kang *et al*. also addressed the question of what physical mechanism links ozone depletion with changes in tropical precipitation. Their model calculations show that the ozone decline is associated with a poleward expansion of the Hadley cell (a tropical circulation pattern characterized by air masses that rise near the equator, flow poleward in the upper troposphere, then descend in the subtropics and flow back toward the equator in the lower troposphere). What process drives the Hadley cell expansion? Previous studies have shown that an important driver of the Hadley cell is the momentum flux associated with synoptic-scale waves (the atmospheric waves that correspond to day-to-day weather) (*10*, *11*); indeed, Kang *et al*. find that the Hadley cell changes are linked to changes in wave momentum flux. This relationship between ozone depletion and wave momentum flux is tied to a fundamental question: What is the physical mechanism that connects wind and temperature change in the lower stratosphere to changes in these and other variables in the troposphere? This is an open question, and a number of researchers are actively pursuing an answer. One common factor underlying most proposed mechanisms involves changes to synoptic- and planetary-scale waves, particularly their instability (linear and nonlinear), propagation, breaking, and feedback features (*12*–*16*), all of which influence the wave momentum flux. Additional diagnostics studies with observational and model data could go a long way toward enhancing our understanding of both stratosphere/troposphere interaction in general and the linkage between the Antarctic ozone hole and tropical precipitation in particular.

References

1. S. Solomon, *Rev. Geophys.* **37**, 275 (1999).
2. J. C. Farman, B. G. Gardiner, J. D. Shanklin, *Nature* **315**, 207 (1985).
3. S.-W. Son *et al*., *Science* **320**, 1486 (2008).
4. D. W. J. Thompson, S. Solomon, *Science* **296**, 895 (2002).
5. J. M. Arblaster, G. A. Meehl, *J. Clim.* **19**, 2896 (2006).
6. N. P. Gillett, D. W. J. Thompson, *Science* **302**, 273 (2003).
7. L. M. Polvani, D. W. Waugh, G. J. P. Correa, S.-W. Son, *J. Clim.* **24**, 795 (2011).
8. S.-W. Son, N. F. Tandon, L. M. Polvani, D. W. Waugh, *Geophys. Res. Lett.* **36**, L15705 (2009).
9. S. M. Kang *et al*., *Science* **332**, 951 (2011).
10. H.-K. Kim, S. Lee, *J. Atmos. Sci.* **58**, 2859 (2001).
11. R. L. Pfeffer, *J. Atmos. Sci.* **38**, 1340 (1981).
12. G. Chen, I. M. Held, *Geophys. Res. Lett.* **34**, L21805 (2007).
13. P. J. Kushner, L. M. Polvani, *J. Clim.* **17**, 629 (2004).
14. Y. Song, W. A. Robinson, *J. Atmos. Sci.* **61**, 1711 (2004).
15. I. R. Simpson, M. Blackburn, J. D. Haigh, *J. Atmos. Sci.* **66**, 1347 (2009).
16. M. A. H. Wittman, A. J. Charlton, L. M. Polvani, *J. Atmos. Sci.* **64**, 479 (2007).

10.1126/science.1206834

PALEONTOLOGY

Evolving Large and Complex Brains

X-ray studies of two Early Jurassic fossils offer insight into the evolution of mammalian brains.

R. Glenn Northcutt

During the Mesozoic (~250 million to 65 million years ago), two distantly related groups of reptiles—the cynodont (or mammal-like) reptiles and the coelurosaurian theropod dinosaurs—gave rise to mammals and birds, respectively. Both mammals and birds evolved brains some 10 times as large, relative to a given body weight, as those of their ancestors (*1*). In both groups, these brains contributed to the evolution of the ability to control body temperature (endothermy) and complex social interactions, including parental care and a reliance on learning that even involves tool use (*2*, *3*). The size of most parts of the brain increased in birds and mammals, but the cerebral hemispheres and cerebellum, both of which are involved in sensory and motor integration, underwent particularly spectacular development (see the figure). Although mammals and birds evolved from distantly related groups of reptiles, the higher integrative centers and circuitry of their cerebral hemispheres are very similar, and comparative neurobiologists continue to vigorously debate whether these centers evolved from the same ancestral neural centers (*4*, *5*) or from different ones (*6*–*8*). Speculation about the evolutionary steps leading to large and complex mammalian and avian brains is equally contentious and unresolved, in part because of the rarity of fossil skulls and, until recently, the need to destroy such skulls in order to expose the endocasts (casts molded by the cranial cavity). Typically, endocasts are the only record of the brain's outward appearance in a transitional form, because brains themselves are rarely fossilized.

On page 955 of this issue, Rowe *et al*. (*9*) offer new insights into the early evolution of mammalian brains. Using high-resolution x-ray computed tomography, they reconstructed the endocasts of *Morganucodon* and *Hadrocodium*, two basal mammaliaforms from the Early Jurassic (~199 million to 175 million years ago). These data allow the authors to postulate that the evolution of these large and complex brains occurred in three major steps.

Triassic cynodont reptiles appear to have had relatively poor olfaction and vision, insensitive hearing, and a lack of fine motor coordination (*9*, *10*). Their brains were characterized by small olfactory bulbs, narrow and tubular cerebral hemispheres (exceeded in width by the cerebellum), and a dorsally exposed midbrain. The *Morganucodon* endocast reconstructed by Rowe *et al*. indicates that the brain was almost 50% larger than that of the earlier Triassic cynodonts, with the olfactory bulbs and cerebral hemispheres showing the greatest expansion, and the cerebral hemispheres now wider than the cerebellum and covering the midbrain. It is also likely that *Morganucodon* had body hair. The

Laboratory of Comparative Neurobiology, Scripps Institution of Oceanography and Department of Neurosciences, University of California, San Diego, La Jolla, CA 92093, USA. E-mail: rgnorthcutt@ucsd.edu

characteristics of its pelt are unknown, but the pelt of a closely related basal mammaliaform, *Castorocauda*, comprised guard hairs and an underfur. An initial phase in the evolution of mammalian brains was therefore characterized by an enlargement of the olfactory bulb, cerebral hemispheres, and cerebellum, suggesting increased olfactory sensitivity and neuromuscular coordination. The presence of body hair also indicates tactile sensitivity and suggests that endothermy and parental care likely occurred at this stage as well.

The reconstructed endocast of *Hadrocodium*, the closest known fossil relative of living mammals, indicates that a second phase in mammalian brain evolution occurred, with brain size again increasing by almost 50%, bringing it within the range of relative brain size in living mammals, with the olfactory bulbs and cerebral hemispheres accounting for most of the increase. In *Hadrocodium*, the relative size of the cerebellum had also increased, which suggests that sensory-motor integration as well as olfactory enhancement characterized this second phase in mammalian brain evolution.

Rowe *et al*. note that the origin of living mammals was apparently accompanied by a third phase in their brain evolution, marked by an increase in olfactory elaboration. The olfactory epithelium expanded by a factor of 10 and was supported by newly evolved nasal bones. The expanded epithelium was also apparently accompanied by a vast increase in odorant receptor genes and by the presence of different types of olfactory receptors, resulting in the high-resolution olfaction that is unique to mammals.

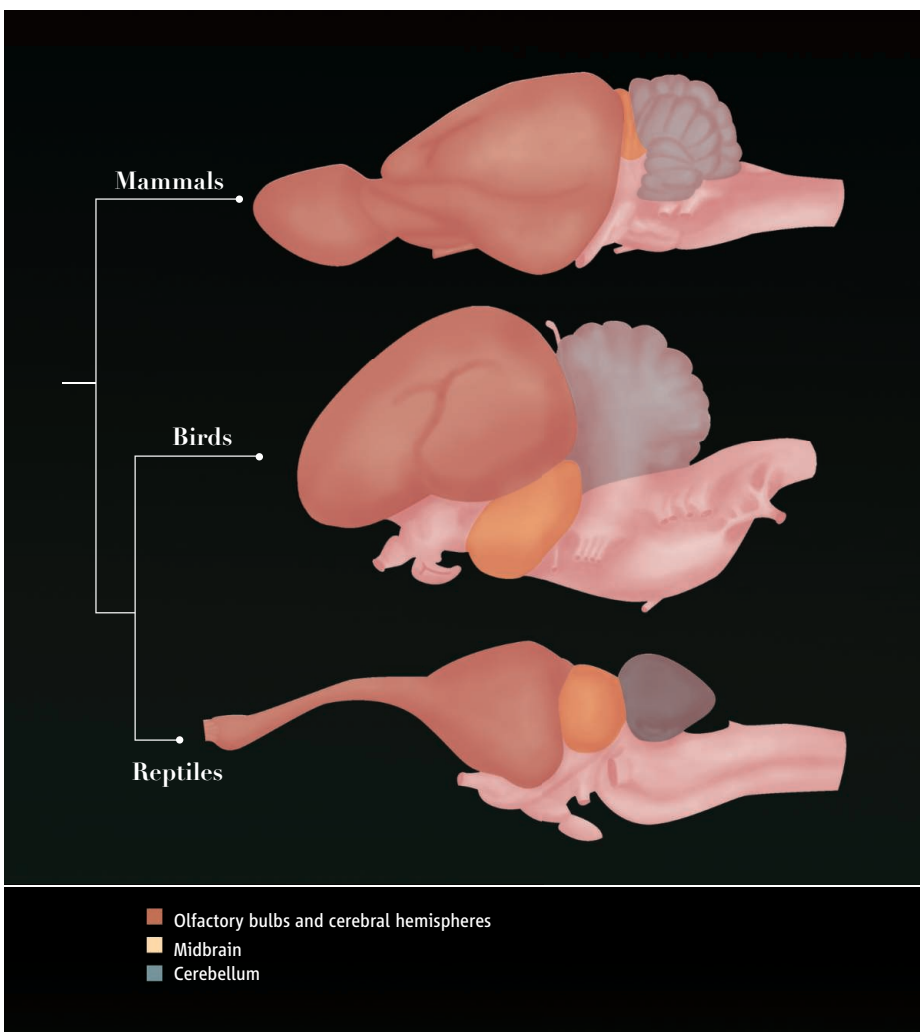

Bigger brains. In terrestrial vertebrates, large brains evolved, independently, twice. Relative brain size in living mammals and birds has increased by at least a factor of 10 over that in living reptiles. Pictured brains show the relative dimensions of the olfactory bulbs and cerebral hemispheres, the midbrain, the cerebellum, and the medulla. In birds, the midbrain lobes have been displaced laterally and ventrally by the expansion of the cerebral hemispheres, and the expansion of the cerebellum in both mammals and birds has resulted in pronounced foliation (folding) of the cerebellum.

CREDIT: N. KEVITIYAGALA/*SCIENCE*

The endocasts of *Morganucodon* and *Hadrocodium* provide the first solid evidence of the stages in mammalian brain evolution. Unfortunately, far less is known about the emergence of the brains of living birds. The endocast of the oldest known Late Jurassic bird, *Archaeopteryx*, reveals reduced olfactory bulbs, large cerebral hemispheres that are in contact with an expanded cerebellum, and lateroventrally displaced midbrain lobes (*11*). All of these neural traits also characterize living birds, and, not surprisingly, the relative size of the brain of *Archaeopteryx* appears to have been intermediate between that of living reptiles and that of living birds (*11*, *12*). All these derived neural traits, plus its skeletal characteristics, suggest that *Archaeopteryx* was capable of flight. The missing part of this story is the appearance of the brain in the coelurosaurian theropod dinosaurs that gave rise to birds. The endocasts of these dinosaurs have not been described, but the endocast of an oviraptorid theropod, *Conchoraptor*, revealed reduced olfactory bulbs, enlarged cerebral hemispheres, displaced midbrain lobes, and an enlarged cerebellum (*13*), as in living birds. Furthermore, the relative brain size in *Conchoraptor* was similar to that in *Archaeopteryx*. This suggests that the neural traits of *Conchoraptor* may have evolved parallel to those of avian theropods, but it is also possible that these neural traits were widely distributed among theropods. If so, many "avian" neural traits may have already been present in coelurosaurian theropods and were co-opted for flight.

References and Notes

1. P. A. M. van Dongen, in *The Central Nervous System of Vertebrates*, *Vol. 3*, R. Nieuwenhuys, H. J. ten Donkelaar, C. Nicholson, Eds. (Springer, Berlin, 1998), pp. 2099–2134.
2. M. J. Burish, H. Y. Kueh, S. S. Wang, *Brain Behav. Evol.* **63**, 107 (2004).
3. B. Kenward, A. A. Weir, C. Rutz, A. Kacelnik, *Nature* **433**, 121 (2005).
4. H. J. Karten, *Proc. Natl. Acad. Sci. U.S.A.* **94**, 2800 (1997).
5. A. Reiner, K. Yamamoto, H. J. Karten, *Anat. Rec.* **287A**, 1080 (2005).
6. R. G. Northcutt, J. H. Kaas, *Trends Neurosci.* **18**, 373 (1995).
7. G. F. Striedter, *Brain Behav. Evol.* **49**, 179 (1997).
8. L. L. Bruce, in *Evolution of Nervous Systems*, *Vol. 2*, J. H. Kaas, T. H. Bullock, Eds. (Elsevier, San Diego, CA, 2007), pp. 125–156.
9. T. B. Rowe, T. E. Macrini, Z.-X. Luo, *Science* **332**, 955 (2011).
10. J. A. Hopson, in *Biology of the Reptilia*, *Vol. 9, Neurology A*, C. Gans, R. G. Northcutt, P. Ulinski, Eds. (Academic Press, New York, 1979), pp. 39–146.
11. P. D. Alonso, A. C. Milner, R. A. Ketcham, M. J. Cookson, T. B. Rowe, *Nature* **430**, 666 (2004).
12. J. A. Hopson, *Annu. Rev. Ecol. Syst.* **8**, 429 (1977).
13. M. Kundrát, *Naturwissenschaften* **94**, 499 (2007).
14. I thank M. S. Northcutt for editing. Supported by NSF grant IBN-0919077.

10.1126/science.1206915

Published by AAAS

RETROSPECTIVE

Lewis R. Binford (1931–2011)

An archaeologist viewed artifacts with an anthropological lens and gave cultural adaptations prominence in the field.

Robert L. Kelly

On 11 April 2011, Lewis Roberts Binford died of congestive heart failure at the age of 79 in Kirksville, Missouri. An era in archaeology ended with his death.

Lew was born in 1931 in Norfolk, Virginia. He attended Virginia Polytechnic Institute until 1952, when he joined the military. While on duty in Japan he became interested in anthropology, and after leaving the service, he attended the University of North Carolina, graduating with a degree in anthropology in 1957. He continued studies in the discipline and received his MA in 1958 and, in 1964, his Ph.D. from the University of Michigan. He taught at the University of Michigan, the University of Chicago, the University of California at the Santa Barbara and Los Angeles campuses, and from 1968 to 1991, he was on the faculty of the University of New Mexico. He then taught at Southern Methodist University in Dallas, Texas until his retirement in 2003. Lew published more than 20 books and 150 papers, dating back to 1959. He lectured throughout Europe, Asia, and North and South America. His many honors included election to the United States National Academy of Sciences, the Huxley Memorial Medal from the Royal Anthropological Institute of Great Britain, and the Society for American Archaeology's Lifetime Achievement Award.

To say that Lewis Binford was a mover and shaker is putting it mildly. Beginning with his 1962 paper, "Archaeology as Anthropology," Lew wanted nothing less than to completely change how archaeologists approached archaeology. In the 1950s, many archaeologists saw the purpose of their enterprise as classification and artifacts as reflections of "mental templates," useful for tracking the migration of "cultures" or the diffusion of ideas. Lew challenged archaeologists to do more by fully participating in anthropology. Kinship, for example, was a hot topic, so two of his first students, William Longacre and James Hill, used ceramics to study kinship in southwestern pueblos. Lew pushed archaeologists to work scientifically with analytical rigor, to create research designs, to pay attention to sampling, and to use statistically analyzed data to test hypotheses. He demanded that archaeologists understand why cultures change over time. Although he ceased traditional archaeological fieldwork by the 1970s, his research among the Nunamiut Inuit, the Navajo, and Australia's Alyawara helped pioneer ethnoarchaeology—the study of living communities—to create ways to interpret archaeological remains. He also pushed forward taphonomy, the study of how natural processes create assemblages of animal bones. As the chief architect of the "new archaeology," later called "processual archaeology," Lew focused on the adaptive processes of cultural change. He never found a lost temple, a new hominin species, or the oldest evidence of anything. Nonetheless, Lewis Binford was the most influential archaeologist of the 20th century.

Lew thrived on controversy. Challenging orthodoxy, he argued that agriculture was not an inevitable cultural advance, but an adaptation to population pressure. He debated the eminent French archaeologist François Bordes, arguing that variation in Mousterian stone tool assemblages reflected functional differences rather than different "tribes" of Neandertals. Reanalyzing faunal assemblages from sites of considerable importance to human evolution, including Olduvai Gorge in Africa and Zhoukoudian in China, he replaced the cherished idea of big game hunting in the Lower Paleolithic with a vision of our human ancestors as lowly scavengers of carcasses. He was a harsh critic and argued with many, but I recall him saying that he only argued with people from whom he thought he could learn something.

Lew focused on understanding how prehistoric societies were adaptive organizations. His 2001 magnum opus, *Constructing Frames of Reference*, used a database of ethnographic information and environmental data to examine the organization of hunter-gatherer societies, his lifelong interest, to understand how group size, food storage, mobility, diet, and social organization were adaptations to the environment.

He also focused on what he labeled "middle-range theory," arguments to make inferences from patterns in archaeological data. His books *Nunamiut Ethnoarchaeology* (1978) and *Bones: Ancient Men and Modern Myths* (1981) showed how to interpret patterns in assemblages of animal bones in terms of butchering strategies and natural processes. He developed concepts (residential and logistical mobility, site structure, site furniture, expedient and curated technology) that led archaeologists the world over to think about spatial distributions of artifacts and technology in new ways.

Lew was a brilliant speaker and teacher. As his graduate assistant, I would watch him develop lectures as he walked across campus to class. His conference presentations were standing room only, and his courses were routinely attended by non-enrolled students. He gave so willingly of his time to students and visitors that he rarely wrote in his university office. Instead, he wrote at home, where he kept two typewriters (in the days before computers) on two desks so he could work on two manuscripts simultaneously. Some 30 years later, his hunter-gatherer seminar remains vivid in my memory. Lew would often slip into a southern Baptist preacher mode and talk . . . and talk. One evening, a particular class that began at 7 PM found him still lecturing at midnight—and his audience still listening. Every time we walked out of that seminar, we felt as if the world had changed.

Lew taught archaeologists to look at the big picture, to search for patterns, and to realize that our knowledge of the past is limited only by the imagination and effort we bring to creating methods to infer that past from its material remains. He saw the past not simply as a historical record of events, but as a record of adaptation. He moved the field from a largely descriptive effort to a more scientific, explanatory enterprise. And no one will move it as far for a long, long time.

10.1126/science.1207836

Department of Anthropology, University of Wyoming, Laramie, WY 82070, USA. E-mail: RLKELLY@uwyo.edu

Published by AAAS

A Diiron Protein Autogenerates a Valine-Phenylalanine Cross-Link

Richard B. Cooley,[1] Timothy W. Rhoads,[1] Daniel J. Arp,[2]* P. Andrew Karplus[1]*

Many proteins generate covalent cross-links between two or more of their own amino acids to create a cofactor near their active site (*1*). Although the mechanisms of cross-link formation and the function of the cross-linked group are not always understood, all characterized cross-links to date involve side chains with nitrogen, oxygen, or sulfur functional groups to facilitate the making and breaking of the covalent bond(s).

Following up our earlier work on π helices in proteins (*2*), we have solved the structure of a rubrerythrin-like protein that appears to conserve certain ancestral features of the ferritin-like superfamily. We call this protein symerythrin to reflect its high level of internal symmetry. The 1.20 Å resolution structure of symerythrin from the photosynthetic eukaryote *Cyanophora paradoxa* (R/R_{free} = 0.101/0.125, Fig. 1A, fig. S1, and table S1) reveals an unusual covalent cross-link connecting the aliphatic $C_{\gamma1}$-atom of Val^{127} to the aromatic C_{δ}-atom of Phe^{17} (Fig. 1B) adjacent to its carboxylate-bridged diiron metallocenter. Liquid chromatography–tandem mass spectrometry (LC-MS/MS) analysis of in-solution proteolytic digests confirmed the location of the cross-link and its presence in the protein before crystallization (Fig. 1C). This cross-link is notable because it occurs between unfunctionalized side chains.

From our symerythrin expression system, cross-linked (~10%) and non–cross-linked (~90%) forms could be purified separately, allowing us to prove that the cross-link was generated by symerythrin's own metallocenter. Indeed, aerobic incubation of non–cross-linked, iron-reconstituted protein with an electron donor led to complete conversion to the cross-linked form (Fig. 1D). The dependency of cross-link formation on a reductant, O_2, and an intact diiron center implies that symerythrin's metallocenter forms high-valent diiron-oxygen intermediates resembling those in soluble methane monooxygenase (*3*) and also proposed to be involved in formation of a recently discovered Tyr-Val ether cross-link in a ribonucleotide reductase R2-like protein (*4*). By analogy with these systems (*5*), we hypothesize that, as a Q-type [i.e., Fe(IV)-Fe(IV)] intermediate forms, Val^{127} rotates so its $C_{\gamma1}$-atom contacts the activated metal-bound oxygen, which abstracts a hydrogen atom to generate a primary alkyl radical. Val^{127} then rotates back and adds to the Phe^{17} phenyl ring to create a cyclohexadienyl radical. Transfer of a single electron to the diiron center, coupled with deprotonation, then generates the cross-link.

Although the physiological function of symerythrin remains unknown, evidence shows that the diiron center is stabilized by the cross-link (Fig. 1E), which both anchors the N-terminal tail to the core of protein and creates a putative substrate binding pocket (Fig. 1B). Given the nature of the cross-link and the substantial effort that has been placed in characterizing such hydrocarbon chemistry for its relevance in biological, bioenergetic, and environmental applications (*6*), further study will be of great interest.

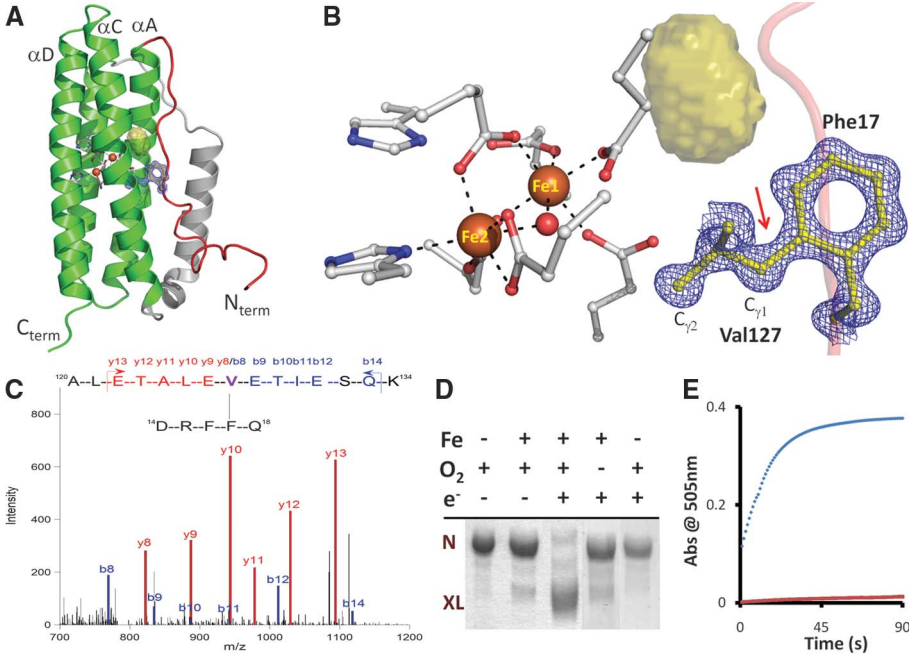

Fig. 1. The Val-Phe cross-link. (**A**) The core four helices of symerythrin (green ribbon with helices αA, αC, and αD labeled), the N-terminal tail (red coil), the putative substrate binding cavity (olive surface), the diiron center (brown spheres), and the ligating residues (C, N, and O atoms are gray, blue, and red, respectively) are shown. Electron density (blue mesh contoured at 2.2 ρ_{rms}) shows the covalent bond linking Val^{127} and Phe^{17} (yellow atoms). (**B**) Close-up of the cross-link (indicated by the red arrow) and diiron center (having one additional Glu ligand compared with rubrerythrins) with the same coloring as (**A**). Val^{127} $C_{\gamma2}$ is 4.5 Å from the bridging oxygen. (**C**) The MS/MS fragmentation pattern from the triply charged parent ion at mass/charge (m/z) = 791.07 identified in proteolytic digests of cross-linked symerythrin. The parent ion mass (2370.181 daltons) matches that of residues 120 to 134 linked to residues 14 to 18 (calculated molecular weight of 2370.182). A, Ala; D, Asp; E, Glu; F, Phe; I, Ile; K, Lys; L, Leu; Q, Gln; R, Arg; S, Ser; T, Thr; and V, Val. (**D**) Purified non–cross-linked symerythrin (N, lane 1) was reconstituted with iron and exposed to O_2 (lane 2) before a 40-hour incubation with an electron source (e^-) during which all symerythrin is converted to the cross-linked form (XL, lane 3). Cross-link formation required O_2 (lane 4) and iron (lane 5). (**E**) Incubation of a chromogenic iron chelator to diferrous non–cross-linked symerythrin (blue) shows rapid iron removal compared with that of diferrous cross-linked symerythrin (red).

References and Notes

1. L. Xie, W. A. van der Donk, *Proc. Natl. Acad. Sci. U.S.A.* **98**, 12863 (2001).
2. R. B. Cooley, D. J. Arp, P. A. Karplus, *J. Mol. Biol.* **404**, 232 (2010).
3. L. Shu *et al.*, *Science* **275**, 515 (1997).
4. C. S. Andersson, M. Högbom, *Proc. Natl. Acad. Sci. U.S.A.* **106**, 5633 (2009).
5. D. A. Kopp, S. J. Lippard, *Curr. Opin. Chem. Biol.* **6**, 568 (2002).
6. R. G. Bergman, *Nature* **446**, 391 (2007).

Acknowledgments: This work was supported in part by NIH grant GM R01-083136 (P.A.K.), the Oregon Agricultural Experiment Station (D.J.A.), and National Institute of Environmental Health Sciences Environmental Health Sciences Center grant ES00210. We thank J. M. Bollinger and C. Krebs for discussions. Coordinates and structure factors are deposited as Protein Data Bank entry 3QHB.

Supporting Online Material

www.sciencemag.org/cgi/content/full/332/6032/929/DC1
Materials and Methods
Fig. S1
Table S1
References

16 March 2011; accepted 15 April 2011
10.1126/science.1205687

[1]Department of Biochemistry and Biophysics, 2011 Agriculture and Life Sciences Building, Oregon State University, Corvallis, OR 97331, USA. [2]Department of Botany and Plant Pathology, 2082 Cordley Hall, Oregon State University, Corvallis, OR 97331, USA.

*To whom correspondence should be addressed. E-mail: karplusp@science.oregonstate.edu (P.A.K.); Dan.J.Arp@oregonstate.edu (D.J.A.)

Comparative Functional Genomics of the Fission Yeasts

Nicholas Rhind,[1]¶ Zehua Chen,[2] Moran Yassour,[3,4,5]‖ Dawn A. Thompson,[3]‖ Brian J. Haas,[2]‖ Naomi Habib,[5,6]‖ Ilan Wapinski,[3,7]‖ Sushmita Roy,[3,8]‖ Michael F. Lin,[8] David I. Heiman,[2] Sarah K. Young,[2] Kanji Furuya,[9] Yabin Guo,[10] Alison Pidoux,[11] Huei Mei Chen,[12] Barbara Robbertse,[13]* Jonathan M. Goldberg,[2] Keita Aoki,[9] Elizabeth H. Bayne,[11]† Aaron M. Berlin,[2] Christopher A. Desjardins,[2] Edward Dobbs,[11] Livio Dukaj,[1] Lin Fan,[2] Michael G. FitzGerald,[2] Courtney French,[6] Sharvari Gujja,[2] Klavs Hansen,[14]‡ Dan Keifenheim,[1] Joshua Z. Levin,[2] Rebecca A. Mosher,[15]§ Carolin A. Müller,[16] Jenna Pfiffner,[2] Margaret Priest,[2] Carsten Russ,[2] Agata Smialowska,[17,18] Peter Swoboda,[17] Sean M. Sykes,[2] Matthew Vaughn,[14] Sonya Vengrova,[19] Ryan Yoder,[13] Qiandong Zeng,[2] Robin Allshire,[11] David Baulcombe,[15] Bruce W. Birren,[20] William Brown,[16] Karl Ekwall,[17,18] Manolis Kellis,[8,3] Janet Leatherwood,[12] Henry Levin,[10] Hanah Margalit,[6] Rob Martienssen,[14] Conrad A. Nieduszynski,[16] Joseph W. Spatafora,[13] Nir Friedman,[5,21] Jacob Z. Dalgaard,[19] Peter Baumann,[22,23,24] Hironori Niki,[9] Aviv Regev,[3,4,24]¶ Chad Nusbaum[2]¶

The fission yeast clade—comprising *Schizosaccharomyces pombe*, *S. octosporus*, *S. cryophilus*, and *S. japonicus*—occupies the basal branch of Ascomycete fungi and is an important model of eukaryote biology. A comparative annotation of these genomes identified a near extinction of transposons and the associated innovation of transposon-free centromeres. Expression analysis established that meiotic genes are subject to antisense transcription during vegetative growth, which suggests a mechanism for their tight regulation. In addition, trans-acting regulators control new genes within the context of expanded functional modules for meiosis and stress response. Differences in gene content and regulation also explain why, unlike the budding yeast of Saccharomycotina, fission yeasts cannot use ethanol as a primary carbon source. These analyses elucidate the genome structure and gene regulation of fission yeast and provide tools for investigation across the *Schizosaccharomyces* clade.

The fission yeast genus *Schizosaccharomyces* forms a broad and ancient clade within the Ascomycete fungi (Fig. 1A) with a distinct life history from other yeasts (*1*). Fission yeast grow preferentially as haploids, divide by medial fission rather than asymmetric budding, and have evolved a single-celled life-style independently from the budding yeasts (Saccharomycotina). Fission yeasts share important biological processes with metazoans, including chromosome structure and metabolism—relatively large chromosomes, large repetitive centromeres, low-complexity replication origins, heterochromatic histone methylation, chromodomain heterochromatin proteins, small interfering RNA (siRNA)–regulated heterochromatin, and TRF family telomere-binding proteins—G_2/M cell cycle control, cytokinesis, the mitochondrial translation code, the RNA interference (RNAi) pathway, the signalosome pathway, and spliceosome components. These features are absent or highly diverged in budding yeast. In general, core orthologous genes in fission yeast more closely resemble those of metazoans than do those of other Ascomycetes (*2*). Fission yeasts have also evolved innovations in carbon metabolism, including aerobic fermentation of glucose to ethanol (*3*). This convergent evolution with the budding yeast *Saccharomyces cerevisiae* offers insight into the evolution of complex phenotypes.

S. pombe is widely used as a model for basic biological processes in the cell and to study genes implicated in human disease. To better understand its evolution and natural history, we have compared the genomes and transcriptomes of *S. pombe*, *S. japonicus*, *S. octosporus*, and *S. cryophilus*, which constitute all known fission yeasts.

Genome sequence and phylogeny. We sequenced and assembled the genomes of *S. octosporus*, *S. cryophilus*, and *S. japonicus* using clone-based and clone-free whole-genome shotgun (WGS) approaches (table S1). Each genome is ~11.5 Mb in size. *S. octosporus* and *S. cryophilus* are 38% GC; *S. japonicus* is 44%. By comparison, the *S. pombe* genome is 12.5 Mb in size and 36% GC. We assembled the *S. octosporus* and *S. japonicus* scaffolds into three full-length chromosomes of quality similar to that of the finished *S. pombe* genome (Fig. 1B, figs. S1 and S2, and tables S2 and S3) and identified telomeric sequence using WGS data (*4*). Telomere repeats in *S. japonicus* (GTCTTA), *S. octosporus* (GGGTTACTT), and *S. cryophilus* (GGGTTACTT) matched a one-and-a-half repeat–unit sequence at the putative telomerase-RNA locus, similar to the configuration in *S. pombe* (GGTTAC) (*5*). Using these motifs, we extended the *S. japonicus* and *S. octosporus* chromosomes into subtelomeric and telomeric sequence (*4*).

We constructed a phylogeny of the Schizosaccharomycetes within Ascomycota (Fig. 1A and fig. S3) from 440 single-copy core orthologs, placing the monophyletic *Schizosaccharomyces* species as a basal sister group to the clade, including the filamentous fungi (Pezizomycotina) and budding yeast (Saccharomycotina). We found an average amino acid identity of 55% between all 1:1 orthologs when we compared *S. pombe* and *S. japonicus*, similar to that between humans and the cephalochordate amphioxus (table S4). For the most closely related species, *S. cryophilus* and *S. octosporus*, 1:1 orthologs share 85% iden-

[1]Biochemistry and Molecular Pharmacology, University of Massachusetts Medical School, 364 Plantation Street, Worcester, MA 01605, USA. [2]Broad Institute of Massachusetts Institute of Technology and Harvard, 320 Charles Street, Cambridge, MA 02141, USA. [3]Broad Institute of Massachusetts Institute of Technology and Harvard, 7 Cambridge Center, Cambridge, MA 02142, USA. [4]Department of Biology, Massachusetts Institute of Technology, 77 Massachusetts Avenue, Cambridge, MA 02139, USA. [5]School of Computer Science and Engineering, Hebrew University, Jerusalem 91904, Israel. [6]Department of Microbiology and Molecular Genetics, Faculty of Medicine, Hebrew University, Jerusalem 91120, Israel. [7]Department of Systems Biology, Harvard Medical School, 200 Longwood Avenue, Alpert 536, Boston, MA 02115, USA. [8]Computer Science and Artificial Intelligence Laboratory, Massachusetts Institute of Technology, 32 Vassar Street 32-D510, Cambridge, MA 02139, USA. [9]Microbial Genetics Laboratory, Genetic Strains Research Center, National Institute of Genetics, 1111 Yata, Mishima, Shizuoka 411-8540, Japan. [10]Eunice Kennedy Shriver National Institute of Child Health and Human Development, National Institutes of Health, Bethesda, MD 20892, USA. [11]Wellcome Trust Centre for Cell Biology, Institute of Cell Biology, School of Biological Sciences, The University of Edinburgh, 6.34 Swann Building, Mayfield Road, Edinburgh EH9 3JR, UK. [12]Department of Molecular Genetics and Microbiology, Life Science, Room 130, State University of New York, Stony Brook, NY 11794, USA. [13]Department of Botany and Plant Pathology, Oregon State University, Corvallis, OR 97331, USA. [14]Cold Spring Harbor Laboratory, 1 Bungtown Road, Cold Spring Harbor, NY 11724, USA. [15]Department of Plant Sciences, University of Cambridge, Downing Street, Cambridge CB2 3EA, UK. [16]Centre for Genetics and Genomics, University of Nottingham, Queen's Medical Centre, Nottingham NG7 2UH, UK. [17]Center for Biosciences, Department of Biosciences and Nutrition, Karolinska Institute, 141 38 Huddinge, Sweden. [18]Department of Life Sciences, Södertörns Högskola, 141 89 Huddinge, Sweden. [19]Warwick Medical School, University of Warwick, Gibbet Hill Campus, Coventry CV4 7AL, UK. [20]Broad Institute of Massachusetts Institute of Technology and Harvard, 301 Binney Street, Cambridge, MA 02141, USA. [21]Alexander Silberman Institute of Life Sciences, Hebrew University, Jerusalem 91904, Israel. [22]Stowers Institute for Medical Research, Kansas City, MO 64110, USA. [23]Department of Molecular and Integrative Physiology, University of Kansas Medical School, Kansas City, KS 66160, USA. [24]Howard Hughes Medical Institute.

*Present address: National Center for Biotechnology Information, National Library of Medicine, National Institutes of Health, Department of Health and Human Services, 45 Center Drive, Bethesda, MD, 20892, USA.

†Present address: Wellcome Trust Centre for Gene Regulation and Expression, College of Life Sciences, University of Dundee, Dundee DD1 5EH, Scotland, UK.

‡Present address: Evolva Biotech A/S, Bülowsvej 25, 1870 Frederiksberg C, Denmark.

§Present address: The University of Arizona, The School of Plant Sciences, 303 Forbes Building, 1140 East South Campus Drive, Tucson, AZ 87421, USA.

‖These authors made equivalent contributions.

¶To whom correspondence should be addressed. E-mail: nick.rhind@umassmed.edu (N.R.); aregev@broad.mit.edu (A.R.); chad@broadinstitute.org (C.N.)

tity on average, similar to humans and dogs. The genetic diversity within *S. pombe* is low. Comparing the *S. pombe* 972 strain to WGS analysis of *S. pombe* NCYC132 and *S. pombe* var. *kambucha*, two phenotypically distinct strains, revealed less than 1% nucleotide difference between the three strains (fig. S4 and table S5).

Eradication of transposons and reorganization of centromere structure. Transposons and other repetitive sequences are thought to be crucial for centromeric function through the maintenance of heterochromatin (*6*). These sequences evolve rapidly, but the evolutionary relation among centromeres, transposons, and heterochromatin is unclear, in part because fungal centromeres have not generally been included in genome assemblies. The *S. japonicus* genome harbors 10 families of gypsy-type retrotransposons (*4*) (fig. S5 and table S6). Sequence divergence of their reverse transcriptases suggests that these transposon families predate the last common ancestor of the Ascomycetes. However, a dramatic loss of transposons occurred after the divergence of *S. japonicus*; *S. pombe* harbors two related retrotransposons, Tf1 and Tf2; *S. cryophilus* has a single related retrotransposon, Tcry1; *S. octosporus* contains no transposons, but contains sequences related to reverse transcriptase and integrase that may represent extinct transposons (fig. S5 and table S6).

The disappearance of transposons in the evolution of fission yeast species after *S. japonicus* correlates with the appearance of the *cbp1* gene family, which suggests a transition in the control of centromere function. In *S. pombe*, Cbp1 proteins bind centromeric repeats and are required for transposon silencing and genome stability (*7*, *8*). Although described as orthologs of CENP-B, a human centromere-binding protein, Cbp1 proteins apparently evolved independently within the *Schizosaccharomyces* lineage from a domesticated Pogo-like DNA transposase (*9*). The appearance of the *cbp1* gene family also correlates with the switch from RNAi-mediated transposon silencing in *S. japonicus* (see below) to a Cbp1-based mechanism in *S. pombe*, which suggests that this shift to Cbp1-based transposon control allowed the eradication of most transposons from the fission yeast genomes, possibly by promoting recombinational deletion between long terminal repeats (LTRs) (*8*). Furthermore, the *cbp1* family is evolving rapidly (fig. S6), which suggests that Cbp1-based transposon silencing is a *Schizosaccharomyces*-specific innovation that arose after the divergence of *S. japonicus*.

The loss of transposons was accompanied by a substantial reorganization of chromosome architecture that conserves centromere function, which suggests that the evolution of novel

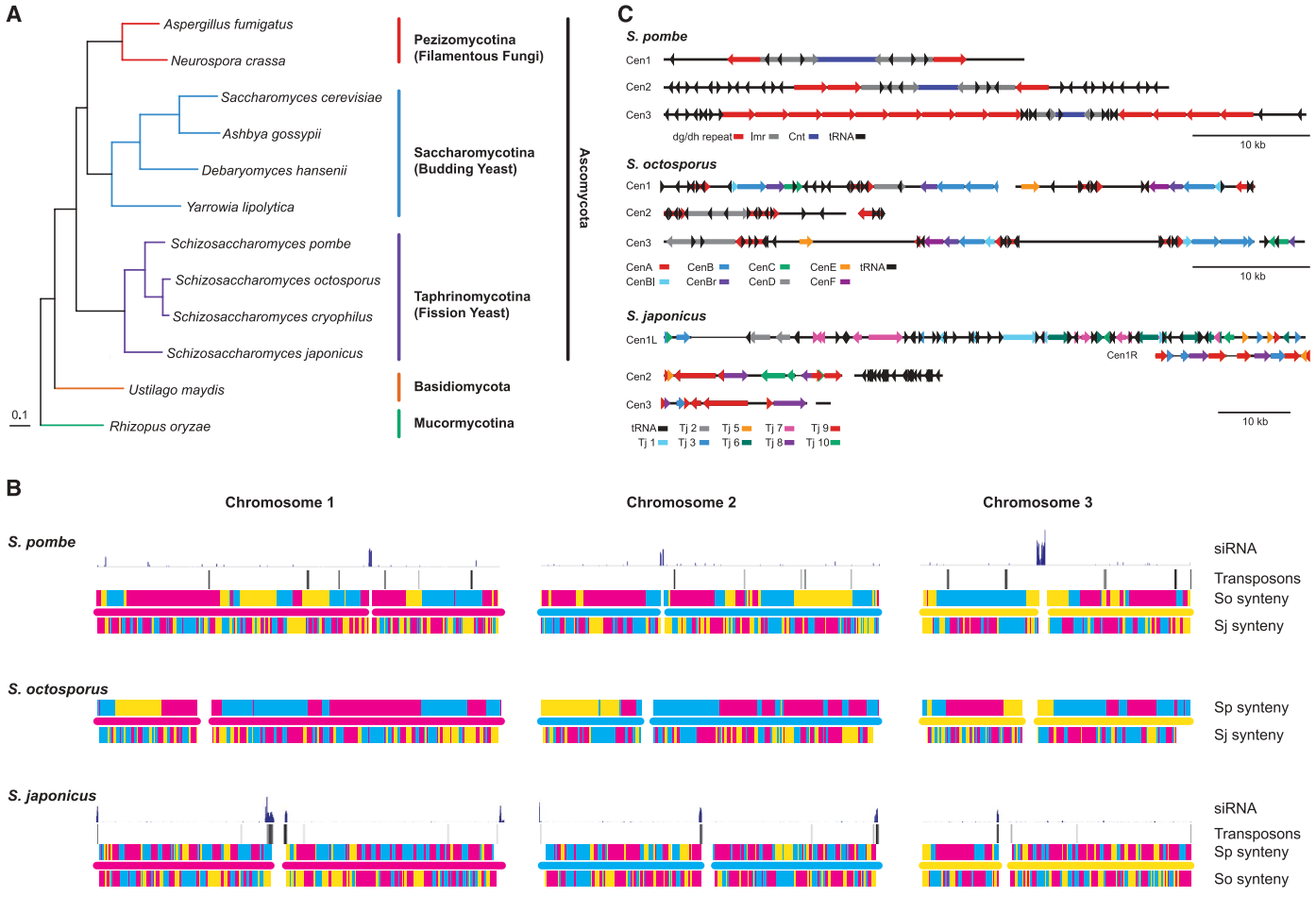

Fig. 1. *Schizosaccharomyces* phylogeny and chromosome structure. (**A**) A maximum-likelihood phylogeny of 12 fungal species from 440 core orthologs (each occurring once in each of the genomes) from fly to yeast. A maximum-parsimony analysis produces the same topology. Both approaches have 100% bootstrap support for all nodes. (**B**) The chromosome structure of *S. pombe*, *S. octosporus*, and *S. japonicus*. The middle bar in each figure represents the chromosome and its centromere: red for chromosome 1, blue for chromosome 2, and yellow for chromosome 3. Depicted above and below each chromosome are the chromosomes in the other two species to which the genes on the chromosome of interest map, using the same color scheme. Depicted above the *S. pombe* and *S. japonicus* chromosomes are the distributions of transposons and mapping of siRNAs. *S. cryophilus* is not included, because its genome has not been assembled into complete chromosomes. (**C**) The centromeric repeat structures of *S. pombe*, *S. octosporus*, and *S. japonicus*. Due to their repetitive nature, they are unlikely to represent the exact genomic structure. The *S. pombe* portion of the figure is adapted from (*11*).

centromere structures compensated for the loss of transposons. In *S. japonicus*, transposons cluster next to telomeres and centromeres, as in metazoans (Fig. 1, B and C). In the other Schizosaccharomycetes, the subtelomeres and pericentromeres are also repetitive, but lack transposons (Fig. 1C). However, like *S. japonicus*, the centromeric and subtelomeric repeats are confined to pericentromeric and subtelomeric regions, respectively, with one exception—a centromeric repeat involved in transcriptional silencing at the *S. pombe* mating-type locus (*10*). We confirmed that the centromeres are heterochromatic by histone H3 lysine 9 (H3K9) methylation mapping (fig. S7) and showed that the *S. japonicus* centromeres are functional by meiotic mapping (table S2).

Although centromeric repeats evolve rapidly, differing even between related strains (*11*), individual repeat sequences tend to be similar within strains (Fig. 1C). No similarity was observed between the centromeric repeats of *S. pombe*, *S. octosporus*, or *S. cryophilus*. However, both *S. pombe* and *S. octosporus* centromeres contain repeated elements, highly similar between chromosomes, that are arrayed in a larger inverted repeat structure around a unique core sequence (Fig. 1C), which suggests that they are homogenized by nonreciprocal recombination. This contrasts with a lack of symmetry in *S. japonicus* and implies that transposition occurs more rapidly than homogenization by recombination. Thus, the suppression of transposition likely led both to the degeneration of transposon sequences and to the evolution of symmetric centromeric repeats.

Despite the divergence of centromere sequence and of gene order on the chromosome arms, karyotype and pericentromeric gene order are conserved between *S. pombe* and *S. octosporus* (fig. S8). Thus, although gene conversion maintains the similarity of centromeric repeats between the different centromeres, crossover recombination between centromeres is suppressed. We observed neither centromeric translocations nor neocentromere events within these lineages, even though centromeres can occur at novel locations in manipulated *S. pombe* strains (*12*). The retention of repetitive elements in the centromeres of *S. pombe*, *S. octosporus*, and *S. cryophilus*, even as they have lost their transposons, implies that centromeric repeats have an important function.

Because siRNAs are involved in both transposon silencing and centromere function (*13*), we investigated these roles in the *Schizosaccharomyces* lineage. In *S. pombe*, the centromeric repeats produce dicer-dependent siRNAs required for maintenance of centromeric structure, function, and transcriptional silencing via Argonaute-dependent heterochromatin formation (*14*). However, transposons are silenced in *S. pombe* by RNAi-independent mechanisms and do not produce abundant siRNAs (Fig. 1B and fig. S9) (*7*). To investigate whether centromere-directed siRNA production is conserved within the transposon-rich centromeres of *S. japonicus*, we sequenced small RNAs from log-phase *S. japonicus* cultures (which have a modal size of 23 nucleotides) (*4*) and found that 94% map to transposons, both telomeric and centromeric (Fig. 1B and fig. S9). The fact that siRNAs map to transposons in *S. japonicus* but not in *S. pombe* suggests that either the fission yeast RNAi pathway targets repetitive sequences instead of mobile elements per se or that the pathway evolved away from an ancestral role in transposon control to a dedicated role in heterochromatin function.

Evolution of mating-type loci. The structure of the mating-type loci and the cis-acting elements that regulate mating-type switching is highly conserved across all four species (fig. S10). The expressed *mat1* locus can contain either the plus (P) or the minus (M) allele and switches between the two by epigenetically programmed gene conversion (*15*–*17*) from two heterochromatically silenced donor cassettes: *mat2-P* and *mat3-M* (figs. S10 and S11). cis-Acting regulatory sequences required for epigenetic imprinting and recombinational switching (*18*–*20*) are conserved (*4*) (fig. S11), as is the epigenetically programmed genomic mark associated with *mat1* (*15*).

In contrast, none of the cis-acting sequences involved in transcriptional repression of the silent cassettes in *S. pombe* are identifiable in the other species, although the donor cassettes are enriched for H3K9me heterochromatin (fig. S7). In *S. japonicus*, the silent *mat* loci are found to directly abut the centromere of chromosome 3, which suggests that they may be silenced by a positional effect. In *S. octosporus* and *S. cryophilus*, the *mat* loci are distant from the centromeres, but each contains a conserved region of transposon remnants, which may be silencing triggers. They also contain inverted repeats, albeit shorter and less similar to each other than the inverted repeats that flank the *mat2/3* locus in *S. pombe* (*21*). Thus, their silencing strategies may share elements from both *S. pombe* and *S. japonicus*. These results suggest that the mechanisms of imprinting and switching have been conserved, but that the strategies for establishing heterochromatin are plastic.

Comparative annotation of transcriptomes. We annotated the three genomes using standard methods and compared them with *S. pombe* (*4*). We then deep-sequenced poly(A)-enriched, strand-specific cDNA (*22*–*24*) (RNA-Seq) and constructed de novo transcript models (fig. S12) for log phase, glucose depletion, early stationary phase, and heat shock from *S. pombe*, *S. octosporus*, and *S. japonicus* and log phase, glucose depletion, and heat shock from *S. cryophilus*.

In *S. pombe*, we reconstructed 4277 out of 5064 previously annotated genes; of the remain-

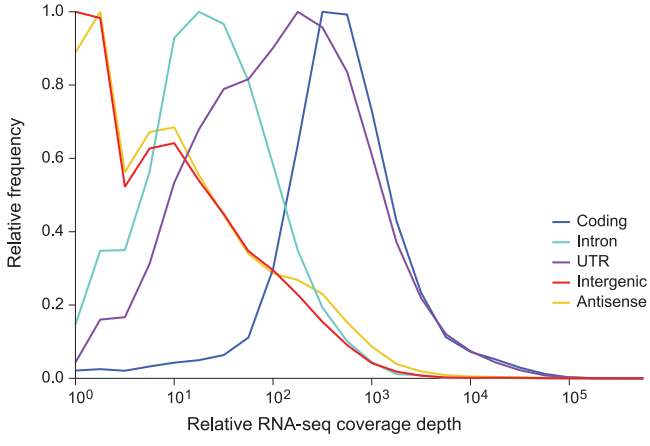

Fig. 2. Polyadenylated transcription is predominantly confined to protein-coding genes. The *S. pombe* genome was divided into four different feature classes: protein-coding sequence, intron sequence, untranslated sequence (5′ and 3′ UTRs), and intergenic sequence (all nucleotides between UTRs of protein-coding genes). The frequency of RNA-Seq reads was calculated over sequential 20–base pair windows across these features; for coding sequence, the frequency of antisense reads was also calculated. Frequency was normalized to the maximum frequency within each feature class to compensate for the different class sizes.

Table 1. Conservation of gene content and structure. See Fig. 5 legend for abbreviations.

Organism and total	Orthologous groups				Introns		
	Same	Gain	Loss	Dup	Same	Gain	Loss
S. pombe	4218	321	83	23	2901	297	27
S. octosporus	4218	133	48	5	2901	25	8
S. cryophilus	4218	283	73	11	2901	75	4
Ancestor of *Soct* and *Scry*	4218	103	44	15	2901	396	0
Ancestor of *Spom*, *Soct*, and *Scry*	4218	339	159	29	2901	415	412
S. japonicus	4218	242	0	18	2901	708	214
Ancestor of *Schizosaccharomyces*		640	745				
Total		2061	1152	101		1916	665

ing 788 genes, 60% were covered over at least 90% of their length. Four hundred of our transcript models change coding exon structure of the gene, 95% of which maintained or improved conserved coding capacity (tables S7 and S8 and fig. S12) (*25*). In addition, we identified 253 untranslated region (UTR) introns. Last, we found 89 new protein-coding genes in *S. pombe*, 53 of which are conserved (table S7 and fig. S13). We found no evidence that intron-rich fission yeast genes engage in metazoan-like alternative splicing (*26*). We found evidence for 433 alternative splicing events in *S. pombe* in the form of intron retention and alternative splice-donor or splice-acceptor usage, but no evidence of exon skipping or alternative exons; we found similar levels of splice variants in the other species (table S9). However, because many of these variants disrupt the coding capacity (figs. S14 and S15) and only a minority of intron retentions (146 out of 393) are conserved between two or more species, we suspect that much of alternative splicing in fission yeast represents nonproductive splicing variants. It is interesting that, in some cases, the nonspliced variant may be the protein-coding isoform (figs. S14, C and D, and S15, and table S10).

Transcription primarily represents protein-coding transcripts. The majority of stable fission yeast transcripts originate from annotated protein-coding genes. Most of the *S. pombe* genome is transcribed (*22*), with 91% of nucleotides covered by at least one RNA-Seq read. However, most transcription, as measured by steady-state poly(A)-enriched RNA levels, is associated with well-defined transcripts, most of which are protein coding. Specifically, 37% of intergenic nucleotides (between the UTRs of annotated protein-coding transcripts) are not detectibly expressed, and 90% of transcribed intergenic nucleotides account for only 0.16% of the poly(A)-enriched transcript signal. Moreover, the median expression level of exonic sequence (99.1% of which are detectably expressed) is 305 times that of intergenic sequence (Fig. 2 and table S11), with intergenic transcription enriched within origins of DNA replication (fig. S16)—gene-free loci with nucleosome-free regions (*27*–*29*) that may provide permissive loci for ectopic transcriptional initiation (*30*).

Transcription of coding genes is heavily biased to the sense strand. Of the coding genes, 73% have <5% of their RNA-Seq reads on the antisense strand. Genes with >5% antisense reads are enriched for convergent transcripts with intergenic distances of <200 bp ($P < 10^{-8}$, hypergeometric test), but not with those of >200 bp ($P > 0.1$), which suggests that much antisense transcription is due to readthrough of 3′-termination sites (*31*) (fig. S17). Thus, stable transcripts in fission yeast genomes are primarily associated with known transcription units. We discuss notable exceptions below.

Conservation of gene content and structure. Despite the evolutionary breadth of the fission-yeast clade, as measured by amino acid divergence, their gene content and structure are remarkably conserved. Of ~5000 coding genes in fission yeast species, 4218 are 1:1:1:1 orthologs across the clade, with the remainder of the orthologous groups containing genes that have been duplicated or deleted since their last common ancestor (Table 1 and fig. S12). Protein kinases are even more conserved in gene content; 93% (102 out of 110) of *S. pombe* protein kinases are 1:1:1:1 orthologs (*4*). Moreover, of 3601 *S. pombe* introns in 2616 spliced 1:1:1:1 orthologs, 2901 (81%) are identical across the four species (table S13). Overall, the conservation of gene content, gene order, and gene structure within *Schizosaccharomyces* is higher than expected given the level of amino acid divergence. From amino acid divergence, we estimate that the fission yeast clade arose about 220 million years ago (fig. S3). However, the conservation of gene content is significantly higher than that within *Saccharomyces* or *Kluyveromyces*, both of which have much lower amino acid divergence (table S15), which suggests that fission yeast amino acid sequences are evolving anomalously quickly or that genome structures are unusually stable.

The majority of gene changes are due to the gain of species- and clade-specific genes (table S12 and S14) (*4*). We tested whether gene gain is due to rapid divergence of orthologous genes by

A

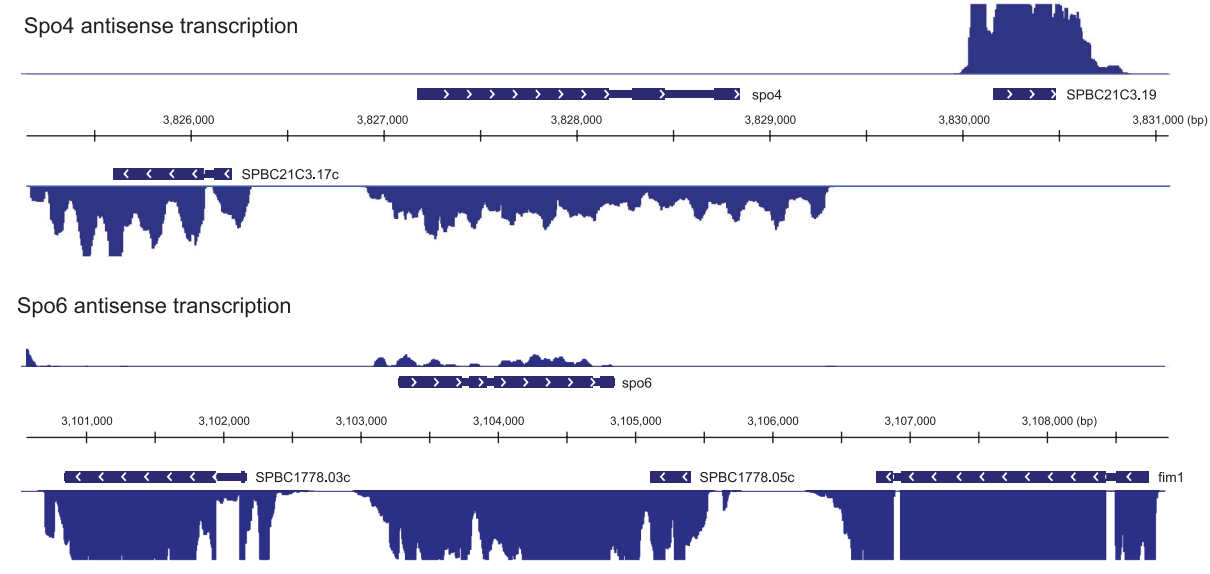

B

S. pombe GO annotation	p value
Meiosis	1.33×10^{-10}
Meiotic chromosome segregation	1.53×10^{-8}
Meiotic recombination	4.38×10^{-6}
Nuclear chromosome	4.54×10^{-3}
Ascospore formation	5.60×10^{-3}

Fig. 3. Meiotic genes are subject to antisense transcription. (**A**) Examples of antisense transcription of meiotic genes. Above and below the chromosome coordinates are the coding sequence annotations on the top and bottom strand, respectively. Above and below these are the strand-specific RNA-Seq read densities on a 0 to 300 scale; signal above 300 is truncated to make the low-amplitude signal visible. (**B**) Enrichment of Gene Ontology (GO) annotations within the set of protein-coding genes with more antisense than sense transcription. All terms with a *P* value of <0.01 are included, except for high-level terms (i.e., biological process and molecular function).

looking for colinearity in regions with species-specific genes, and we examined these regions for signs of sequence similarity. We found that 94 out of 317 *S. pombe*–specific genes are in the same position relative to neighboring genes as genes specific to other species (table S16). Of these, nine show > 15% identity to a cognate gene in another species, which suggests that they are rapidly diverged orthologs (*4*).

We also found 34 *S. pombe* candidates for horizontal gene transfer from bacteria, including two published examples (*4*, *32*, *33*) (table S17), and similar numbers in the other species. Of these, 16 appear to have occurred before the radiation of the clade, and 9 appear to be specific to *S. pombe*.

Evidence for intergenic and antisense noncoding transcripts. We identified 1097 putative transcript models in *S. pombe* supported by strand-specific RNA-Seq data, but containing no obvious coding capacity and having no correspondence to well-defined noncoding RNAs (ncRNAs) (*22*, *24*, *34*) (fig. S18 and tables S18 and S19). Of these potential ncRNAs, 449 are intergenic and 648 are antisense, overlapping a coding gene on the other strand by at least 30%. Of the ncRNAs, 213 overlap an annotated UTR on the same strand, which suggests that they may be alternative UTRs. Nevertheless, the data support 338 of the intergenic and 546 of the antisense ncRNAs as distinct transcripts (*4*).

Of the 338 distinct intergenic ncRNAs in *S. pombe*, 138 are conserved in location in at least one other species (table S41). Moreover, 26 of the intergenic ncRNAs are conserved in sequence, and of these, 9 are conserved in both location and sequence, which suggests that they represent potentially biologically important noncoding RNAs. The transcripts that are conserved in location but not in sequence may represent functional transcripts that have diverged beyond recognition. Of the antisense transcripts, 328 (51%) are conserved across two or more genomes (table S20), which suggests that they are biologically important (*35*).

Antisense regulation of meiotic transcription. Across fission yeast, the ~250 genes with greater

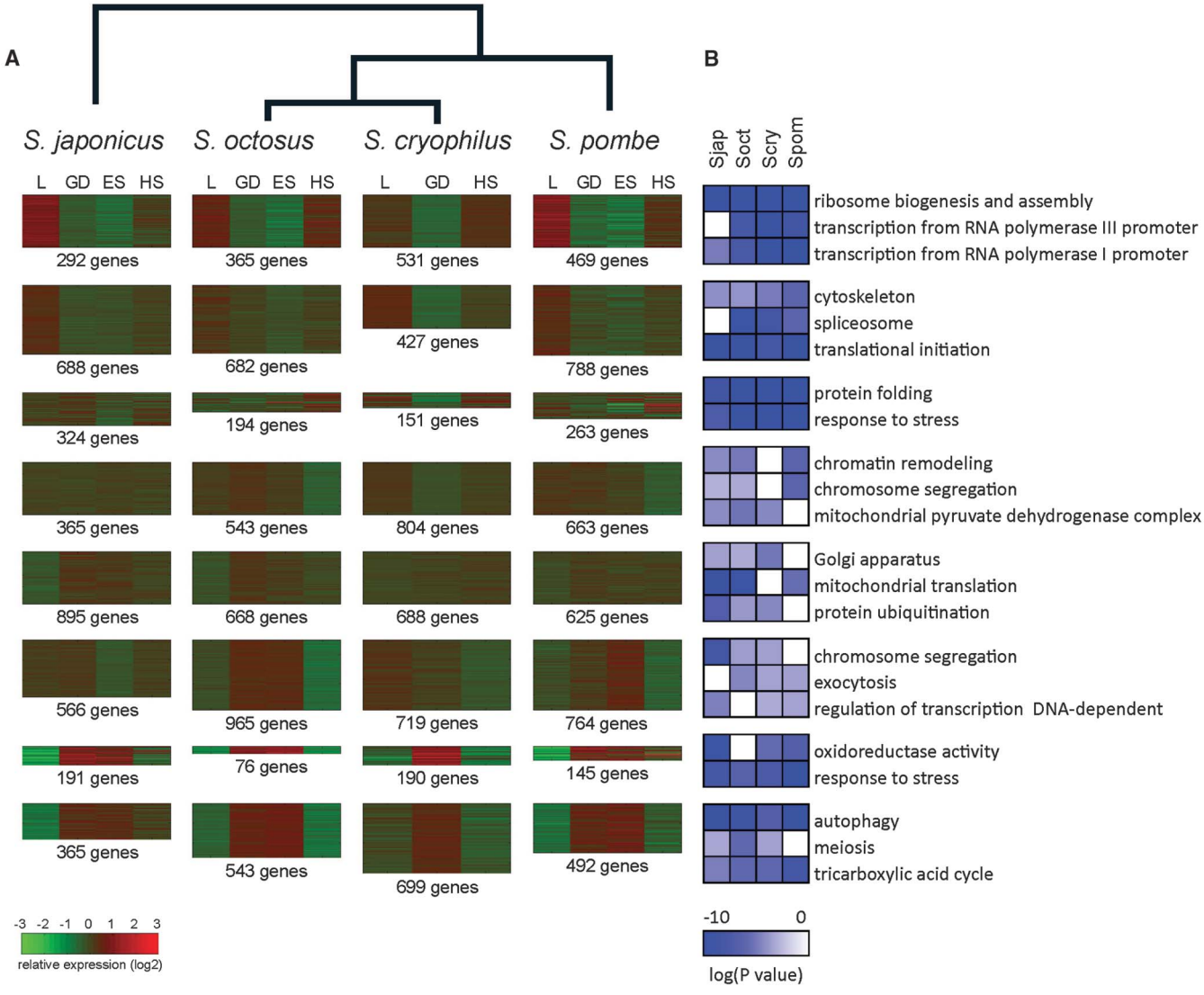

Fig. 4. Expression profiles cluster into similar patterns with conserved biological functions. (**A**) Expression clusters for each species. Gene expression profiles for each species were clustered (*4*). The size of each heat map is proportional to the number of genes in the cluster and the number of genes in each is indicated. Similar cluster sizes and patterns reflect similar expression patterns between the species. The heat shock transcription profile is similar to log-phase growth because the transcriptional response on the 15-min time scale used here is limited to a relatively small number of genes. L, log phase; GD, glucose depletion; ES, early stationary phase; HS, heat shock. (**B**) A selection of enriched GO terms for each cluster. The color intensity is proportional to the negative logarithm of the hypergeometric *P* value enrichment on a continuous scale of 0 to 10. Complete GO term enrichments are shown in table S26.

antisense transcription than sense transcription (table S21) are significantly enriched for meiotic genes ($P = 10^{-10}$ for *S. pombe*, hypergeometric test) (Fig. 3, fig. S19, and tables S22 and S23), consistent with observations in *S. pombe* and *S. cerevisiae* (*24*, *35*). Several antisense-transcribed genes have been proposed to be regulated by intron retention (*36*, *37*); however, these studies did not use strand-specific approaches, which makes it impossible to distinguish unspliced sense transcripts from antisense transcripts. We find no evidence of alternative splicing of any of these genes.

Antisense transcription of meiotic genes does not uniformly decrease as cognate sense transcription increases during meiosis (fig. S20). This observation suggests that antisense transcription does not inhibit sense transcription, in contrast to the anticorrelation observed in *S. cerevisiae* (*30*, *35*). Furthermore, meiotic genes are not enriched among genes with >5% antisense transcription but <100% antisense transcription ($P = 0.47$, hypergeometric test), consistent with a stoichiometric mechanism of regulation in which antisense transcripts directly bind to and inhibit the stability or translation of sense transcripts.

Global conservation of expression programs within fission yeasts. To identify conserved modules of coexpressed genes, we examined expression patterns across the four conditions and between the four fission yeast with phylogenic clustering (Fig. 4). We found that patterns of gene expression between species grown in similar conditions are generally conserved, with dominant patterns associated with growth (log phase and heat shock) and stress (glucose depletion and early stationary phase). Moreover, similar expression clusters are enriched for similar gene annotations across the species.

Fission yeast up-regulate genes involved in mitosis, including those involved in the kinetochore, the spindle pole body, and the anaphase-promoting complex, in response to glucose depletion (table S24). In contrast, several classes of genes involved in growth are down-regulated (*4*). None of these genes are extensively regulated in glucose depletion in *S. cerevisiae* (*38*).

cis-Regulatory mechanisms are associated with novel and expanded functions. Promoter motifs with conserved regulatory function across Ascomycota show new functionality among the *Schizosaccharomyces*. For example, the motif bound by Rtg3 in *S. cerevisiae* is associated with amino acid metabolism genes across the phylum. In fission yeast, however, it is also enriched in genes responsive to various stress responses (Fig. 5A). Of the stress genes that have Rtg3 motifs in *S. pombe*, 36% are found only in the *Schizosaccharomyces* clade, and many are also associated with the Atf1 motif, a conserved regulator of the stress response (Fig. 5B). Rtg3 does not have a detectable ortholog in the *Schizosaccharomyces*

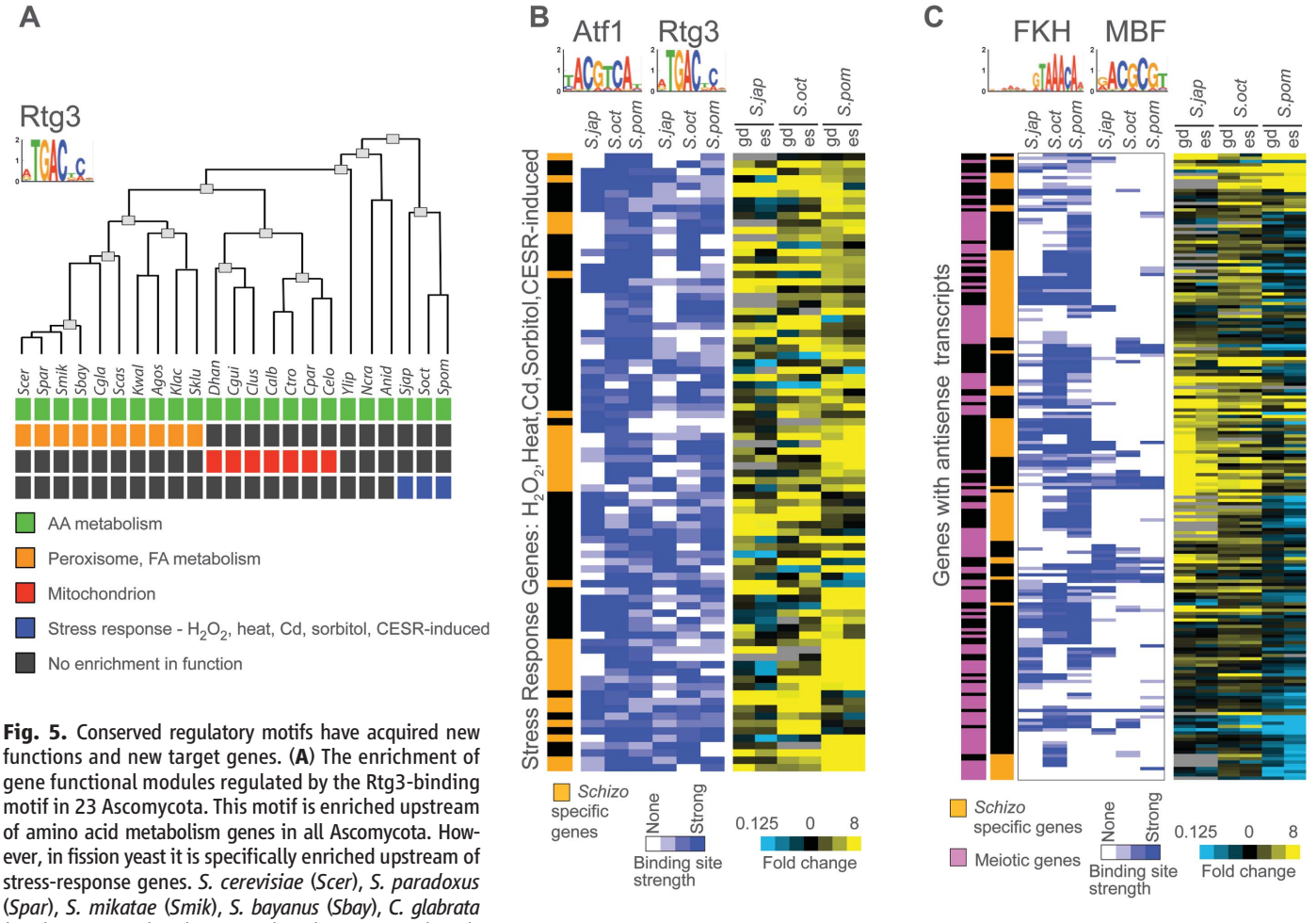

Fig. 5. Conserved regulatory motifs have acquired new functions and new target genes. (**A**) The enrichment of gene functional modules regulated by the Rtg3-binding motif in 23 Ascomycota. This motif is enriched upstream of amino acid metabolism genes in all Ascomycota. However, in fission yeast it is specifically enriched upstream of stress-response genes. *S. cerevisiae* (*Scer*), *S. paradoxus* (*Spar*), *S. mikatae* (*Smik*), *S. bayanus* (*Sbay*), *C. glabrata* (*Cgla*), *S. castellii* (*Scas*), *K. waltii* (*Kwal*), *A. gossypii* (*Agos*), *K. lactis* (*Klac*), *S. kluyveri* (*Sklu*), *D. hansenii* (*Dhan*), *C. guilliermondii* (*Cgui*), *C. lusitaniae* (*Clus*), *C. albicans* (*Calb*), *C. tropicalis* (*Ctro*), *C. parapsilosis* (*Cpar*), *C. elongosporus* (*Celo*), *Y. lipolytica* (*Ylip*), *N. crassa* (*Ncra*), *A. nidulans* (*Anid*), *S. japonicus* (*Sjap*), *S. octosporus* (*Soct*), and *S. pombe* (*Spom*). (**B**) Enrichment of Rtg3- and Atf1-binding sites in the promoters of stress-response genes. Each row represents a gene. The strength of the strongest regulatory site upstream of the gene is indicated in the blue heat map. The expression of the gene in glucose depletion (gd) and early-stationary phase(es) relative to log phase is indicated in the blue-yellow heat map. Genes specific to the fission yeast clade are indicated in orange. (**C**) Enrichment of FKH- and MBF-binding sites in front of antisense-transcribed genes. As in (B), but each row represents a gene with greater antisense than sense transcription. Genes associated with meiosis (*44*) are indicated in magenta. CESR, core environmental stress response.

clade (*39*), but the motif recognized by Rtg3 in *S. cerevisiae* is clearly identifiable in fission yeast, which suggests that these regulatory motifs are more conserved than their binding proteins. We also found a similar acquisition of *Schizosaccharomyces*-specific genes by the FKH- and MBF-associated motifs, which regulate meiotic transcription in *S. pombe* (*4*, *40*, *41*). In particular, these two motifs were enriched in genes with antisense transcripts (Fig. 5C). Most of the FKH (a motif bound by Mei4 in *S. pombe*) target genes with antisense transcripts (80%, 47 genes) are meiotic genes, the majority of which are specific to the *Schizosaccharomyces* clade (Fig. 5C).

Gene content reflects glucose-dependent lifestyle. Fission yeast and budding yeast of the *Saccharomyces* clade independently evolved the ability to produce ethanol by aerobic fermentation (*3*, *42*). In contrast to the convergent evolution of ethanol production, the utilization of ethanol has not converged; although budding yeast can efficiently catabolize ethanol, fission yeast cannot use ethanol as a primary carbon source. The evolution of aerobic fermentation in budding yeast involved changes in gene content, most notably following a whole-genome duplication (WGD) event and in regulatory mechanisms of glucose repression (*3*, *43*).

Like budding yeast, fission yeast have duplicate copies of the pyruvate decarboxylase (*pdc*) gene, needed to funnel pyruvate to fermentation. They also have orthologs of several activators and repressors of respiratory genes, including Hap2/3/4/5 complex members, the Adr1, Tup, and Mig transcriptional regulators, and the Snf1–Sip1 and 2 kinase (*3*). However, there are substantial distinctions in gene content between fission yeast and the post-WGD budding yeast (fig. S21). We identified loss of the glyoxylate cycle, loss of the glycogen biosynthesis, fewer glycolytic paralogs, loss of the gluconeogenic enzyme phosphoenolpyruvate carboxykinase, lack of expanded *adh* genes, and lack of transcriptional regulators of glucose repression as differences that illuminate the distinct metabolic capacities of fission yeast (*4*). All of these adaptations are consistent with the inability of fission yeast to consume ethanol as a sole carbon source. The loss of conserved enzymes highlights how fission yeast came to depend solely on glucose.

In both fission yeast and budding yeast, as glucose is depleted, the expression of respiratory genes [oxidative phosphorylation enzymes or tricarboxylic acid (TCA) cycle] is induced. However, unlike *S. cerevisiae* (*38*), in fission yeast the expression of the genes encoding the pyruvate dehydrogenase complex and *adh1* is reduced, which prevents the efficient use of pyruvate for respiration. Instead, the expression of the *ald* genes is induced, which may provide an alternative mechanism for generating acetyl–coenzyme A in fission yeast.

Thus, the lack of efficient ethanol catabolism by fission yeast demonstrates that aerobic fermentation did not evolve to create a consumable by-product. Instead, ethanol is a waste product, possibly produced because it is toxic to competing microorganisms. It is interesting that aerobic fermentation appears to have evolved as early as 200 million years ago in fission yeast (fig. S3), long before the WGD and subsequent evolution of aerobic fermentation in budding yeast.

Conclusions. Our comparative analysis of genome structure and expression in the fission yeast, especially the analysis of centromere structure and evolution, demonstrates how chromosomal features can be rearranged while retaining function and maintaining stable positions across taxa. We also provide insight into centromeric biology and elucidate conserved antisense transcription that may play a systematic role in meiotic gene regulation. Last, this study informs our understanding of the major evolutionary innovation of aerobic alcohol fermentation in microbial metabolism that arose in parallel in the fission yeast and budding yeast lineages. As these results demonstrate, comparative analyses improve the power of fission yeast as a model for eukaryotic biology.

References and Notes

1. S. L. Forsburg, *Trends Genet.* **15**, 340 (1999).
2. V. Wood *et al.*, *Nature* **415**, 871 (2002).
3. C. L. Flores, C. Rodríguez, T. Petit, C. Gancedo, *FEMS Microbiol. Rev.* **24**, 507 (2000).
4. Materials and methods are available as supporting material on *Science* Online.
5. J. Leonardi, J. A. Box, J. T. Bunch, P. Baumann, *Nat. Struct. Mol. Biol.* **15**, 26 (2008).
6. L. H. Wong, K. H. Choo, *Trends Genet.* **20**, 611 (2004).
7. H. P. Cam, K. Noma, H. Ebina, H. L. Levin, S. I. Grewal, *Nature* **451**, 431 (2008).
8. M. Zaratiegui *et al.*, *Nature* **469**, 112 (2011).
9. C. Casola, D. Hucks, C. Feschotte, *Mol. Biol. Evol.* **25**, 29 (2008).
10. S. I. Grewal, A. J. Klar, *Genetics* **146**, 1221 (1997).
11. N. C. Steiner, K. M. Hahnenberger, L. Clarke, *Mol. Cell. Biol.* **13**, 4578 (1993).
12. K. Ishii *et al.*, *Science* **321**, 1088 (2008).
13. S. I. Grewal, *Curr. Opin. Genet. Dev.* **20**, 134 (2010).
14. T. A. Volpe *et al.*, *Science* **297**, 1833 (2002).
15. D. H. Beach, *Nature* **305**, 682 (1983).
16. R. Egel, *Curr. Genet.* **8**, 205 (1984).
17. S. Vengrova, J. Z. Dalgaard, *Genes Dev.* **18**, 794 (2004).
18. S. Sayrac, S. Vengrova, E. L. Godfrey, J. Z. Dalgaard, *PLoS Genet.* **7**, e1001328 (2011).
19. M. Kelly, J. Burke, M. Smith, A. Klar, D. Beach, *EMBO J.* **7**, 1537 (1988).
20. B. Arcangioli, A. J. Klar, *EMBO J.* **10**, 3025 (1991).
21. G. Singh, A. J. Klar, *Genetics* **162**, 591 (2002).
22. B. T. Wilhelm *et al.*, *Nature* **453**, 1239 (2008).
23. J. Z. Levin *et al.*, *Nat. Methods* **7**, 709 (2010).
24. T. Ni *et al.*, *PLoS ONE* **5**, e15271 (2010).
25. M. F. Lin, I. Jungreis, M. Kellis, *Nature Precedings*, published online 18 August 2010 (http://hdl.handle.net/10101/npre.2010.4784.1).
26. N. F. Käufer, J. Potashkin, *Nucleic Acids Res.* **28**, 3003 (2000).
27. M. Gómez, F. Antequera, *EMBO J.* **18**, 5683 (1999).
28. M. L. Eaton, K. Galani, S. Kang, S. P. Bell, D. M. MacAlpine, *Genes Dev.* **24**, 748 (2010).
29. A. B. Lantermann *et al.*, *Nat. Struct. Mol. Biol.* **17**, 251 (2010).
30. Z. Xu *et al.*, *Nature* **457**, 1033 (2009).
31. M. Zofall *et al.*, *Nature* **461**, 419 (2009).
32. T. Matsuzawa *et al.*, *Appl. Microbiol. Biotechnol.* **87**, 715 (2010).
33. T. Uo, T. Yoshimura, N. Tanaka, K. Takegawa, N. Esaki, *J. Bacteriol.* **183**, 2226 (2001).
34. N. Dutrow *et al.*, *Nat. Genet.* **40**, 977 (2008).
35. M. Yassour *et al.*, *Genome Biol.* **11**, R87 (2010).
36. A. Moldón *et al.*, *Nature* **455**, 997 (2008).
37. N. Averbeck, S. Sunder, N. Sample, J. A. Wise, J. Leatherwood, *Mol. Cell* **18**, 491 (2005).
38. J. L. DeRisi, V. R. Iyer, P. O. Brown, *Science* **278**, 680 (1997).
39. I. Wapinski, A. Pfeffer, N. Friedman, A. Regev, *Nature* **449**, 54 (2007).
40. N. F. Lowndes, C. J. McInerny, A. L. Johnson, P. A. Fantes, L. H. Johnston, *Nature* **355**, 449 (1992).
41. H. Abe, C. Shimoda, *Genetics* **154**, 1497 (2000).
42. J. Piskur, E. Rozpedowska, S. Polakova, A. Merico, C. Compagno, *Trends Genet.* **22**, 183 (2006).
43. M. Kellis, N. Patterson, M. Endrizzi, B. Birren, E. S. Lander, *Nature* **423**, 241 (2003).
44. J. Mata, R. Lyne, G. Burns, J. Bähler, *Nat. Genet.* **32**, 143 (2002).

Acknowledgments: Assemblies and annotations are available at GenBank (*S. octosporus*, ABHY04000000; *S. cryophilus*, ACQJ02000000; *S. japonicus*, AATM02000000), the Broad Institute's *Schizosaccharomyces* Web site (www.broadinstitute.org/annotation/genome/schizosaccharomyces_group), which provides search and visualization tools and pomBase (www.pombase.org). The RNA-Seq and single-nucleotide polymorphism (SNP) data are at the National Center for Biological Information (NCBI), NIH, Sequence Read Archive (see table S42). The *S. japonicus* siRNA data sets are at NCBI GEO as GSE26902 and GSE27837. This work was supported by the National Human Genome Research Institute (NHGRI), NIH. C.N. and M.F.L. were supported by NHGRI; M.Y. was supported by a Clore Fellowship; I.W. is the Howard Hughes Medical Institute (HHMI) fellow of the Damon Runyon Cancer Research Foundation; S.R. was supported by NSF; R.M. was supported by NIH; K.H. was supported by Danish Research Council; C.A.N and C.A.M were supported by the Biotechnology and Biological Science Research Council; P.B. was supported by the Stowers Institute and HHMI; Y.G. and H.L. were supported by the National Institute of Child Health and Human Development, NIH; M.K. was supported by the NIH, an NSF CAREER award, and the Sloan Foundation; A.R. was supported by the Human Frontier Science Program, a Career Award at the Scientific Interface from the Burroughs Wellcome Fund, the Sloan Foundation, an NIH Director's PIONEER award and HHMI. We thank the Broad Institute Sequencing Platform; A. Fujiyama and A. Toyoda for generating DNA sequence; M. Lara and N. Stange-Thomann for developing molecular biology protocols; J. Robinson, M. Garber, and P. Muller for technical advice and support; A. Klar for providing *S. pombe* var. *kambucha* (SPK1820); L. Gaffney for assistance with the figures; K. Mar and J. Mwangi for administrative support; and C. Cuomo for comments on the manuscript.

Supporting Online Material

www.sciencemag.org/cgi/content/full/science.1203357/DC1
Materials and Methods
Figs. S1 to S25
Tables S1 to S42
References

26 January 2011; accepted 7 April 2011
Published online 21 April 2011;
10.1126/science.1203357

Dimensionality Control of Electronic Phase Transitions in Nickel-Oxide Superlattices

A. V. Boris,[1]* Y. Matiks,[1] E. Benckiser,[1] A. Frano,[1] P. Popovich,[1] V. Hinkov,[1] P. Wochner,[2] M. Castro-Colin,[2] E. Detemple,[2] V. K. Malik,[3] C. Bernhard,[3] T. Prokscha,[4] A. Suter,[4] Z. Salman,[4] E. Morenzoni,[4] G. Cristiani,[1] H.-U. Habermeier,[1] B. Keimer[1]*

The competition between collective quantum phases in materials with strongly correlated electrons depends sensitively on the dimensionality of the electron system, which is difficult to control by standard solid-state chemistry. We have fabricated superlattices of the paramagnetic metal lanthanum nickelate ($LaNiO_3$) and the wide-gap insulator lanthanum aluminate ($LaAlO_3$) with atomically precise layer sequences. We used optical ellipsometry and low-energy muon spin rotation to show that superlattices with $LaNiO_3$ as thin as two unit cells undergo a sequence of collective metal-insulator and antiferromagnetic transitions as a function of decreasing temperature, whereas samples with thicker $LaNiO_3$ layers remain metallic and paramagnetic at all temperatures. Metal-oxide superlattices thus allow control of the dimensionality and collective phase behavior of correlated-electron systems.

Since the discovery of high-temperature superconductivity two decades ago, much effort has been undertaken to explore and understand the quantum physics of strongly correlated electrons in transition metal oxides (TMOs) (*1*). The electronic phases can exhibit radically different physical properties, and a new generation of electronic devices will become possible if the competition between these phases can be systematically controlled (*2*). However, the control options offered by conventional solid-state chemistry are limited. The charge carrier concentration in a TMO compound, for instance, can be modified by chemical substitution (*3*), but only at the expense of altering the local lattice structure and electronic energy levels in an uncontrolled manner. The dimensionality of the electron system, D, is another key control parameter, because low-dimensional metals are known to be more susceptible to collective ordering phenomena (including spin- and charge-ordering instabilities, as well as unconventional superconductivity) than their higher-dimensional counterparts. Some level of dimensionality control has been achieved by synthesizing compounds in the Ruddlesden-Popper series of perovskite structures, which comprise N consecutive TMO layers per unit cell. In principle, the dimensionality of the electron system in these materials can thus be tuned from $D = 2$ to 3 by increasing N. In practice, however, the synthesis requirements become rapidly more demanding for large N, and many Ruddlesden-Popper phases have turned out to be unstable.

Recent advances in the synthesis of TMO heterostructures with atomically sharp interfaces indicate an alternative route toward control of correlated-electron systems (*2*). In principle, the carrier concentration in a heterostructure can be tuned by a gate voltage in a field-effect arrangement, without introducing substitutional disorder, and the dimensionality can be modified by means of the deposition sequence of electronically active and inactive TMO layers. In practice, however, attempts to implement this approach have faced many of the same difficulties encountered in the chemical synthesis of bulk materials. For instance, defects created by interdiffusion or strain relaxation can influence the transport properties of the interfacial electron system in an uncontrolled manner. These difficulties are compounded by the paucity of experimental methods capable of probing the collective phase behavior of electrons in TMO heterostructures. Whereas ferromagnetism and ferroelectricity can be detected on the basis of the macroscopic magnetic- or electric-field distribution, the identification of two of the most common collective ordering phenomena of correlated electrons—namely, charge order and antiferromagnetism—in TMO heterostructures and superlattices is much more difficult.

Motivated by the desire to overcome these difficulties and to realize the potential of TMO heterostructures in controlling collective quantum phases, we have carried out a comprehensive experimental study of superlattices based on the correlated metal $LaNiO_3$, in which the dimensionality of the electron system was used as a control parameter, but the influence of epitaxial strain and defects was carefully monitored. An extensive body of earlier work on bulk nickelates provides an excellent background for our study. Whereas bulk $LaNiO_3$ is a three-dimensional (3D) Fermi liquid (*4*) that remains paramagnetic

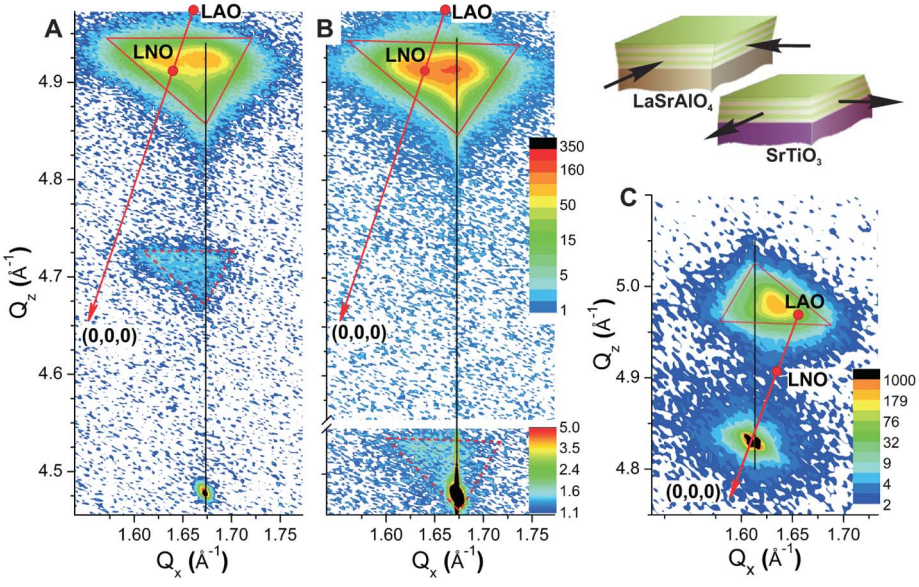

Fig. 1. Reciprocal-space maps of 100-nm-thick $LaNiO_3$ [N unit cells (u.c.)]/$LaAlO_3$ (N u.c.) superlattices grown under compressive strain on $LaSrAlO_4$ (001) with (**A**) $N = 4$, (**B**) $N = 2$, and (**C**) under tensile strain on $SrTiO_3$ (001) with $N = 2$. The black vertical lines indicate the in-plane (Q_x) position of the $LaSrAlO_4$ (109) and $SrTiO_3$ (103) reflections. The strain state of the perovskite epilayers is identified by the intensity distribution in the vicinity of the (103) layer Bragg peak and its superlattice satellite, which are delineated by solid- and dashed-line triangles, respectively. The reciprocal spacings of 103 strain-free pseudocubic $LaNiO_3$ (LNO) and $LaAlO_3$ (LAO) are indicated by the red circles. The red arrows point toward the origin.

[1]Max-Planck-Institut für Festkörperforschung, Heisenbergstrasse 1, D-70569 Stuttgart, Germany. [2]Max-Planck-Institut für Metallforschung, Heisenbergstrasse 3, D-70569 Stuttgart, Germany. [3]Department of Physics, University of Fribourg and Fribourg Center for Nano Materials, CH-1700 Fribourg, Switzerland. [4]Laboratory for Muon Spin Spectroscopy, Paul Scherrer Institute (PSI), CH-5232 Villigen PSI, Switzerland.

*To whom correspondence should be addressed. E-mail: A.Boris@fkf.mpg.de (A.V.B.); B.Keimer@fkf.mpg.de (B.K.)

and metallic at all temperatures, other lanthanide nickelates ($RNiO_3$) with smaller electronic bandwidths exhibit collective metal-insulator transitions with decreasing temperature (*3*). In the insulating low-temperature phase, they exhibit a periodic superstructure of the valence-electron charge and a noncollinear antiferromagnetic ordering pattern of spins on the Ni atoms (*5*–*8*). This implies that the itinerant conduction electrons of $LaNiO_3$ are highly correlated and on the verge of localization. Experiments on a controlled number of atomically thin $LaNiO_3$ layers separated by the electronically inactive wide-gap insulator $LaAlO_3$ are thus well suited for attempts to control the phase behavior of a correlated-electron system via its dimensionality. We have used wide-band spectroscopic ellipsometry to accurately determine the dynamical electrical conductivity and permittivity, which (in contrast to the dc conductivity) are not influenced by misfit dislocations. Low-energy muons, which are stopped in the superlattice (SL) before they reach the substrate, served as a sensitive probe of the internal magnetic field distribution. Two consecutive, sharp phase transitions in the charge and spin sector revealed by this experimental approach demonstrate that the electronic properties of our SLs are determined by electron correlations and not by interfacial disorder. By changing the $LaNiO_3$ layer thickness, we demonstrate full dimensionality control over the collective phase behavior.

The SLs were grown by pulsed-laser deposition (*9*, *10*) and comprised N consecutive layers of $LaNiO_3$ and the $LaAlO_3$. To discriminate between the influence of dimensionality and epitaxial strain, we have grown SLs on both $SrTiO_3$, which induces tensile strain in the overlayer, and $LaSrAlO_4$, which induces compressive strain. Figure 1 shows contour maps of the diffracted x-ray intensity distribution in the vicinity of the 103 perovskite Bragg peak for three representative samples: $N = 4$ and $N = 2$ SLs grown on $LaSrAlO_4$ (001) and an $N = 2$ SL on $SrTiO_3$ (001). Both the position and shape of the overlayer reflection are strongly affected by inversion of the type of substrate-induced strain (Fig. 1, B and C), but they remain essentially unchanged by varying the individual layer thicknesses N (Fig. 1, A and B). A detailed analysis of the substrate-induced strain and relaxation effects is provided in the Supporting Online Material (SOM) (*10*). In the following text, we show that the transport and magnetic properties of the SLs are only weakly influenced by the strain-induced local structural distortions and interfacial defects, but they are qualitatively transformed by varying the number of consecutive unit cells within the $LaNiO_3$ layers.

The charge transport properties of the SLs were determined by spectral ellipsometry, which yields the frequency-dependent complex dielectric function $\varepsilon(\omega) = \varepsilon_1(\omega) + i\varepsilon_2(\omega)$, related to the optical conductivity $\sigma(\omega)$ by $\varepsilon(\omega) = 1 + 4\pi i\sigma(\omega)/\omega$. This method is very sensitive to thin-film properties because of the oblique incidence of light, and it is insensitive to the influence of strain-induced extended defects on the current flow through the atomically thin layers (*10*, *11*). Figure 2, A and B, shows the infrared spectra of $\varepsilon_2(\omega)$ for $N = 4$ and 2 SLs grown on $LaSrAlO_4$ and $SrTiO_3$, respectively, which are representative of the in-plane dielectric response of the metallic $LaNiO_3$ layers. The insets show the corresponding temperature dependencies of ε_2 at a fixed photon energy $\hbar\omega = 30$ meV ($\hbar$, Planck's constant h divided by 2π). The gradual evolution of ε_2 with temperature over the far-infrared range confirms that the $N = 4$ SLs remain metallic at all temperatures. The $N = 2$ SLs, on the other hand, show clear evidence of a metal-insulator (MI) transition upon cooling, with a sharp onset at the transition temperatures $T_{MI} = 150$ and 100 K for SLs grown on $LaSrAlO_4$ and $SrTiO_3$, respectively. For $T \gtrsim T_{MI}$, the infrared $\varepsilon(\omega)$ spectrum of $N = 2$ SL is well described by a broad Drude response $\varepsilon(\omega) = \varepsilon_\infty - \omega_{pl}^2/(\omega^2 + i\omega\gamma)$ with a ratio of scattering rate and plasma frequency $\gamma/\omega_{pl} \approx 0.2$ (lower shaded line in Fig. 2A) that is typical for bulk complex oxides. The effective mass enhancement m^*/m is estimated from the plasma frequency as $m^*/m = \frac{4\pi n_{Ni}}{m\omega_{pl}^2}$, where $n_{Ni} = \frac{1}{2} \times 1.7 \times 10^{22}$ cm^{-3}, by assuming one electron per Ni atom. With $\omega_{pl} \approx 1.1$ eV [Fig. 2A and fig. S7

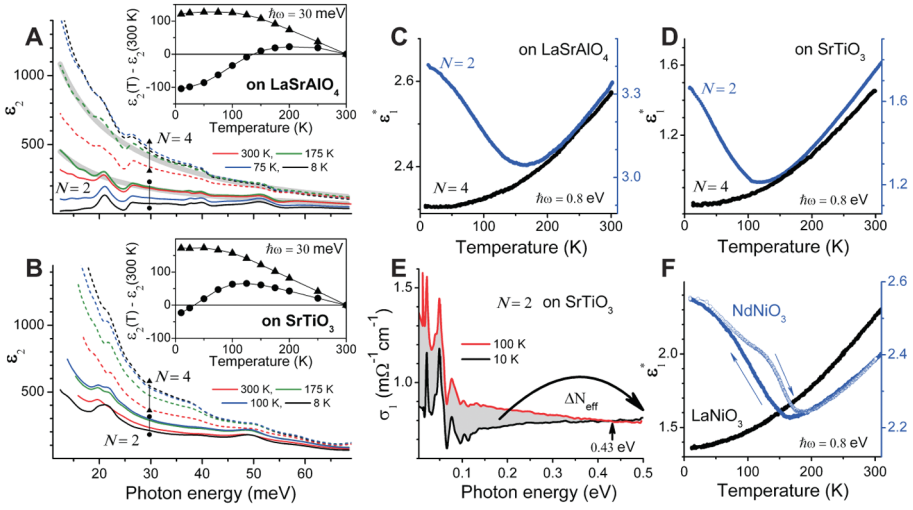

Fig. 2. (**A** and **B**) $\varepsilon_2(\omega)$ spectra of the $N = 2$ (solid lines, circles) and $N = 4$ (dashed lines, triangles) SLs on (A) $LaSrAlO_4$ and (B) $SrTiO_3$ substrates measured at representative temperatures. The shaded lines in (A) represent the Drude model fit to $\varepsilon_2(\omega)$ at 175 K for the $N = 2$ ($N = 4$) SL with $\omega_{pl} = 1.05$ eV (1.10 eV) and $\gamma = 200$ meV (90 meV). The insets provide the corresponding temperature dependencies of ε_2 at a photon energy of $\hbar\omega = 30$ meV for the $N = 2$ (circles) and $N = 4$ (triangles) SLs. (**C** and **D**) Temperature dependence of the as-measured pseudodielectric permittivity ε_1^* at $\hbar\omega = 0.8$ eV in the $N = 2$ (blue) and $N = 4$ (black) SLs on (C) $LaSrAlO_4$ and (D) $SrTiO_3$. (**E**) The difference between the optical conductivity spectra $\sigma_1(100\text{ K}, \omega)$ and $\sigma_1(10\text{ K}, \omega)$ (shaded area) quantifies the reduction of the effective charge density, $\Delta SW \approx 0.03$ per Ni atom, within the gap energy range below 0.43 eV at the charge ordering transition in the $N = 2$ superlattice on $SrTiO_3$. (**F**) Temperature dependence of ε_1^* at 0.8 eV of reference 100-nm films of $LaNiO_3$ (black) and $NdNiO_3$ (blue).

Fig. 3. Time evolution of the zero-field muon spin polarization at various temperatures for the (**A**) $N = 2$ and (**B**) $N = 4$ superlattice on $LaSrAlO_4$. (**C** and **D**) Muon spin relaxation spectra in a weak transverse magnetic field of 100 G in the superlattices as in (A) and (B), respectively. (A) to (D) use the color coding in the legend shown in (B).

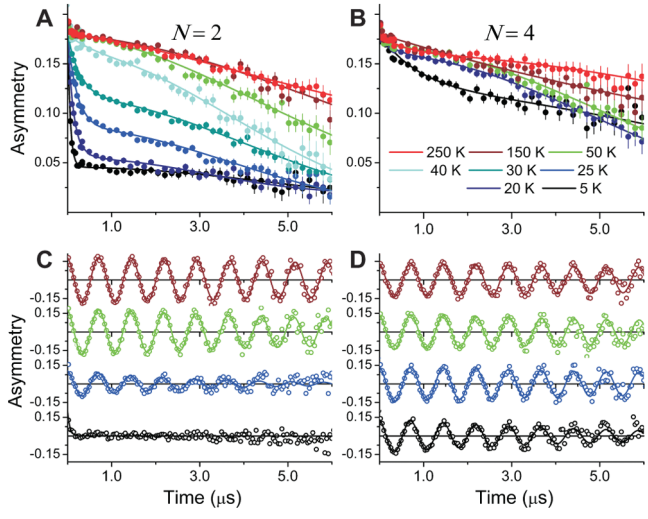

in the SOM (*10*)], we obtain $m^*/m \approx 10$, which is in good agreement with the value for bulk $LaNiO_3$ obtained from specific heat measurements (*12*). Using the Fermi energy $E_F = 0.5$ eV derived from the thermopower of $LaNiO_3$ (*12*) and γ from the Drude model fit to the infrared spectra, we estimate the mean free path as $l = \frac{1}{2\pi c\gamma}\sqrt{2E_F/m*}$ (c, speed of light). For the $N = 2$ and $N = 4$ SLs on both substrates, we obtain $l = 5$ to 6 Å and 10 to 12 Å, respectively (*10*). Remarkably, the mean free path correlates with the individual $LaNiO_3$ layer thickness, testifying to the high quality of the interfaces.

The charge-carrier localization at lower temperature can be readily identified through a rapid drop in $\varepsilon_2(T)$ and progressive deviation of $\varepsilon_2(\omega)$ from the Drude function due to the formation of a charge gap. The temperature evolution of the real part of the dielectric function provides complementary information about the optical spectral-weight redistribution at T_{MI}. Figure 2, C and D, show the temperature dependence of the as-measured permittivity, ε_1^*, at an energy above the gap ($\hbar\omega$ = 0.8 eV). In the metallic phase, ε_1^* decreases with decreasing temperature, following the temperature dependence of the scattering rate $\gamma(T)$. This is characteristic of a narrowing of the Drude peak where the spectral weight is removed from the high-energy tail and transferred to the far-infrared range near the origin. The charge-gap formation below T_{MI} in $N = 2$ SLs leads to the reverse spectral-weight transfer from the inner-gap region to excitations across the gap and, as a consequence, to an increase in ε_1^*.

The consistent temperature evolution of ε_1 and ε_2 over a broad range of photon energies demonstrates the intrinsic nature of the charge-localization transition observed in SLs with $N = 2$ and provides clues to its origin. The spectral-weight reduction within the gap can be quantified in terms of the effective number of charge carriers per Ni atom and extracted from a sum-rule analysis as $\Delta SW = \frac{2m}{\pi e^2 n_{Ni}}\int_0^{\Omega_G}[\sigma_1(T \approx T_{MI},\omega) - \sigma_1(T << T_{MI},\omega)]d\omega$, where m is the free-electron mass, e is the charge on the electron, and n_{Ni} is the density of Ni atoms. The upper integration limit, $\Omega_G \approx 0.43$ eV, is a measure of the charge gap and can be identified with the equal-absorption (or isosbestic) point, where $\sigma_1(\omega)$ curves at different temperatures intersect (Fig. 2E). The charge-gap formation on this energy scale can be attributed to a charge-ordering instability, as in the case of bulk lanthanide nickelates ($RNiO_3$) with smaller R-ion radius (*5*–*8*). The spectral weight $\Delta SW \approx 0.03$ below $\Omega_G \approx 0.43$ eV determined for the $N = 2$ SLs (Fig. 2E) is of the same order as, albeit somewhat lower than, the corresponding quantity $\Delta SW = 0.058$ below $\Omega_G \approx 0.3$ eV reported at the metal-insulator transition in bulk $NdNiO_3$, which is known to be due to charge order (*13*). To highlight the analogy to the behavior in bulk nickelates, Fig. 2F shows reference measurements on single 100-nm-thick films of $NdNiO_3$ and $LaNiO_3$, measured under the same conditions as in Figs. 2, C and D. Because ε_1^* at 0.8 eV for the single $NdNiO_3$ film displays closely similar temperature dependence as found for $N = 2$ SLs, we conclude that the gap formation in the latter case also reflects charge ordering. In $NdNiO_3$, the metal-insulator transition occurs as a first-order transition with a concomitant noncollinear antiferromagnetic ordering at the Néel temperature $T_N = T_{MI}$ (*6*–*8*). The thermal hysteresis in the $\varepsilon_1^*(T)$ curve in Fig. 2F is consistent with the first-order character of the transition, with uniform and charge-ordered phases coexisting over a broad temperature range. In contrast, there is no discernible hysteresis observed in $\varepsilon_1^*(T)$ of $N = 2$ SLs (Fig. 2, C and D), which suggests a second-order transition. Continuing the analogy with the bulk nickelate series, one would then expect another second-order transition due to the onset of antiferromagnetic ordering at $T_N < T_{MI}$ in the $N = 2$ SLs, as in $RNiO_3$ with small R (Lu through Sm).

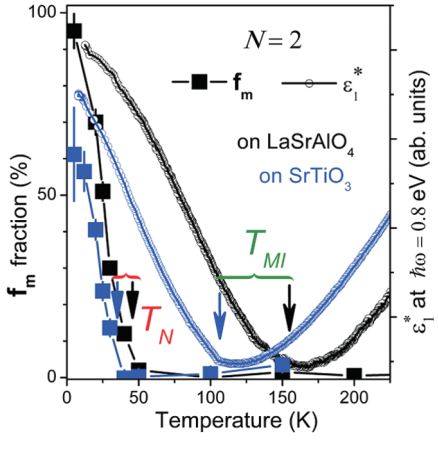

Fig. 4. Temperature dependencies of the fraction of muons experiencing static local magnetic fields, f_m, and the normalized permittivity ε_1^* at 0.8 eV (in arbitrary units) in the $N = 2$ superlattices. The black and blue arrows mark the magnetic (T_N) and metal-insulator (T_{MI}) transition temperatures for the superlattices on $LaSrAlO_4$ and $SrTiO_3$, respectively.

To test this hypothesis, we carried out low-energy muon spin rotation (μSR) measurements using the μE4 beamline at the Paul Scherrer Institute (*10*, *14*), where positive muons with extremely reduced velocity can be implanted into specimens and brought to rest between the substrate and the $LaAlO_3$ capping layer. Because the muons decay into positrons preferentially along the spin direction, they act as highly sensitive local magnetic probes. Figure 3A shows muon decay asymmetry data from a SL with $N = 2$ at selected temperatures with no external field. At $T > 50$ K, the asymmetry is described by a Gaussian with relatively slow relaxation, σ, given by $A(0) \times \exp(-\sigma^2 t^2/2)$, where t is time (solid lines in Fig. 3A), typical of dipolar magnetic fields generated by nuclear moments of La and Al. As the temperature decreases, there is a gradual increase in σ from 0.17 μs^{-1} at 250 K to 0.27 μs^{-1} at 20 K. Below 50 K the asymmetry drops sharply, and the μSR spectra can be fitted well by introducing an additional exponential relaxation $\exp(-\Lambda t)$. The fast depolarization rate Λ reaches a value of ≈17 μs^{-1} at 5 K, implying a resulting Lorentzian distribution of local fields with half width at half maximum $\Delta B = 0.75\Lambda/\gamma_\mu \approx 150$ G, where $\gamma_\mu = 2\pi \times 13.55$ MHz/kG is the muon's gyromagnetic ratio (*10*). The fast increase in Λ with decreasing temperature below 50 K is similar to the behavior in bulk $NdNiO_3$ (*15*) and $(Y,Lu)NiO_3$ (*16*) below T_N, caused by static internal fields from ordered Ni magnetic moments. The wide field distribution ΔB and the absence of a unique muon precession frequency reflects the SL structure with several inequivalent muon stopping sites in the alternating magnetic ($LaNiO_3$) and nonmagnetic ($LaAlO_3$) layers, probably compounded by a complex noncollinear spin structure as in the bulk nickelates (*15*, *16*).

We used 100-G transverse field (TF) measurements to determine the fraction of muons, f_m, experiencing static local magnetic fields $B_{loc} > B_{TF}$ (i.e., showing no detectable precession with $\omega = \gamma_\mu B_{TF}$) (*10*). Figure 3C indicates that the $N = 2$ SL shows a transition from an entirely paramagnetic muon environment ($f_m = 0$) to a nearly full volume of static internal fields, with a sharp onset at $T_N \sim 50$ K. The magnetic state at 5 K is robust against externally applied transverse fields up to 3 kG (not shown in Fig. 3), which is the limit of time resolution of our setup. The continuous temperature dependence of f_m (Fig. 4) and the absence of thermal hysteresis indicate that the magnetic transition for the $N = 2$ SLs is second-order. At the same time, Fig. 3, B and D, show that SLs with thicker $LaNiO_3$ layers remain paramagnetic down to the lowest temperatures, as in bulk $LaNiO_3$. An additional slow exponential relaxation with $\Lambda = 0.9$ μs^{-1} is seen only at $T = 5$ K (black symbols and curve in Fig. 3B). This results in a small increase in relaxation rate, but no loss in asymmetry of the TF μSR signal (Fig. 3D). The effect is probably due to weak dynamical spin correlations that are quenched already in a field of 100 G, in clear contrast to the long-range static magnetic order observed in the $N = 2$ samples.

As a local probe, μSR does not allow definite conclusions about the magnetic ordering pattern in the $N = 2$ SLs. However, we can rule out ferromagnetism on the basis of an estimate of the ordered moment, μ_{Ni}, on the Ni sites from the distribution of local fields experienced by the muons. The highest local field at the shortest μ-Ni distance, $c/4$ (where c is the lattice parameter of the orthorhombic unit cell) ≈ 1.92 Å (*15*), is 4 to 5 times ΔB, which corresponds to $\mu_{Ni} \gtrsim 0.5\mu_B$. If these moments were co-aligned in the ordered state, the corresponding total moment $M = \mu_{Ni} n_{Ni} V_{SL} \gtrsim 7.7 \times 10^{-4}$ emu (where V_{SL} is the volume of the superlattice) would have been readily detected in magnetization measurements. The absence of such an effect is confirmed in magnetometric measurements with sensitivity $\sim 10^{-7}$ emu.

Figure 4 summarizes the phase behavior of the SLs with $N = 2$, which undergo a sequence of two sharp, collective electronic phase transitions upon cooling. We have provided strong evidence that the two transitions correspond to the onset of charge and spin order. By showing that the $N = 4$ counterparts remain uniformly metallic and paramagnetic at all temperatures, we have demonstrated full dimensionality control of these collective instabilities. The higher propensity toward charge and spin order in the 2D systems probably reflects enhanced nesting of the $LaNiO_3$ Fermi surface. The phase behavior is qualitatively similar to the one observed in bulk $RNiO_3$ with small radius of the R anions, which results from bandwidth narrowing due to rotation of NiO_6 octahedra, but the transition temperatures and the order parameters are substantially lower, probably because of the reduced dimensionality. Because the transitions occur in the $N = 2$ SLs, regardless of whether the substrate-induced strain is compressive (Fig. 1B) or tensile (Fig. 1C), structural parameters such as rotation and elongation of the NiO_6 octahedra can be ruled out as primary driving forces. We note, however, that the infrared conductivity is higher (Fig. 2, A and B) and the transition temperatures are lower (Fig. 4) in the $N = 2$ SL grown under tensile strain. The more metallic response of these SLs, compared with those grown under compressive strain, may reflect a widening of the Ni 3*d*-electron bandwidth and/or an enhanced occupation of the Ni $d_{x^2-y^2}$ orbital polarized parallel to the $LaNiO_3$ layers. A small orbital polarization was indeed detected by soft x-ray reflectometry in our superlattices (*17*). This indicates further opportunities for orbital control of the collective phase behavior of the nickelates, which may enable experimental tests of theories predicting high-temperature superconductivity (*18*, *19*) or multiferroicity (*20*) in these systems.

References and Notes

1. E. Dagotto, *Science* **309**, 257 (2005).
2. J. Mannhart, D. G. Schlom, *Science* **327**, 1607 (2010).
3. M. Imada, A. Fujimori, Y. Tokura, *Rev. Mod. Phys.* **70**, 1039 (1998).
4. R. Eguchi *et al.*, *Phys. Rev. B* **79**, 115122 (2009).
5. I. I. Mazin *et al.*, *Phys. Rev. Lett.* **98**, 176406 (2007).
6. J. L. García-Muñoz, M. A. G. Aranda, J. A. Alonso, M. J. Martínez-Lope, *Phys. Rev. B* **79**, 134432 (2009).
7. V. Scagnoli *et al.*, *Phys. Rev. B* **73**, 100409(R) (2006).
8. V. Scagnoli *et al.*, *Phys. Rev. B* **77**, 115138 (2008).
9. H.-U. Habermeier, *Mater. Today* **10**, 34 (2007).
10. Materials and methods are available as supporting materials on *Science* Online.
11. J. W. Freeland *et al.*, *Phys. Rev. B* **81**, 094414 (2010).
12. X. Q. Xu, J. L. Peng, Z. Y. Li, H. L. Ju, R. L. Greene, *Phys. Rev. B* **48**, 1112 (1993).
13. T. Katsufuji, Y. Okimoto, T. Arima, Y. Tokura, J. B. Torrance, *Phys. Rev. B* **51**, 4830 (1995).
14. T. Proksch *et al.*, *Nucl. Instrum. Methods Phys. Res. A* **595**, 317 (2008).
15. J. L. García-Muñoz, P. Lacorre, R. Cywinski, *Phys. Rev. B* **51**, 15197 (1995).
16. J. L. García-Muñoz *et al.*, *Physica B* **374–375**, 87 (2006).
17. E. Benckiser *et al.*, *Nat. Mater.* **10**, 189 (2011).
18. J. Chaloupka, G. Khaliullin, *Phys. Rev. Lett.* **100**, 016404 (2008).
19. P. Hansmann *et al.*, *Phys. Rev. Lett.* **103**, 016401 (2009).
20. G. Giovannetti, S. Kumar, D. Khomskii, S. Picozzi, J. van den Brink, *Phys. Rev. Lett.* **103**, 156401 (2009).

Acknowledgments: We thank Y.-L. Mathis and R. Weigel for support at the infrared IR1 and Max-Planck-Institut für Metallforschung x-ray beamlines of the synchrotron facility Angström Quelle Karlsruhe (ANKA) at the Karlsruhe Institute of Technology. We thank G. Khaliullin and O. K. Andersen for discussions, W. Sigle and P. A. van Aken for support and discussions of transmission EM results, A. Szökefalvi-Nagy for x-ray software support, and G. Logvenov for support in sample growth and characterization. This work was supported by the Deutsche Forschungsgemeinschaft, grant TRR80, project C1. V.K.M. and C.B. were supported by the Schweizerische Nationalfonds via grants 200020-129484 and NCCR-MaNEP.

Supporting Online Material

www.sciencemag.org/cgi/content/full/332/6032/937/DC1
Materials and Methods
Figs. S1 to S10
Table S1
References

10 January 2011; accepted 21 March 2011
10.1126/science.1202647

Competition of Superconducting Phenomena and Kondo Screening at the Nanoscale

K. J. Franke,* G. Schulze, J. I. Pascual

Magnetic and superconducting interactions couple electrons together to form complex states of matter. We show that, at the atomic scale, both types of interactions can coexist and compete to influence the ground state of a localized magnetic moment. Local spectroscopy at 4.5 kelvin shows that the spin-1 system formed by manganese-phthalocyanine (MnPc) adsorbed on Pb(111) can lie in two different magnetic ground states. These are determined by the balance between Kondo screening and superconducting pair-breaking interactions. Both ground states alternate at nanometer length scales to form a Moiré-like superstructure. The quantum phase transition connecting the two (singlet and doublet) ground states is thus tuned by small changes in the molecule-lead interaction.

When a magnetic atom or molecule is adsorbed on the surface of a superconductor, its magnetic moment can interact with itinerant electrons (with spin s = 1/2) and with Cooper pairs (s = 0). Normal-state electrons tend to screen the local magnetic moment and form a many-particle ground state with a total spin S = 0. A fingerprint of this so-called Kondo effect (*1*) is a resonance at the Fermi level, whose width reflects the energy scale of the magnetic coupling. The magnetic impurity can also weaken the local coherence of the superconducting state by the creation of spin-polarized bound states in its proximity (*2–4*). They appear as narrow resonances inside the superconducting energy gap (*5–10*). The energy position of these intragap states reflects the pair-breaking exchange interaction strength of the magnetic impurity with Coopers pairs (*9*, *10*).

These interactions compete to produce two different magnetic ground states depending on their relative strength. A Kondo singlet is formed if the screening energy scale is larger than the pairing energy of the Cooper quasiparticles, that is, $k_B \cdot T_K >> \Delta$, where k_B (the Boltzmann constant), T_K (the Kondo temperature) determines the energy scale of the screening, and the order parameter Δ governs the superconductor pairing interaction. When $k_B \cdot T_K << \Delta$, the opening of the superconducting energy gap reduces the density of normal electrons available for screening, and the Kondo effect is incomplete (*11*). The poorly screened magnetic impurity creates bound quasiparticle states that locally reduce the pairing strength of the superconducting quasiparticles and drive the system into a magnetic ground state (S > 0) (*12*).

In the limit of $k_B \cdot T_K \sim \Delta$, both Kondo screening and superconducting pairing are predicted to coexist (*12–14*). Changes in their relative strength can drive the system through a quantum phase transition separating the two different magnetic ground states. Here we experimentally elucidate this competition between pair-breaking and Kondo screening on individual magnetic manganese-phthalocyanine (MnPc) molecules deposited on top of a superconducting Pb(111) substrate. Using scanning tunneling microscopy (STM) and spectroscopy (STS) at 4.5 K, we resolved a complex Kondo fingerprint coexisting with localized bound states within the superconducting gap. On the Pb(111) surface, the MnPc molecule lies in a spin-1 state and is screened by two separate Kondo channels with different strength. The weaker channel competes with the creation of spin-polarized bound states. This competition leads to two different magnetic

Institut für Experimentalphysik, Freie Universität Berlin, Arnimallee 14, 14195 Berlin, Germany.

*To whom correspondence should be addressed. E-mail: franke@physik.fu-berlin.de

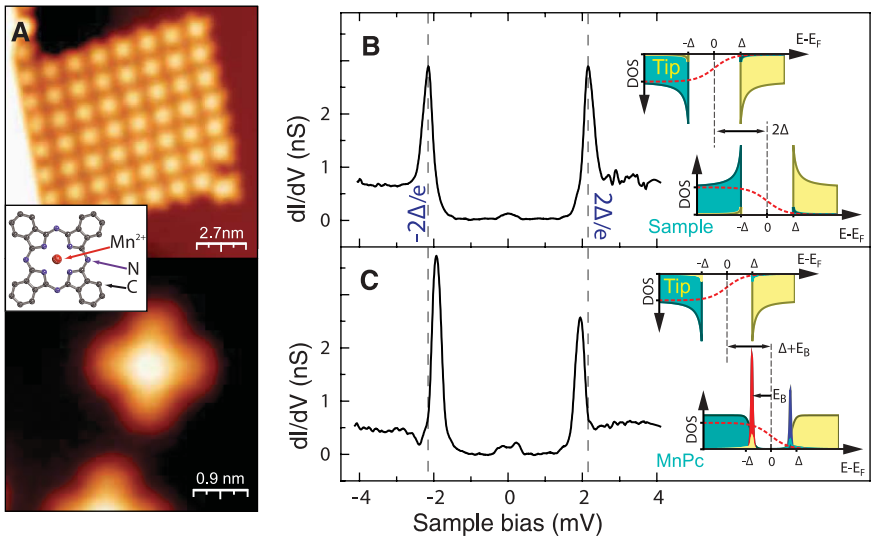

Fig. 1. (**A**) STM image of a densely packed MnPc island and a single molecule (V_s = 200 mV, I = 8.6 pA). (Inset) Molecular structure (*32*). Experimental details are described in SOM 1 (*15*). (**B**) Differential conductance spectrum of the SIS tunneling junction formed by the clean Pb(111) surface and a lead-coated STM tip. Tunneling between quasiparticle peaks of the Bardeen-Cooper-Schrieffer (BCS)–like density of states (DOS) leads to a doubling of the superconducting gap [see SOM 2 (*15*)]. (**C**) The corresponding spectrum on an isolated molecule shows intragap states, which can be related to its magnetic state [corresponding STM image in (A), lower panel].

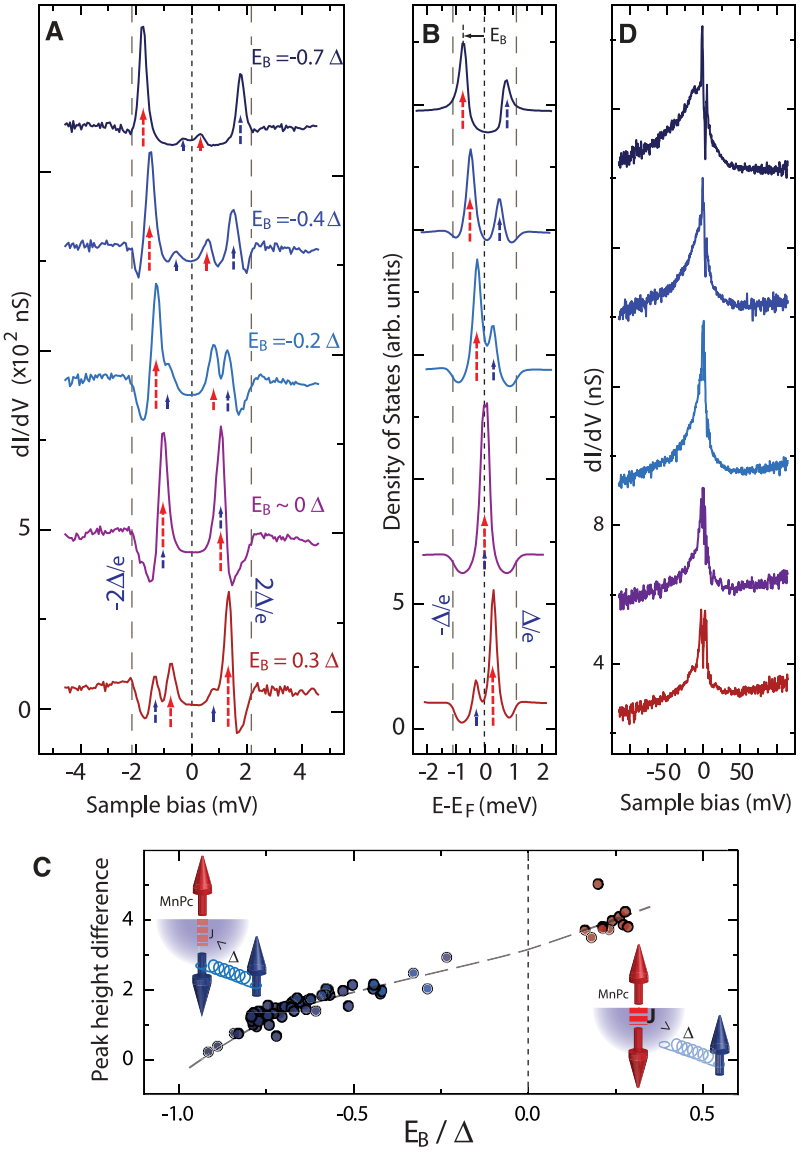

Fig. 2. (**A**) *dI*/*dV* spectra around the superconducting gap on five characteristic MnPc molecules (feedback opened at V_s = 8.6 mV, I = 0.45 nA; the spectra are shifted for clarity). All of the spectra show that the quasiparticle peaks at $E = \pm 2\Delta$ and the thermal excitation peaks at $E = 0$ are substituted by four peaks inside the superconducting gap: the particle and hole impurity-induced bound states probed by the superconducting tip. The superconducting gap edge, observed in this SIS junction at $\pm 2\Delta$, is indicated with a dashed line. (**B**) Corresponding Mn/Pb(111) DOS obtained by numerical deconvolution of the superconducting tip DOS [SOM 3 (*15*)]. (**C**) The position of the larger bound state E_B is correlated with a monotonous increase in the peak asymmetry, reflecting a continuous gain in its spin polarization at the impurity (the dashed line is added as a guide). Points are omitted near $E_B = 0$ because there both particle- and hole-like states overlap [as shown in (A) and (B)]. The schemes represent the two ground states, a bound Cooper pair ($E_B < 0$) and a bound broken pair ($E_B > 0$). (**D**) Conductance spectra in a larger sample bias window for the same set of molecules as in (A). A broad zero-bias conductance anomaly is revealed, whose specific line shape appears correlated with the alignment of intragap bound states (V_s = 130 mV, I = 0.47 nA).

ground states. In MnPc islands, we observed a transition between the two ground states along a quasi-periodic Moiré pattern, revealing that their different quantum state is tuned by small variations of their interaction with the superconducting substrate. The result is a molecular superstructure wherein superconductivity and magnetism alternate at nanoscopic length scales.

The Pb substrate is a type I superconductor with a critical temperature T_c of 7.2 K. At 4.5 K, the electron density of states is depleted within an energy gap of width $2\Delta = 2.2$ meV around the

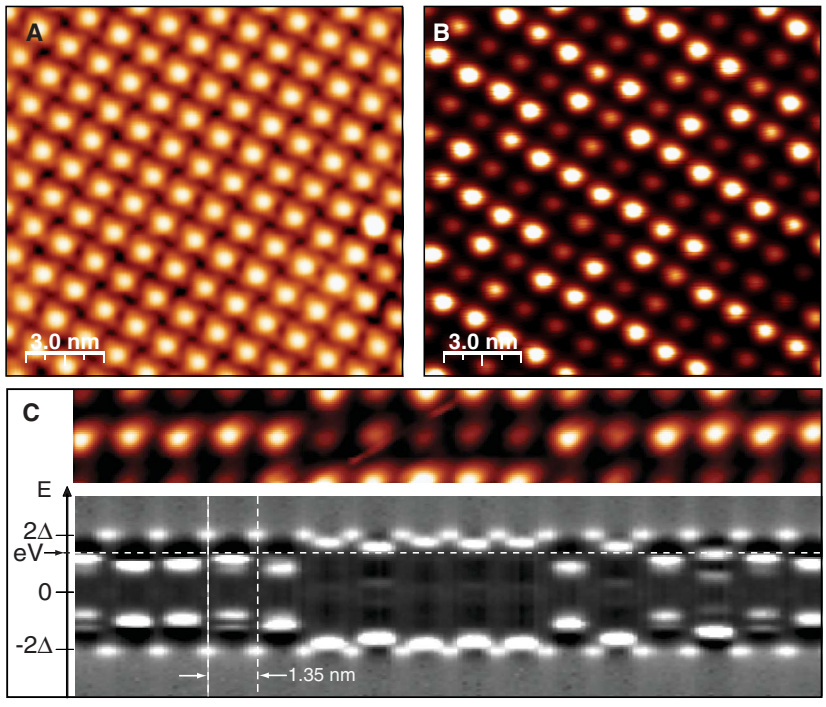

Fig. 3. (**A**) Constant-current STM image of a MnPc island ($V_s = 11$ mV, $I = 27$ pA). (**B**) Corresponding constant-height STM image at $V_s = 1.6$ mV (feedback opened at $V_s = 11$ mV, $I = 27$ pA). A Moiré pattern emerges, revealing that the molecules in the compact islands lie in different adsorption sites with respect to the Pb(111) atomic lattice. (**C**) Current image at constant height of a molecular row of the Moiré pattern and, below, false-color scale *dI/dV* spectra taken along a line crossing through the centers of these molecules. The horizontal dashed line corresponds to the bias value of current images in (B) and (C). Vertical lines point to sites between molecules, where spectra of a bare SIS junction are recovered.

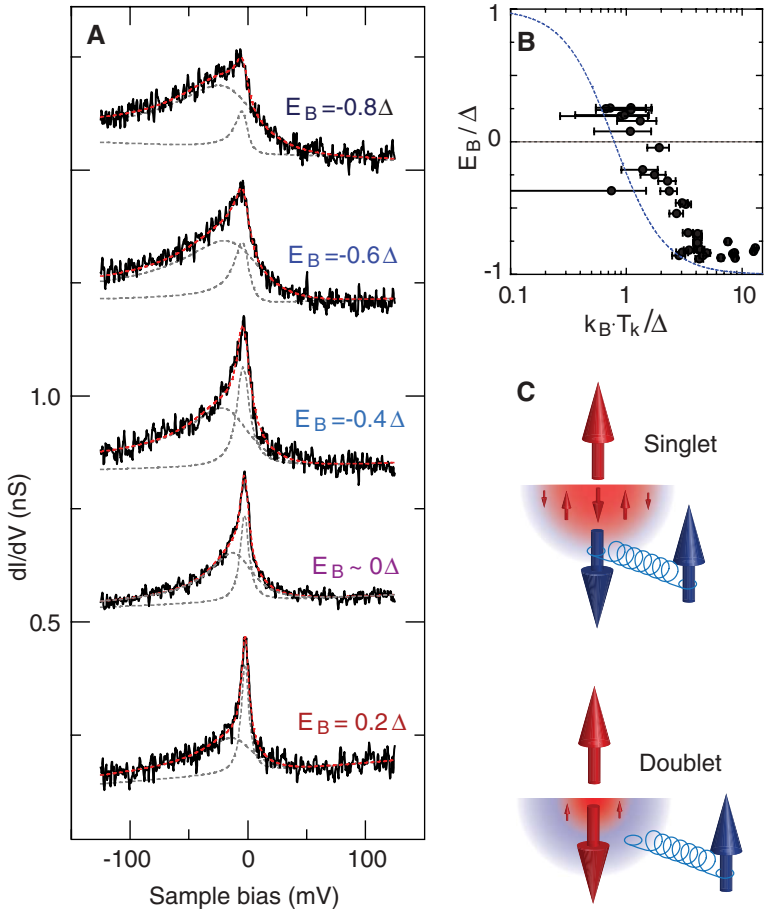

Fig. 4. (**A**) Zero-bias conductance anomalies at 8.8 K (above the T_c of lead) and the resulting fit (dashed red line) using two Fano curves with very different line width (gray dashed lines), representing two screening channels. On the bare Pb(111), flat spectra of a normal metal are obtained (feedback opened at $V_s = 150$ mV, $I = 27$ pA; the spectra are shifted for clarity). (**B**) Relation between the energy scale of the narrower screening channel $k_B \cdot T_K$, obtained at 8.8 K as in (A) (experimental broadening corrected), and the position of the large intragap state E_B, obtained for the same set of MnPc molecules at 4.5 K. The dashed blue line is based on the theory of Matsuura (*13*), modified to simulate the phase transition around $k_B \cdot T_K \sim \Delta$ (*22*, *31*). The weaker the Kondo channel, the larger is the magnetic coupling with superconducting quasiparticles (larger E_B) and the larger is the spin polarization of the total system. (**C**) Simple scheme of the two ground states: a total singlet for $E_B < 0$, formed by a Kondo singlet and a weakly bound Cooper pair; a total doublet for $E_B > 0$, where Kondo screening is incomplete and a broken pair ($s = 1/2$) is bound to the magnetic impurity ($s = 0$).

Fermi energy (E_F). To explore the sub–millielectron volt energy scale in our STS measurements, we used a Pb-coated superconducting tip [see SOM 1 (*15*)]. In this way, the energy resolution is far beyond the limit imposed by the thermal broadening of the Fermi edge of a normal tip [see SOM 2 (*15*)]. The superconductor-insulator-superconductor (SIS) tunnel configuration is revealed in the differential conductance (dI/dV) spectra by two sharp peaks at $\pm 2\Delta = \pm 2.2$ meV, twice the superconducting gap (Fig. 1B), representing the tunneling between the quasiparticle peaks.

MnPc molecules self-assemble in densely packed islands with a square lattice (Fig. 1A). Each molecule is imaged as a fourfold clover-shaped structure with a central protrusion representing the Mn ion. As a reference, we first probe the spectroscopic fingerprint around the E_F of isolated MnPc molecules that were dragged out of the islands with the STM tip. These molecules, all resting on their preferred adsorption site, exhibit similar dI/dV spectra (Fig. 1C) in which the quasiparticle peaks at $\pm 2\Delta$ are substituted by pronounced peaks of asymmetric height within the superconducting gap [at $\pm(E_B + \Delta)$, with $E_B < \Delta$]. The asymmetry between the electron ($V < 0$) and hole-like ($V > 0$) states is an expression of the breaking of time-reversal symmetry by the magnetic interaction between MnPc and Cooper pairs (*2*–*5*, *12*). The close proximity of these new quasiparticle peaks to the superconducting gap edges reflects the rather weak magnetic interaction for these isolated species (*9*, *10*).

The spectra of molecules in the densely packed islands also show molecule-induced bound states, but with a large variety of positions within the energy gap and height asymmetries, depending on the molecule. Figure 2A shows five representative spectra taken on different MnPc molecules. To remove the influence of the superconducting density of states of the tip, we numerically deconvolute its quasiparticle density of states from the dI/dV spectrum [SOM 3 (*15*)]. The resulting plots (Fig. 2B) represent the quasiparticle excitation spectra of the molecule-substrate system with electron and hole-like states at $\pm E_B$ and within the superconducting gap. A shift of the larger (smaller) bound state away from the negative (positive) superconducting gap edge indicates a smaller pairing energy of the Cooper pairs. The decrease in pairing energy is accompanied by an increase in the asymmetry between the peaks of large and small spectral weight as the poles move toward the Fermi level (Fig. 2C) (*9*, *10*, *12*). The crossing of the bound states through the Fermi level ($E_B = 0$) corresponds to the special case when the electron and hole states are degenerate and a quantum phase transition to a different ground state occurs. When the magnetic interaction becomes larger than the pairing energy, the bound Cooper pair is broken (*12*), resulting in a so-called (s = 1/2) Bogoliubov quasiparticle (*5*). This new superconducting ground state is thus characterized by intragap states with larger weight in the hole-like peak (as shown in the lower spectra in Fig. 2, A and B), representing excitations of the (bound) broken pair.

The origin of the different interaction strengths between MnPc molecules and superconducting quasiparticles was determined from an analysis of constant-height current maps of the islands measured at a sample bias $V_s = 1.6$ meV, which is within the superconducting gap (Fig. 3B). In the map, the molecules appear with different brightness, forming a Moiré-like superstructure. A correlation between Moiré pattern and bound states is shown in a series of dI/dV spectra taken along a high-symmetry direction of the superstructure (Fig. 3C). The gray-scale–coded conductance reveals that the bound-state resonances of dark molecules in Fig. 3B lie above the applied bias energy eV_s (similar to the top spectrum in Fig. 2A). Hence, they correspond to MnPc molecules weakly interacting with Cooper pairs. Brighter molecules have bound states below eV_s contributing to the tunneling current and, thus, reveal a larger magnetic interaction with the quasiparticles. Between the molecules, the density of states of the bare SIS junction could be recovered, indicating a very narrow localization of the magnetic bound states (*12*). The Moiré pattern is a geometrical effect, resulting from the quadratic molecular lattice on top of the hexagonal atomic Pb(111) structure [see SOM 4 (*15*)]. Thus, each MnPc molecule is found in a slightly different bonding configuration with the substrate. The direct correlation of the energy alignment of the bound states with the Moiré structure evidences that the magnetic state is strongly influenced by the adsorption site.

We found an additional magnetic fingerprint of the MnPc-lead interaction by exploring dI/dV spectra in a larger energy scale, well outside the superconducting gap. All of the molecules show a pronounced background peak, which has been assigned to tunneling through a Kondo resonance (Fig. 2C) (*16*–*19*). The large energy scale of such zero-bias conductance anomalies revealed that screening of the magnetic molecule by the itinerant electrons of the substrate is very efficient, with T_K roughly between 200 and 400 K, depending on the molecule (*18*, *19*). For such high T_K ($k_B \cdot T_K >> \Delta$), the screening of a spin 1/2 impurity would be complete before the opening of the superconducting energy gap at $T_c = 7.2$ K. This result is in apparent contradiction with the observation of the intragap bound states shown in Fig. 2A. A more complex interpretation of the zero-bias anomaly is needed than one based on a simple spin 1/2 MnPc molecule.

A closer look into the line shape of the background peak reveals that it cannot be simply reproduced by a single Fano function (*18*), as it is characteristic of the Kondo effect. To rule out a distortion of the peak shape by the superconductor bound states, we increased the temperature of the STM to 8.8 K, above the T_c for superconductivity in lead. The spectra maintain their shape, roughly described by a zero-bias sharp peak on top of a wider Fano-like anomaly (Fig. 4A). The best fit to reproduce the resulting plots requires the use of two resonances with very different line widths, representing two different Kondo screening channels, characteristic of a spin-1 system (*20*). The large difference in the energy scales (~1 to 5 meV and ~15 to 45 meV; the exact values depend on the particular molecule in Fig. 2A) of both Kondo processes justifies treating the system as two independent screening channels (*21*).

The energy scale of the narrower Kondo resonance lies in the same range as the superconducting energy gap ($\Delta = 1.1$ meV), thus leading to competing effects in the quasiparticle pairing for temperatures below T_c. Upon opening of the superconducting energy gap, the spin channel becomes underscreened because the density of the itinerant electrons participating in the Kondo screening is depleted. The Kondo screening then competes with magnetically induced bound states like those shown in Fig. 2A. This picture is corroborated in Fig. 4B, where we plot the energy value of the subgap states in the superconducting phase as a function of $k_B \cdot T_K/\Delta$ (i.e., the energy scale of this screening channel). The weaker the Kondo channel, the more strongly bound are the intragap states, qualitatively resembling early theoretical predictions by Matsuura (*13*). According to our results, the crossing of the intragap states through the Fermi level takes place for $k_B \cdot T_K/\Delta \sim 1$ (*22*). At this point, the bounded superconducting quasiparticle goes through a quantum phase transition from a singlet to a doublet ground state (the broken pair). The correlation between T_K and E_B in Fig. 4B further reveals that the screening channel also follows the Moiré pattern shown in Fig. 3. We can then infer that seemingly small changes in adsorption site have an immense impact in the magnetic moment of the underscreened spin (*19*) and, consequently, on the energies of the intragap quasiparticle states.

The observed double Kondo screening can be rationalized considering that the free MnPc molecule lies in a S = 3/2 spin state, with the three unpaired electrons in an electron configuration $(d_{xy})^1(d_\pi)^3(d_{z^2})^1$ (*23*). The interaction of MnPc with the lead surface is rather weak. However, the magnetic moment associated with the d_{z^2} orbital is expected to be quenched (*18*), resulting in a spin-1 system. The double Kondo spectral features are then ascribed to the screening of the two remaining localized spins in the d_{xy} and d_π orbitals, coupled independently with normal electrons of the surface at different energy scales $k_B \cdot T_K$. The broader Kondo channel, with T_K ~200 to 400 K (*24*), fully screens the magnetic moment of one of the orbitals. The other orbital is only partially screened by the low-energy Kondo channel, thus interacting with superconducting quasiparticles depending on the commensuration with the lead atomic lattice underneath. The resulting quantum state of the complete system is a singlet or doublet (Fig. 4C),

depending on the particle or hole character of the larger intragap state, respectively. Such different quantum systems coexist and alternate between neighboring molecules because of their high localization at the impurity site.

The MnPc molecular superstructure thus represents a useful nanoscopic workbench where magnetic coupling with the substrate can be measured from the alignment of the bound states and tuned by choosing the appropriate molecule. The interaction of these bound states with other intragap excitations [e.g., multiple Andreev reflections in contact junctions (*25*–*27*)] or with superconductors with other symmetries [e.g., p-wave (*28*–*30*)] represents a fascinating application of this study to ongoing problems in condensed-matter physics.

References and Notes

1. J. Kondo, *Prog. Theor. Phys.* **32**, 37 (1964).
2. L. Yu, *Acta Phys. Sin.* **21**, 75 (1965).
3. H. Shiba, *Prog. Theor. Phys.* **40**, 435 (1968).
4. A. I. Rusinov, *Zh. Eksp. Teor. Fiz.* **56**, 2047 (1969) [*Sov. Phys. JETP* **29**, 1101 (1969)].
5. A. V. Balatsky, I. Vekhter, J.-X. Zhu, *Rev. Mod. Phys.* **78**, 373 (2006).
6. A. Yazdani, B. A. Jones, C. P. Lutz, M. F. Crommie, D. M. Eigler, *Science* **275**, 1767 (1997).
7. S.-H. Ji *et al.*, *Phys. Rev. Lett.* **100**, 226801 (2008).
8. C. P. Moca, E. Demler, B. Janko, G. Zarand, *Phys. Rev. B* **77**, 174516 (2008).
9. M. E. Flatté, J. M. Byers, *Phys. Rev. B* **56**, 11213 (1997).
10. M. Flatté, J. Byers, *Phys. Rev. Lett.* **78**, 3761 (1997).
11. M. R. Buitelaar, T. Nussbaumer, C. Schönenberger, *Phys. Rev. Lett.* **89**, 256801 (2002).
12. M. I. Salkola, A. V. Balatsky, J. R. Schrieffer, *Phys. Rev. B* **55**, 12648 (1997).
13. T. Matsuura, *Prog. Theor. Phys.* **57**, 1823 (1977).
14. O. Sakai, Y. Shimizu, H. Shiba, K. Satori, *J. Phys. Soc. Jpn.* **62**, 3181 (1993).
15. Materials and methods are available as supporting material on *Science* Online.
16. V. Madhavan V, W. Chen, T. Jamneala, M. F. Crommie, N. S. Wingreen, *Science* **280**, 567 (1998).
17. J. Li, W.-D. Schneider, R. Berndt, B. Delley, *Phys. Rev. Lett.* **80**, 2893 (1998).
18. Y.-S. Fu *et al.*, *Phys. Rev. Lett.* **99**, 256601 (2007).
19. S.-H. Ji *et al.*, *Chin. Phys. Lett.* **27**, 087202 (2010).
20. J. J. Parks *et al.*, *Science* **328**, 1370 (2010).
21. A. Posazhennikova, P. Coleman, *Phys. Rev. Lett.* **94**, 036802 (2005).
22. The crossing point differs from the estimated value $k_B \cdot T_K/\Delta \sim 0.3$ (*13*, *14*). Recent renormalization group theory calculations find that the quantum phase transition may vary depending on the parameters (*31*). We note that the more complex double Kondo state of MnPc may influence the transition.
23. M.-S. Liao, J. D. Watts, M.-J. Huang, *Inorg. Chem.* **44**, 1941 (2005).
24. L. Gao *et al.*, *Phys. Rev. Lett.* **99**, 106402 (2007).
25. M. Ternes *et al.*, *Phys. Rev. B* **74**, 132501 (2006).
26. A. Eichler *et al.*, *Phys. Rev. Lett.* **99**, 126602 (2007).
27. T. Sand-Jespersen *et al.*, *Phys. Rev. Lett.* **99**, 126603 (2007).
28. G. E. Volovik, *JEPTP Lett.* **70**, 609 (1999).
29. N. Read, D. Green, *Phys. Rev. B* **61**, 10267 (2000).
30. D. A. Ivanov, *Phys. Rev. Lett.* **86**, 268 (2001).
31. J. Bauer, A. Oguri, A. C. Hewson, *J. Phys. Condens. Matter* **19**, 486211 (2007).
32. I. Horcas *et al.*, *Rev. Sci. Instrum.* **78**, 013705 (2007).

Acknowledgments: We thank F. von Oppen and A. Strozecka for stimulating discussions and E.K.U. Gross for motivating us to study this topic. This research was supported by the Focus area "Nanoscale Materials" of the Freie Universität Berlin and by the Deutsche Forschungsgemeinschaft through the collaborative projects Sfb 658 and SPP 1243.

Supporting Online Material

www.sciencemag.org/cgi/content/full/332/6032/940/DC1
Materials and Methods
Figs. S1 to S4

27 December 2010; accepted 6 April 2011
10.1126/science.1202204

Chlorinated Indium Tin Oxide Electrodes with High Work Function for Organic Device Compatibility

M. G. Helander,[1*†] Z. B. Wang,[1*†] J. Qiu,[1] M. T. Greiner,[1] D. P. Puzzo,[1] Z. W. Liu,[1*] Z. H. Lu[1,2*]

In organic light-emitting diodes (OLEDs), a stack of multiple organic layers facilitates charge flow from the low work function [~4.7 electron volts (eV)] of the transparent electrode (tin-doped indium oxide, ITO) to the deep energy levels (~6 eV) of the active light-emitting organic materials. We demonstrate a chlorinated ITO transparent electrode with a work function of >6.1 eV that provides a direct match to the energy levels of the active light-emitting materials in state-of-the art OLEDs. A highly simplified green OLED with a maximum external quantum efficiency (EQE) of 54% and power efficiency of 230 lumens per watt using outcoupling enhancement was demonstrated, as were EQE of 50% and power efficiency of 110 lumens per watt at 10,000 candelas per square meter.

Transparent tin-doped indium oxide (ITO) electrodes are used in several classes of devices, including liquid crystal displays, organic photovoltaics, and organic light-emitting diodes (OLEDs) (*1*–*11*). Despite the dominance of ITO in the flat-panel display industry, its surface electronic properties are less than ideal for organic devices. In particular, the low work function of ITO complicates the design of organic optoelectronic devices in terms of charge injection from the electrodes because of the large mismatch between the low work function of ITO (~4.7 eV) and the energy levels of the active organic materials used in devices (*12*, *13*) (typically 5.7 to 6.3 eV). For example, the highest occupied molecular orbital (HOMO) of commonly used host materials in state-of-the-art phosphorescent OLEDs is typically ~6 eV, which is much too deep to directly inject charge from ITO.

As a result, multiple transport layers are required to match the energy levels in a stepwise fashion. An additional injection layer is also typically used, with the most common examples being copper phthalocyanine (*14*), poly(3,4-ethylenedioxythiophene) (PEDOT) (*15*), transition-metal oxides (*16*), or p-doped organic layers (*17*–*19*). Each additional layer that is required greatly increases the manufacturing costs and also introduces additional hetero-junctions into the device that can be detrimental to device stability and performance (*20*, *21*). A transparent electrode with a tunable high work function that matches the energy levels of the active organic material would avoid the requirement for multiple transport and injection layers.

To address this issue, we functionalized the surface of ITO with a controlled amount of electronegative halogen atoms that were derived from an inert halogenated solvent precursor that was activated with ultraviolet (UV) radiation. An air-stable electrode with a work function greater than 6.1 eV was achieved in the case of chlorinated ITO (Cl-ITO) without altering the surface roughness, transparency, and conductivity of the electrode. The tunable high work function enabled the fabrication of a highly simplified OLED with a high efficiency and brightness.

To fabricate Cl-ITO, we placed bare substrates in a closed Pyrex reaction vessel with *o*-dichlorobenzene and treated them with UV radiation from a low-pressure mercury lamp (SEN Lights PL16-110) for up to 10 min [see (*22*) for details]. Cl radicals liberated from the solvent displaced oxygen on the surface of the electrode. After treatment with UV radiation, the substrates were exposed to UV-generated ozone for an additional 3 min to fully oxidize any residual chlorocarbon fragments on the surface (fig. S3). X-ray photoelectron spectroscopy (XPS) was used to characterize the work function and surface composition of the Cl-ITO electrode. The secondary electron cut-off of Cl-ITO as a function of increasing UV treatment time from 0 to 10 min monotonically shifted to lower binding energy, indicating an increase in work function (Fig. 1A). The intensity of the Cl 2p peak (Fig. 1B)

[1]Department of Materials Science and Engineering, University of Toronto, 184 College Street, Toronto, Ontario, Canada M5S 3E4. [2]Department of Physics, Yunnan University, 2 Cuihu Beilu, Yunnan, Kunming 650091, People's Republic of China.

*To whom correspondence should be addressed. E-mail: michael.helander@utoronto.ca (M.G.H.); zhibin.wang@utoronto.ca (Z.B.W.); zhiwei.liu@utoronto.ca (Z.W.L); zhenghong.lu@utoronto.ca (Z.H.L)
†These authors contributed equally to this work.

also increased with treatment time, indicating an increase in the surface coverage of Cl. Beyond 10 min of treatment time, the secondary electron cut-off and Cl 2p peak remained unchanged, suggesting that the surface was saturated with Cl.

To determine the distribution of Cl atoms in the Cl-ITO, we performed angle-resolved XPS (AR-XPS) measurements on a sample treated for 10 min. The measured intensities of the Cl 2p (from the overlayer) and In 3d (from the substrate) core levels as a function of photoelectron take-off angle (θ) are shown in Fig. 1C. The surface sensitivity of XPS increases at low photoelectron take-off angles because of a reduction in photoelectron escape depth. Hence, the increase in signal intensity of the Cl 2p core level at low photoelectron take-off angles indicates that the Cl atoms are confined to the surface of the Cl-ITO. The AR-XPS data also indicate that the surface coverage of Cl is close to one monolayer for the Cl-saturated surface (*23*).

The work function determined from the secondary electron cut-off as a function of surface coverage Θ (determined from the Cl 2p signal intensity and AR-XPS results) increased linearly with the Cl surface coverage (Fig. 1D). For the highest Cl surface coverage (Θ ≈ 1), corresponding to a treatment time of 10 min, we measured a work function of 6.13 eV. This value is particularly high considering that the electrode is prepared in ambient air. The high work function was also found to be stable with time, changing less than 2% after 24 hours.

The C 1s, Cl 2s, and Cl 2p core levels of Cl-ITO with Θ = 0 (bare surface) and Θ ≈ 1 (saturated surface) are shown in Fig. 2A. The C 1s peak is essentially identical on the two samples, indicating that the Cl was not in the form of a chloro-carbon fragment. We have also confirmed that the Cl is not from residual chlorinated solvent on the surface by measuring a sample dipped into chlorinated solvent; no Cl was detected (fig. S4). This finding suggests that the Cl is chemically bonded to the surface. To determine the nature of the Cl chemical bond we examined high-resolution XPS spectra of the Cl 2p core level and found that it could be fit using a single doublet peak (fig. S5), which indicates that only a single chemical species of Cl is present. The Cl $2p_{3/2}$ binding energy of this species is 199.06 eV, which rules out chlorate and perchlorate (*24*). The Cl 2p core level of Cl-ITO and $InCl_3$ are identical (Fig. 2B), which demonstrates that the Cl is bonded to In at the surface. We could not resolve a separate peak in the In 3d core level for the In-Cl bond because of the similarity in binding energies between In-O and In-Cl. Also, it is unlikely that the Cl bonds to Sn as tin chloride is readily hydrolyzed to tin oxide upon exposure to air.

Figure 2C shows the valence band of Cl-ITO with Θ = 0 (bare surface) and Θ ≈ 1 (saturated surface) measured with XPS and ultraviolet photoelectron spectroscopy (UPS). The valence band maximum of both samples is located 3.1 eV below the Fermi level (E_F), indicating that the Cl does not alter the doping level. Because ITO is an *n*-type degenerate semiconductor, the finite density of states (DOS) at E_F is representative of the partially filled conduction band. The DOS at E_F, which is a sensitive indication of surface electronic structure, is nearly identical on both samples. The high work function of Cl-ITO cannot be a result of a change in E_F (i.e., electrochemical potential), doping level, or surface electronic structure. By definition, the work function of a uniform surface of a conductor is the difference between the electrochemical potential $\bar{\mu}$ of electrons in the bulk and the electrostatic potential energy $-e\Phi_{vac}$ of an electron in the vacuum just outside the surface (*25*)

$$e\phi_m = -e\Phi_{vac} - \bar{\mu} \quad (1)$$

The Cl must change the electrostatic potential just outside the surface. Our XPS data show that Cl is bonded to In at the surface. The large difference in electronegativity between In and Cl (i.e., 1.78 compared to 3.16) means that the In-Cl bonds at the surface are polar, which is equivalent to introducing a layer of dipoles across the surface. These dipoles would increase the electrostatic potential energy just outside the surface, resulting in a much higher work function (fig. S6).

To demonstrate the benefits of the tunable high work function of Cl-ITO for device applications, we fabricated simplified phosphorescent OLEDs using the high work function of Cl-ITO

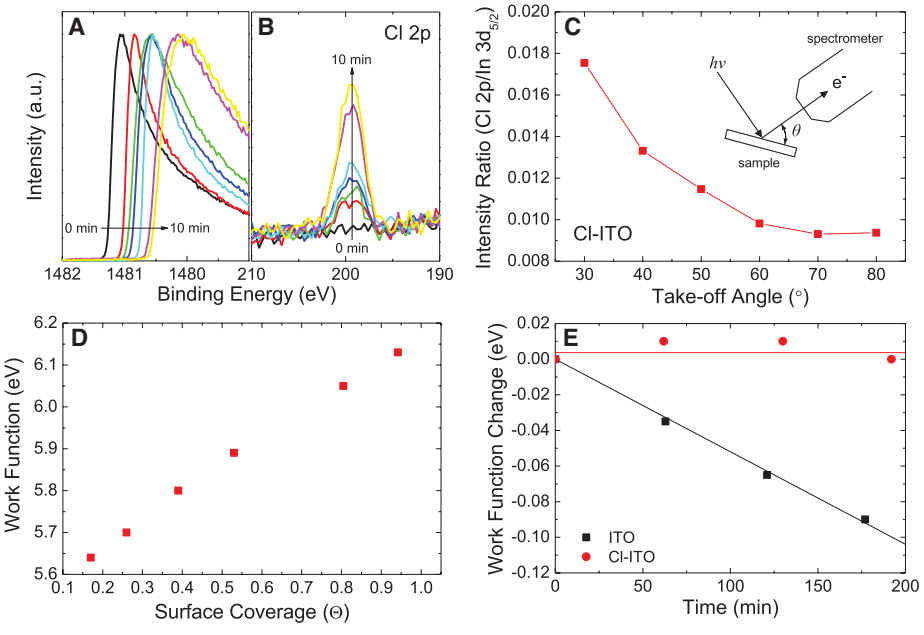

Fig. 1. Work function and Cl surface coverage. (**A**) Secondary electron cut-off and (**B**) Cl 2p peak as a function of increasing UV treatment time. (**C**) Angle-resolved XPS measurements showing the Cl 2p/In $3d_{5/2}$ intensity ratio of Cl-ITO as a function of photoelectron take-off angle (θ). The inset shows the measurement geometry. (**D**) Work function as a function of Cl surface coverage (Θ); Θ = 1.0 corresponds to one monolayer. (**E**) Change in work function of Cl-ITO and ITO as a function of time. The lines are a guide for the eye.

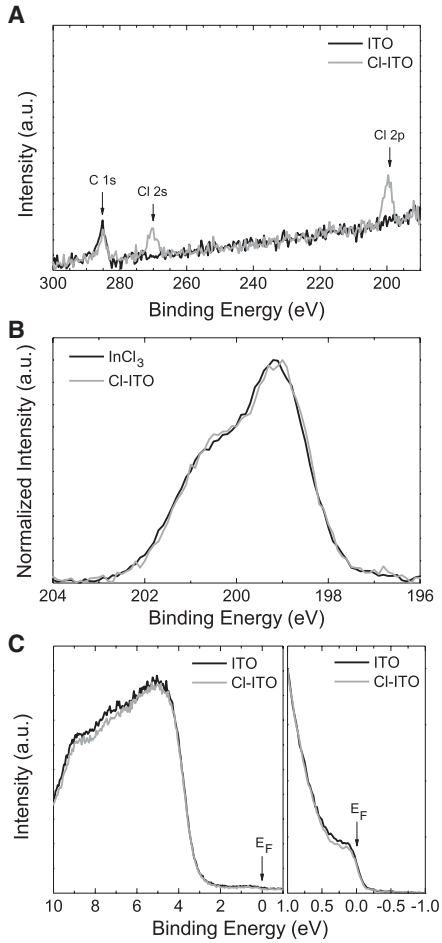

Fig. 2. Surface composition of Cl-ITO. (**A**) C 1s, Cl 2s, and Cl 2p core levels for Θ = 0 (bare surface) and Θ ≈ 1 (saturated surface). (**B**) The Cl 2p core level of Cl-ITO compared to $InCl_3$. (**C**) (Left) Valence band for Θ = 0 and Θ ≈ 1, and (right) density of states at the Fermi level (E_F) for Θ = 0 and Θ ≈ 1.

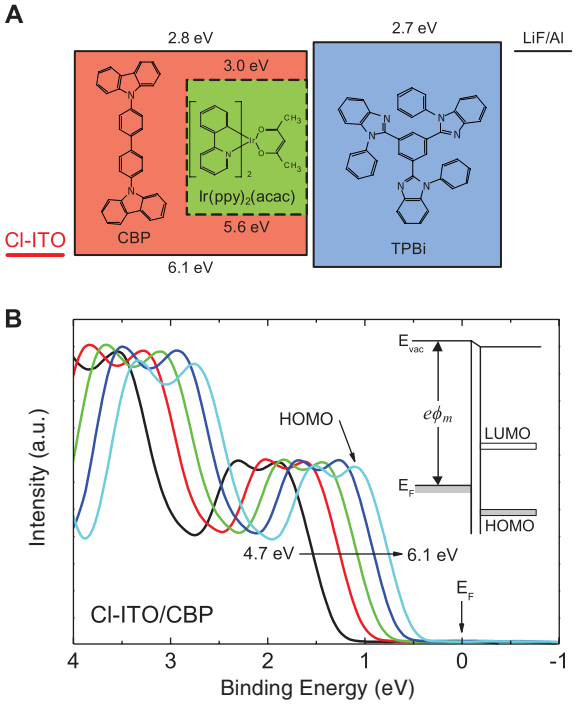

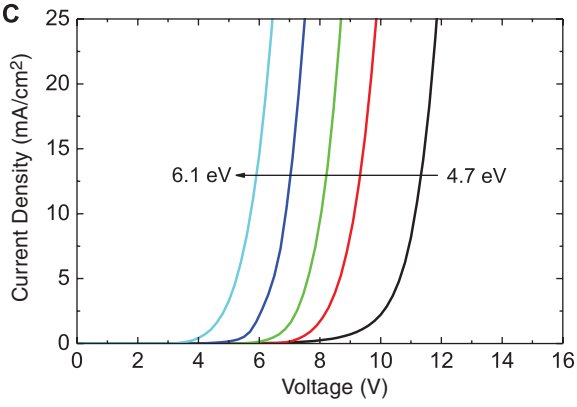

Fig. 3. Energy-level alignment between Cl-ITO and CBP. (**A**) Schematic energy-level diagram of the simplified OLED: Cl-ITO/CBP (35 nm)/CBP:Ir(ppy)$_2$(acac) (15 nm, 8%)/TPBi (65 nm)/LiF (1 nm)/Al (100 nm). (**B**) UPS spectra of CBP deposited on Cl-ITO with different work function. The inset shows a schematic energy-level diagram of the Cl-ITO/CBP interface. LUMO, lowest unoccupied molecular orbital. (**C**) Current density as a function of voltage for CBP-based OLEDs fabricated on Cl-ITO with different work function.

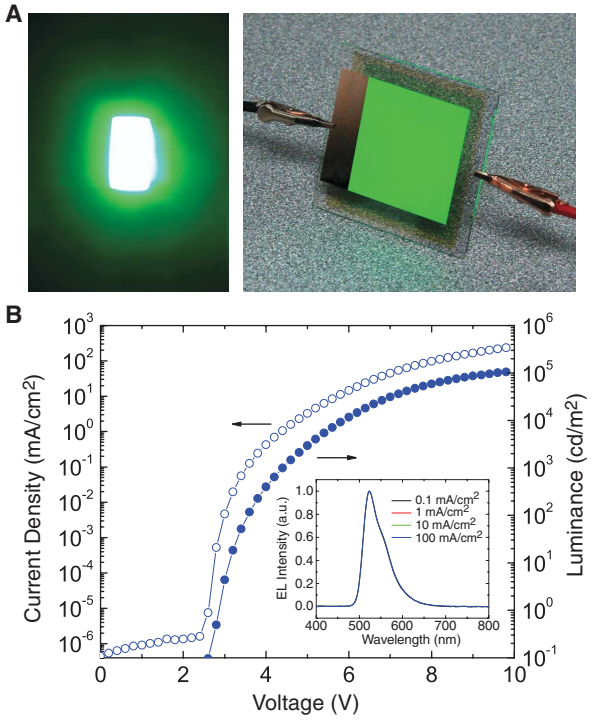

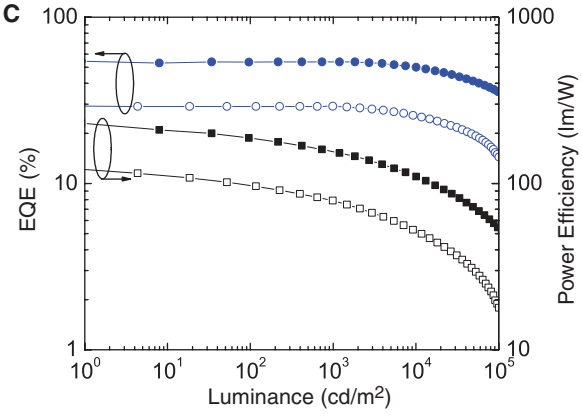

Fig. 4. Device performance of OLEDs with Cl-ITO electrode. (**A**) (Left) Photograph of a device (1 mm by 2 mm) operating at a high brightness of 5000 cd/m^2 and (right) a large-area prototype device (50 mm by 50 mm). (**B**) Current density and luminance as a function of voltage. The inset shows the EL spectra as a function of current density. (**C**) EQE and power efficiency as a function of luminance. The open symbols are without outcoupling enhancement, and the solid symbols are with lens-based outcoupling enhancement.

to enable direct injection of holes into 4,4′-*N*,*N*′-dicarbazole-biphenyl (CBP), the host material used for the phosphorescent emitter. A complex multilayer hole injection and transport stack is typically required to match the deep HOMO of CBP (6.1 eV). Using Cl-ITO, however, allows us to tune the work function of the anode to match the deep HOMO of CBP without having to introduce any additional injection and transport layers, thus greatly simplifying the device design and fabrication. Such a simplified device design also has the potential to greatly improve device performance because it eliminates several of the heterojunctions in the device that can block carrier transport and contribute to exciton quenching (*21*).

A schematic energy-level diagram of the simplified OLED with Cl-ITO as an anode is shown in Fig. 3A, in which part of the CBP layer is doped with the phosphorescent emitter to form the emission zone. The HOMO-derived peak of CBP deposited on Cl-ITO with different work functions measured with UPS (Fig. 3B) shows that by tuning the work function of the Cl-ITO to match the deep ionization potential of the CBP, the barrier height at the interface can be reduced by ~0.7 eV. The current density as a function of voltage of OLEDs fabricated on Cl-ITO with

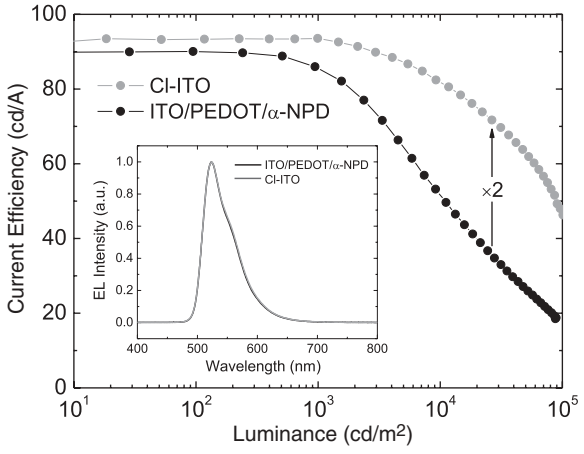

Fig. 5. Effect of stepwise injection on device performance. Current efficiency as a function of luminance for devices with Cl-ITO anode in comparison to devices using a traditional stepwise injection structure. The ITO was coated with 5 nm of PEDOT, and the 35-nm-thick undoped region of CBP was replaced with a separate layer of α-NPD of the same thickness, yielding ITO/PEDOT (5 nm)/α-NPD (35 nm)/CBP:Ir(ppy)$_2$(acac) (15 nm, 8%)/TPBi (65 nm)/LiF (1 nm)/Al (100 nm).

different work functions is shown in Fig. 3C. With increasing work function, the operating voltage of the OLED was markedly reduced because of the lower barrier height at the Cl-ITO/CBP interface as shown by the UPS results. Photographs of a Cl-ITO–based green-emitting OLED operating at high brightness, as well as a large-area prototype device, are shown in Fig. 4A, and the current-voltage-luminance characteristics of an optimized device with a Cl-ITO anode is shown in Fig. 4B (the white-looking emission is due to the high brightness of the OLED saturating the detector of the camera). A reference device fabricated on ITO (same organic layer structure) exhibited an extremely high driving voltage and no visible electroluminescence (EL) in the voltage range tested because of the poor energy-level matching between ITO and CBP. The external quantum efficiency (EQE) of the Cl-ITO device (Fig. 4C) reaches 29.1% (93 cd/A) at 100 cd/m^2, 29.2% (94 cd/A) at 1000 cd/m^2, and 25.4% (81 cd/A) at 10,000 cd/m^2. Although a similarly high efficiency can be achieved in a traditional device with *N*,*N*′-diphenyl-*N*,*N*′-bis-(1-naphthyl)-1-1′-biphenyl-4,4′-diamine (α-NPD) hole-transport layer and PEDOT hole-injection layer at low luminance (90 cd/A at 100 cd/m^2), the efficiency is much lower at high luminance (50 cd/A at 10,000 cd/m^2), as shown in Fig. 5. The drastic efficiency roll-off in the traditional device (i.e., ITO/PEDOT/α-NPD) is due to the additional organic-organic heterojunctions in the device, which block carrier transport and contribute to exciton quenching (*21*). Even at an ultrahigh luminance of 100,000 cd/m^2, the EQE of the Cl-ITO device is still as high as 14.3% (46 cd/A). The power efficiency of the Cl-ITO device reaches 97 lm/W at 100 cd/m^2, 79 lm/W at 1000 cd/m^2, and 51 lm/W at 10,000 cd/m^2, which is better than state-of-the-art *p-i-n* phosphorescent organic light-emitting diodes, which require six or more organic layers (*19*, *26*).

The use of a simple lens-based structure to help outcouple trapped light at the glass-air interface (*7*, *8*) can further enhance the device performance, and the EQE can be further increased to 54% at 1000 cd/m^2, 50% at 10,000 cd/m^2, and 35% at 100,000 cd/m^2. The maximum power efficiency is also increased to 230 lm/W. At 10,000 cd/m^2 the power efficiency is still as high as 110 lm/W, more than double the value of the best previously reported OLED (*27*). These high efficiencies are achieved with a simplified device design using readily available materials and without using chemically doped layers. Using a high-index substrate instead of glass could further help to improve the efficiency by outcoupling more light trapped in the ITO modes (*7*, *28*).

References and Notes

1. J. Kido, M. Kimura, K. Nagai, *Science* **267**, 1332 (1995).
2. Z. Shen, P. Burrows, V. Bulovic, S. Forrest, M. Thompson, *Science* **276**, 2009 (1997).
3. R. H. Friend *et al.*, *Nature* **397**, 121 (1999).
4. M. A. Baldo, M. E. Thompson, S. R. Forrest, *Nature* **403**, 750 (2000).
5. C. D. Müller *et al.*, *Nature* **421**, 829 (2003).
6. Y. Sun *et al.*, *Nature* **440**, 908 (2006).
7. S. Reineke *et al.*, *Nature* **459**, 234 (2009).
8. Y. Sun, S. R. Forrest, *Nat. Photonics* **2**, 483 (2008).
9. M. D. Irwin, D. B. Buchholz, A. W. Hains, R. P. H. Chang, T. J. Marks, *Proc. Natl. Acad. Sci. U.S.A.* **105**, 2783 (2008).
10. T. Sekitani *et al.*, *Nat. Mater.* **8**, 494 (2009).
11. W. H. Koo *et al.*, *Nat. Photonics* **4**, 222 (2010).
12. N. R. Armstrong, P. A. Veneman, E. Ratcliff, D. Placencia, M. Brumbach, *Acc. Chem. Res.* **42**, 1748 (2009).
13. X. H. Sun *et al.*, *Chem. Phys. Lett.* **370**, 425 (2003).
14. S. A. Van Slyke, C. H. Chen, C. W. Tang, *Appl. Phys. Lett.* **69**, 2160 (1996).
15. S. A. Carter, M. Angelopoulos, S. Karg, P. J. Brock, J. C. Scott, *Appl. Phys. Lett.* **70**, 2067 (1997).
16. S. Tokito, K. Noda, Y. Taga, *J. Phys. D* **29**, 2750 (1996).
17. X. Zhou *et al.*, *Appl. Phys. Lett.* **78**, 410 (2001).
18. D. Tanaka *et al.*, *Jpn. J. Appl. Phys.* **46**, L10 (2007).
19. G. He *et al.*, *Appl. Phys. Lett.* **85**, 3911 (2004).
20. H. Aziz, Z. D. Popovic, N. X. Hu, A. M. Hor, G. Xu, *Science* **283**, 1900 (1999).
21. Z. B. Wang *et al.*, *J. Appl. Phys.* **108**, 024510 (2010).
22. Materials and methods are available as supporting material on *Science* Online.
23. S. Oswald, M. Zier, R. Reiche, K. Wetzig, *Surf. Interface Anal.* **38**, 590 (2006).
24. V. I. Nefedov, É. K. Zhumadilov, T. Y. Kopytova, *J. Struct. Chem.* **18**, 549 (1977).
25. C. Herring, M. H. Nichols, *Rev. Mod. Phys.* **21**, 185 (1949).
26. S. Watanabe, N. Ide, J. Kido, *Jpn. J. Appl. Phys.* **46**, 1186 (2007).
27. S.-J. Su, H. Sasabe, Y.-J. Pu, K.-i. Nakayama, J. Kido, *Adv. Mater.* **22**, 3311 (2010).
28. S. Mladenovski, K. Neyts, D. Pavicic, A. Werner, C. Rothe, *Opt. Express* **17**, 7562 (2009).

Acknowledgments: Z.H.L. is a Canada Research Chair in Organic Optoelectronics, Tier I. We acknowledge funding for this research from the Natural Sciences and Engineering Research Council (NSERC) of Canada. We are grateful to T. P. Bender and G. A. Ozin (University of Toronto) for helpful discussions.

Supporting Online Material

www.sciencemag.org/cgi/content/full/science.1202992/DC1
Materials and Methods
Figs. S1 to S14
Tables S1 to S3
References

18 January 2011; accepted 28 March 2011
Published online 14 April 2011;
10.1126/science.1202992

Probing Asthenospheric Density, Temperature, and Elastic Moduli Below the Western United States

Takeo Ito[1,2]* and Mark Simons[1]

Periodic ocean tides continually provide a cyclic load on Earth's surface, the response to which can be exploited to provide new insights into Earth's interior structure. We used geodetic observations of surface displacements induced by ocean tidal loads to constrain a depth-dependent model for the crust and uppermost mantle that provides independent estimates of density and elastic moduli below the western United States and nearby offshore regions. Our observations require strong gradients in both density and elastic shear moduli at the top and bottom of the asthenosphere but no discrete structural discontinuity at a depth of 220 kilometers. The model indicates that the asthenosphere has a low-density anomaly of ~50 kilograms per cubic meter; a temperature anomaly of ~300°C can simultaneously explain this density anomaly and inferred colocated minima in elastic moduli.

Ocean tides on Earth are a well-known phenomenon resulting from periodic variations in gravitational forcing from the Sun and Moon. Variations of density and elastic moduli within Earth's interior control the response to ocean tidal loads (OTLs). Conversely,

observations of the solid Earth's OTL response can thus be used to estimate these properties, providing essential constraints on our understanding of mantle convection and the evolution of the overlying tectonic plates. Previous attempts to infer interior structure using tidal observations from instruments such as gravimeters, strainmeters, and tiltmeters (*1*, *2*) have been largely unsuccessful because of limitations in sensitivity and/or spatial coverage. For example, strain and tilt measurements are intrinsically more sensitive to local variations in crustal material properties, thereby confounding their ability to constrain regional structures.

Dense arrays of global positioning system (GPS) receivers have the potential to overcome these limitations by collecting observations of tidally induced displacements down to 1 mm accuracy (*3*–*6*). Tidally related surface displacements comprise two primary components: solid Earth body tides, which are relatively well understood, and the OTL response (*7*–*10*). The OTL response has a rich spatial structure including power at regional length scales (a few hundred kilometers), with typical amplitudes on the centimeter scale. OTL responses are reasonably well predicted by global ocean tidal models convolved with Earth elastic response (*11*). In traditional GPS processing, OTL effects are modeled and removed from GPS time series. Here, instead of modeling these signals out, we estimate the OTL response directly from the data.

We focus on GPS data for the western United States from the Plate Boundary Observatory (PBO), the geodetic component of the EarthScope project (*12*). Using the OTL response as estimated from GPS observations, we infer depth-dependent material property variations in the mantle down to ~350 km depth. Seismologists are already adept at producing shear wave velocity (V_S) and compressional wave velocity (V_P) models (*13*, *14*) but, for the crust and uppermost mantle, these models have limited ability to separate the effects of variations in density and elastic moduli. Typically, estimates of these parameters are obtained by combining and/or scaling V_S and V_P models—a step that is fraught with uncertainty. In contrast, by considering the spatial variation of the horizontal and vertical response (amplitude and phase) to OTL, we can independently constrain the depth dependence of density and elastic moduli.

We estimate the OTL response as the residual after removing the solid Earth body tide for 15 constituents (*15*) and map out the spatial distribution of the OTL response field of the three components of each tidal constituent (fig. S1). In general, the cyclic particle motion for a given tidal constituent measured at the surface can be described by an ellipse that is arbitrarily oriented in three-dimensional (3D) space (Fig. 1B). If the particle motion ellipse (PME) is eccentric, the orientation of the semimajor axis points in the direction of the dominant portions of the OTL distribution (Fig. 1B and fig. S2). The M2 OTL constituent has the largest amplitudes, which in our study area is maximum offshore of the northwest United States (Fig. 1A). Hence, the direction of maximum amplitude of the OTL response is predominantly toward the northwest for the M2 constituent (*16*).

To calculate the OTL response for a given radial Earth model, we adopt the FES2004 OTL model (*17*). FES2004 is derived by assimilating data from tide gauges, as well as satellite altimetric crossover points from Topex/Poseidon and European Remote Sensing satellites, into a hydrodynamic ocean tide model. For future comparison purposes, we evaluate the variance reduction and the sum total of the predicted maximum principal amplitude of OTL response for each tidal constituent on the basis of FES2004, using the globally averaged radial model of density and elastic moduli from the seismologically derived Preliminary Reference Earth Model (PREM) (Fig. 1D and table S1) (*16*, *18*).

Similar to PREM, we parameterize our new 1D structure model with continuous cubic splines, and include the freedom to have discrete discontinuities at depths of 15 km, 24.4 km, and 220 km. Traditionally, material properties in seismological models are parameterized in terms of V_P and V_S. In contrast, we parameterize our models directly in terms of bulk modulus κ, shear modulus μ, and density ρ (Fig. 2). In total, there are 45 model parameters.

Before formally inverting for interior density and elastic moduli, we consider the theoretical sensitivity, K, of our observations to small perturbations in these parameters (*16*). K is broadly similar for both horizontal and vertical components of displacements (Fig. 2). K_κ and K_μ, the indicators of sensitivity to perturbations in the elastic moduli, are clearly different. Although horizontal components of displacement are more sensitive to perturbations in elastic structure than are vertical components, their observed amplitudes are typically smaller than those observed for vertical displacements (Fig. 2, top). To illustrate the difference in sensitivity to shear moduli

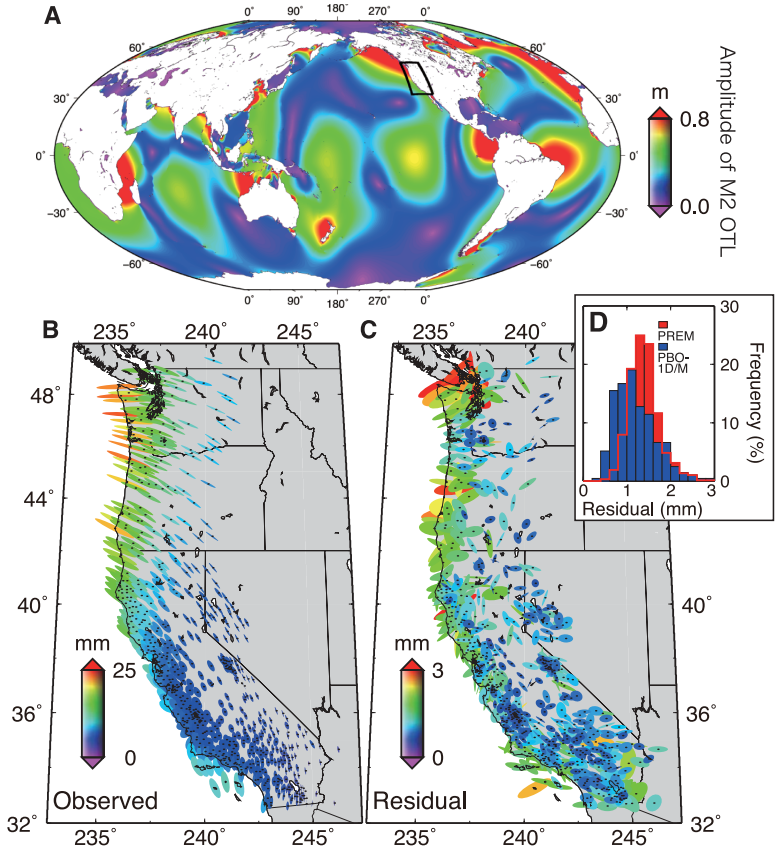

Fig. 1. Spatial distribution of the amplitude of the OTL, and observed and residual M2 OTL response. (**A**) Amplitude of the OTL distribution for the M2 constituent from FES2004 (*17*). (**B**) The particle motion ellipses (PMEs) of the spatial distribution of OTL response using three components. The PMEs are shown rotated into the horizontal plane. (**C**) PMEs of the spatial distribution of residuals of the observed OTL response after removal of the predictions using PBO-1D/M. The large residuals in the north near Puget Sound are presumed to result from limitations in the OTL model. For both (B) and (C), color is proportional to the semimajor axis of the PMEs. (**D**) Histograms of the residual using PREM and PBO-1D/M.

[1]Seismological Laboratory, Division of Geological and Planetary Sciences, California Institute of Technology, Pasadena, CA 91125, USA. [2]Research Center for Seismology, Volcanology and Disaster Mitigation, Nagoya University, Nagoya, Aichi 464-8602, Japan.

*To whom correspondence should be addressed. E-mail: takeo_ito@nagoya-u.jp

and density, we consider the absolute value of the ratio of K_μ to K_ρ (Fig. 2, bottom). We find that sensitivities to perturbations in density and shear moduli vary strongly as a function of distance to the applied load and the component of displacement being considered. On the basis of this sensitivity analysis (*16*), we conclude that our OTL-based model is mostly sensitive to structure in the upper 350 km of the mantle. Therefore, at depths greater than 355 km, we fix the structure to be the same as PREM.

We adopt a fully probabilistic approach to estimating the model parameters, where the posterior probability density function (PDF) results from a likelihood function based on data misfit. We sample the posterior PDFs by means of a Markov Chain Monte Carlo method. We obtain posterior PDFs of a new radial model, PBO-1D, that is consistent with our set of OTL response data (Fig. 3). We refer to the model constructed from the median of the distribution of a given parameter at each knot in PBO-1D as PBO-1D/M (table S3). The values for elastic moduli and implied seismic velocities (Fig. 3) have been converted from the original estimates associated with our observations at tidal periods of ~12 and ~24 hours to equivalent values at 1 s period using a model of attenuation from PREM (*16*).

As an initial point of reference, the variance reduction in the OTL response data for PBO-1D/M is 91.0%, an improvement relative to PREM of ~2% (table S2). Such an improvement may seem small but is in fact substantial, as evidenced by the extent to which many of the seismic models fall outside of the distributions inferred in PBO-1D (Fig. 3). The improvement in variance reduction is also greater than differences found when adopting different OTL models (e.g., Fig. 1, figs. S6 and S7, and table S4). The spatial distribution of residuals shows regional variations that are most likely due to 3D variations in elastic and density structure. These residuals would be spatially random if they were mainly attributable to GPS observation error.

Relative to global models such as PREM, a robust feature of PBO-1D/M is a region of low μ between 0 and 200 km depth. PBO-1D also has a preference for models that do not include a discontinuity at 220 km depth (Fig. 3 and fig. S8). Typical differences in κ and μ relative to PREM are ±10%, whereas differences in ρ are generally in the range of ±1% except near the 220-km discontinuity and at depths shallower than 24.5 km. The density profile of PBO-1D/M is similar to the STW105 1D reference model (*19*) except in the top 100 km. PBO-1D has a distinct sublithospheric density minimum.

Using each sample of the posterior PDFs for μ, κ, and ρ, we calculate the implied PDFs for V_P and V_S (Fig. 3 and fig. S9). We also estimate the a posteriori correlation coefficient between all of the unknown parameters (*16*). None of the estimated parameters have correlations in excess of ±0.3, which suggests that our model is well resolved.

Our PBO-1D model represents a mix of continental and oceanic structure. Our depth resolution is controlled by the wavelength of the OTL. For a given OTL distribution, shorter-wavelength components probe with higher spatial resolution but only at shallow depths, while longer-wavelength components probe deeper into Earth but with lower spatial resolution. Consistent with this discussion of resolution, we find that at depths shallower than 80 km, PBO-1D overlaps the TNA (*20*) and T7 (*21*) seismic models, both of which focus on regional continental structure (Fig. 3). In the same vein, V_S values in PBO-1D from 100 to 220 km depth overlap the seismic model PAC06 (*22*), which focuses on the Pacific upper mantle structure.

PBO-1D is notable for its lack of a 220-km discontinuity. The absence of this discontinuity has been previously described by seismologists (*19*, *23*). For instance, the T7 *P*-wave model and the TNA and PAC06 *S*-wave models, both regional seismic body wave models for the western United States, also have no discontinuity at 220 km depth (*16*). There is a more prominent low-velocity zone in PBO-1D, which is a regional model, than found in the PREM or STW105 global 1D seismic models (Fig. 3). In particular, we focus on the differences in the depth profiles of ρ and μ. We would typically expect ρ to increase with depth; however, in PBO-1D, we see a minimum between 80 and 100 km depth. This density profile reflects depth variations in pressure, temperature, melt fraction, and chemistry. We can account for pressure with the Adams-Williamson formulation (*24*) (Fig. 4B), where we used the value at 300 km depth as an arbitrary but convenient reference. In the adjusted density profile, the minimum is around 150 km, with a low-density anomaly of ~50 kg/m^3 between 80 and 250 km depth. Assuming that this density anomaly is due purely to temperature, we make a rough estimate for the associated anomaly, ΔT_ρ, required to account for the local minimum. We find a maximum in ΔT_ρ of ~300°C, where we have assumed a volumetric coefficient of thermal expansion of 3×10^{-5} K^{-1}.

We now consider the impact of ΔT_ρ on μ. Our observations are made at periods of 12 to 24 hours, much longer than those associated with seismic

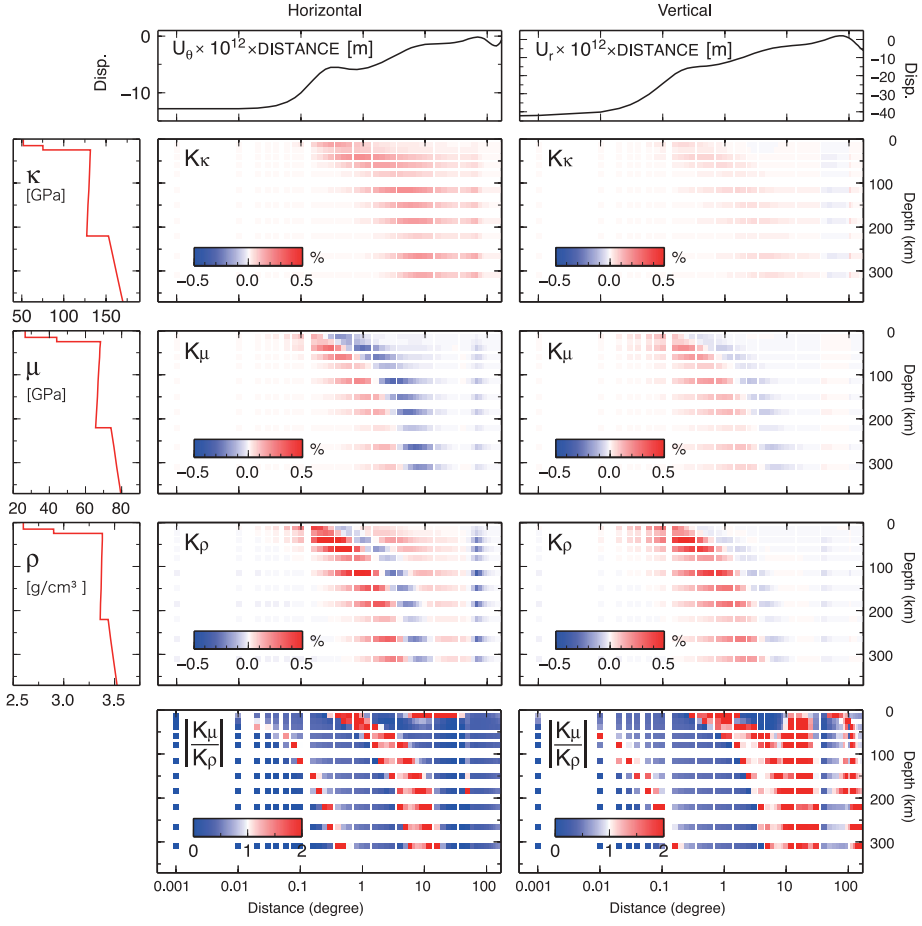

Fig. 2. Sensitivity and absolute value for load Green's functions for 24-hour tidal periods. Center and right columns correspond to horizontal, U_θ, and vertical, U_r, components, respectively. The left column shows PREM in terms of κ, μ, and ρ. Top row denotes the normalized absolute value of load Green's functions for each component (horizontal and vertical), with the predicted displacements multiplied by the distance from the load. The second, third, and fourth rows correspond to K_κ, K_μ, and K_ρ components, respectively. Red and blue colors show positive and negative sensitivity of load Green's function. The bottom row shows the absolute value of the ratio of K_μ to K_ρ.

studies at periods of seconds to about an hour. In Fig. 3, we converted μ to equivalent values at 1 Hz with the use of an attenuation model, Q_{PREM}, taken from PREM. Unfortunately, there are no direct measurements of Q for the upper mantle in the tidal frequency band. The differences between μ_{tidal} as originally estimated at tidal periods (Fig. 4) and values in the global 1D models are magnified relative to the predictions at 1 Hz. μ_{tidal} is characterized by two regions of sharp gradients at ~80 km and 220 km depth, which we associate with the top and bottom of the asthenosphere. In all likelihood, the 220-km discontinuity in PREM is a reflection of this strong but apparently not discrete change in properties.

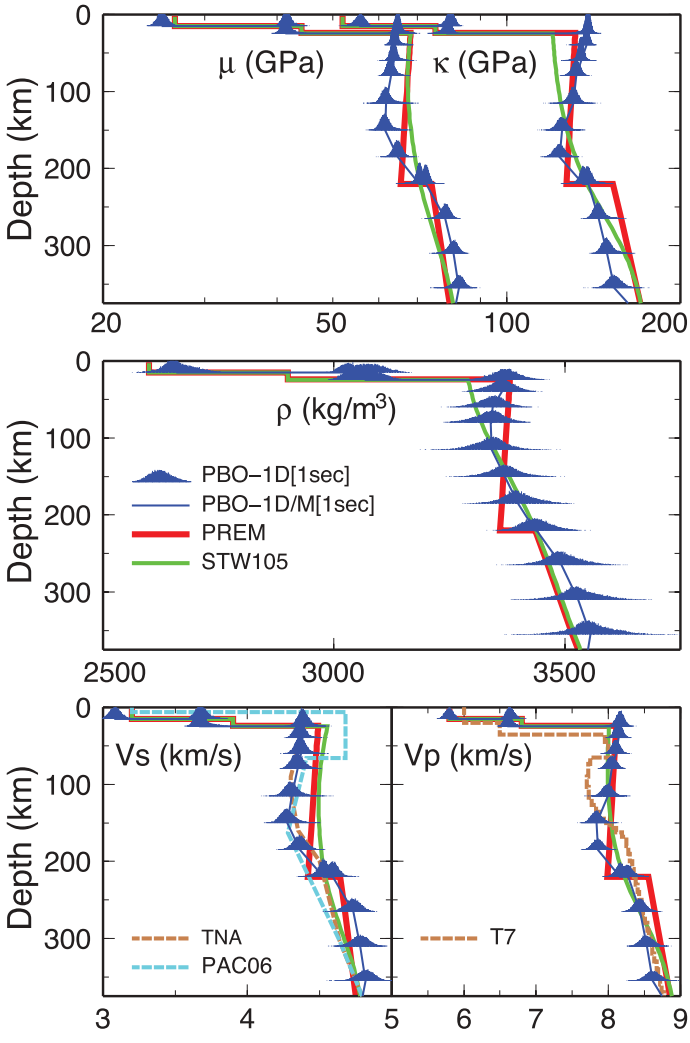

Fig. 3. Comparison of 1D crust and upper mantle models. Models are as indicated in the key. Blue histograms show the marginal posterior probability distributions for PBO-1D. V_P and V_S of PBO-1D are derived from κ, μ, and ρ. All PBO-1D values of moduli and velocities have been converted from their original values associated with tidal periods to 1 s period effective values using the PREM attenuation model (*16*). TNA (*20*) and T7 (*21*) seismic models both focus on regional continental structure. The seismic model PAC06 (*22*) focuses on the Pacific upper mantle structure. STW105 (*19*) is a global seismic model.

We can correct for the impact of ΔT_ρ on μ_{tidal} with laboratory-derived estimates of the temperature sensitivity of the shear modulus at mantle pressures. Here, we use a value of –13.6 MPa K^{-1} measured for single-crystal orthoenstatite (*25*). This correction for temperature has the effect of largely removing the distinct minima in the profile of μ_{tidal} (Fig. 4A). The profile of $\mu_{tidal}^{\Delta T_\rho}$ has a similar shape to that derived from the global average component of STW105, μ_{STW105}, but has systematically lower values above 220 km depth.

It is possible to attribute the systematic differences between $\mu_{tidal}^{\Delta T_\rho}$ and STW105 to effects associated with attenuation, Q, and its variations with depth. We estimate effective values of attenuation, Q_μ^{eff}, required to reconcile our estimates of $\mu_{tidal}^{\Delta T}$ with those in STW105. This approach makes physical sense only where $\mu_{tidal}^{\Delta T}$ is inferred to be lower than μ at seismic periods. The resulting values of Q_μ^{eff} are about 30% lower than those in STW105 (Fig. 4C) but are consistent with Q_μ estimated in tectonically active regions (*26*, *27*).

Establishing the presence of a regional low-density anomaly, regardless of it being thermal or compositional in origin, is important for furthering our understanding of the evolution of long-wavelength topography in the region (*28*–*30*). However, given the 1D nature of our model, it is not currently possible to precisely quantify the horizontal extent of the low-density region and thus to make direct predictions of dynamic

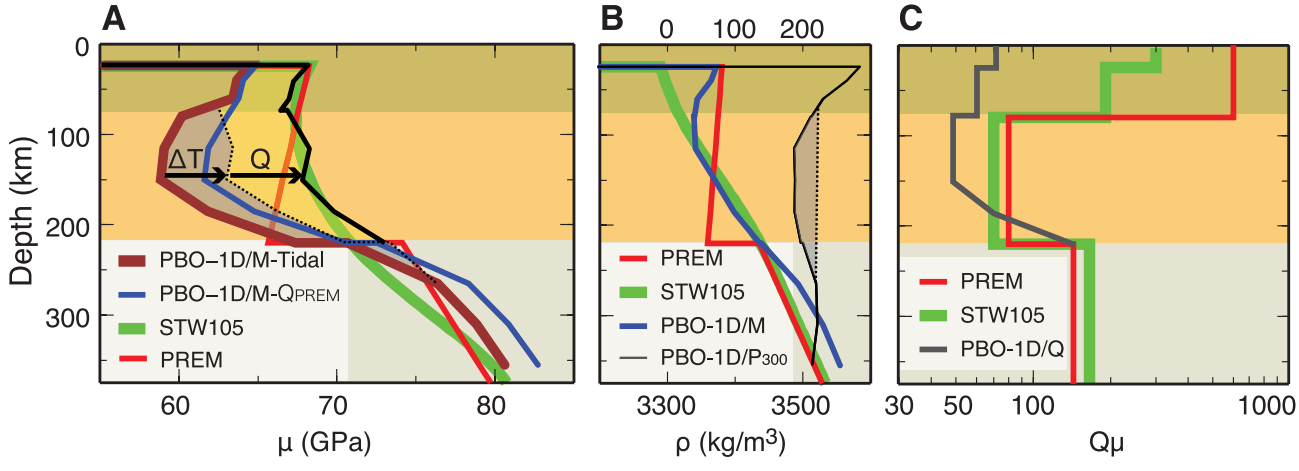

Fig. 4. Profiles of μ, ρ, and Q_μ. In all three panels, STW105 1D and PREM are indicated by green and red lines, respectively. (**A**) Profiles of shear moduli. Brown line, μ_{tidal} from PBO-1D/M; blue line, μ_{tidal} converted to 1 s period effective values using Q_{PREM}; dashed black line, $\mu_{tidal}^{\Delta T_\rho}$, the result of correcting μ_{tidal} for the effect of the inferred temperature anomaly; solid black line, the result of the additional correction using Q_μ^{eff}. Note that the *x* axis is linear, whereas in Fig. 3 it is logarithmic. (**B**) Density profile from PBO-1D/M (blue line) and the profile corrected for pressure effects (solid black line). The dashed black line indicates the reference used to estimate the approximate density anomaly from which we infer a temperature anomaly. (**C**) Q_μ^{eff} (black line) derived from forcing PBO-1D/M to map nearly one-for-one to STW105 in the depth range of 0 to 220 km.

topography. In due time, we expect a new generation of 3D models derived by integrating seismology and geodesy. Indeed, we expect that dense GPS arrays will eventually be deployed even in tectonically quiescent regions of the world, purely to constrain models of Earth's internal structure.

References and Notes

1. N. N. Pariisky, *Tectonophysics* **1**, 439 (1965).
2. M. S. M. Mantovani, W. Shukowsky, S. R. C. de Freitas, B. B. B. Neves, *Earth Planet. Sci. Lett.* **230**, 397 (2005).
3. N. T. Penna, M. A. King, M. P. Stewart, *J. Geophys. Res.* **112**, B02402 (2007).
4. M. A. King, C. S. Watson, N. T. Penna, P. J. Clarke, *Geophys. Res. Lett.* **35**, L03302 (2008).
5. T. Ito, M. Okubo, T. Sagiya, *J. Geodyn.* **48**, 253 (2009).
6. M. Vergnolle *et al.*, *J. Geophys. Res.* **115**, B08403 (2010).
7. G. Y. Fu, W. K. Sun, *J. Geophys. Res.* **112**, B06409 (2007).
8. K. Latychev, J. X. Mitrovica, M. Ishii, N. H. Chan, J. L. Davis, *Earth Planet. Sci. Lett.* **277**, 86 (2009).
9. R. H. G. Hart, M. T. Gladwin, R. L. Gwyther, D. C. Agnew, F. K. Wyatt, *J. Geophys. Res.* **101**, 25553 (1996).
10. E. Roeloffs, *J. Geophys. Res.* **115**, B06405 (2010).
11. M. Vergnolle *et al.*, *Geophys. J. Int.* **173**, 444 (2008).
12. Earthscope project (www.earthscope.org).
13. A. Dziewonski, X.-F. Liu, W.-J. Su, in *Earth's Deep Interior*, D. J. Crossley, Ed. (Gordon and Breach Science, Newark, NJ, 1997), 11.
14. A. M. Dziewonski, B. Romanowicz, *Treatise of Geophysics* (Elsevier, 2007), vol. 1.
15. G. H. Darwin, *The Tides and Kindred Phenomena in the Solar System* (Houghton Mifflin, Boston, 1899).
16. See supporting material on *Science* Online.
17. F. Lyard, F. Lefevre, T. Letellier, O. Francis, *Ocean Dyn.* **56**, 394 (2006).
18. A. M. Dziewonski, D. L. Anderson, *Phys. Earth Planet. Inter.* **25**, 297 (1981).
19. B. Kustowski, G. Ekstrom, A. M. Dziewonski, *J. Geophys. Res.* **113**, B06306 (2008).
20. S. P. Grand, D. V. Helmberger, *Geophys. J. R. Astron. Soc.* **76**, 399 (1984).
21. L. J. Burdick, D. V. Helmberger, *J. Geophys. Res.* **83**, 1699 (1978).
22. Y. Tan, D. V. Helmberger, *J. Geophys. Res.* **112**, B08301 (2007).
23. B. L. N. Kennett, E. R. Engdahl, *Geophys. J. Int.* **105**, 429 (1991).
24. S. Stein, M. Wysession, *An Introduction to Seismology, Earthquakes, and Earth Structure* (Blackwell, Boston, 2003).
25. J. M. Jackson, S. V. Sinogeikin, J. D. Bass, *Phys. Earth Planet. Inter.* **161**, 1 (2007).
26. N. Fuji, K. Kawai, R. J. Geller, *Phys. Earth Planet. Inter.* **180**, 118 (2010).
27. Y. Y. Ruan, Y. Zhou, *Geophys. J. Int.* **181**, 479 (2010).
28. B. H. Hager, R. W. Clayton, in *Mantle Convection: Plate Tectonics and Global Dynamics*, W. Peltier, Ed. (Gordon and Breach Science, Newark, NJ, 1989), 657.
29. R. Moucha *et al.*, *Earth Planet. Sci. Lett.* **271**, 101 (2008).
30. S. Spasojevic, L. J. Liu, M. Gurnis, *Geochem. Geophys. Geosyst.* **10**, Q05W02 (2009).

Acknowledgments: We thank H. Kanamori, D. L. Anderson, M. Gurnis, and two reviewers for informative discussions and helpful reviews of early versions of this work. This material is based on raw data provided by the Plate Boundary Observatory operated by UNAVCO for EarthScope (www.earthscope.org). Supported by NSF grants EAR-0350028 and EAR-0732947, Ministry of Education, Culture, Sports, Science & Technology of Japan grant-in-aid for scientific research 20740254, JSPS Postdoctoral Fellowships for Research Abroad, and the Gordon and Betty Moore Foundation. Data are available from UNAVCO Archive collections (http://facility.unavco.org/data/). This paper is Caltech Tectonics Observatory contribution 150 and Seismolab contribution 10056. We thank T. Takasu for providing us his GPS analysis codes (GPS Tools, version 0.6.4).

Supporting Online Material

www.sciencemag.org/cgi/content/full/science.1202584/DC1
Materials and Methods
Figs. S1 to S12
Tables S1 to S4
References *31* to *54*

7 January 2011; accepted 23 March 2011
Published online 14 April 2011;
10.1126/science.1202584

Impact of Polar Ozone Depletion on Subtropical Precipitation

S. M. Kang,[1]* L. M. Polvani,[1,2] J. C. Fyfe,[3] M. Sigmond[4]

Over the past half-century, the ozone hole has caused a poleward shift of the extratropical westerly jet in the Southern Hemisphere. Here, we argue that these extratropical circulation changes, resulting from ozone depletion, have substantially contributed to subtropical precipitation changes. Specifically, we show that precipitation in the southern subtropics in austral summer increases significantly when climate models are integrated with reduced polar ozone concentrations. Furthermore, the observed patterns of subtropical precipitation change, from 1979 to 2000, are very similar to those in our model integrations, where ozone depletion alone is prescribed. In both climate models and observations, the subtropical moistening is linked to a poleward shift of the extratropical westerly jet. Our results highlight the importance of polar regions for the subtropical hydrological cycle.

The Southern Hemisphere mid- to high-latitude circulation has undergone marked climate change over the past few decades (*1*, *2*). One of the most pronounced features is a poleward displacement of the Southern Hemisphere westerly jet, which has been accompanied by a poleward shift of mid- to high-latitude precipitation associated with the extratropical storm track (*3*–*6*). Modeling and observational studies have demonstrated that in austral summer these Southern Hemisphere trends have been caused largely by stratospheric ozone depletion, with a smaller contribution from an increased atmospheric concentration of well-mixed greenhouse gases (*7*–*13*).

Although these mid- to high-latitude circulation changes have been the focus of most recent studies on the impact of the ozone hole, several hints of its impacts on the tropics can be found in the literature. For instance, a poleward shift of the southern edge of the Hadley cell has been reported (*8*, *9*, *13*), as well as a change in the latitude of the poleward edge of the subtropical dry zones (*8*). Furthermore, in both observations and climate models, poleward displacements in the latitude of the Southern Hemisphere westerly jet have been linked to the expansion of subtropical dry zones (*14*), as well as to increased rainfall over eastern Australia and southern South Africa (*15*). Because the Southern Hemisphere westerly jet in austral summer is influenced by ozone depletion, one may suspect that the ozone hole might play an important role not only in the extratropical circulation but also in the hydrological cycle at lower latitudes. Indeed, during the period of ozone depletion between 1979 and 2000, observations (Fig. 1A) exhibit a very noticeable moistening trend in austral summer in the subtropical band between 15°S and 35°S (highlighted box); this is even clearer in the zonal mean (Fig. 1B). The aim of this paper is to use state-of-the-art climate models to demonstrate that stratospheric ozone depletion over the South Pole has contributed to the observed change in subtropical precipitation.

It is well known that results pertaining to precipitation can be highly model dependent. In view of this, we use two independently developed climate models that are very different in their physical parameterizations (*16*). One is the Canadian Middle Atmosphere Model (CMAM) (*17*), and the other the National Center for Atmospheric Research (NCAR) Community Atmospheric Model (CAM3) (*18*). All experiments presented here consist of pairs of so-called "time-slice" integrations with prescribed monthly varying ozone concentrations (*16*): one "reference" integration that uses ozone fields before the formation of the ozone hole, and one "ozone hole" integration in which stratospheric ozone is severely depleted, notably over the South Pole. The climate response to ozone depletion is obtained by subtracting the climatologies of these two integrations.

Experiments were conducted with four distinct model configurations: (i) the coupled CMAM with interactive ocean and sea ice; (ii) the uncoupled CMAM with prescribed monthly mean, annually

[1]Department of Applied Physics and Applied Mathematics, Columbia University, New York, NY, USA. [2]Department of Earth and Environmental Sciences, Columbia University, New York, NY, USA. [3]Canadian Centre for Climate Modelling and Analysis, Environment Canada, Victoria, British Columbia, Canada. [4]Department of Physics, University of Toronto, Toronto, Ontario, Canada.

*To whom correspondence should be addressed. E-mail: smk2182@columbia.edu

varying sea surface temperatures and sea ice concentrations taken from the coupled reference integration; (iii) the uncoupled CAM3 with observed sea surface temperatures and sea ice concentrations averaged over the pre–ozone hole period (*19*); and (iv) the uncoupled CAM3, but with ozone changes confined to latitudes southward of 40°S. These substantially different configurations allow us to evaluate whether the effect of ozone depletion on subtropical precipitation is fundamentally dependent on atmosphere-ocean interactions and physical model parameterizations. Experiment (iv) is crucial in determining whether polar or subtropical ozone depletion is the key player.

The impact of the ozone hole on precipitation is clearly evident in Fig. 2, where the response due to the ozone depletion is shown for each of the four experiments, in austral summer. First, note the considerable similarity among the four experiments: This confirms the robustness of our result. As reported in previous studies (*8*, *9*, *20*), there is decreased precipitation around 45°S and increased precipitation around 60°S, associated with a poleward-shifted storm track. The focus of this paper, however, is the ozone-hole–induced moistening (green patches) in the highlighted region of the subtropics, most pronounced over the southwestern Indian Ocean, eastern Australia, and southern flank of the Southern Pacific Convergence Zone, where the climatological mean precipitation is large. In these regions, our models show that the precipitation response to the ozone hole is unaffected by atmosphere-ocean interactions (contrast Fig. 2, A and B), is largely independent of the physical parameterizations of any one model or the sea surface temperatures used (contrast Fig. 2, B and C), and originates almost entirely from ozone depletion in the southern polar regions (contrast Fig. 2, C and D).

Second, contrast the modeled ozone-hole–induced precipitation changes in Fig. 2 with the observed changes in Fig. 1A. Although the observed changes in precipitation at individual tropical locations are generally larger in magnitude than in our experiments, there is good agreement in the overall patterns. Spatial agreement is strikingly evident in the zonal mean profiles (contrast Fig. 1B with Fig. 3A), all of which show a very clear tripole pattern consisting of high-latitude moistening, mid-latitude drying, and subtropical moistening. Between 15°S and 35°S, these precipitation changes correspond to about a 10% increase relative to the climatology, with larger increases in some subregions. We emphasize that the increased precipitation in the highlighted 15°S to 35°S region is statistically significant in observations and in all four experiments. As an example, in Fig. 3A we show the 95% confidence interval (red shading) for one of the CAM3 experiments; this interval is computed using the Student's *t* test, assuming independent and randomly distributed residuals. Furthermore, as shown in Fig. 3B, these subtropical precipitation changes are largely associated with changes in moisture convergence by the time-mean zonal-mean flow (with smaller contributions from transient and stationary eddies), rather than to local changes in atmospheric humidity (fig. S1). In Fig. 3C, we further show, from a regression of precipitation on jet latitude, that these subtropical precipitation changes are highly congruent with changes in the latitude of the extratropical westerly jet (*16*). Moreover, as in our model experiments, the observed moistening in the 15°S to 35°S region is also linked to a poleward jet shift (Fig. 1B), which itself is substantially the consequence of polar ozone depletion (*1*, *3*, *8*).

We next elucidate the mechanism causing these subtropical precipitation changes. The zonal-mean changes due to ozone depletion in temperature, zonal wind, and mean meridional mass stream function are shown in Fig. 4. For brevity, we show only results for the coupled CMAM (top row) and the uncoupled CAM3 with high-latitude ozone depletion only (bottom row); the other two experiments are very similar. Ozone depletion causes severe cooling in the lower stratosphere (Fig. 4, A and D), which in turn is accompanied by a lifting of the polar tropopause and a concomitant poleward shift of the extratropical westerly jet (Fig. 4, B and E). This sequence of high-to-mid latitude cause and effect is well documented (*11*).

The poleward shift of the extratropical westerly jet is reflected in the convergence and divergence of transient eddy momentum fluxes on its poleward and equatorward flanks, respectively (fig. S3). This poleward jet shift is also associated with a poleward shift of the subtropical edge of the Hadley cell (seen as the blue/red shading centered around 25°S in Fig. 4, C and F). Accompanying the poleward shift of this edge, an anomalous upper-level mass divergence between 15°S and 35°S is found, and it is largely associated with changes in the transient eddy momentum fluxes (fig. S4). This upper-level divergence drives anomalous rising motion in the subtropics (arrows around 25°S in Fig. 4, C and F), inducing low-level moisture convergence and hence increased precipitation there. In short, our experiments expose a sequence of high-to-low latitude causes and effects linking stratospheric polar ozone depletion all the way to subtropical moistening. This mechanism does not, however, explain the longitudinal variations in the precipitation response seen in Fig. 2. These will need to be addressed in a future study.

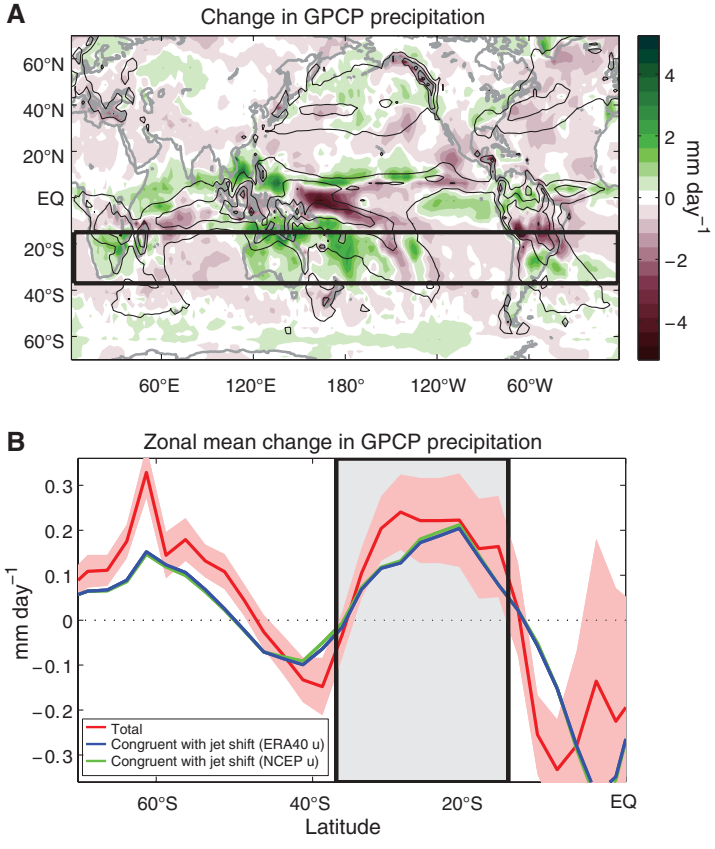

Fig. 1. Observed precipitation change between 1979 and 2000 in austral summer (December to February mean). (**A**) Precipitation change based on Global Precipitation Climatology Project (GPCP) data (*25*), calculated from the linear trend multiplied by 22 years. Black contours show the mean precipitation for 1979 to 1983, with contour interval of 3 mm day^{-1}. (**B**) Zonal-mean precipitation change (red line) with 95% confidence interval (red shading), and the change congruent (*16*) with a change in the latitude of the westerly jet obtained from ERA40 (*26*) (blue line) and National Centers for Environmental Prediction (NCEP)/NCAR (*27*) (green line) reanalysis data.

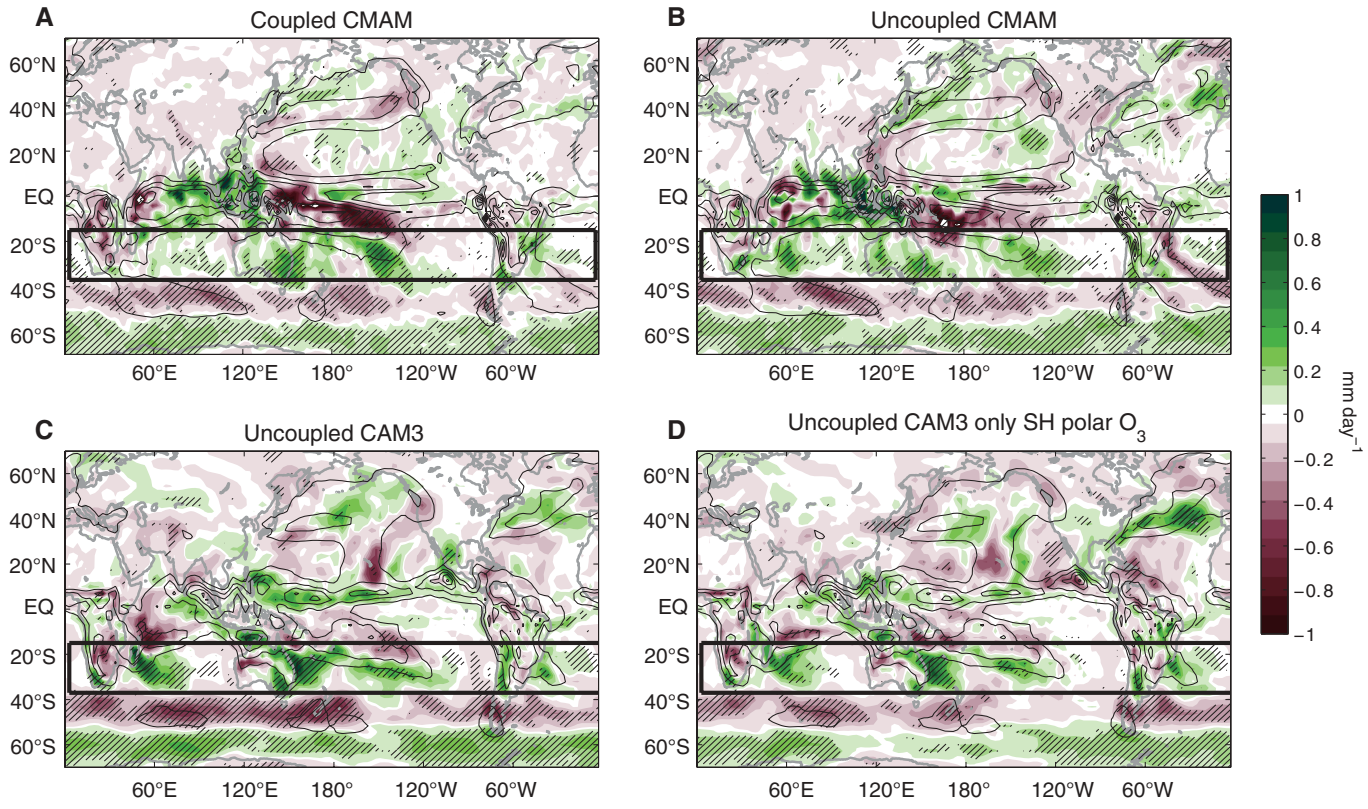

Fig. 2. Modeled precipitation change caused by the ozone hole. Shading shows austral summer precipitation difference (in mm day^{-1}) induced by ozone depletion in (**A**) the coupled CMAM, (**B**) the uncoupled CMAM, (**C**) the uncoupled CAM3, and (**D**) the uncoupled CAM3 with ozone depletion confined to 40°S to 90°S. Black contours show the mean precipitation in the respective reference integrations, with contour interval of 3 mm day^{-1}. Locations where the response is significant at the 95% confidence level are hatched.

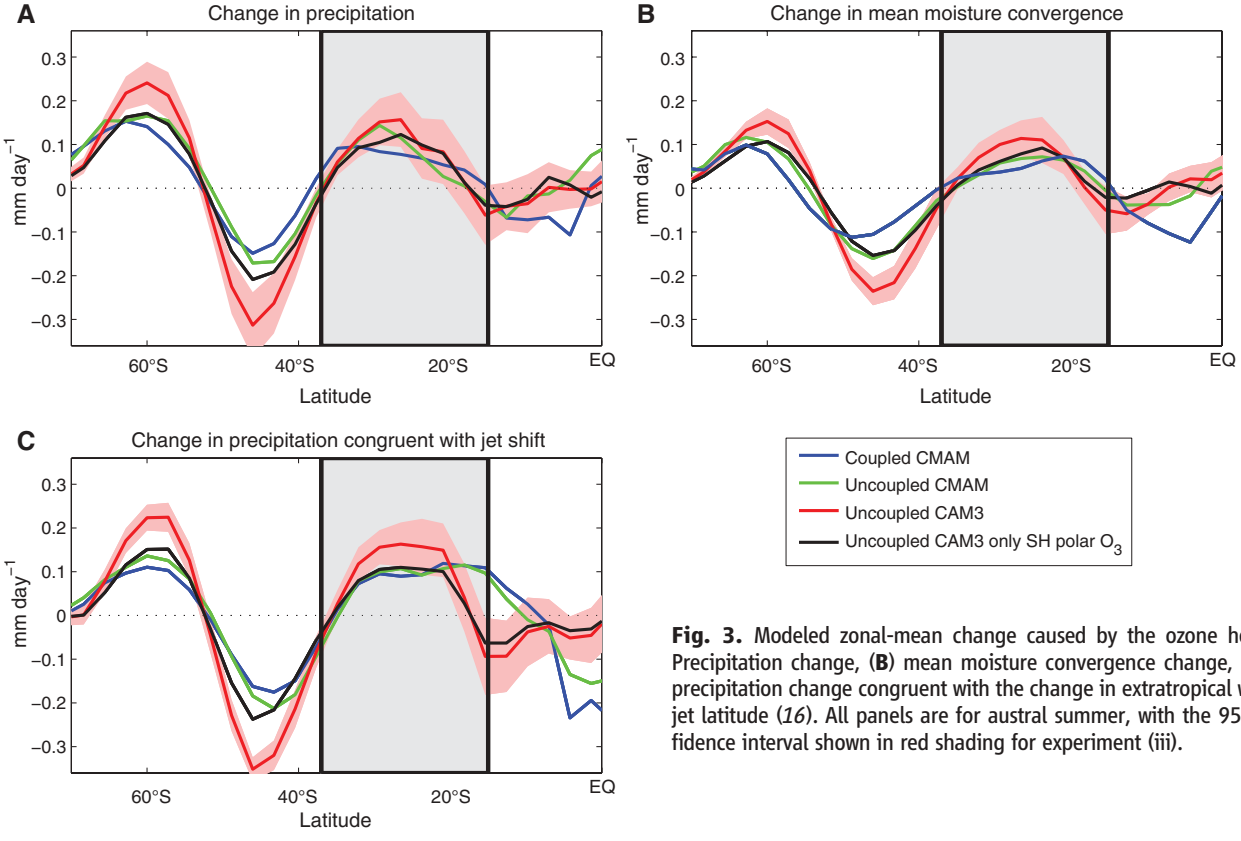

Fig. 3. Modeled zonal-mean change caused by the ozone hole. (**A**) Precipitation change, (**B**) mean moisture convergence change, and (**C**) precipitation change congruent with the change in extratropical westerly jet latitude (*16*). All panels are for austral summer, with the 95% confidence interval shown in red shading for experiment (iii).

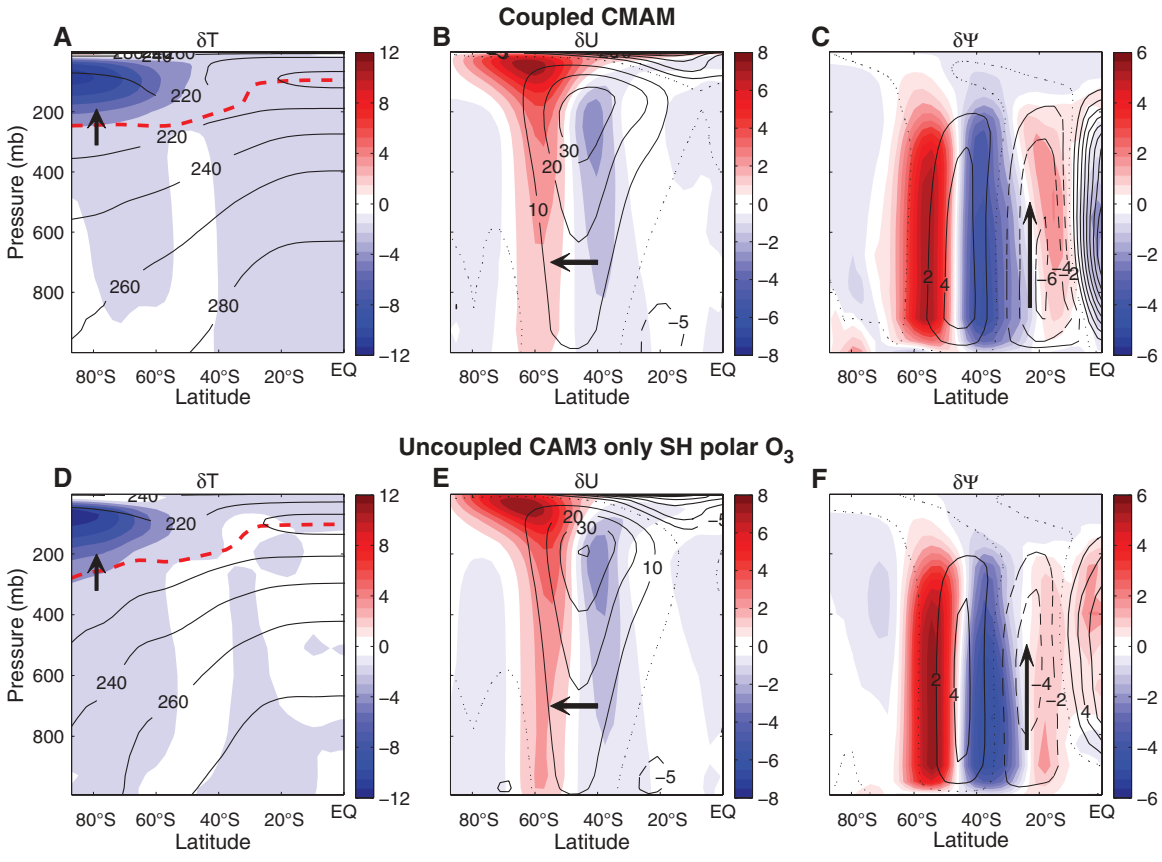

Fig. 4. Mechanism linking the ozone hole to subtropical precipitation change. Shading is the zonal-mean response in austral summer of (**A** and **D**) temperature (in K), (**B** and **E**) zonal wind (in m s^{-1}), and (**C** and **F**) mean meridional mass stream function (in 10^9 kg s^{-1}). Black solid contours in (A) and (D) are the mean temperatures, and red dashed lines indicate the tropopause height in the reference integrations; the arrows illustrate the lifting of tropopause in response to ozone depletion. Black solid (dashed) contours in (B) and (E) are the mean westerlies (easterlies) in the reference integrations, and the arrows illustrate the direction of extratropical westerly jet shift. Black solid (dashed) contours in (C) and (F) are the clockwise (counter-clockwise) mean meridional circulation in the reference integrations, and the arrows illustrate the direction of anomalous vertical motion induced by ozone depletion. (Top row) The coupled CMAM integrations [experiment (i)]. (Bottom row) The uncoupled CAM3 integrations with ozone depletion confined to 40°S to 90°S [experiment (iv)].

We recognize that other radiative agents, such as anthropogenic greenhouse gases or sulfate aerosols, may also have played a role in changing precipitation at low latitudes. This has been confirmed in a recent study (*21*), where observed 20th-century changes in annual-mean and zonal-mean land precipitation were linked to anthropogenic greenhouse gas and sulfate aerosol forcings. That study noted, in addition, that models tend to underestimate the magnitude of the observed changes, especially at low latitudes. Similar discrepancies in amplitude were reported with precipitation responses to volcanic eruption (*22*). In our study, we find that both the pattern and the magnitude of zonal mean precipitation changes in austral summer agree well between observations and climate models forced with polar ozone depletion alone. This, therefore, strongly implicates polar stratospheric ozone depletion as being an important driver of the southern subtropical moistening observed in austral summer over the latter part of the 20th century.

In a broader perspective, the impact of polar ozone depletion on tropical precipitation discussed here provides one more instance of how changes in high latitudes are able to affect the tropics. Other well-known examples are the effect of Arctic sea ice (*23*) and of the Atlantic thermohaline circulation (*24*) on the position of the Intertropical Convergence Zone. Hence, we need to deepen our understanding of polar to tropical linkages to accurately predict tropical precipitation.

References and Notes

1. D. W. J. Thompson, S. Solomon, *Science* **296**, 895 (2002).
2. K. Trenberth *et al*. *Climate Change 2007: The Physical Science Basis. Contribution of Working Group I to the Fourth Assessment Report of the Intergovernmental Panel on Climate Change* (Cambridge Univ. Press, Cambridge, 2007).
3. R. L. Fogt *et al*., *J. Clim.* **22**, 5346 (2009).
4. G. J. Marshall, *J. Clim.* **16**, 4134 (2003).
5. D. W. J. Thompson, J. M. Wallace, G. C. Hegerl, *J. Clim.* **13**, 1018 (2000).
6. C. Archer, K. Caldeira, *Geophys. Res. Lett.* **35**, L08803 (2008).
7. J. M. Arblaster, G. A. Meehl, *J. Clim.* **19**, 2896 (2006).
8. L. M. Polvani, D. W. Waugh, G. J. P. Correa, S.-W. Son, *J. Clim.* **24**, 795 (2011).
9. S.-W. Son, N. F. Tandon, L. M. Polvani, D. W. Waugh, *Geophys. Res. Lett.* **36**, L15705 (2009).
10. N. P. Gillett, D. W. J. Thompson, *Science* **302**, 273 (2003).
11. S. W. Son *et al*., *Science* **320**, 1486 (2008).
12. J. Perlwitz, S. Pawson, R. L. Fogt, J. E. Nielsen, W. D. Neff, *Geophys. Res. Lett.* **35**, L08714 (2008).
13. S. W. Son *et al*., *J. Geophys. Res.* **115**, D00M07 (2010).
14. M. Previdi, B. G. Liepert, *Geophys. Res. Lett.* **34**, L22701 (2007).
15. A. Sen Gupta, M. H. England, *J. Clim.* **19**, 4457 (2006).
16. Materials and methods are available as supporting material on *Science* Online.
17. J. F. Scinocca, N. A. McFarlane, M. Lazare, J. Li, D. Plummer, *Atmos. Chem. Phys.* **8**, 7055 (2008).
18. W. D. Collins *et al*., *J. Clim.* **19**, 2122 (2006).
19. N. A. Rayner *et al*., *J. Geophys. Res.* **108**, (D14), 4407 (2003).
20. M. Sigmond, J. C. Fyfe, J. F. Scinocca, *Geophys. Res. Lett.* **37**, L12706 (2010).
21. X. Zhang *et al*., *Nature* **448**, 461 (2007).
22. N. P. Gillett, A. J. Weaver, F. W. Zwiers, M. F. Wehner, *Geophys. Res. Lett.* **31**, L12217 (2004).
23. J. C. H. Chiang, C. M. Bitz, *Clim. Dyn.* **25**, 477 (2005).
24. R. Zhang, T. L. Delworth, *J. Clim.* **18**, 1853 (2005).
25. R. F. Adler *et al*., *J. Hydrometeorol.* **4**, 1147 (2003).
26. S. M. Uppala *et al*., *Q. J. R. Meteorol. Soc.* **131**, 2961 (2005).
27. R. Kistler *et al*., *Bull. Am. Meteorol. Soc.* **82**, 247 (2001).

Acknowledgments: We are grateful to I. Held, D. Frierson, I.-S. Kang, A. Sobel, G. Flato, B. Merryfield, and N. Gillett for comments on early versions of this work, and to G. Correa for helping with the CAM3 model integrations. L.M.P. and S.M.K. are supported in part by a grant from the U.S. National Science Foundation to Columbia University. M.S. is a member of the Canadian Stratospheric Processes and their Role in Climate (CSPARC) network and gratefully acknowledges the support of the Canadian Foundation for Climate Atmospheric Sciences.

Supporting Online Material

www.sciencemag.org/cgi/content/full/science.1202131/DC1
Materials and Methods
SOM Text
Figs. S1 to S4
References

23 December 2010; accepted 8 April 2011
Published online 21 April 2011;
10.1126/science.1202131

Fossil Evidence on Origin of the Mammalian Brain

Timothy B. Rowe,[1]* Thomas E. Macrini,[2] Zhe-Xi Luo[3]

Many hypotheses have been postulated regarding the early evolution of the mammalian brain. Here, x-ray tomography of the Early Jurassic mammaliaforms *Morganucodon* and *Hadrocodium* sheds light on this history. We found that relative brain size expanded to mammalian levels, with enlarged olfactory bulbs, neocortex, olfactory (pyriform) cortex, and cerebellum, in two evolutionary pulses. The initial pulse was probably driven by increased resolution in olfaction and improvements in tactile sensitivity (from body hair) and neuromuscular coordination. A second pulse of olfactory enhancement then enlarged the brain to mammalian levels. The origin of crown Mammalia saw a third pulse of olfactory enhancement, with ossified ethmoid turbinals supporting an expansive olfactory epithelium in the nasal cavity, allowing full expression of a huge odorant receptor genome.

Brain size and sensory faculties diversified dramatically as mammals evolved to fill an immense variety of ecological niches, and much attention has been devoted to reconstructing the organization and origin of the ancestral mammalian brain. Among living taxa, mammals have the largest brains relative to body size and are unique in possessing the neocortex (isocortex) (Fig. 1). Accordingly, research has focused on origin of the neocortex (*1*–*5*) and evolutionary increases in brain size [measured as a function of body mass, or "encephalization quotient" (EQ) (*6*, *7*)].

Mammalia arose in or before the Early Jurassic [~200 million yeas ago (Ma)] (*8*–*11*). The oldest fossils are mostly tiny isolated jaws and teeth, and until now the rare skulls offered little detail on early brain evolution because internal access required destructive sampling. Comparative and developmental anatomy of living mammals has been our chief source of information. Such studies postulated numerous drivers for increased encephalization and origin of the neocortex, including innovations in hearing, feeding, taste, olfaction, miniaturization, parental care, endothermy, elevated metabolism, and nocturnality (*1*–*7*). Although deeply informative, few details have emerged on timing or sequences of historical events.

Here, we ask what sequence of evolutionary events culminated in the origin of the mammalian brain, and how was the brain in the ancestral mammal different from its closest extinct relatives? For this study, we used high-resolution x-ray computed tomography (*12*) to nondestructively scan tiny fossil skulls of two basal mammaliaforms from the Early Jurassic of China (Fig. 1), *Morganucodon oehleri* (*9*–*11*) and *Hadrocodium wui* (*13*). As a test of postulated neurobiological drivers, we digitally extracted casts of their endocranial cavities (endocasts), which closely approximate the size and shape of the brain, and compared them with endocasts of seven more primitive fossils and 27 crown mammals (*14*). The scans yielded digital measurements and anatomical details (Fig. 2) that offer a nuanced sequence of historical events in early brain evolution.

The mammalian lineage (Synapsida) diverged from other tetrapods in the Carboniferous (~300 Ma) (*15*). The braincase initially lacked fully ossified walls and floor; hence, little is known of early brain form, and EQ estimates are imprecise. The first detailed view of the pre-mammalian brain is seen in basal Cynodontia, a clade originating in the Late Permian (~260 Ma) that includes living mammals and their proximate extinct relatives. The cynodont endocranial cavity is more fully enclosed, with EQs initially measuring from ~0.16 to 0.23 (Fig. 3) (*16*–*20*). The olfactory bulbs were small (*12*), and the nose lacked ossified turbinals. The forebrain was narrow and featureless, the midbrain exposed dorsally, and the pineal eye persisted. The cerebellum was wider than the forebrain, and the spinal cord was narrow (*12*). The middle ear ossicles remained massive and attached to the lower jaw, and the cochlea occupied only a shallow bony recess (*16*, *21*, *22*). Compared with their living descendants, early cynodonts possessed low-resolution olfaction, poor vision, insensitive hearing, coarse tactile sensitivity, and unrefined motor coordination. Sensory-motor integration commanded little cerebral territory.

Morganucodon is the basal-most member of Mammaliaformes, a clade including mammals and their closest extinct relatives (*9*–*11*, *13*, *15*). It records a first major pulse in encephalization with an EQ of ~0.32, which is nearly 50% larger than in basal cynodonts (Fig. 3). The olfactory bulb and olfactory (pyriform) cortex are by far the regions of greatest expansion (Fig. 2). A deep annular fissure encircles the olfactory tract, marking a distinctive external division of the mammalian brain between the olfactory bulb and cortex. The cortex is inflated and wider than the cerebellum, covering the midbrain and the pineal

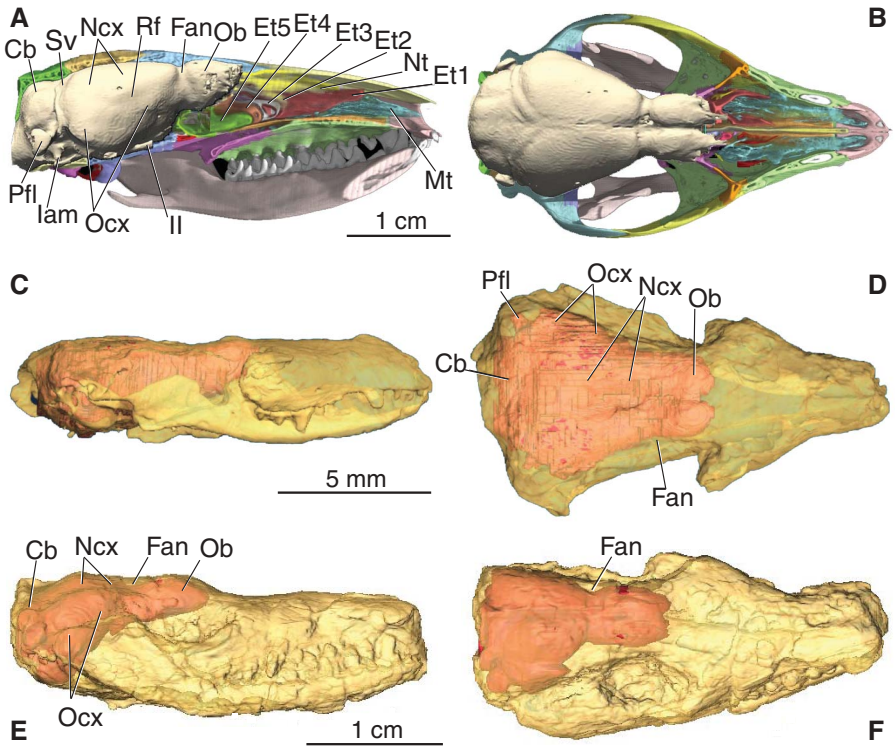

Fig. 1. HRXCT images of (**A** and **B**) *Monodelphis*, (**C** and **D**) *Hadrocodium*, and (**E** and **F**) *Morganucodon*, in lateral and dorsal views, with bone cutaway [(A) and (B)] and rendered translucent [(C) to (F)] to show endocasts. Cb, cerebellum; Et, endoturbinals 1 to 5; Fan, annular fissure; Iam, internal acoustic meatus; II, optic nerve; Mt, maxilloturbinal; Ncx, neocortex; Nt, nasoturbinal; Ob, olfactory bulb; Ocx, olfactory (pyriform) cortex; Pfl, paraflocculus; Rf, rhinal fissure; and Sv, venous sinus.

[1]Jackson School of Geosciences, University of Texas, C1100, Austin, TX 78712, USA. [2]Department of Biological Sciences, St. Mary's University, San Antonio, TX 78228, USA. [3]Section of Vertebrate Paleontology, Carnegie Museum of Natural History, Pittsburgh, PA 15213, USA.

*To whom correspondence should be addressed. E-mail: rowe@mail.utexas.edu

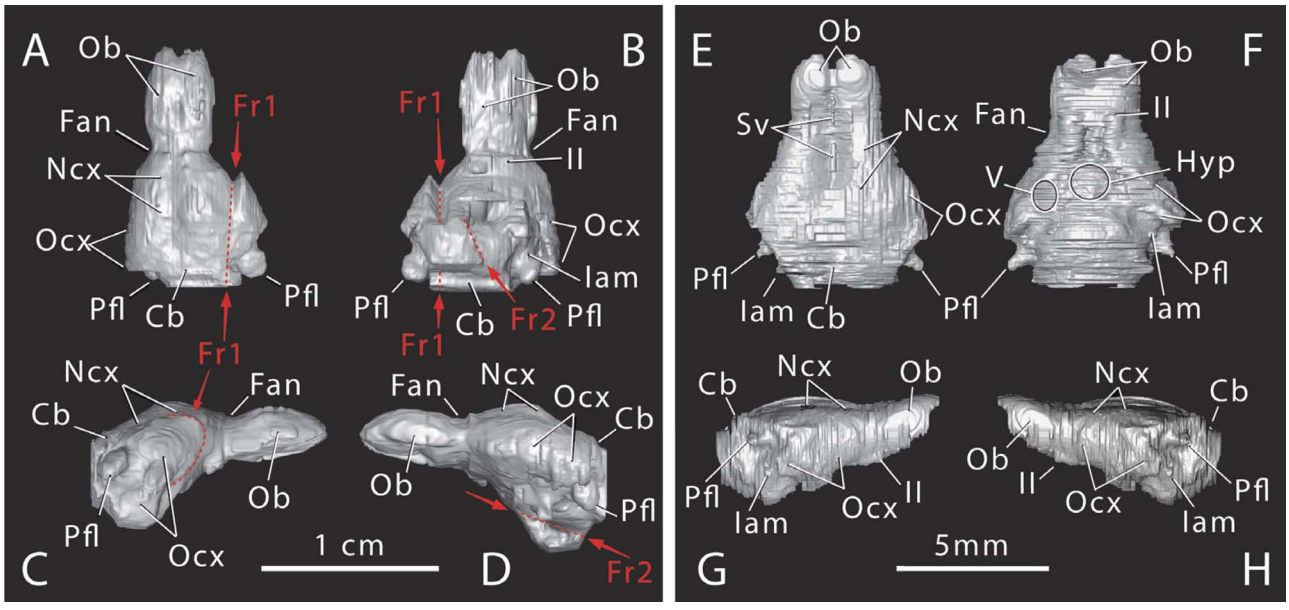

Fig. 2. Digital endocasts of (**A** to **D**) *Morganucodon* and (**E** to **H**) *Hadrocodium* in dorsal [(A) and (E)], ventral [(B) and (F)], right lateral [(C) and (G)] and left lateral [(D) and (H)] views. Cb, cerebellum; Fr1 and Fr2, postmortem fractures displacing parts of endocast; Fan, annular fissure; Hyp, hypophysis; Iam, internal acoustic meatus; II, optic nerve; Ncx, neocortex; Ob, olfactory bulb; Ocx, olfactory (pyriform) cortex; Pfl, paraflocculus; Sss, superior sagittal sinus; and V, trigeminal nerve.

stalk. The cerebellum is also enlarged, implying expansion of the basal nuclei, thalamus, and medulla, and the spinal cord is thicker. The brain now resembles living mammals more than basal cynodonts in shape and proportions.

Elaboration of the neocortex probably also contributed to encephalization in basal mammaliformes. Dominating the neocortex is a single primary somatosensory field (*1*) that maps sensation from mechanoreceptors in the skin, hair follicles, muscle spindles, and joint receptors (Fig. 4A). Its conscious component involves tactile exploration and body surface monitoring (*3*). Peripheral somatosensory input is mapped to the neocortex as an "animunculus" (Fig. 4A). A parallel neocortical motor map contains pyramidal neurons that give rise to the pyramidal tract (Fig. 4B), which projects via the brainstem into the spinal column to program and execute skilled movements requiring precise control of distal musculature (*3*, *23*–*25*).

In living mammals, the boundary between neocortex and olfactory cortex is marked by the rhinal fissure. This structure is not visible on the endocast of *Morganucodon* or *Hadrocodium* and is faint (Fig. 1A) or invisible on endocasts in most small living mammals, although observable on the brain itself (*6*, *22*, *26*). However, another basal mammaliaform, *Castorocauda lutrasimilis* (*27*), preserves integumentary evidence suggesting that the neocortex was well developed. *Castorocauda* is a Middle Jurassic (~165 Ma) docodont (*27*), a clade first appearing in the Late Triassic and closely related to *Morganucodon* (*9*–*11*). *Castorocauda* is known from a flattened skeleton that preserves the oldest evidence of a thick pelt that covered the body. Both guard hairs and an underfur of vellus hairs left carbonized residues and physical impressions as thin grooves and traces.

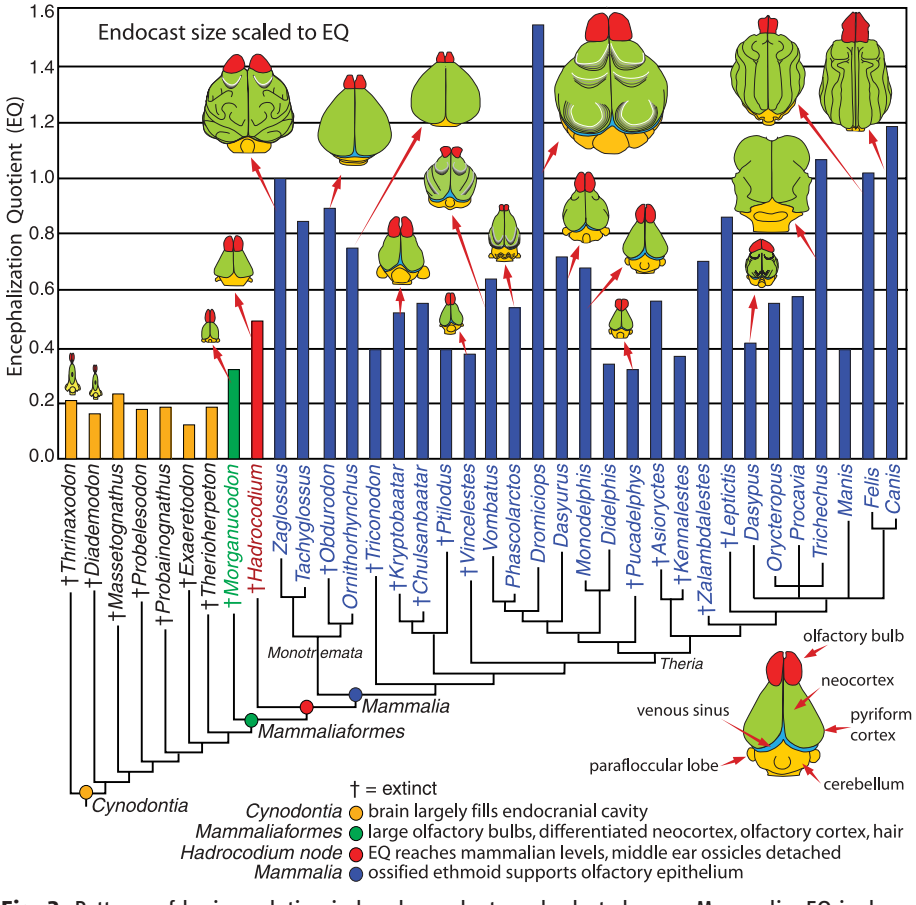

Fig. 3. Patterns of brain evolution in basal cynodonts and selected crown Mammalia. EQ is shown in bar chart; selected endocasts are scaled to EQ (*12*).

Body hair develops as migrating neural crest cells induce patterns of tiny placodes that mature into hair follicles equipped with mechanoreceptors (*25*). These include lanceolate endings (velocity detectors excited by hair deflection), Ruffini receptors (tension receptors activated as hair is bent), and Merkel cells (slowly adapting sensors) (Fig. 4C). In ontogeny, hair is first sensory, and

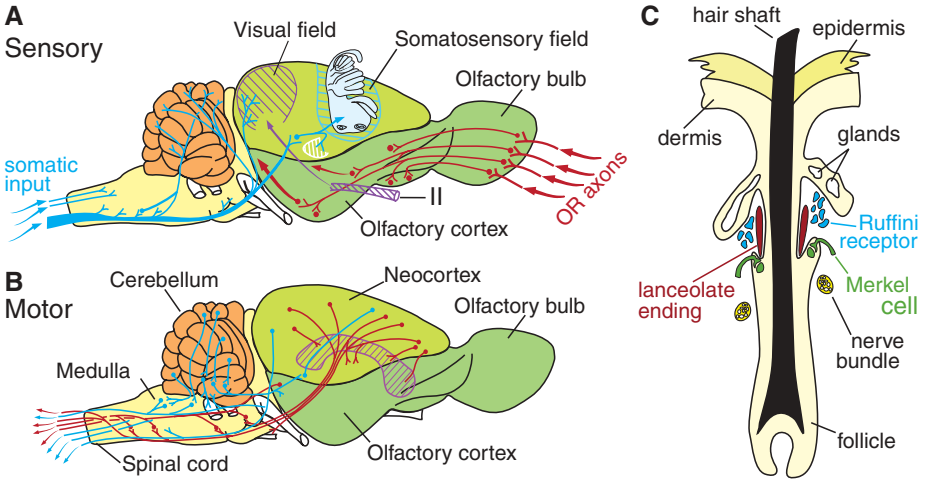

Fig. 4. Circuitry schematic of modern opossum (*Didelphis*) brain showing (**A**) sensory input and (**B**) motor outputs [modified after (*3*)]. (**C**) Schematic innervation of an opossum guard hair [modified after (*28*)].

only later does it insulate, as underfur thickens and thermoregulation matures (*28*). Tactile signals are transmitted to the primary somatosensory field, where their morphogenic action induces formation of the sensory and motor maps (*23*–*25*). The pelt in *Castorocauda*, in addition to the size and shape of the endocast in *Morganucodon*, implies that the neocortex differentiated early in mammaliaform history.

Increased sensitivity in olfaction, and improved tactile resolution and motor coordination account for much of the first pulse in pre-mammalian encephalization. Enhanced high-frequency hearing is also implicated. The middle ear ossicles are highly reduced (but still attached to the lower jaw), and the cochlea is now prolonged into a short, curved tube (9). Comparative neuroanatomy (*1*) suggests that neocortical expansion also supported an enhanced visual field (Fig. 4A), but bony correlates are lacking in these fossils.

Hadrocodium is the closest known extinct relative of crown Mammalia (*9*, *11*, *13*). It marks a second encephalization pulse, with an EQ of ~0.5 that lies within the mammalian range (Fig. 3). Expanded olfactory bulbs and olfactory cortex account for most of the increase. The middle ear ossicles are now detached from the jaw and suspended beneath the cranium, a condition otherwise confined to crown Mammalia (*10*, *11*, *13*, *15*). Growth of the olfactory cortex in early ontogeny of the living didelphid *Monodelphis* separates the auditory ossicles from their primary (and ancestral) attachment to the mandible (*20*, *21*) to develop the same anatomical relations seen in *Hadrocodium*. This famous transformation evidently had little effect on hearing performance because the size and complexity of the cochlea is no different than in *Morganucodon* (*9*, *13*, *22*, *29*). The cerebellum in *Hadrocodium* bulges backward, bending the occipital plate into an arch that transmitted a thick spinal cord, implying enhanced motor-sensory integration.

The origin of crown Mammalia marks a third pulse of olfactory elaboration, as the ethmoid turbinals ossify to form both the cribriform plate and a rigid scaffold in the nasal cavity for epithelium containing the odorant receptor (OR) neurons (*10*, *15*). Activation of OR genes induces olfactory epithelial growth, in turn inducing turbinal growth and ossification (*30*). Ossified turbinals afford a 10-fold (or more) increase in olfactory epithelial surface within the nasal cavity. The maxilloturbinal also ossifies at this same time, affecting a sevenfold (or more) increase in respiratory epithelial surface (*30*). It functions in water balance, and its appearance in Mammalia ancestrally may reflect elevated metabolism.

Our data suggest that in basal mammaliaforms, a first pulse of encephalization was driven by increasing resolution in olfaction and tactile sensitivity and enhanced neuromuscular coordination. With a pelt, basal mammaliaforms were probably also endothermic, and the ontogeny of thermoregulation implies parental care (*28*). Endothermy may have been a consequence of encephalization because a large brain is metabolically expensive to maintain (*5*). However, metabolism is under hormonal regulation that does not command large cerebral regions, and thus did not itself drive encephalization (*3*). *Hadrocodium* records a second pulse of encephalization, probably also driven principally by olfaction.

The ancestral species of Mammalia amplified these inheritances in a third pulse of olfactory elaboration because its ossified ethmoid complex allowed full expression of its huge OR genome, which is an order of magnitude larger than in most other vertebrates (*31*). Only much later did acute visual and auditory systems evolve among mammals (*29*). In some descendents, the olfactory system was further elaborated, whereas in others it was reduced and supplanted by alternate sensory modalities, such as electroreception and sonar. But at its start, the brain in the ancestral mammal differed from even its closest extinct relatives specifically in its degree of high-resolution olfaction, as it exploited a world of information dominated to an unprecedented degree by odors and scents.

References and Notes

1. J. H. Kaas, in *Evolutionary Neuroscience*, J. H. Kaas, Ed. (Academic Press, New York, 2009), pp. 523–544.
2. F. Aboitiz, J. Montiel, *Adv. Anat. Embryol. Cel.* **193**, 1 (2007).
3. R. Nieuwenhuys, H. J. Ten Donkelaar, C. Nicholson, Eds., *The Central Nervous System of Vertebrates* (Springer-Verlag, Berlin, 1998).
4. R. G. Northcutt, J. H. Kaas, *Trends Neurosci.* **18**, 373 (1995).
5. J. Allman, *Neurosciences* **2**, 257 (1990).
6. H. J. Jerison, *Evolution of the Brain and Intelligence* (Academic Press, New York, 1973).
7. H. J. Jerison, in *Evolutionary Neuroscience*, J. H. Kaas, Ed. (Academic Press, New York, 2009), pp. 497–508.
8. T. B. Rowe, T. H. Rich, P. Vickers-Rich, M. Springer, M. O. Woodburne, *Proc. Natl. Acad. Sci. U.S.A.* **105**, 1238 (2008).
9. Z. Kielan-Jaworowska, R. L. Cifelli, Z.-X. Luo, *Mammals from the Age of Dinosaurs: Origin, Evolution, and Structure* (Columbia Univ. Press, New York, 2004).
10. T. B. Rowe, *J. Vertebr. Paleontol.* **8**, 241 (1988).
11. Z.-X. Luo, *Nature* **450**, 1011 (2007).
12. Materials and methods are available as supporting material on *Science* Online.
13. Z.-X. Luo, A. W. Crompton, A.-L. Sun, *Science* **292**, 1535 (2001).
14. T. E. Macrini, dissertation, University of Texas, Austin, (2006).
15. J. A. Gauthier, A. G. Kluge, T. Rowe, *Cladistics* **4**, 105 (1988).
16. T. B. Rowe, W. Carlson, W. Bottorff, *Thrinaxodon: Digital Atlas of the Skull.* (Univ. of Texas Press, Austin, TX, CD-ROM, ed. 2, 1995).
17. J. A. Hopson, in *Biology of the Reptilia*, C. Gans, R. G. Northcutt, P. Ulinski, Eds. (Academic Press, New York, 1979), pp. 39–46.
18. J. C. Quiroga, *J. Hirnforsch.* **21**, 299 (1980).
19. J. C. Quiroga, *J. Hirnforsch.* **25**, 285 (1984).
20. T. S. Kemp, *J. Vertebr. Paleontol.* **29**, 1188 (2009).
21. T. B. Rowe, *Science* **273**, 651 (1996).
22. T. B. Rowe, *Cal. Acad. Sci. Memoir* **20**, 71 (1996).
23. K. C. Catania, in *Evolutionary Neuroscience*, J. H. Kaas, Ed. (Academic Press, New York, 2009), pp. 697–714.
24. L. Krubitzer, D. L. Hunt, in *Evolutionary Neuroscience*, J. H. Kaas, Ed. (Academic Press, New York, 2009), pp. 545–568.
25. J. Zelená, *Nerves and Mechanoreceptors: the Role of Innervation in the Development and Maintenance of Mammalian Mechanoreceptors* (Chapman & Hall, London, 1994).
26. T. E. Macrini, T. B. Rowe, J. L. VandeBerg, *J. Morphol.* **268**, 844 (2007).
27. Q. Ji, Z.-X. Luo, C.-X. Yuan, A. R. Tabrum, *Science* **311**, 1123 (2006).
28. A. J. Hulbert, in *The Developing Marsupial. Models for Biomedical Research*, C. H. Tyndale-Biscoe, P. A. Janssens, Eds. (Springer-Verlag, Berlin, 1988), pp. 148–161.
29. Z.-X. Luo, I. Ruf, J. A. Schultz, T. Martin, *Proc. Biol. Sci.* **278**, 28 (2011).
30. T. B. Rowe, T. P. Eiting, T. E. Macrini, R. A. Ketcham, *J. Mamm. Evol.* **12**, 303 (2005).
31. Y. Niimura, *Genome Biol. Evol.* **1**, 34 (2010).

Acknowledgments: This research was funded by NSF DEB 0309369 (T.E.M. and T.R.), NSF EAR-0948842 (T.R.), AToL 0531767 (T.R.), the University of Texas Jackson School of Geosciences (T.R. and T.E.M.), and funded by NSF DEB 0316558 and EF0129959, NSF of China, Humboldt Foundation (Germany), and NGS to Z.-X.L. Endocasts and computed tomography imagery are online at www.DigiMorph.org.

Supporting Online Material

www.sciencemag.org/cgi/content/full/332/6032/955/DC1
Materials and Methods
Figs. S1 to S4
Tables S1 to S3
References

20 January 2011; accepted 4 April 2011
10.1126/science.1203117

Industrial Melanism in British Peppered Moths Has a Singular and Recent Mutational Origin

Arjen E. van't Hof,[1] Nicola Edmonds,[1] Martina Dalíková,[2] František Marec,[2] Ilik J. Saccheri[1]*

The rapid spread of a novel black form (known as *carbonaria*) of the peppered moth *Biston betularia* in 19th-century Britain is a textbook example of how an altered environment may produce morphological adaptation through genetic change. However, the underlying genetic basis of the difference between the wild-type (light-colored) and *carbonaria* forms has remained unknown. We have genetically mapped the *carbonaria* morph to a 200-kilobase region orthologous to a segment of silkworm chromosome 17 and show that there is only one core sequence variant associated with the *carbonaria* morph, carrying a signature of recent strong selection. The *carbonaria* region coincides with major wing-patterning loci in other lepidopteran systems, suggesting the existence of basal color-patterning regulators in this region.

Industrial melanism in the peppered moth (*Biston betularia*) is one of the most widely recognized examples of contemporary evolutionary change (*1*–*3*), but beyond the fact that it is a single-locus dominant allele (*4*), the genetic basis and developmental mechanism distinguishing the black (*carbonaria*) form from the wild-type [typical (*typica*)] form are unknown. This knowledge gap undermines our understanding of a comprehensive example of adaptation encompassing the mutational source of a morphological novelty, its mode of action through development, the agent of selection, and the documented spread of the trait in a natural population. Because melanism is widespread in Lepidoptera, and industrial melanism has arisen in many species (*1*, *5*), reconstructing the genetic origins of melanic forms is likely to yield insight into the role of developmental constraint and the importance of "hotspot genes" to morphological evolution (*6*). Moreover, it is uncertain whether peppered moth industrial melanism in Britain was due to a single recent mutation or to different mutations of varying age. Nineteenth-century records suggest that the spread of the *carbonaria* morph across Britain emanated from a single point source in greater Manchester, but do not establish a single mutational origin (*1*), particularly in view of anectodal evidence for recurrent mutation to melanic forms in *B. betularia*.

In vertebrates, melanism is often associated with mutations within the *melanocortin-1-receptor* gene (*7*). In insects, although melanin biosynthesis is well understood in terms of enzyme-mediated substrate transformations (*8*), the mechanism of regulation is far more diverse, most commonly involving modification of cis-regulatory elements of key genes in the melanization pathway, such as *ebony*, *tan*, and *yellow* (*9*). The extent of this regulatory diversity is underscored by our recent finding that in *B. betularia*, the *carbonaria* morph is not associated with molecular variation within any of the canonical melanization pathway genes (*10*). This suggests that the *carbonaria* phenotype is controlled by an undescribed developmental switch with major phenotypic effects.

The failure of a candidate gene approach to identify the genetic basis for melanism led to the construction of a linkage map to identify the chromosomal region containing the locus controlling the *carbonaria*-typical polymorphism, and to examine the molecular evidence for the hypothesis that the *carbonaria* morph in the United Kingdom is descended from a single mutation of recent origin. The *carbonaria* morph mapped to a linkage group (LG) that is orthologous to *Bombyx mori* chromosome 17 in the main mapping family and in a second, independent, *carbonaria*-typical cross, added to construct a denser combined map for LG17 (Fig. 1) (*11*). The identity of the "*carbonaria* chromosome" was confirmed with the use of fluorescence in situ hybridization (FISH) (*11*) (fig. S1). The linkage and physical maps show complete shared synteny to *Bombyx mori* chromosome 17 (Fig. 1); however, the physical positions of genes are much more similar to those in the *Bombyx mori* chromosome than to those in the *B. betularia* recombinational map. In particular, the positioning of *sulfamidase* at the very top of the painted chromosome and *chitinase* just below it revealed that the upper half of LG17 is deformed by the large gap between *rpl38* and *myosin HC*, which has the effect of shifting the *carbonaria* locus downward. This gap was present in both mapping families, suggesting that the discrepancy between physical and centimorgan distances is due to a recombination hotspot near the upper end of the chromosome. The core region under investigation displays normal recombination dynamics.

To determine whether the same core haplotype distinguishes all UK *carbonaria* morphs, we conducted population genetic surveys at two spatial scales: one on a sample of *B. betularia* males caught in 2002 from two sites close to Leeds (32 *carbonaria* and 32 typicals), and one on a larger UK-wide sample (78 sites) spanning the period 1925–2009 (median year of collection = 1974) (fig. S3 and table S4). Both samples were scored for single-nucleotide polymorphisms (SNPs) at six widely spaced loci within the region (additional closely linked polymorphisms corroborated allele identities at these test loci, collectively defining "mini haplotypes"). In the Leeds sample, the distribution of SNP genotypes among morphs (Fig. 2) revealed significant morph-genotype associations (P_{MG}) at loci *a*, *b*, *c*, and *d*, with weaker associations at *e* and *f*. A similar pattern

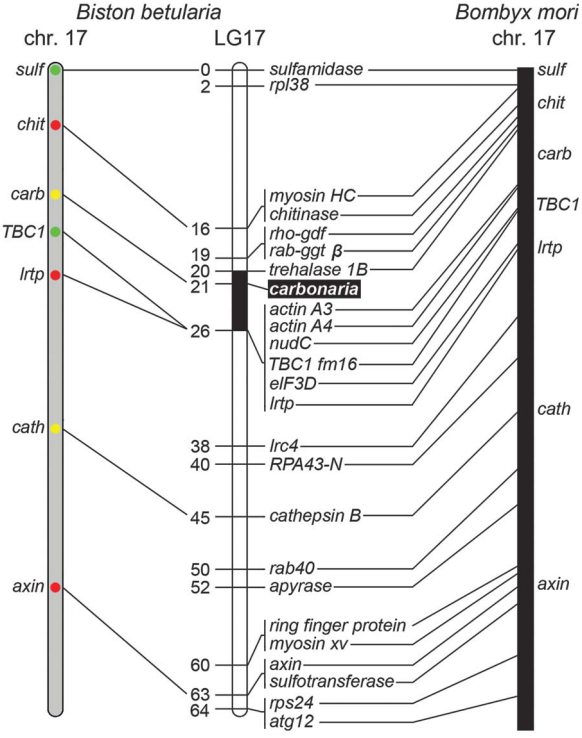

Fig. 1. Chromosomal localization of the *carbonaria* locus and synteny between *B. betularia* and *Bombyx mori* chromosome 17. The recombinational positions of genes mapped to *B. betularia* linkage group 17 (LG17) are related to their physical positions in *Bombyx mori* chromosome 17 (righthand vertical bar) by interconnecting lines. A scheme of bacterial artificial chromosome (BAC)–FISH–painted *B. betularia* chromosome 17 (lefthand vertical bar) shows the physical positions of seven loci (derived from the FISH-painted chromosomes 17 presented in fig. S2). The region in *Bombyx mori* indicated as *carb* is defined by *heat repeat-containing protein* and *proteasome 26S non-ATPase subunit 4*, which are located on the fluorescent *carbonaria* BAC on the *B. betularia* chromosomes. A 1.4-Mb BAC tilepath centered on the *carbonaria* locus (black box within LG17) is presented in more detail in Fig. 2.

[1]Institute of Integrative Biology, University of Liverpool, Liverpool, UK. [2]Institute of Entomology, Biology Centre of the Academy of Sciences of the Czech Republic, and Faculty of Science, University of South Bohemia, České Budějovice, Czech Republic.

*To whom correspondence should be addressed. E-mail: saccheri@liv.ac.uk

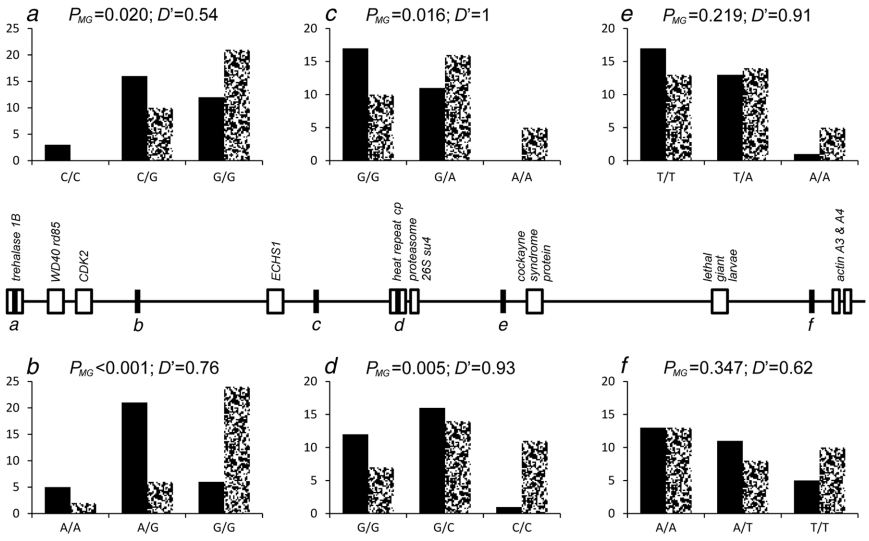

Fig. 2. Association between morph type and SNP genotype at six marker loci within the *carbonaria* region in a sample of wild *B. betularia* from Leeds in 2002. A chromosome section, approximately 1.4 Mb in length, is represented as a horizontal line along which the relative positions of the genetic markers (*a* to *f*) and 10 genes (boxes) are indicated (gene abbreviations are as follows: *WD40 repeat domain 85, cyclin-dependent kinase 2, enoyl-CoA hydratase precursor 1, heat repeat-containing protein,* and *proteasome 26S non-ATPase subunit 4*). For each marker locus, the correspondingly labeled bar chart (*a* to *f*) shows the frequency distribution of SNP genotypes, separately for *carbonaria* (black bars) and typical (stippled bars) samples. P_{MG}, the probability of the observed pattern of association between morph and genotype occurring by chance, and estimates of *D'*, a standardized measure of linkage disequilibrium, are also presented for each marker locus. Marker positions are approximations based on the the size distribution of BACs in our library and the distances between orthologous genes in *Bombyx mori*.

Table 1. Frequency of reconstructed core haplotypes carrying *carbonaria* and *typica* alleles. Multilocus haplotypes were defined for three (*b*, *c*, and *d*) of the six marker loci. Locus positions are shown in Fig. 2. The inferred six-locus haplotype of the original *carbonaria* mutant is CAGGTA (on the upper strand of the schematic sequence in Fig. 2).

Marker locus						Morph allele	
a	***b***	***c***	***d***	***e***	***f***	***carbonaria***	***typica***
C/G	A	G	G	A/T	A/T	0.60	0.02
C/G	G	G	G	A/T	A/T	0.34	0.27
C/G	A	G	C	A/T	A/T	0.04	0.03
C/G	G	G	C	A/T	A/T	0.02	0.30
C/G	A	A	G	A/T	A/T	0	0.01
C/G	G	A	G	A/T	A/T	0	0.16
C/G	A	A	C	A/T	A/T	0	0.02
C/G	G	A	C	A/T	A/T	0	0.19
Sum						1	1

Table 2. Deficiency of repulsion-phase morph-marker haplotypes. The ratio of observed repulsion-phase (recombinant) haplotypes to their expected frequency if morph and marker alleles were randomly associated, for each morph allele (*carbonaria* and *typica*) and marker locus in the Leeds sample, is shown. For each morph allele, the identity of the repulsion-phase marker allele is indicated in parentheses. Locus positions are shown in Fig. 2. *P* values for a X^2 test with 1 d.f. are indicated by asterisks: $*P < 0.5$, $**P < 0.01$, and $***P < 0.001$; n.s., not significant.

Locus	*carbonaria*	*typica*
a	(G) 0.46***	(C) 0.53**
b	(G) 0.24***	(A) 0.48***
c	(A) 0***	(G) 0.87*
d	(C) 0.07***	(G) 0.79*
e	(A) 0.09***	(T) 0.88 n.s.
f	(T) 0.38**	(A) 0.88 n.s.

of association was detected in the UK-wide sample (fig. S4). Most notably, across both samples the A/A genotype at locus *c* is absent in all 97 *carbonaria* specimens, effectively establishing that all *carbonaria* morphs carry a G at this position (the A in G/A heterozygotes is presumed to be carried on the *typica* haplotype). This 100% association leads to the conclusion not only that the same chromosomal region (locus) underlies the genetic determination of all *carbonaria* in the sample but that all *carbonaria* in the United Kingdom are derived from a single ancestral haplotype. Our inference is additionally supported by the rarity of *carbonaria* morphs with the C/C genotype at locus *d* (A/A for locus *e* was also rare in the Leeds sample), implying that the ancestral *carbonaria* haplotype was defined by the alternative alleles, G and G, at loci *c* and *d*, respectively. Clearly, however, given the occurrence of the G allele at locus *c* in typicals, this cannot be the actual morph locus.

The pattern of morph-genotype association for typicals is more complex than for *carbonaria* (Fig. 2 and fig. S4). In particular, at loci *c* to *f*, the high frequency of typicals that are homozygous for the *carbonaria*-type marker allele (the leftmost genotype class) contrasts with the relative absence of *carbonaria* that are homozygous for the typical-type marker allele (the rightmost genotype class). At loci *a* and *b*, however, typicals homozygous for the *carbonaria*-type marker allele are completely or nearly absent (these *typica* haplotypes do occur in heterozygotes at both loci in both samples). The likely explanation for this pattern is that the ancestral *carbonaria* haplotype arose by mutation from a *typica* haplotype, so that many polymorphisms in the region will not be unique to *carbonaria* (that is, high frequencies of typicals either heterozygous or homozygous for the marker allele coupled to *carbonaria* at loci *c* to *f*). By chance, some variants defining the progenitor *carbonaria* haplotype were uncommon in the ancestral typical population (for example, at loci *a* and *b*). Thus, the marker allele frequencies we now see in the typical population reflect both what was originally present and what has been introduced via the spread and introgression of the *carbonaria* haplotype.

In Fig. 2 (and fig. S4), the dominance of the *carbonaria* allele obscures the true frequencies of morph-marker haplotypes by masking the presence of *typica* haplotypes in *carbonaria*/*typica* heterozygotes (phenotypically *carbonaria*). Reconstruction of the core multilocus haplotype frequencies for *carbonaria* and *typica* alleles (Table 1) clarifies the identity of the ancestral *carbonaria* haplotype within a more diverse population of *typica* haplotypes. The ancestral *carbonaria* haplotype defines the coupling phase for the *carbonaria* allele, as well as the repulsion phase composed of the alternative SNP alleles at each marker locus, generated by recombination (which is also taken to be the coupling phase for *typica*).

We assessed the degree of nonrandom association between the morph and marker alleles with a standardized measure of linkage disequilibrium,

D' (*12*), ranging between values of 0 (a fully random association) to 1 (a complete association between allele pairs). Because the underlying model assumes random mating within the population from which the sample was taken, it is only appropriate to calculate this statistic for the Leeds sample. D' was high (>0.5) for all markers across the 1.4-Mb sequence examined, defining a region of approximately 400 kb where $D' > 0.9$, with a maximum D' at locus *c* (Fig. 2). Interpolation of D' values at loci *b*, *c*, and *d* suggests that the genetic polymorphism controlling the morph phenotype is located within 100 kb on either side of locus *c*. Further consideration of the "missing" (repulsion-phase) haplotypes separately for *carbonaria* and *typica* (Table 2) emphasizes the deficit of repulsion-phase *carbonaria* haplotypes across all six loci. In contrast, *typica* haplotypes show only weak deficits of *carbonaria*-type marker alleles, which is consistent with the view that these alleles were segregating in the population before the genesis of *carbonaria*. At loci *a* and *b*, the deficit for *typica* is greater because the *carbonaria*-type alleles (C and A, respectively) were rare in the ancestral population. These two loci suggest that *carbonaria*-to-*typica* haplotype introgression has been weak.

Bombyx mori chromosome 17 and its orthologs in other lepidopterans are rich in major color-patterning genes, such as *black moth* and *wild wing spot* (*13*). These *Bombyx mori* genes do not map closely to the *carbonaria* locus (fig. S5). However, *Bicyclus anynana* LG17 contains two pigment-patterning mutants, *067* and *Bigeye*, that both affect eyespot size, with *Bigeye* predicted to reside within the *carbonaria* region (*14*). The *Bigeye* and *carbonaria* phenotypes are clearly very different, but they share a large increase in the proportion of melanized scales. The *carbonaria* core region also overlaps the mimetic patterning locus in four *Heliconius* species, collectively referred to as the *Yb-P-Yb/Sb-Cr* locus (*15*–*17*). The *B. betularia* genes identified in this region so far correspond entirely with those described for the *Yb-P-Yb/Sb-Cr* region. A major feature distinguishing *Heliconius* forms is the amount and distribution of black, as with the various *B. betularia* morphs (*4*). This unlikely coincidence suggests that the control of melanin pattern formation in these deeply diverged lepidopterans may have a common genetic basis, the functional units of which have yet to be identified.

The rapid spread of an initially unique haplotype, driven by strong positive selection, is expected to generate the profile of linkage disequilibrium we have observed (*18*), establishing that UK industrial melanism in the peppered moth was seeded by a single recent mutation that spread to most parts of mainland Britain and also colonized the Isle of Man (fig. S4). Paradoxically, although the *carbonaria* morph is now strongly disadvantageous and consequently rare in the United Kingdom, the rapidity of its decline (*19*) has minimized the eroding effect of *typica* introgression on the molecular footprint of strongly positive selection created during its ascendency.

References and Notes

1. M. E. N. Majerus, *Melanism: Evolution in Action* (Oxford Univ. Press, Oxford, 1998).
2. L. M. Cook, *Q. Rev. Biol.* **78**, 399 (2003).
3. I. J. Saccheri, F. Rousset, P. C. Watts, P. M. Brakefield, L. M. Cook, *Proc. Natl. Acad. Sci. U.S.A.* **105**, 16212 (2008).
4. L. M. Cook, J. Muggleton, *Entomol. Gaz.* **54**, 211 (2003).
5. D. R. Lees, in *Genetic Consequences of Man Made Change*, J. A. Bishop, L. M. Cook, Eds. (Academic Press, London, 1981), pp. 129–176.
6. D. L. Stern, *Evolution, Development and the Predictable Genome* (Roberts and Company Publishers, Greenwood Village, CO, 2010).
7. M. E. N. Majerus, N. I. Mundy, *Trends Genet.* **19**, 585 (2003).
8. J. R. True, *Trends Ecol. Evol.* **18**, 640 (2003).
9. P. J. Wittkopp, S. B. Carroll, A. Kopp, *Trends Genet.* **19**, 495 (2003).
10. A. E. van't Hof, I. J. Saccheri, *PLoS ONE* **5**, e10889 (2010).
11. Materials and additional results are available as supporting material on *Science* Online.
12. P. Hedrick, S. Kumar, *Eur. J. Hum. Genet.* **9**, 969 (2001).
13. M. R. Goldsmith, A. S. Wilkins, *Molecular Model Systems in the Lepidoptera* (Cambridge Univ. Press, Cambridge, 1995).
14. P. Beldade, S. V. Saenko, N. Pul, A. D. Long, *PLoS Genet.* **5**, e1000366 (2009).
15. R. Papa, A. Martin, R. D. Reed, *Curr. Opin. Genet. Dev.* **18**, 559 (2008).
16. M. Joron *et al.*, *PLoS Biol.* **4**, e303 (2006).
17. M. R. Kronforst, D. D. Kapan, L. E. Gilbert, *Genetics* **174**, 535 (2006).
18. P. Pfaffelhuber, A. Lehnert, W. Stephan, *Genetics* **179**, 527 (2008).
19. L. M. Cook, S. L. Sutton, T. J. Crawford, *J. Hered.* **96**, 522 (2005).

Acknowledgments: This work was funded by Natural Environment Research Council grant NE/C003101/1 to I.J.S. Cytogenetic experiments were financed by Grant Agency of the Academy of Sciences of the Czech Republic grant IAA600960925, Entomology Institute project Z50070508, and Grant Agency of the Czech Republic 521/08/H042 grants to F.M. and M.D. Specimens for the UK-wide survey were made available by several museums and private collectors, listed in table S4. J. Delf produced fig. S3. GenBank accession numbers are listed in table S1.

Supporting Online Material

www.sciencemag.org/cgi/content/full/science.1203043/DC1
Materials and Methods
Figs. S1 to S5
Tables S1 to S4
References

19 January 2011; accepted 30 March 2011
Published online 14 April 2011;
10.1126/science.1203043

The Selaginella Genome Identifies Genetic Changes Associated with the Evolution of Vascular Plants

Jo Ann Banks,[1]* Tomoaki Nishiyama,[2,3] Mitsuyasu Hasebe,[3,4,5] John L. Bowman,[6,7] Michael Gribskov,[8] Claude dePamphilis,[9,10,11] Victor A. Albert,[12] Naoki Aono,[4] Tsuyoshi Aoyama,[4,5] Barbara A. Ambrose,[13] Neil W. Ashton,[14] Michael J. Axtell,[9] Elizabeth Barker,[14] Michael S. Barker,[15] Jeffrey L. Bennetzen,[16] Nicholas D. Bonawitz,[17] Clint Chapple,[17] Chaoyang Cheng,[3] Luiz Gustavo Guedes Correa,[18] Michael Dacre,[19] Jeremy DeBarry,[16] Ingo Dreyer,[20] Marek Elias,[21,22] Eric M. Engstrom,[23] Mark Estelle,[24] Liang Feng,[25] Cédric Finet,[26] Sandra K. Floyd,[6] Wolf B. Frommer,[27] Tomomichi Fujita,[28] Lydia Gramzow,[29] Michael Gutensohn,[30,31] Jesper Harholt,[32] Mitsuru Hattori,[33,34] Alexander Heyl,[35] Tadayoshi Hirai,[3,36] Yuji Hiwatashi,[4,5] Masaki Ishikawa,[3] Mineko Iwata,[3] Kenneth G. Karol,[13] Barbara Koehler,[18] Uener Kolukisaoglu,[37,38] Minoru Kubo,[3] Tetsuya Kurata,[3,39] Sylvie Lalonde,[27] Kejie Li,[8] Ying Li,[8,40] Amy Litt,[13] Eric Lyons,[41] Gerard Manning,[19] Takeshi Maruyama,[42] Todd P. Michael,[43,44] Koji Mikami,[45] Saori Miyazaki,[4,46] Shin-ichi Morinaga,[4,47] Takashi Murata,[4,5] Bernd Mueller-Roeber,[48] David R. Nelson,[49] Mari Obara,[3,50] Yasuko Oguri,[3] Richard G. Olmstead,[51] Naoko Onodera,[3,52] Bent Larsen Petersen,[32] Birgit Pils,[53,54] Michael Prigge,[24] Stefan A. Rensing,[55,56,57] Diego Mauricio Riaño-Pachón,[58,59] Alison W. Roberts,[60] Yoshikatsu Sato,[3] Henrik Vibe Scheller,[41,61] Burkhard Schulz,[30] Christian Schulz,[62] Eugene V. Shakirov,[63] Nakako Shibagaki,[64] Naoki Shinohara,[3,65] Dorothy E. Shippen,[63] Iben Sørensen,[32,66] Ryo Sotooka,[65] Nagisa Sugimoto,[3] Mamoru Sugita,[33] Naomi Sumikawa,[4] Milos Tanurdzic,[67] Günter Theißen,[29] Peter Ulvskov,[32] Sachiko Wakazuki,[3] Jing-Ke Weng,[17,68] William W.G.T. Willats,[32] Daniel Wipf,[69] Paul G. Wolf,[70] Lixing Yang,[16] Andreas D. Zimmer,[55,71] Qihui Zhu,[16] Therese Mitros,[72] Uffe Hellsten,[73] Dominique Loqué,[61] Robert Otillar,[73] Asaf Salamov,[73] Jeremy Schmutz,[73] Harris Shapiro,[73] Erika Lindquist,[73] Susan Lucas,[73] Daniel Rokhsar,[72,73] Igor V. Grigoriev[73]

Vascular plants appeared ~410 million years ago, then diverged into several lineages of which only two survive: the euphyllophytes (ferns and seed plants) and the lycophytes. We report here the genome sequence of the lycophyte *Selaginella moellendorffii* (Selaginella), the first nonseed vascular plant genome reported. By comparing gene content in evolutionarily diverse taxa, we found that the transition from a gametophyte- to a sporophyte-dominated life cycle required far fewer new genes than the transition from a nonseed vascular to a flowering plant, whereas secondary metabolic genes expanded extensively and in parallel in the lycophyte and angiosperm lineages. *Selaginella* differs in posttranscriptional gene regulation, including small RNA regulation of repetitive elements, an absence of the trans-acting small interfering RNA pathway, and extensive RNA editing of organellar genes.

Selaginella moellendorffii, like all lycophytes, has features typical of vascular plants, including a dominant and complex sporophyte generation (Fig. 1, A and B) having vascular tissues with lignified cell types. Lycophytes also share traits with nonseed plants, most notably

the release of haploid spores (Fig. 1C) from the sporophyte and a gametophyte generation that develops independently of the sporophyte. Because the lycophytes are an ancient lineage that diverged shortly after land plants evolved vascular tissues (Fig. 2A) (*1*), we sequenced the Selaginella genome to provide a resource for identifying genes that may have been important in the early evolution of developmental and metabolic processes specific to vascular plants.

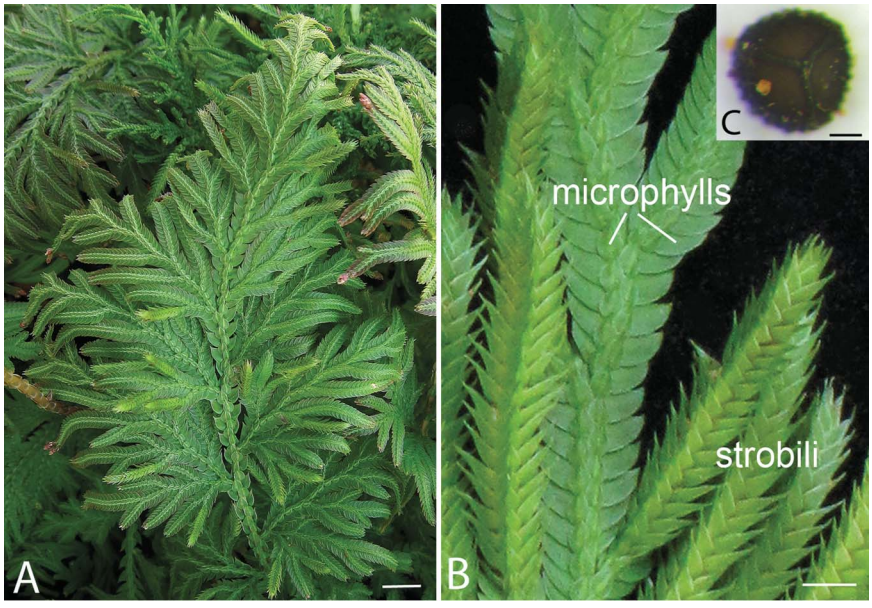

Fig. 1. Selaginella morphology. (**A**) The diploid sporophyte body. Bar, 10 mm. (**B**) A shoot with two ranks of microphylls ("leaves") and strobili. Each microphyll of a strobilus has either a mega- or a microsporangium where mega- or microspores are produced. Bar, 2 mm. (**C**) An orange microspore on top of a dark megaspore. These single-celled haploid spores represent the beginning of the independent haploid gametophyte generation. The microgametophye produces motile sperm and the megagametophyte eggs. Bar, 0.1 mm.

The Selaginella genome was sequenced by whole-genome shotgun sequencing (*2*). The assembled genome size (212.6 Mbp) is twice that determined by flow cytometry (*3*), indicating that the assembled genome includes two haplotypes of ~106 Mbp that are 98.5% identical at the nucleotide level. A deduced haplotype has 22,285 predicted protein-coding genes, of which 37% are supported by expressed sequence tag sequences, and 58 microRNA (miRNA) loci (*2*, *4*). The Selaginella genome lacks evidence of an ancient whole-genome duplication or polyploidy (*2*), unlike all other sequenced land-plant genomes (*5*–*7*). Gene density in Selaginella and *Arabidopsis*, which has a slightly larger genome size, is very similar (*2*), and both genomes have gene-poor regions rich in transposable elements (TEs) and other repetitive sequences (*2*). Although fewer genes and smaller introns (*2*) contribute to a genome size smaller than *Arabidopsis*, this is offset by a greater proportion of TEs in Selaginella (37.5% versus 15% in *Arabidopsis*) (*2*). Long terminal repeat retrotransposons are the most abundant TEs, occupying one-third of the Selaginella genome (*2*).

Plant TEs and *MIRNA* loci are important sources of small RNAs (sRNAs) that function

[1]Department of Botany and Plant Pathology, Purdue University, West Lafayette, IN 47907, USA. [2]Advanced Science Research Center, Kanazawa University, Kanazawa 920-0934, Japan. [3]ERATO, Japan Science and Technology Agency, Okazaki 444-8585, Japan. [4]National Institute for Basic Biology, Okazaki 444-8585, Japan. [5]Department of Basic Biology, School of Life Science, The Graduate University for Advanced Studies, Okazaki 444-8585, Japan. [6]School of Biological Sciences, Monash University, Clayton Campus, Melbourne, Victoria 3800, Australia. [7]Section Plant Biology, University of California, Davis, CA 95616, USA. [8]Department of Biological Sciences, Purdue University, West Lafayette, IN 47907, USA. [9]Department of Biology and Huck Institutes of Life Sciences, Pennsylvania State University, University Park, PA 16802, USA. [10]Graduate Program in Plant Biology, Pennsylvania State University, University Park, PA 16802, USA. [11]Institute of Molecular Evolutionary Genetics, Pennsylvania State University, University Park, PA 16802, USA. [12]Department of Biological Sciences, University at Buffalo, Buffalo, NY 14260, USA. [13]The New York Botanical Garden, Bronx, NY 10458, USA. [14]Department of Biology, University of Regina, 3737 Wascana Parkway, Regina, SK S4S 0A2, Canada. [15]Department of Ecology and Evolutionary Biology, University of Arizona, Tucson, AZ 85721, USA. [16]Department of Genetics, University of Georgia, Athens, GA 30602, USA. [17]Department of Biochemistry, Purdue University, West Lafayette, IN 47907, USA. [18]Department of Molecular Biology, University of Potsdam, Potsdam-Golm 14476, Germany. [19]Razavi Newman Center for Bioinformatics, Salk Institute for Biological Studies, 10010 North Torrey Pines Road, La Jolla, CA 92037, USA. [20]Heisenberg-Group Biophysics and Molecular Plant Biology, University of Potsdam, Potsdam-Golm 14476, Germany. [21]Charles University in Prague, Faculty of Science, Department of Botany, 128 01 Prague 2, Benatska 2, Czech Republic. [22]University in Prague, Faculty of Science, Chittussiho 10, 710 00 Ostrava, Czech Republic. [23]Department of Biology, The College of William and Mary, Williamsburg, VA 23187, USA. [24]Section of Cell and Developmental Biology, University of California, San Diego, La Jolla, CA 92093, USA. [25]Institute of Bioinformatics, University of Georgia, Athens, GA 30602, USA. [26]Laboratoire de Reproduction et Développement des Plantes, Ecole Normale Supérieure de Lyon, Lyon F-69364, France. [27]Department of Plant Biology, Carnegie Institution for Science, Stanford, CA 94305, USA. [28]Faculty of Science, Hokkaido University, Sapporo 060-0810, Japan. [29]Department of Genetics, Friedrich Schiller University Jena, D-07743 Jena, Germany. [30]Department of Horticulture and Landscape Architecture, Purdue University, W. Lafayette, IN 47907, USA. [31]Institute of Biology, Martin Luther University Halle-Wittenberg, Halle/Saale 06120, Germany. [32]Department of Plant Biology and Biotechnology, University of Copenhagen, Frederiksberg C 1871, Denmark. [33]Center for Gene Research, Nagoya University, Nagoya 464-8602, Japan. [34]Department of Chemistry, School of Science, The University of Tokyo 7-3-1 Hongo, Bunkyo-ku, Tokyo 113-0033, Japan. [35]Institute for Biology–Applied Genetics, Dahlem Centre of Plant Sciences, Freie Universität Berlin, 14195 Berlin, Germany. [36]Graduate School of Life and Environmental Sciences, Gene Research Center, University of Tsukuba, Tsukuba 305-8572, Japan. [37]Center for Life Science Automation, University of Rostock, D-18119 Rostock, Germany. [38]Studiengangskoordination Nano-Science, Universität Tübingen, Tübingen 72076, Germany. [39]Plant Global Education Project, Graduate School of Biological Sciences, Nara Institute of Science and Technology, Nara 630-0192, Japan. [40]Division of Biomedical Statistics and Informatics, Mayo Clinic, 200 First Street SW, Rochester, MN 55905, USA. [41]Department of Plant and Microbial Biology, University of California, Berkeley, CA 94720, USA. [42]Graduate School of Life Science, Hokkaido University, Sapporo 060-0810, Japan. [43]Department of Plant Biology and Pathology, Rutgers, The State University of New Jersey and Waksman Institute of Microbiology, 190 Frelinghuysen Road, Piscataway, NJ 08854–8020, USA. [44]The Genome Analysis Center, Monsanto, St. Louis, MO 63167, USA. [45]Faculty of Fisheries Sciences, Hokkaido University, Hakodate 041-8611, Japan. [46]National Institute of Genetics, Mishima 411-8540, Japan. [47]Graduate School of Arts and Sciences, The University of Tokyo, Tokyo 153-8902, Japan. [48]Bernd Max-Planck Institute of Molecular Plant Physiology, Potsdam-Golm 14476, Germany. [49]Department of Microbiology, Immunology and Biochemistry, University of Tennessee, Memphis, TN 38163, USA. [50]Japan Science and Technology Agency, Sapporo 060-0819, Japan. [51]Department of Biology, University of Washington, Seattle, WA 98195–5325, USA. [52]Department of Biochemistry and Molecular Biology, Dalhousie University, Halifax, Nova Scotia B3H 4R2, Canada. [53]Wellcome Trust Centre for Human Genetics, Oxford, OX3 7BN, UK. [54]Sias AG, CH-8634 Hombrechtikon, Switzerland. [55]Faculty of Biology, University of Freiburg, Freiburg 79104, Germany. [56]BIOSS Centre for Biological Signaling Studies, University of Freiburg, Freiburg 79104, Germany. [57]Freiburg Initiative for Systems Biology (FRISYS), University of Freiburg, Freiburg 79104, Germany. [58]GabiPD team, Bioinformatics Group, Max Planck Institute of Molecular Plant Physiology, Potsdam-Golm 14476, Germany. [59]Departamento de Ciencias Biológicas, Universidad de los Andes, Bogotá D.C., Colombia. [60]Department of Biological Sciences, University of Rhode Island, Kingston, RI 02881, USA. [61]Joint BioEnergy Institute, Feedstocks Division, Emeryville, CA 94608, USA. [62]Department of Evolution and Biodiversity of Plants, Ruhr-University Bochum, Bochum 44780, Germany. [63]Department of Biochemistry and Biophysics, Texas A&M University, College Station, TX 77843, USA. [64]Graduate School of Engineering, Osaka University, Osaka 565-0871, Japan. [65]School of Science, Hokkaido University, Sapporo 060-0810, Japan. [66]Department of Plant Biology, Cornell University, Ithaca, NY 14850, USA. [67]Cold Spring Harbor Laboratory, Cold Spring Harbor, NY 11724, USA. [68]The Jack H. Skirball Center for Chemical Biology and Proteomics, The Salk Institute for Biological Studies, La Jolla, CA 92037, USA. [69]UMR INRA 1088/CNRS 5184, Université Bourgogne Plant-Microbe-Environment, Dijon 21065, France. [70]Department of Biology, Utah State University, Logan, UT 84322-5305, USA. [71]Plant Biotechnology, University of Freiburg, Freiburg 79104, Germany. [72]Department of Molecular and Cell Biology, University of California, Berkeley, CA 94720, USA. [73]U.S. Department of Energy Joint Genome Institute, Walnut Creek, CA 94598, USA.

*To whom correspondence should be addressed. E-mail: banksj@purdue.edu

to epigenetically regulate TE and gene activity (*8*). Several observations suggest that some aspects of epigenetic or posttranscriptional gene regulation in Selaginella are unique among plants. For one, the proportion of sRNAs 23 to 24 nucleotides (nt) in length is extraordinarily small in the Selaginella sRNA population (*2*) compared to angiosperms (*9*). Nearly three-quarters of the Selaginella sRNAs (*4*) map to *MIRNA* loci and are predominantly 21 nt in length (*2*). In angiosperms, 24-nt siRNAs, which are generated primarily from TEs, function to silence TE activity through the RNA-dependent DNA methylation pathway (*10*–*12*) and accumulate massively in specific cells of the female gametophyte (*13*). Because the Selaginella sRNA population was generated from sporophytic tissues, the 24-nt siRNA pathway may only be deployed during gametophyte development in Selaginella. A second distinction is the absence of *DCL4*, *RDR6*, and *MIR390* loci in Selaginella, which are required for the biogenesis of trans-acting siRNAs (tasiRNAs) in angiosperms (*2*). Their absence suggests that tasiRNA-regulated processes in angiosperms, including leaf polarity (*14*) and developmental phase changes in the sporophyte (*15*, *16*), are regulated differently in Selaginella, and possibly reflects the independent origins of foliar organs in the lycophyte and angiosperm lineages (*17*, *18*). Finally, the Selaginella plastome sequence reveals an extraordinarily large number of RNA-edited sites (*2*), as do other lycophyte organellar genomes (*19*, *20*). This coincides with an exceptionally large number of PPR genes in Selaginella (>800) (*2*), some of which guide RNA editing events in angiosperms (*21*).

Because Selaginella is a member of a vascular plant lineage that is sister to the euphyllophytes, we used comparative and phylogenetic approaches to identify gene origins and expansions coinciding with evolutionary innovations and losses in land plants. To identify such genes without regard to function, we compared the proteomes of the green alga Chlamydomonas, the moss Physcomitrella, Selaginella, and 15 angiosperm species; identified gene families that are related by homology by hierarchical clustering (*2*); and then mapped them onto a phylogenetic tree (Fig. 2B). The 3814 families with gene members present in all plant lineages define the minimum set of genes that were likely to be present in the common ancestor of all green plants and their descendants and include genes essential for plant function. The transition from single-celled green algae to multicellular land plant approximately doubled the gene number with the acquisition of 3006 new genes. The transition from nonvascular to vascular plant is associated with a gain of far fewer new genes (516) than the transition from a basal vascular plant to a basal euphyllophyte whose descendants include the angiosperms (1350). These numbers show that the evolution of traits specific to euphyllophytes or angiosperms required the evolution of about three times more new genes than the transition from a plant having a dominant gametophyte and simple, leafless, and nonvascularized sporophyte (typified by modern bryophytes) to a plant with a dominant, vascularized, and branched sporophyte with leaves.

In a second approach, we analyzed the phylogenies of genes known to function in *Arabidopsis* development (*2*). We identified 424 monophyletic groups of developmental genes, each group containing putatively all genes descended from a common land-plant ancestral gene (table S6). Selaginella and Physcomitrella genes are present in 377 (89%) and 356 (84%) of the 424 land-plant orthologous gene groups, respectively, indicating that the common ancestor of land plants had most of the gene families known to direct angiosperm development. Conspicuous expansions of families within different lineages resulted in different numbers of land-plant orthologs in each genome (table S6). The 27 vascular plant-specific orthologous groups likely represent genes associated with developmental innovations of vascular plants. Among them are genes regulating the meristem (*CLV1* and *CLV2*), hormone signaling (*GID1* and *CTR1*), and flowering (*TFL2* and *UFO*). Homologs of genes involved in the specification of xylem (*NST* and *VND*) (*22*) and phloem (*APL*) (*23*) in *Arabidopsis* are present in Physcomitrella and Selaginella, suggesting that the developmental programs for patterning and differentiation of vascular tissues were either present in, or co-opted from, preexisting genetic programs in the ancestral land plant. The 43 groups lacking genes from Physcomitrella and Selaginella (table S6) likely identify genes that were necessary for euphyllophyte or angiosperm developmental innovations. Among this group are genes that regulate light signaling (*FAR1*, *MIF1*, *OBP3*, and *PKS1*), shoot meristem development (*AS2* and *ULT1*), hormone signaling and biosynthesis (*BRI1*, *BSU1*, *ARF16*, *ACS*, and *ACO*), and flowering (*HUA1*, *EMF1*, *FT*, *TFL1*, and *FD*). Altogether, these results suggest that the evolutionary transitions from a nonvascular plant to a vascular angiosperm included the stepwise addition of components of some developmental pathways, especially those regulating meristem and hormone biology, as previously noted for the gibberellin signaling pathway (*24*, *25*).

Genes involved in secondary metabolism were also investigated because plants synthesize numerous secondary metabolites that they use to interact with their environment. Three gene families involved in their biosynthesis, including those encoding cytochrome P450-dependent monooxygenases (P450s), BAHD acyltransferases (BAHDs), and terpene synthases (TSs), were analyzed. The largest of these in Selaginella is the P450 family, accounting for 1% of its predicted proteome (table S7) (*2*). All three families show similar evolutionary trends, with the inferred ancestral vascular plant having a small number of genes that radiated extensively but independently within the lycophyte and angiosperm lineages (figs. S6 to S13). *BAHD* and *TS* genes, which are known to be involved in the biosynthesis of volatile odorants, are apparent only in seed plants (figs. S12 to S13), likely reflecting the coevolution of seed plants with animals that pollinate flowers or disperse seeds. The independent diversification of these gene families plus the large number of Selaginella genes suggest that Selaginella not only has the potential to synthesize a repertoire of secondary metabolites that rivals the angiosperms in complexity, but that many of them are likely to be unique. Some have been shown to be of pharmaceutical value [e.g., (*26*)].

We have used the compact Selaginella genome sequence to uncover genes associated with major evolutionary transitions in land plants. Understanding their functions in Selaginella and other taxa, as well as acquiring the genome sequences of other informative taxa, especially charophytes, ferns, and gymnosperms, will be key to understanding the evolution of plant form and function.

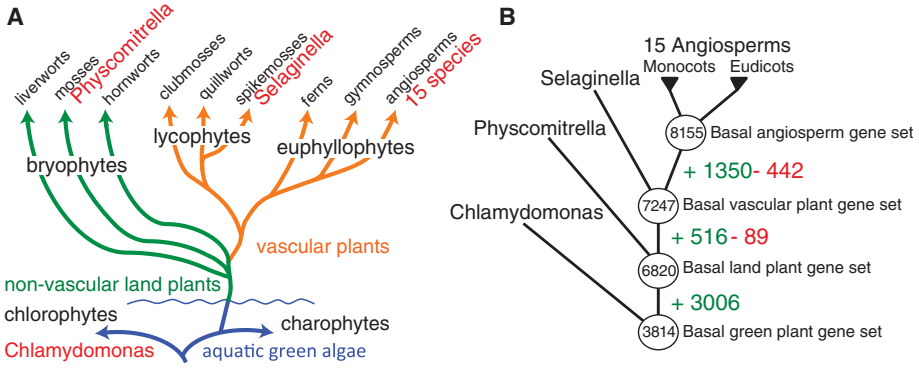

Fig. 2. (**A**) Phylogeny of plants. Taxa in red have sequenced genomes. (**B**) Gene family gains (+) and losses (–) mapped onto the plant phylogenetic tree. The minimum numbers of gene families present in the ancestors of different plant lineages are circled.

References and Notes

1. P. Kenrick, P. R. Crane, *Nature* **389**, 33 (1997).
2. Details are given in the supporting materials on *Science* Online.
3. W. Wang *et al.*, *BMC Plant Biol.* **5**, 10 (2005).

4. M. J. Axtell, J. A. Snyder, D. P. Bartel, *Plant Cell* **19**, 1750 (2007).
5. M. S. Barker, H. Vogel, M. E. Schranz, *Genome Biol. Evol.* **1**, 391 (2009).
6. H. Tang *et al.*, *Science* **320**, 486 (2008).
7. H. Tang *et al.*, *Genome Res.* **18**, 1944 (2008).
8. M. Ghildiyal, P. D. Zamore, *Nat. Rev. Genet.* **10**, 94 (2009).
9. D. Chen *et al.*, *Bioinformatics* **26**, 1391 (2010).
10. K. D. Kasschau *et al.*, *PLoS Biol.* **5**, e57 (2007).
11. K. Nobuta *et al.*, *Nat. Biotechnol.* **25**, 473 (2007).
12. S. H. Cho *et al.*, *PLoS Genet.* **4**, e1000314 (2008).
13. D. Bourc'his, O. Voinnet, *Science* **330**, 617 (2010).
14. D. H. Chitwood *et al.*, *Genes Dev.* **23**, 549 (2009).
15. A. Peragine, M. Yoshikawa, G. Wu, H. L. Albrecht, R. S. Poethig, *Genes Dev.* **18**, 2368 (2004).
16. Z. Xie, E. Allen, A. Wilken, J. C. Carrington, *Proc. Natl. Acad. Sci. U.S.A.* **102**, 12984 (2005).
17. S. K. Floyd, J. L. Bowman, *Curr. Biol.* **16**, 1911 (2006).
18. C. J. Harrison *et al.*, *Nature* **434**, 509 (2005).
19. S. Tsuji *et al.*, *J. Plant Res.* **120**, 281 (2007).
20. F. Grewe *et al.*, *Nucleic Acids Res.* **39**, 2890 (2011).
21. V. Knoop, *Cell. Mol. Life Sci.* **68**, 567 (2011).
22. T. Demura, H. Fukuda, *Trends Plant Sci.* **12**, 64 (2007).
23. M. Bonke, S. Thitamadee, A. P. Mähönen, M. T. Hauser, Y. Helariutta, *Nature* **426**, 181 (2003).
24. K. Hirano *et al.*, *Plant Cell* **19**, 3058 (2007).
25. Y. Yasumura, M. Crumpton-Taylor, S. Fuentes, N. P. Harberd, *Curr. Biol.* **17**, 1225 (2007).
26. Y. Cao *et al.*, *Fitoterapia* **81**, 253 (2010).

Acknowledgments: Selaginella sequences were deposited at GenBank with the accession numbers GL377566 to GL378322.1 and HM173080. Genome sequencing and analysis were performed by the U.S. Department of Energy (DOE), Joint Genome Institute, supported by the Office of Science of the U.S. DOE, Contract DE-AC02-05CH11231 (I.V.G., U.H., D.L., E.L., S.L., T.M., R.O., D.R., A.S., J.S., H.V.S.). Support was provided by NSF 0844413 (J.A.B.); Japan Society for the Promotion of Science (M.H., T.N., T.F., K.M., T.M., M.S.); Ministry of Education, Culture, Sports, Science, and Technology, Japan (M.H., T.N., T.F.); NSF 0515435 and Australian Research Council FF0561326 (J.L.B.); NSF 0519970 (M.G.); NSF 0638595 (C.D.); NSF 0922742 (V.A.A.); The Lewis B and Dorothy Cullman Program (B.A.A., A.L.); NSF 1020443 (B.A.A.); Natural Sciences and Engineering Research Council of Canada (NSERC) 2982 (N.W.A.); NIH GM84051 (M.J.A.); NSERC (E.I.B.); NIH T32 GM007757 and NSERC PGS-D (M.S.B.); NSF 0607123 (J.L.B.); Life Sciences Research Foundation (NDB); National Human Genome Research Institute (NHGRI) HG004164 (M.D.); German Science Foundation (Deutsche Forschungsgemeinschaft, DFG) DR 430/4-2 (I.D.); Czech Ministry of Education 21620828 (M.E.); Jeffress Memorial Trust J-938 (E.M.E.); NSF 0744800 (M.E. and M.P.); DOE DE-FG02-04ER15542 (W.B.F. and S.L.); The Danish Council for Independent Research, Technology and Production Sciences 009-066624/274-09-0314 (J.H.); The Villum Kann Rasmussen Foundation (J.H., I.S., B.P., P.U., W.W.); NIH T32-HG00035, NSF 1020660, and NSF 1036466 (K.G.K.); NSF 0735191 (E.L.); NHGRI HG004164 (G.M); U.S. Department of Agriculture (USDA) DE-FG02-08ER64630 (T.P.M.); NSF 0228660 (R.G.O.); The Danish Council for Strategic Research 09-063090 (B.L.P. and P.U.); Marie Curie FP6 RTN ZOONET (B.P.); DFG RE 837/10-2, BMBF FRISYS 0313921 (S.A.R.); Bundesministerium fuer Bildung und Forschung, Germany, GABI-FUTURE grant 0315046 (D.M.R.); USDA NRI 2007-35318-18389 (A.W.R.); NSF 0421604 (C.S.); NIH GM065383 (D.E.S.); Burgundy Regional Council 20100112095254682-1 (D.W.); and DFG RE 837/10-2 (A.D.Z.). K. Wall, D. Hurley, and S. Hentel provided computational assistance.

Supporting Online Material

www.sciencemag.org/cgi/content/full/science.1203810/DC1
SOM Text
Figs. S1 to S14
Tables S1 to S8
References

4 February 2011; accepted 8 April 2011
Published online 5 May 2011;
10.1126/science.1203810

Chromatin "Prepattern" and Histone Modifiers in a Fate Choice for Liver and Pancreas

Cheng-Ran Xu,[1] Philip A. Cole,[2] David J. Meyers,[2] Jay Kormish,[1]* Sharon Dent,[3] Kenneth S. Zaret[1]†

Transcriptionally silent genes can be marked by histone modifications and regulatory proteins that indicate the genes' potential to be activated. Such marks have been identified in pluripotent cells, but it is unknown how such marks occur in descendant, multipotent embryonic cells that have restricted cell fate choices. We isolated mouse embryonic endoderm cells and assessed histone modifications at regulatory elements of silent genes that are activated upon liver or pancreas fate choices. We found that the liver and pancreas elements have distinct chromatin patterns. Furthermore, the histone acetyltransferase P300, recruited via bone morphogenetic protein signaling, and the histone methyltransferase Ezh2 have modulatory roles in the fate choice. These studies reveal a functional "prepattern" of chromatin states within multipotent progenitors and potential targets to modulate cell fate induction.

Early pluripotent cells of the mammalian embryo develop into multipotent endoderm, ectoderm, and mesoderm germ layers. In pluripotent cells, silent genes that will be activated later in development often exist with histone modifications and/or bound transcription factors that reflect the chromatin being "poised" for activity (*1*–*3*). It is unclear whether such poised states exist for silent genes in germ layer cells and, if so, whether genes poised for different tissue fates exhibit different chromatin features. Furthermore, it is not known whether enzymes that establish chromatin states can control germ layer fate choices. Embryonic germ layer cells are few in number, they have not been purified, and chromatin analysis on small cell populations is challenging (*4*). Yet germ layer cells represent the first lineage-restricted, multipotent progenitors of the embryo and a paradigm for all subsequent fate decisions.

Ventral foregut endoderm cells undergo a fate choice for liver or ventral pancreas progenitors (*5*, *6*). FoxA1 or FoxA2, GATA4 or GATA6, vHNF1, and Hnf6 (also known as Oc1) are necessary in the endoderm for both liver and ventral pancreas induction (*7*). In the absence of any set of the factors, the earliest liver marker genes *Alb1*, *Afp*, and *Ttr* and the ventral pancreas transcription factor gene *Pdx1* fail to be activated, or expression is delayed, and tissue buds fail to form (*7*). It is not clear how the same group of factors can be necessary for both liver and ventral pancreas and how signaling promotes the different fates. We sought to map chromatin states at silent liver- and pancreas-specific regulatory sequences in endoderm cells, to discover the factors or relevant histone-modifying enzymes, and test the enzymes' functions in the liver-versus-pancreas decision.

We used fluorescence-activated cell sorting (FACS) with the ENDM1 antibody to isolate ventral foregut endoderm cells from embryonic day 8.25 (E8.25) mouse embryos with four to six somite pairs (4-6S) (*8*) (fig. S1), just prior to the induction of hepatic and pancreatic fates (*5*, *9*). We also used the liver-specific antibody Liv2 to isolate nascent hepatoblasts expressing *Alb1*, *Afp*, and *Ttr* from E9.5 embryos (fig. S2) (*10*). Chromatin marks in ENDM1$^+$ and Liv2$^+$ populations were identified with a low–cell number chromatin immunoprecipitation (ChIP) protocol (*4*) for H3K9acK14ac, H3K4me2, H3K4me3, H3K9me3, H3R17me2a, H3K27me3, H3K36me2, H3K36me3, H3K79me2, H4K20me3, H3T3ph, H3S10ph, the histone variant H2A.Z, and the chromatin remodelers Brg1 and SNF2. We assessed the liver-specific promoter and enhancer of *Alb1* (*11*, *12*), the liver-specific promoters of *Afp* and *Ttr* genes (*13*, *14*), and the I, II, III, and IV upstream elements and local promoter of the pancreatic determination gene *Pdx1* (fig. S3). The I, II, and III upstream elements and promoter of *Pdx1* reconstitute pancreas-specific activation (*15*); the IV element may function later (*16*, *17*). All of the target genes are silent in endoderm cells, and only the liver genes become activated in hepatoblasts.

[1]Institute for Regenerative Medicine, Epigenetics Program, Department of Cell and Developmental Biology, University of Pennsylvania School of Medicine, Philadelphia, PA 19104, USA. [2]Department of Pharmacology and Molecular Sciences, Johns Hopkins University School of Medicine, Baltimore, MD 21205, USA. [3]Department of Molecular Carcinogenesis, University of Texas M. D. Anderson Cancer Center, Smithville, TX 78957, USA.

*Present address: Biochemistry and Molecular Biology, University of Calgary, Calgary, Alberta T2N 4N1, Canada.
†To whom correspondence should be addressed. E-mail: zaret@upenn.edu

We also assessed the active *Gapdh* gene (encoding glyceraldehyde-3-phosphate dehydrogenase) as a control. For each mark and target, we performed at least quadruplicate ChIP assays and displayed quantitative polymerase chain reaction (qPCR) results over immunoglobulin G (IgG) ChIP controls. Low–cell number ChIP yields low-amplitude signals; with replicates, statistical significance can be reached (*4*).

Two chromatin marks in undifferentiated endoderm cells exhibited striking differences between the liver and pancreas regulatory elements. H3K9acK14ac, which is associated with gene activity (*18*), was poorly represented at all of the liver regulatory elements, relative to the active *Gapdh* promoter, and enriched at all of the *Pdx1* regulatory elements (Fig. 1, open boxes). H3K27me3, which is associated with gene silencing (*19*), was also poorly represented at the liver elements and *Gapdh*, yet was enriched at the pancreas elements, except at area IV (Fig. 1, open boxes).

Only H3K9acK14ac showed a significant increase at the liver elements when the foregut endoderm cells differentiated into hepatoblasts (Fig. 1, solid boxes, $P < 0.001$). H3K4me2/3, H3K20me3, and H3K36me2 exhibited variable changes, and none of the other chromatin marks changed significantly (fig. S4). Hyperacetylation persisted at the *Pdx1* elements in hepatoblasts, where the gene remained silent, as did H3K27me3 (Fig. 1, solid boxes). By contrast, silent promoters that are active in adipocytes and T cells (*20*, *21*) lacked both marks in endoderm and hepatoblasts (fig. S5). We conclude that the silent liver and pancreas regulatory elements exhibit distinct chromatin states.

The histone acetyltransferase genes *Gcn5l2*, *CBP*, or *P300* are needed for gastrulation, whereas *P/CAF* is dispensable (*22*–*24*). Notably, FACS revealed a statistically significant decrease in the number of hepatoblasts in $P300^{+/-}$ embryos, which were otherwise viable (Fig. 2A and fig. S6, A to C), and no change in $Gcn5l2^{+/-}$ (fig. S7A). Analysis of *Gcn5/2* nulls in the endoderm (*25*) revealed no defects in liver or pancreas induction and no compensatory up-regulation of *P/CAF* (fig. S7, B and C).

We performed ChIP analyses with undifferentiated endoderm, wild-type hepatoblasts, and $P300^{+/-}$ hepatoblasts with the use of antibodies against H3K9acK14ac, H2BK5ac, and H4K5ac, which are all targeted by P300 but not GCN5l2 (*26*, *27*). The acetylations coordinately increased at the liver elements when endoderm cells differentiated into wild-type hepatoblasts and failed to do so in $P300^{+/-}$ hepatoblasts (Fig. 2B).

In situ hybridization for *Afp* RNA revealed that there is a smaller liver bud in $P300^{+/-}$ embryos relative to the wild type (Fig. 2C). $P300^{+/-}$ embryos had more $PDX1^+$ ventral endoderm cells (Fig. 2D, $P < 0.01$), whereas no difference was seen in dorsal pancreatic endoderm (fig. S6D). The expression of the earliest liver-specific genes was diminished in $P300^{+/-}$ hepatoblasts, whereas *Pdx1* expression was increased in $P300^{+/-}$ $Liv2^-$ cells (i.e., the rest of the embryo) (fig. S6E, $P < 0.05$).

These findings show that *Gcn5l2* and *P/CAF* are not necessary for foregut endoderm differentiation, *P300* is necessary for acetylation at the liver-specific regulatory elements and full liver-specific gene activation, and *P300* modulates the specification of liver progenitors over pancreas progenitors. Notably, in $P300^{+/-}$ hepatoblasts there was no significant effect on the expression of the endodermal transcription factors *FoxA1*, *FoxA2*, *Gata4*, *Gata6*, *Hnf1b*, and *Hnf6*, or *Hnf4*, specific for liver, or *Smad4*, a bone morphogenetic protein (BMP) signaling effector (fig. S6F).

To address whether *P300* heterozygosity might have an earlier, indirect effect on endoderm differentiation, we set up cultures of anterior "halves" of 5-6S embryos, which conveniently undergo foregut and heart development in vitro (*28*). After 24 hours in the presence of the P300 inhibitor C646 (P300i) or a control compound (*29*), the growth of the half embryos was normal (fig.

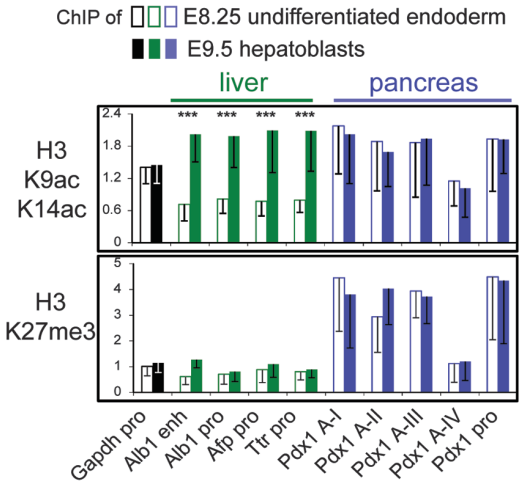

Fig. 1. Distinct chromatin marks at the earliest liver and pancreas genes. Black boxes indicate ChIP for histone modifications at regulatory elements of a constitutive gene; liver genes (green boxes) and a pancreas gene (blue boxes) are shown in undifferentiated endoderm (open boxes) and nascent hepatoblasts (solid boxes). Liver and pancreas genes are silent in endoderm, and only the liver genes become active in hepatoblasts. Signals ($n \geq 5$) over IgG were normalized by values at the *Gapdh* exon1 segment and shown as means ± SD; $^{***}P \leq 0.001$.

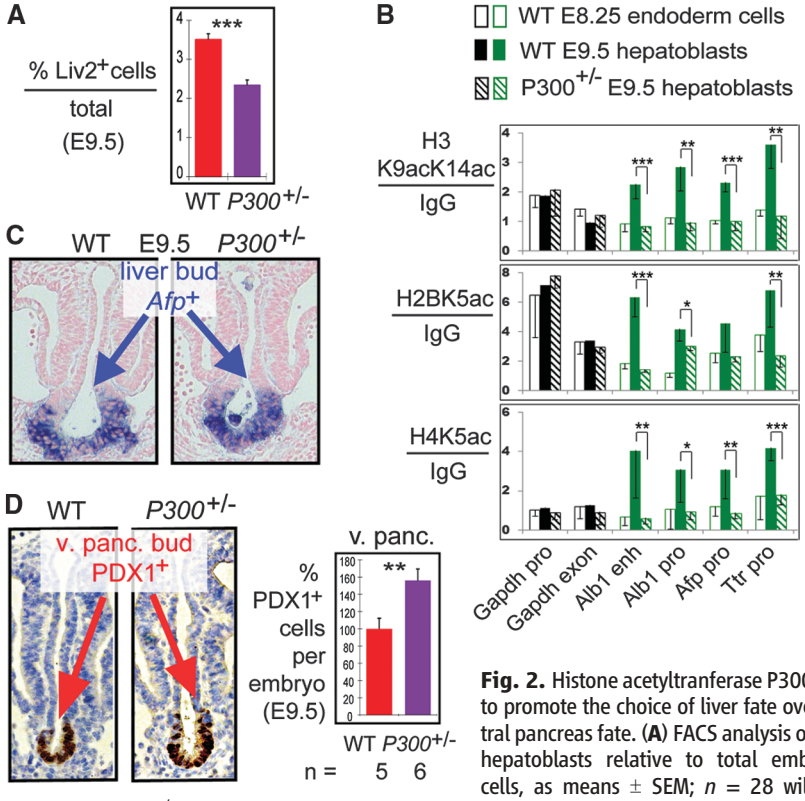

Fig. 2. Histone acetyltranferase P300 helps to promote the choice of liver fate over ventral pancreas fate. (**A**) FACS analysis of $Liv2^+$ hepatoblasts relative to total embryonic cells, as means ± SEM; $n = 28$ wild-type (WT) embryos, 21 $P300^{+/-}$ embryos. (**B**) ChIP assays as in Fig. 1 ($n \geq 5$). (**C**) In situ hybridization for *Afp* RNA in typical E9.5 sections. Largest sections of liver bud are shown. (**D**) Left: Immunohistochemistry for PDX1 in sections of E9.5 embryos; ventral (v.) pancreatic buds. Right: Quantitation of the total number of $PDX1^+$ cells in all sections throughout the ventral pancreatic buds, means ± SEM. $^*P < 0.05$, $^{**}P < 0.01$, $^{***}P < 0.001$.

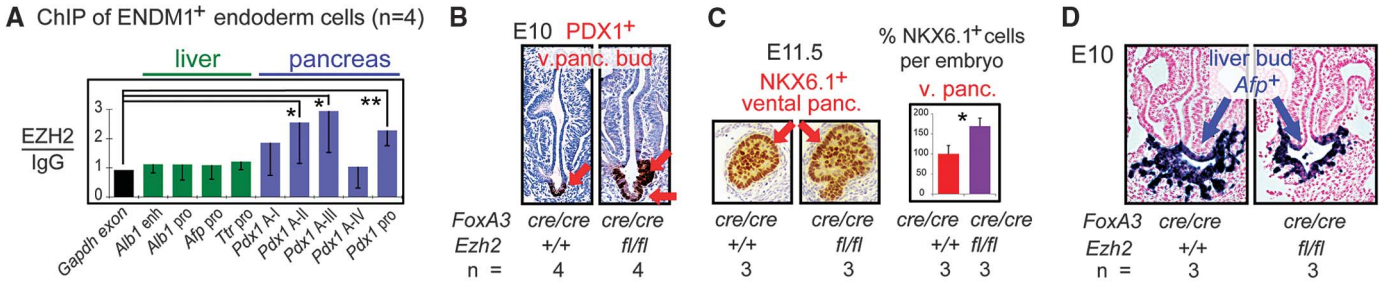

Fig. 3. The H3K27 methyltransferase gene *Ezh2* restricts the extent of ventral pancreas specification. (**A**) ChIP assays ($n = 4$), means ± SD. (**B**) Immunohistochemistry for PDX1 in cross sections of representative E10 embryos. (**C**) Immunohistochemistry for NKX6.1 in cross sections of representative E11.5 embryos, means ± SEM. (**D**) In situ hybridization for *Afp* RNA in cross sections of E10 embryos. $*P < 0.05$, $**P < 0.01$.

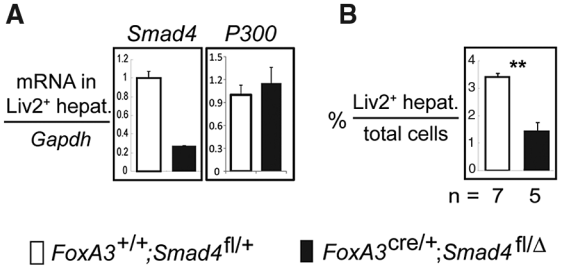

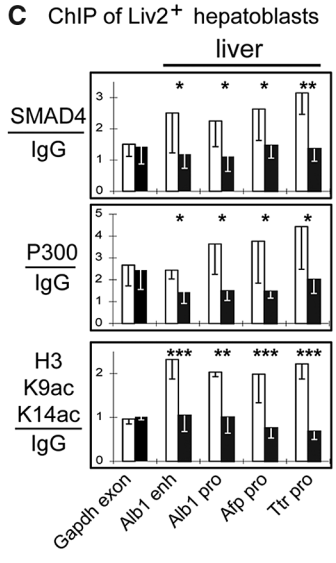

Fig. 4. BMP4 signaling regulates hepatic specification via a pathway to SMAD4 and P300. (**A**) *Smad4* and P300 expression by quantitative reverse transcription PCR relative to levels in Liv2+ WT cells, means ± SEM. (**B**) FACS analysis of the percentage (%) of Liv2+ hepatoblasts among total embryonic cells, means ± SEM. (**C**) ChIP assays ($n \geq 4$) in Liv2+ cells from WT or $FoxA3^{cre/+};Smad4^{CA}$ embryos, means ± SD. $*P < 0.05$, $**P < 0.01$, $***P < 0.001$.

S8A). We observed a significant reduction in the number of hepatoblasts in P300i-treated embryos (fig. S8B, $P < 0.001$). P300i also inhibited the induction of liver genes in hepatoblasts and stimulated *Pdx1* expression in Liv2− cells without affecting the expression of *P300* itself (fig. S8C). Hence, the genetic and pharmacologic data indicate that P300 modulates the choice between liver and pancreas fates.

EZH2, a member of the PRC2 Polycomb complex, is a methyltransferase for H3K27me3 (*30*). ChIP in wild-type endoderm cells revealed that EZH2 was enriched at the upstream elements of the *Pdx1* gene where H3K27me3 was present, and that EZH2 was absent from the liver regulatory elements (Fig. 3A, $P < 0.05$). We used an *Ezh2* conditional allele ($Ezh2^{CA}$) (*31*) and a $FoxA3^{Cre}$ transgene (*32*) to delete *Ezh2* in foregut endoderm cells. Strikingly, the $FoxA3^{Cre/Cre};Ezh2^{CA/CA}$ embryos, by E10, exhibited an expanded PDX1+ ventral pancreatic progenitor domain, with multiple bud-like structures (Fig. 3B, arrows), but no change in the dorsal pancreatic domain (fig. S9A). By E11.5, the size of ventral, but not dorsal, pancreas was markedly increased (Fig. 3C and fig. S9B). There was no change in cell proliferation (fig. S9C). This occurred at the expense of liver development, as the liver bud was smaller and less extensively penetrated the mesenchyme (Fig. 3D). Thus, *Ezh2* indirectly promotes the liver program by restraining the extent of ventral pancreatic specification in the endoderm.

Previously, we found that BMP signaling promotes the liver fate over the pancreas fate in the ventral endoderm, and shortly afterward, BMP enhances pancreatic specification (*28*). SMAD proteins are BMP effectors and interact with P300 (*33*, *34*). FACS analysis of half embryos (3-4S) revealed that the number of Liv2+ hepatoblasts was slightly increased after BMP4 treatment, as was the expression of liver genes in Liv2+ cells, without affecting proliferation (fig. S10, A to D). BMP4 treatment increased histone acetylation only at the liver regulatory elements, not at *Pdx1* elements (fig. S10E, $P < 0.05$).

Deletion of *Smad4* in the foregut endoderm led to an expected (*28*, *35*) decrease in *Smad4* expression in Liv2+ hepatoblasts as well as a decrease in the number of hepatoblasts, but no effect on *P300* was observed (Fig. 4, A and B). ChIP of hepatoblasts from $FoxA3^{Cre};Smad4^{CA}$ embryos revealed a loss of SMAD4 from the liver regulatory elements, a loss of P300 at the liver elements, and diminished H3 acetylation (Fig. 4C, black bars). Taken together, these studies reveal a pathway by which the BMP signal is mediated by SMAD4, which recruits P300 and results in histone acetylation at liver target elements, enhanced liver gene activation, and enhanced liver bud emergence (fig. S11).

By screening chromatin sites that were small in number and necessary for an impending cell choice, for many different chromatin marks in progenitor cells, we obtained clues about relevant histone modifiers. The modifiers function in conjunction with, rather than modify the expression of, known endoderm transcription factors. We suggest that spatially localized signaling to the endoderm with P300 recruitment to particular chromatin sites could help to initiate the liver program. Despite a failure to induce acetylation of liver-specific regulatory elements in $P300^{+/-}$ or $Smad4^{-/-}$ embryos, the induction of liver progenitors was reduced but not eliminated. We thus suggest that the histone modifications or P300 itself, or both, play a modulatory role rather than one of absolute governance of liver induction. Further studies are required to determine how these events at a specific moment in development link to the subsequent maintenance of the hepatic program.

Given that the H3K27me3 mark is not seen at the *Pdx1* sites after the pancreas is induced (*36*), EZH2 complexes in the endoderm restrain pancreatic commitment. The persistence of both H3Ac and H3K27me3 marks on the silent *Pdx1* gene in sorted hepatoblasts is consistent with their coexistence on individual genes. Such has been seen in embryonic stem cells (*37*) and may constitute a new kind of "bivalent" mark at silent genes that are destined for activation in development. These results could explain the results of tissue explant studies indicating that the ventral endoderm is inherently set to express the pancreatic program (*5*). We note that the regulatory elements at silent liver genes in the endoderm lacked the H3K4/H3K27 bivalent marks seen in pluripotent cells (*1*).

The distinct histone modification states at the liver and pancreas regulatory elements in endoderm indicate a chromatin "prepattern" in undifferentiated, multipotent cells. The enzymes that elicit the prepattern play a modulatory role in a

cell fate decision. We suggest that identifying such prepatterns in other progenitors could help to predict lineage-specific developmental potential. Such information from native embryonic cells can be used to define benchmarks of proper progenitor cell programming from stem cells. In addition, the relevant chromatin-modifying enzymes can serve as pharmacologic targets to enhance particular cell fate transitions from stem cells, as we did with P300 from native endoderm.

References and Notes

1. B. E. Bernstein *et al.*, *Cell* **125**, 315 (2006).
2. A. Rada-Iglesias *et al.*, *Nature* **470**, 279 (2011).
3. J. Xu *et al.*, *Genes Dev.* **23**, 2824 (2009).
4. J. A. Dahl, P. Collas, *Nat. Protoc.* **3**, 1032 (2008).
5. G. Deutsch, J. Jung, M. Zheng, J. Lóra, K. S. Zaret, *Development* **128**, 871 (2001).
6. R. Bort, J. P. Martinez-Barbera, R. S. Beddington, K. S. Zaret, *Development* **131**, 797 (2004).
7. K. S. Zaret, *Nat. Rev. Genet.* **9**, 329 (2008).
8. P. Gadue *et al.*, *Stem Cells* **27**, 2103 (2009).
9. R. Gualdi *et al.*, *Genes Dev.* **10**, 1670 (1996).
10. T. Watanabe *et al.*, *Dev. Biol.* **250**, 332 (2002).
11. K. Gorski, M. Carneiro, U. Schibler, *Cell* **47**, 767 (1986).
12. J. K. Liu, C. M. DiPersio, K. S. Zaret, *Mol. Cell. Biol.* **11**, 773 (1991).
13. M. H. Feuerman, R. Godbout, R. S. Ingram, S. M. Tilghman, *Mol. Cell. Biol.* **9**, 4204 (1989).
14. R. H. Costa, D. R. Grayson, J. E. Darnell Jr., *Mol. Cell. Biol.* **9**, 1415 (1989).
15. D. F. Boyer *et al.*, *Dev. Biol.* **298**, 616 (2006).
16. N. Gao *et al.*, *Genes Dev.* **22**, 3435 (2008).
17. K. Gerrish, J. C. Van Velkinburgh, R. Stein, *Mol. Endocrinol.* **18**, 533 (2004).
18. S. Y. Roth, J. M. Denu, C. D. Allis, *Annu. Rev. Biochem.* **70**, 81 (2001).
19. J. A. Simon, R. E. Kingston, *Nat. Rev. Mol. Cell Biol.* **10**, 697 (2009).
20. L. Qiao, J. Shao, *J. Biol. Chem.* **281**, 39915 (2006).
21. F. Seydel *et al.*, *J. Autoimmun.* **31**, 377 (2008).
22. W. Xu *et al.*, *Nat. Genet.* **26**, 229 (2000).
23. T. P. Yao *et al.*, *Cell* **93**, 361 (1998).
24. T. Yamauchi *et al.*, *Proc. Natl. Acad. Sci. U.S.A.* **97**, 11303 (2000).
25. W. Lin *et al.*, *Dev. Dyn.* **237**, 928 (2008).
26. R. L. Schiltz *et al.*, *J. Biol. Chem.* **274**, 1189 (1999).
27. T. Kouzarides, *Cell* **128**, 693 (2007).
28. E. Wandzioch, K. S. Zaret, *Science* **324**, 1707 (2009).
29. E. M. Bowers *et al.*, *Chem. Biol.* **17**, 471 (2010).
30. R. Cao *et al.*, *Science* **298**, 1039 (2002).
31. I. H. Su *et al.*, *Nat. Immunol.* **4**, 124 (2003).
32. C. S. Lee, J. R. Friedman, J. T. Fulmer, K. H. Kaestner, *Nature* **435**, 944 (2005).
33. C. Pouponnot, L. Jayaraman, J. Massagué, *J. Biol. Chem.* **273**, 22865 (1998).
34. M. P. de Caestecker *et al.*, *J. Biol. Chem.* **275**, 2115 (2000).
35. G. C. Chu, N. R. Dunn, D. C. Anderson, L. Oxburgh, E. J. Robertson, *Development* **131**, 3501 (2004).
36. J. van Arensbergen *et al.*, *Genome Res.* **20**, 722 (2010).
37. V. Azuara *et al.*, *Nat. Cell Biol.* **8**, 532 (2006).

Acknowledgments: We thank T. Jiang, R. Hardy, J. Oesterling, and W. DeMuth for assistance; Z. Zhang, J. Xu, and S. Hua for advice; P. Streeter and K. Kaestner for reagents; J. Epstein, E. Wandzioch, D. Metzger, A. Wecker, A. Hines, and D. Freedman-Cass for comments; and E. Pytko for preparing the manuscript. Supported by the FAMRI Foundation and NIH grant U54MH084691 (P.A.C. and D.J.M.), NIH grant RO1 GM067718 (S.D.), and NIH grants R37GM36477 and U01DK072503 (K.S.Z.). There is a patent on P300i: "Methods and compositions for modulating p300/CBP activity" (pub. WO/2008/157680; international application PCT/US2008/067477 to D.J.M. and P.A.C.). P.A.C. is co-founder, owns equity, and receives consulting fees as science advisor to Acylin Therapeutics, which is attempting the development of clinically useful HAT inhibitors and licenses from Johns Hopkins some of our discoveries related to C646.

Supporting Online Material

www.sciencemag.org/cgi/content/full/332/6032/963/DC1
Materials and Methods
Figs. S1 to S12
Tables S1 to S3
References

13 January 2011; accepted 8 April 2011
10.1126/science.1202845

Spatial Coupling of mTOR and Autophagy Augments Secretory Phenotypes

Masako Narita,[1]* Andrew R. J. Young,[1]* Satoko Arakawa,[2] Shamith A. Samarajiwa,[1,3] Takayuki Nakashima,[1]† Sei Yoshida,[4] Sungki Hong,[4] Lorraine S. Berry,[1] Stefanie Reichelt,[1] Manuela Ferreira,[1]‡ Simon Tavaré,[1,3] Ken Inoki,[4] Shigeomi Shimizu,[2] Masashi Narita[1]§

Protein synthesis and autophagic degradation are regulated in an opposite manner by mammalian target of rapamycin (mTOR), whereas under certain conditions it would be beneficial if they occurred in unison to handle rapid protein turnover. We observed a distinct cellular compartment at the trans side of the Golgi apparatus, the TOR-autophagy spatial coupling compartment (TASCC), where (auto)lysosomes and mTOR accumulated during Ras-induced senescence. mTOR recruitment to the TASCC was amino acid– and Rag guanosine triphosphatase–dependent, and disruption of mTOR localization to the TASCC suppressed interleukin-6/8 synthesis. TASCC formation was observed during macrophage differentiation and in glomerular podocytes; both displayed increased protein secretion. The spatial coupling of cells' catabolic and anabolic machinery could augment their respective functions and facilitate the mass synthesis of secretory proteins.

During oncogene-induced senescence (OIS), a dynamic transition in phenotype is mediated by multiple effector mechanisms, including the secretory phenotype (*1*, *2*) and autophagy (*3*). Senescent cells continue to grow in size and produce large amounts of secretory proteins; therefore, protein synthesis also seems to be activated. The active protein turnover caused by coupling protein degradation and synthesis may facilitate acute phenotypic regeneration. To understand how these processes are coregulated during OIS, we examined the spatial relation between mammalian target of rapamycin (mTOR) (*4*, *5*) and autophagy (*6*, *7*) in IMR90 cells stably expressing 4-hydroxytamoxifen (4OHT)–inducible H-*Ras*V12 (ER:Ras) (*3*, *8*).

Autophagy markers, p62 and LC3, formed prominent puncta and colocalized throughout the cytoplasm upon amino acid (AA) starvation in IMR90 cells, whereas growing cells only formed occasional puncta (Fig. 1A) (*9*–*11*). In contrast, during Ras-induced senescence (RIS), cells exhibited distinct cytoplasmic areas that were enriched for p62 and LC3 (Fig. 1A). This autophagic area overlapped with senescence-associated–β-galactosidase activity (a lysosomal enzyme) and LAMP2 (a lysosomal protein), suggesting autolysosome enrichment (Fig. 1A and fig. S1, A and B). Locally concentrated p62 can form detergent-insoluble aggresomes. However, they typically do not colocalize to lysosomes (*11*, *12*), and there was no increase in p62 or LC3 in the Triton X-insoluble fraction during RIS (Fig. 1B), indicating active autophagy (fig. S1C).

We next determined the subcellular localization of mTOR, which also congregated in distinct cytoplasmic areas in RIS cells, but not in growing cells (Fig. 1C). The mTOR-, LAMP2-, and p62-positive areas overlapped (Fig. 1, C and D, and fig. S1D). Furthermore, the mTOR and LAMP2 signals were spatially associated with each other more frequently inside than outside these areas (fig. S2). Thus, protein degradation and synthesis may be spatially coupled during RIS in an area we call the TOR-autophagy spatial coupling compartment (TASCC).

mTOR complex 1 (mTORC1) negatively regulates autophagy upstream of the Atg1/ULK complex, which plays an essential role at the early stage of autophagosome formation (*13*, *14*). To test whether autophagosomes are formed outside the TASCC and then move into the TASCC to form autolysosomes, we examined the location of ULK1 and ATG12, which only localize transiently to developing autophagosomes (*15*–*17*). The developing autophagosomes containing

[1]Cancer Research UK Cambridge Research Institute (CRI), Li Ka Shing Centre, Robinson Way, Cambridge CB2 0RE, UK. [2]Department of Pathological Cell Biology, Medical Research Institute, Tokyo Medical and Dental University, 1-5-45 Yushima, Bunkyo-ku, Tokyo 113-8510, Japan. [3]Department of Oncology, University of Cambridge, Cambridge CB2 0RE, UK. [4]Life Sciences Institute, Department of Molecular and Integrative Physiology and Internal Medicine, University of Michigan, 210 Washtenaw Avenue, Ann Arbor, MI 48109, USA.

*These authors contributed equally to this work.
†Present address: Kyowa Hakko Kirin, Shizuoka 411-8731, Japan.
‡Present address: Instituto de Medicina Molecular, Faculdade de Medicina de Lisboa, 1649-028 Lisbon, Portugal.
§To whom correspondence should be addressed. E-mail: masashi.narita@cancer.org.uk

ULK1/ATG12 were indeed excluded from the TASCC (Fig. 1E, fig. S3, and movie S1). In addition, we used tandem monomeric red fluorescent protein–green fluorescent protein (mRFP-GFP)–LC3, in which GFP is more sensitive to acidic conditions than mRFP. Thus, both signals are active in autophagosomes, but the mRFP signal is predominant in autolysosomes (*10*, *18*). The TASCC was mostly occupied by autolysosomes with a prominent red signal, whereas mixed signals from green and red were found in the isolated puncta surrounding the TASCC (fig. S4). Spatial organization of mTOR and developing autophagosomes may thus allow their simultaneous activation.

Electron microscopy (EM) analysis also revealed a distinctive cytoplasmic compartmentalization in RIS cells, with prominent autophagic vacuoles (Fig. 2, A to E). Well-developed Golgi apparatus (GA) and vesicles were enriched around these compartments and rough endoplasmic reticulum (rER) was often found adjacent to them, suggesting that high levels of protein synthesis take place around them (fig. S5). Confocal images showed that the trans-Golgi network (TGN), which typically exhibited a perinuclear pattern in growing cells, was mostly positioned close to the TASCC (fig. S6). Fluorescence-EM imaging confirmed the spatial relation between the GA, rER, and TASCC (Fig. 2, B to E, and fig. S7). The TASCC-GA association was recapitulated in mouse papillomas, an in vivo OIS model (fig. S8).

Lysosomal, membrane, and secretory proteins newly synthesized at the rER are processed within the GA and sorted into the TGN. To directly visualize this process, we performed metabolic labeling using a Click-iT (Invitrogen, Carlsbad, CA) methionine analog, L-homopropargylglycine (HPG), which allows us to detect nascent proteins by fluorescence (fig. S9). A 30-min pulse of HPG in RIS cells resulted in a cytoplasmic distribution of the nascent proteins, which were excluded from the TASCC but enriched in the TGN (Fig. 2F). After a 90-min chase with normal medium, labeled proteins were readily detected in the TASCC, confirming that proteins actively processed through the rER-GA were enriched in the TASCC (Fig. 2G). Consistently, interleukins 6 and 8 (IL-6/8), senescence-associated secretory proteins, were enriched in the TGN and/or TASCC in RIS cells (fig. S6). After shorter labeling (3 min), nascent proteins were often enriched in the area close to the TASCC (Fig. 2H and fig. S9D). The labeled proteins did not yet overlap with the TGN; thus, the signal is likely to represent sites of protein synthesis. Similarly, *IL-8* mRNA was detected at the marginal regions of the TASCC, particularly during the early phase of RIS (fig. S10).

To further characterize the TASCC, we asked whether the microtubule depolymerizing drug nocodazole affects TASCC formation (fig. S11). The TASCC was intact after 2 hours of treatment on day 4, suggesting that microtubules were not required for TASCC maintenance (Fig. 3A). Similarly, nocodazole did not prevent TASCC induction when added upon Ras induction and subsequently for 24 hours (Fig. 3B). Nocodazole fragments GA, causing "mini-stacks," which are functionally active (*19*). The spatial relation between the TASCC and the mini-stacks was preserved (Fig. 3, C and D), reinforcing the importance of the process of protein transfer through the rER-GA-TASCC. We next assessed the requirement for a functional rER-GA system for TASCC formation using brefeldin A (BFA), which effectively blocks protein transport from the ER to the GA. BFA did not affect TASCC maintenance, but it did prevent TASCC formation (Fig. 3B and fig. S11). Importantly, basal non-TASCC lysosomes were intact (Fig. 3E), suggesting that de novo lysosome biogenesis is critical for TASCC induction. Functional Gene Ontology analysis of day 4 expression microarray data revealed significant enrichment for genes involved in membrane biogenesis, including lysosomes, GA, and ER (fig. S12 and table S1). Thus, activated lysosomal and membrane biogenesis may contribute to TASCC formation in the vicinity of the TGN, where secretory proteins are also processed.

The Rag/Gtr family of small guanosine triphosphatases (GTPases) mediate AA signaling to TORC1 (*20*, *21*). In mammalian cells, in response to AAs, the Rag GTPase complex recruits mTORC1 to lysosomes, where mTOR is activated by Rheb (*20*, *22*). Dominant negative (DN) forms of Rag GTPases can disrupt the AA-mediated mTORC1-lysosome association (*20*–*22*). We tested whether Rag GTPases are involved in TASCC-formation. RagB/C were enriched in the TASCC (fig. S13A). When *RagB*-DN was stably expressed in ER:Ras cells (fig. S13B), there was no obvious effect on LAMP2 enrichment at day 4 (Fig. 4A), nor on total mTOR levels (fig. S13C). However, mTOR enrichment in this area was significantly suppressed (Fig. 4A). The induction of IL-6/8 during RIS was substantially inhibited posttranscriptionally, indicating a role for Rag GTPase–mediated mTOR-lysosome association in the TASCC (Fig. 4B and fig. S13D).

Because Rag GTPases are AA-specific TOR regulators, we asked whether AAs derived from (auto)lysosomes within the TASCC reinforce mTOR recruitment. We treated cells with inhibitors of lysosomal proteases [E64d and pepstatin

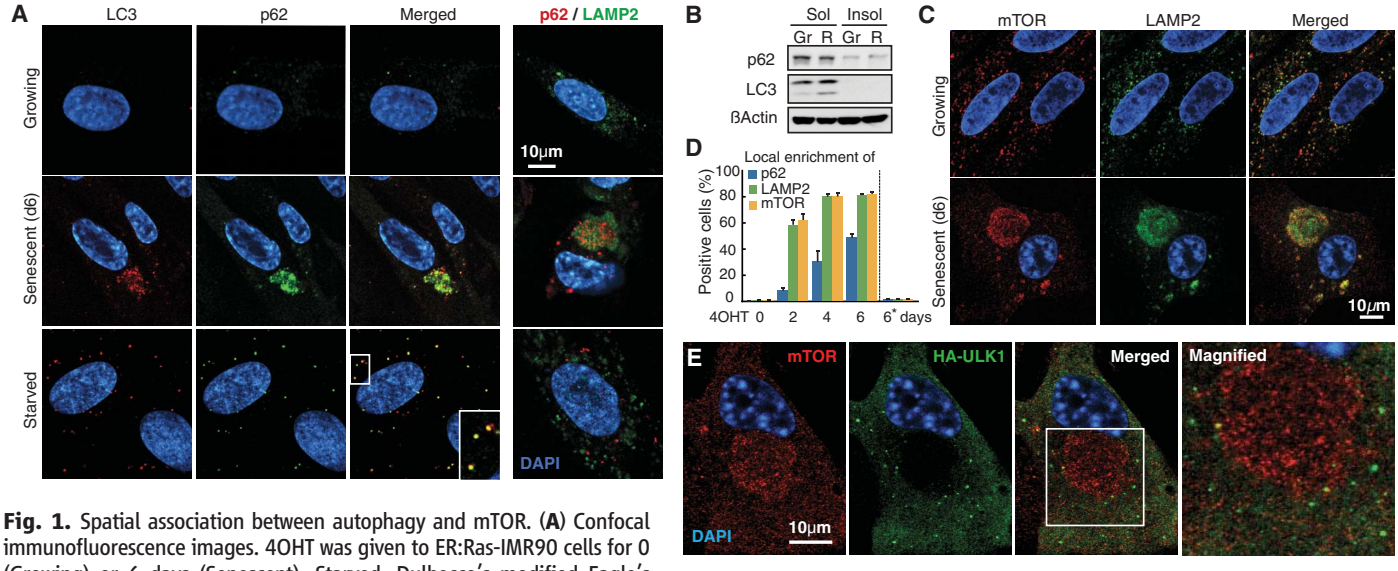

Fig. 1. Spatial association between autophagy and mTOR. (**A**) Confocal immunofluorescence images. 4OHT was given to ER:Ras-IMR90 cells for 0 (Growing) or 6 days (Senescent). Starved, Dulbecco's modified Eagle's medium without amino acids or serum for 2 hours. DAPI, 4′,6-diamidino-2-phenylindole. (**B**) Immunoblot analysis for indicated proteins in 1% Triton-X100 soluble (Sol) and insoluble (Insol) fractions from growing (Gr) and Ras-induced senescent (R) cells. (**C**) Confocal images of mTOR and LAMP2 immunofluorescence. (**D**) Quantification of TASCC-formation kinetics (mean ± SEM; $n \geq 3$ independent experiments). The asterisk indicates parental cells treated with 4OHT for 6 days. (**E**) Confocal images of mTOR and hemagglutinin (HA) immunofluorescence in HA-ULK1–expressing ER:Ras-IMR90 cells.

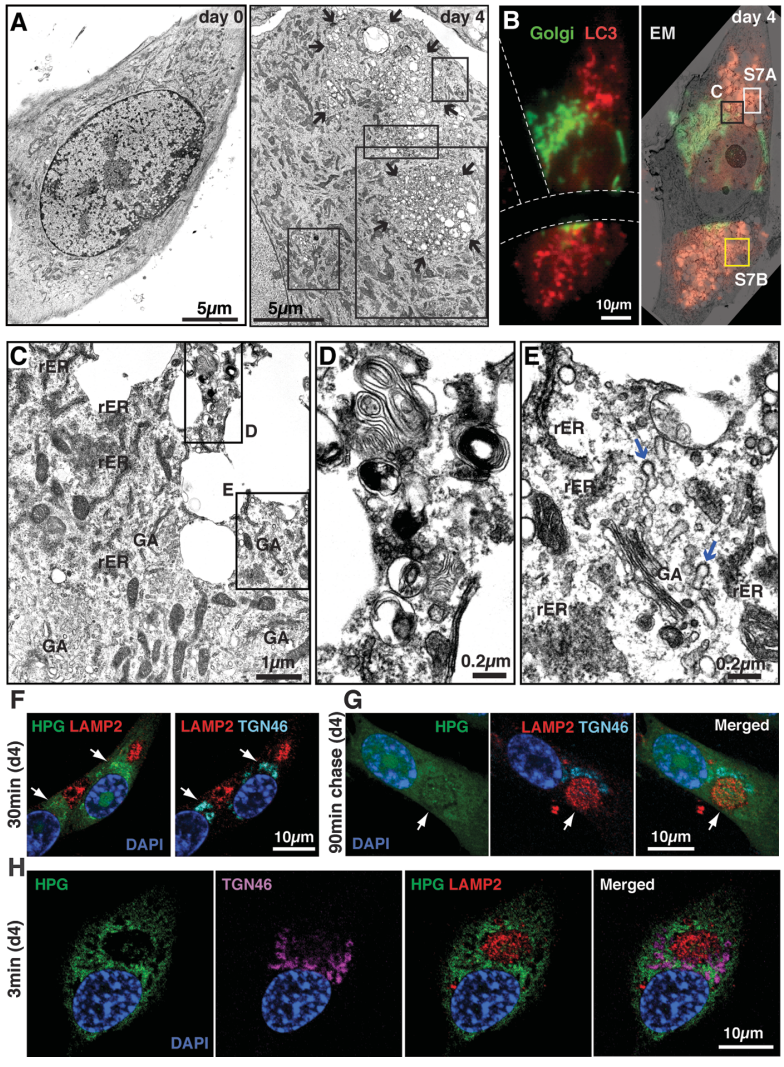

Fig. 2. Spatial association between TASCC and secretory apparatus. (**A**) EM of ER:Ras-IMR90 cells. 4OHT was given for 0 or 4 days. Arrows denote TASCC. Regions indicated by rectangles are magnified in fig. S5. (**B** to **E**) Fluorescence EM. LC3 (RFP) and Golgi (GFP) were BacMam system–labeled at day 4. Dashed lines represent grid on cover slip (B). Regions indicated by rectangles are magnified in corresponding figure panels (see also fig. S7). Blue arrows in (E) denote GA-derived coated vesicles. (**F** to **H**) Visualization of nascent protein synthesis during Ras-induced senescence (see fig. S9). After 30-min labeling with HPG in day 4 Ras-induced senescent cells (d4), nascent protein was accumulated in TGN (arrows), but not in the TASCC (F). After 90-min chase, nascent protein was readily detected in TASCC (arrows) (G). Short-term (3 min) labeling of HPG to visualize sites of protein synthesis (H).

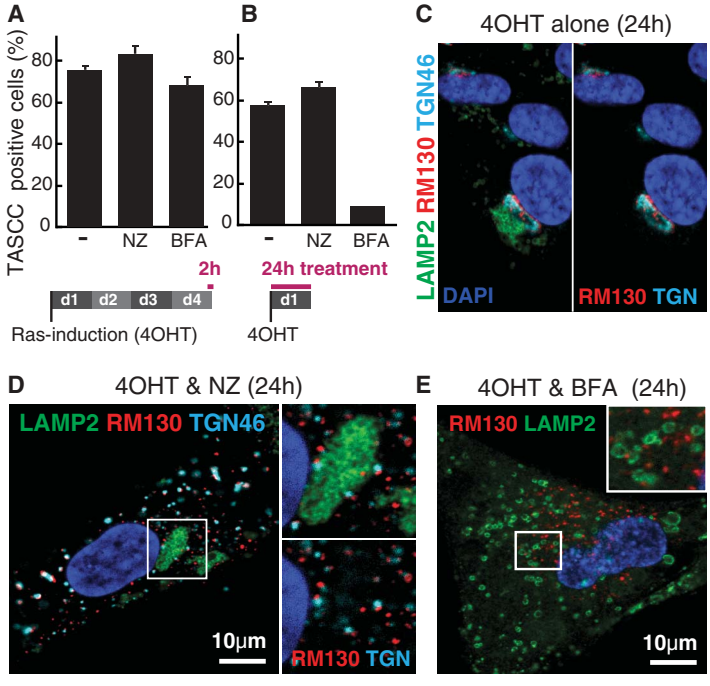

Fig. 3. BFA, but not nocodazole, prevents TASCC formation. (**A** and **B**) ER:Ras-IMR90 cells were treated with 10 μM nocodazole (NZ) or 40 ng/ml BFA, which were added after (A) or before (B) TASCC establishment. TASCC was assessed by mTOR/LAMP2 immunofluorescence. Error bars indicate SEM. (**C** to **E**) Representative confocal images of cells treated as in (B). RM130 and TGN46, cis- and trans-Golgi network markers, respectively.

A (E&P)] and/or AA-free media (Fig. 4C). AA depletion showed no obvious effect on the local accumulation of LAMP2 in RIS cells. Three-hour treatment of day 4 ER:Ras cells with E&P or AA-free medium alone showed only marginal effects on mTOR accumulation in the TASCC. When E&P and AA-free medium were combined, enrichment of mTOR was significantly reduced, whereas enrichment of RagB, which constitutively localizes to lysosomes (*22*), was not reduced (Fig. 4C and fig. S14). The effect of adding E&P to the AA-free medium on mTOR dispersion was also significant, indicating a contribution of (auto)lysosome-derived AAs to mTOR recruitment at the TASCC (Fig. 4C). Similar results were obtained with ATG5 knockdown (fig. S15).

To identify the TASCC in different systems, we chose HL60 human promyelocytic leukemia cells, which can be differentiated into macrophage-like cells by 12-*O*-tetradecanoylphorbol-13-acetate (TPA) with transient up-regulation of *IL-8*. We found that this surge in IL-8 production was associated with the concomitant activation of autophagy (fig. S16, A to C). After TPA treatment, a substantial population of attached cells exhibited local enrichment for mTOR, RagB, lysosomes, and autophagy vacuoles at perinuclear regions, which were spatially associated with IL-8 and TGN, suggesting that the TASCC is also involved in macrophage differentiation (fig. S10C and fig. S16, D to F).

Looking for TASCC in a more physiological setting, we examined mouse renal glomerular podocytes, a core element of the filtration barrier in glomeruli. Podocytes, identified within regions facing capsule space in glomerulus sections (Fig. 4D), play a critical role in the constant turnover of glomerular basement membrane and endothelium maintenance by secreting vascular endothelial growth factor (VEGF) and many other factors. Podocytes exhibit an unusually high level of constitutive autophagy (*23*), suggesting simultaneous activation of anabolic and catabolic processes. We detected prominent GA, which were accompanied by enriched VEGF, mTOR, Lamp2, and LC3 (Fig. 4, E and F).

Recent reports have shown that AA re-addition induces Rag GTPase–dependent mTORC1-lysosome compartmentalization (*20*, *22*), and we now provide evidence for functional relevance for this process. We propose a model that may explain how cells can activate both protein synthesis and autophagic degradation (fig. S17). The spatial integration of rER-GA, autolysosomes, and mTOR creates a self-enhancing system, in which autolysosome-derived AAs reinforce mTOR enrichment and activity (*24*), leading to the efficient synthesis of secretory and lysosomal proteins (*5*). Furthermore, the TASCC might also function to sequester mTOR. Because the TASCC can be found in diverse contexts, it may represent a general mechanism for rapid protein turnover.

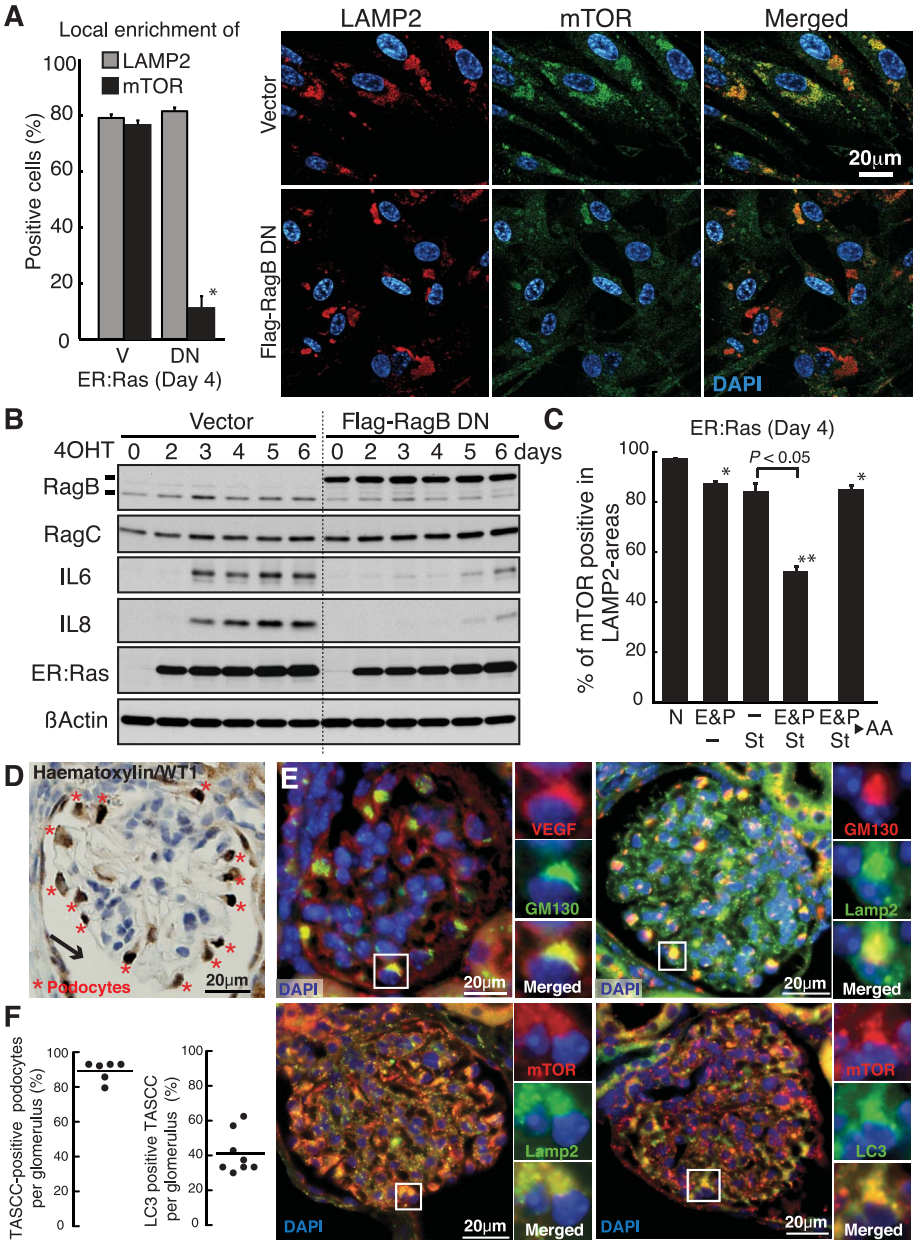

Fig. 4. Functional implication of TASCC. (**A** and **B**) ER:Ras-IMR90 cells expressing vector (V) or dominant negative mutant *RagB*-T54N (DN) were assessed for mTOR enrichment to LAMP2 compartments by immunofluorescence (mean ± SEM; $n = 3$) (A). $^{*}P < 0.01$ relative to V. Immunoblot analysis at time points indicated after Ras-induction (B). (**C**) Effect of AA depletion on mTOR enrichment in LAMP2 compartments as in (A). Cells were incubated with AA-free medium supplemented with 10% dialyzed fetal bovine serum (St) and/or lysosomal protease inhibitors [10 μg/ml E64d and 25 μg/ml pepstatin A (E&P)] for 3 hours. N, normal medium (fig. S14). As an additional control, we restored essential AAs (4AA) for 30 min after E&P/St treatment (mean ± SEM; $n = 3$). $^{*}P < 0.05$; $^{**}P < 0.01$ relative to N. (**D**) Typical immunohistochemical image of mouse glomerulus. WT1, podocyte marker; arrow, capsule space. (**E**) Representative images for indicated proteins in mouse glomeruli show TASCC in podocytes. (**F**) Percentages of TASCC-positive podocytes (left) and LC3 enrichment per TASCC-positive podocytes (right) in each glomerulus section were plotted. The black circles represent glomeruli sampled from two mice.

References and Notes

1. T. Kuilman, D. S. Peeper, *Nat. Rev. Cancer* **9**, 81 (2009).
2. J. P. Coppé, P. Y. Desprez, A. Krtolica, J. Campisi, *Annu. Rev. Pathol.* **5**, 99 (2010).
3. A. R. J. Young *et al.*, *Genes Dev.* **23**, 798 (2009).
4. S. Wullschleger, R. Loewith, M. N. Hall, *Cell* **124**, 471 (2006).
5. X. M. Ma, J. Blenis, *Nat. Rev. Mol. Cell Biol.* **10**, 307 (2009).
6. C. He, D. J. Klionsky, *Annu. Rev. Genet.* **43**, 67 (2009).
7. H. Nakatogawa, K. Suzuki, Y. Kamada, Y. Ohsumi, *Nat. Rev. Mol. Cell Biol.* **10**, 458 (2009).
8. Materials and methods are available as supporting material on *Science* Online.
9. Y. Kabeya *et al.*, *EMBO J.* **19**, 5720 (2000).
10. S. Pankiv *et al.*, *J. Biol. Chem.* **282**, 24131 (2007).
11. M. Komatsu *et al.*, *Cell* **131**, 1149 (2007).

12. J. A. Johnston, C. L. Ward, R. R. Kopito, *J. Cell Biol.* **143**, 1883 (1998).
13. N. Mizushima, *Curr. Opin. Cell Biol.* **22**, 132 (2010).
14. E. Y. Chan, S. Kir, S. A. Tooze, *J. Biol. Chem.* **282**, 25464 (2007).
15. T. Hara *et al.*, *J. Cell Biol.* **181**, 497 (2008).
16. C. H. Jung *et al.*, *Mol. Biol. Cell* **20**, 1992 (2009).
17. N. Mizushima, T. Yoshimori, B. Levine, *Cell* **140**, 313 (2010).
18. S. Kimura, T. Noda, T. Yoshimori, *Autophagy* **3**, 452 (2007).
19. J. Thyberg, S. Moskalewski, *Exp. Cell Res.* **246**, 263 (1999).
20. Y. Sancak *et al.*, *Science* **320**, 1496 (2008); 10.1126/science.1157535.
21. E. Kim, P. Goraksha-Hicks, L. Li, T. P. Neufeld, K.-L. Guan, *Nat. Cell Biol.* **10**, 935 (2008).
22. Y. Sancak *et al.*, *Cell* **141**, 290 (2010).
23. B. Hartleben *et al.*, *J. Clin. Invest.* **120**, 1084 (2010).
24. L. Yu *et al.*, *Nature* **465**, 942 (2010).

Acknowledgments: We thank K. Ryan, N. Mizushima, F. Watt, and R. Rios for reagents; R. Rios, D. Tuveson, T. Kanaseki, I. Mills, N. Dolman, and members of Narita lab for helpful discussion; L. Blackburn for editing; CRI's Genomics, Bioinformatics, Microscopy (J. Harris), and Histopathology facilities for technical support; and the Gurdon Institute's microscopy facility (A. Sossick) for optical microscopy experimental. This work was supported by the Univ. of Cambridge; Cancer Research UK; Hutchison Whampoa; Grants-in-Aid for Scientific Research from Ministry of Education, Culture, Sports, Science and Technology of Japan; the Program for Promotion of Fundamental Studies in the National Institute of Biomedical Innovation (S.A. and S.S.); and Juvenile Diabetes Research Foundation Award and NIH grant DK083491 (K.I.). Expression data are available at the National Center for Biotechnology Information Gene Expression Omnibus under accession number GSE28464.

Supporting Online Material

www.sciencemag.org/cgi/content/full/science.1205407/DC1
Materials and Methods
Figs. S1 to S17
Table S1
References
Movie S1

10 March 2011; accepted 11 April 2011
Published online 21 April 2011;
10.1126/science.1205407

Diet Drives Convergence in Gut Microbiome Functions Across Mammalian Phylogeny and Within Humans

Brian D. Muegge,[1] Justin Kuczynski,[2] Dan Knights,[3] Jose C. Clemente,[3] Antonio González,[3] Luigi Fontana,[4,5] Bernard Henrissat,[6] Rob Knight,[2,7] Jeffrey I. Gordon[1]*

Coevolution of mammals and their gut microbiota has profoundly affected their radiation into myriad habitats. We used shotgun sequencing of microbial community DNA and targeted sequencing of bacterial 16*S* ribosomal RNA genes to gain an understanding of how microbial communities adapt to extremes of diet. We sampled fecal DNA from 33 mammalian species and 18 humans who kept detailed diet records, and we found that the adaptation of the microbiota to diet is similar across different mammalian lineages. Functional repertoires of microbiome genes, such as those encoding carbohydrate-active enzymes and proteases, can be predicted from bacterial species assemblages. These results illustrate the value of characterizing vertebrate gut microbiomes to understand host evolutionary histories at a supraorganismal level.

Comparative culture-independent metagenomic studies of the microbial species assemblages that compose mammalian gut microbiota, and the functions that these communities encode in their aggregate genomes (microbiomes), can provide a complementary perspective to comparative studies of host genomes. A previous bacterial 16*S* ribosomal RNA (rRNA)–based study of 59 mammalian species revealed that their fecal microbiota clustered according to diet rather than host phylogeny (*1*). This finding raises several questions: What is the functional evolution of the gut microbiome in relation to diet? Is the process unique to each mammalian lineage? To what extent does microbial phylogeny predict function within microbial communities? Could analysis of interspecific differences among mammals create a pipeline for deciphering intraspecific differences among humans in response to varied diets or other factors? Therefore, we have extended our 16*S* rRNA studies to a broader sampling of microbial genes in total fecal community DNA prepared from herbivores, omnivores, and carnivores.

We generated shotgun pyrosequencing data sets from 33 mammalian species, along with newly collected bacterial 16*S* rRNA data. These adult animals represent 10 Orders and varied digestive physiologies (hindgut-fermenters, foregut-fermenters, and simple-gut). In some cases, free-living and captive representatives of a given species were sampled (Table 1 and table S1). Methods for classifying diets and for collecting and processing fecal samples for metagenomic analyses have been described (*1*). Multiplex pyrosequencing of amplicons generated from the V2 region of bacterial 16*S* rRNA genes yielded 149,675 high-quality de-noised reads (average = 3838 ± 1080 per sample) (table S2) (*2*). After chimera removal, 8541 operational taxonomic units (OTUs) were identified in the combined data set (an OTU was defined as reads sharing ≥97% nucleotide sequence identity). Shotgun sequencing of the same fecal DNA preparations produced 2,163,286 reads [mean = 55,469 ± 28,724 (SD) per sample; 261 ± 83 nt per read] (table S3) (*2*). Shotgun reads were functionally annotated using three databases: KEGG [for KEGG Orthology (KO) groups and Enzyme Commission (E.C.) numbers], CAZy (for carbohydrate-active enzymes), and MEROPS (for peptidases) (*3*–*5*). When shotgun reads were assigned to phylogenetic bins using the program MEGAN (*6*), the results revealed that fecal microbiomes were dominated by members of Bacteria, had low levels of Eukarya (0.15 to 5.35% of identifiable reads), and archaeons were variably represented (0 to 1.77% of assignable reads, with none detected in any carnivore microbiome). Seventeen samples had reads assigned to known viruses (table S4) (*2*).

Procrustes analysis (least-squares orthogonal mapping) was used to test whether the functional properties of a microbiome can be predicted from the bacterial species that compose it (*2*). Procrustes analysis attempts to stretch and rotate the points in one matrix, such as points obtained by principal coordinates analysis (PCoA), to be as close as possible to points in the other matrix, thus preserving the relative distances between points within each matrix (*7*, *8*) (Fig. 1A). We first took the 16*S* rRNA data set and used the UniFrac metric to compare the overlap between each pair of communities in terms of their evolutionary distance (*9*). The similarity in functional profiles was then determined using the Bray-Curtis distance metric applied to KO groups, E.C.s, CAZYmes, or peptidases. Principal-coordinates reduction was performed separately on the 16*S* rRNA and annotated shotgun (microbiome) data sets, and the point clouds were aligned using Procrustes. For each comparison, the goodness of fit, or M^2 value, of the transformed data sets was measured over the first three dimensions. The statistical significance of the goodness of the fit was measured by a Monte Carlo label permutation approach (*2*).

The agreement between phylogenetic and functional measurements was remarkable for all mammals, regardless of their diet, host lineage, or gut physiology. Figure 1, B to E, shows how the goodness of fit was robust to different functional databases. The analysis was also robust to taxon- or phylogenetic-based species classification, weighted or unweighted metrics, and whether one or more

[1]Center for Genome Sciences and Systems Biology, Washington University School of Medicine, St. Louis, MO 63108, USA. [2]Department of Molecular, Cellular and Developmental Biology, University of Colorado, Boulder, CO 80309, USA. [3]Department of Computer Science, University of Colorado, Boulder, CO 80309, USA. [4]Department of Medicine, Washington University School of Medicine, St. Louis, MO 63108, USA. [5]Division of Nutrition and Aging, Istituto Superiore di Sanità, Rome, Italy. [6]Architecture et Fonction des Macromolécules Biologiques, CNRS and Aix-Marseille Universities, Marseille, France. [7]Howard Hughes Medical Institute, Boulder, CO, USA.

*To whom correspondence should be addressed. E-mail: jgordon@wustl.edu

member of each mammalian species was considered (fig. S1). For both bacterial 16*S* rRNA and whole community gene data sets, the PCoA plots separated carnivores and omnivores from herbivores, emphasizing the importance of diet in differentiating gut microbial communities ($P <$ 0.05) (*2*). Our previous study using full-length 16*S* rRNA sequences revealed that the fecal microbiota of conspecifics were significantly more similar than the communities of different host species (*1*). The V2 16*S* rRNA data generated in this study confirmed this result, using both weighted and unweighted UniFrac distances ($P <$ 0.05 by 1000 Monte Carlo permutations) (*2*).

The Procrustes results prompted us to use a nearest-neighbor model to test whether the functional configuration of a microbiome could be predicted from its 16*S* rRNA sequences. Using a fecal sample's nearest neighbor, as defined by unweighted or weighted UniFrac, to predict the sample's functional profile generated a significantly better prediction than a random neighbor; this was true for KOs, E.C.s, CAZymes, and peptidases ($P < 0.0001$, 10^6 Monte Carlo permutations) (*2*).

The concordance of diet and microbiome structure and function raises the question of whether it is caused primarily by coevolution between mammals and their gut microbiota and microbiome, or by the many parallel dietary shifts that have occurred over the course of mammalian evolution (*10*). We tested which of these hypotheses, which have traditionally been viewed as competing but need not be mutually exclusive, were supported by looking for congruence between mammalian phylogeny and subsets of bacterial species, KOs, CAZymes, peptidases, or other enzymatic activities. Briefly, the mammalian phylogenetic tree defines sets of organisms that are monophyletic; that is, groups containing all and only the descendants of a common ancestor. We reasoned that if bacterial taxa or functions originated rarely, then these taxa or functions should be vertically transmitted during mammalian speciation. Therefore, there should be more cases in which a given taxon or function occurred in all members of a monophyletic mammalian group than chance would predict. Using this analytic approach (*2*), we found

Table 1. Overview of mammals in this study. Sample abbreviations used in figures and tables are noted in parentheses. See table S1 for additional details.

Foregut-fermenting herbivores
- Bighorn sheep 1 (BigHornSD)*
- Bighorn sheep 2 (BigHornW)‡
- Colobus (Colobus)†
- Gazelle (Gazelle3)†
- Giraffe (Giraffe2)†
- Rock hyrax 1 (HyraxSD)*
- Rock hyrax 2 (HyraxSTL)†
- Kangaroo (Kroo3)†
- Okapi 1 (Okapi1)†
- Okapi 2 (Okapi2)†
- Springbok (SpgbkW)‡
- Transcaspian Urial sheep (Urial2)†
- Visayan warty pig (VWPig)*

Carnivores
- Armadillo (Armadillo)†
- Bush dog (BushDog1)†
- Echidna (Echidna)†
- Hyena (Hyena2)†
- Lion 1 (Lion1)†
- Lion 2 (Lion2)†
- Polar bear (PolarBr2)†

Hindgut-fermenting herbivores
- African elephant (AfElphSD3)*
- Black rhinoceros (BlackRhino1)†
- Capybara (Capybara)†
- Gorilla (GorillaSTL)†
- Horse (Horse1)‡
- Orangutan (Orang1)†
- European rabbit (Rabbit)†
- Zebra (ZebraSTL1)†

Omnivores
- Baboon 1 (BaboonSTL)†
- Baboon 2 (BaboonW)‡
- Black bear (BlackBr2)†
- Black lemur (BlackLemur)†
- Callimicos (Callimicos)†
- Chimpanzee 1 (Chimp1)†
- Chimpanzee 2 (Chimp2)†
- Ringtailed lemur (RTLemur)†
- Saki (Saki)†
- Spectacled bear (SpecBr2)†
- Squirrel (Squirrel)†

*San Diego Zoological Park. †St. Louis Zoo. ‡Wild, free-living.

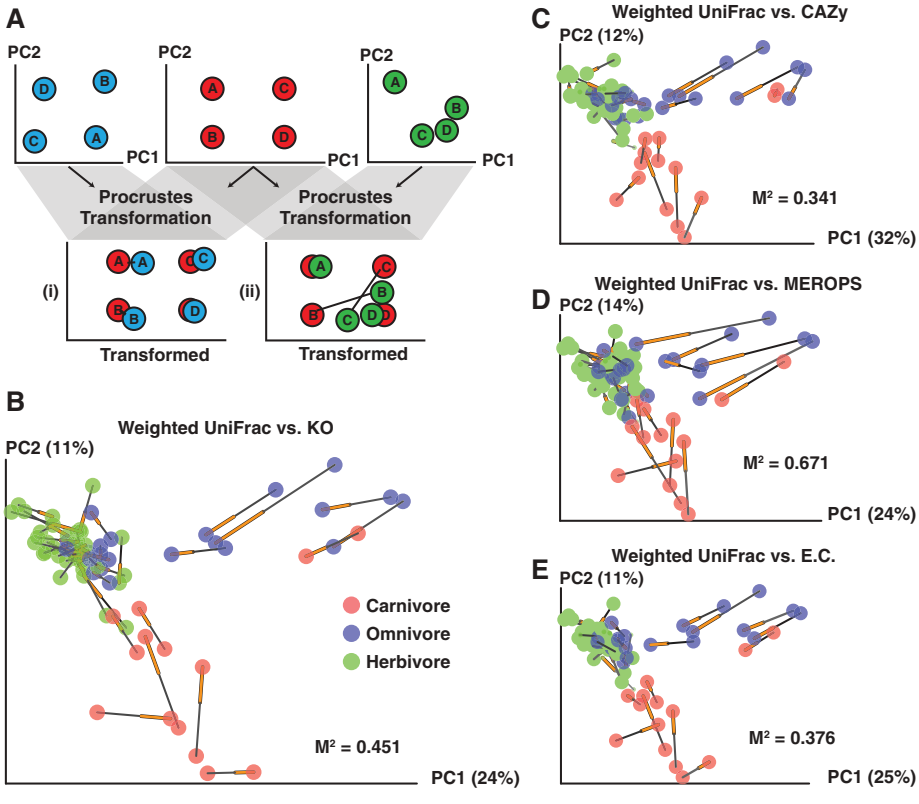

Fig. 1. Procrustes analysis shows that mammalian gut bacterial lineages and microbiome gene content give similar clustering patterns. (**A**) Cartoon illustrating Procrustes analysis. The Procrustes transformation of the blue and red data types (i) results in a good fit, whereas the transformation of the green and red data (ii) yields a worse fit, with large distances separating data from samples B and C. (**B** to **E**) Procrustes analysis of 16*S* rRNA sequences (weighted UniFrac) against KO groups, CAZymes (glycoside hydrolases), MEROPS peptidases, and E.C.s. Every sphere represents a single mammalian fecal community and is colored by host diet. The black end of each line connects to the 16*S* rRNA data for the sample, whereas the orange end is connected to the functional annotation data. The fit of each Procrustes transformation over the first three dimensions is reported as the M^2 value.

that the overall distribution of microbial species and microbiome functions in the gut does not mirror mammalian phylogeny. 198 different named bacterial genera were detected in our data set; of these, only 3 were significantly associated with the mammalian phylogenetic tree more than would be expected by chance (Prevotella, Barnesiella, and Bacteroides). No CAZymes or peptidases and only 18 of the 3866 KOs tested were associated with host phylogeny. We repeated the analysis using a more relaxed constraint that a taxon or function occurs in a given monophyletic group more frequently than expected by chance rather than requiring strict presence or absence agreement (*2*). The relaxed definition gave similar results; only three additional genera and a total of 90 KOs were detected as having a significant association with the mammalian tree. We concluded that bacterial taxa and functions are evolutionarily labile and do not explain the concordance between bacterial communities and microbiome functions.

Bipartite network analysis provided an additional tool for exploring the interrelationship between host diet, host lineage, gut physiology, and shared and unique bacteria taxa (*1*). Mammalian hosts and bacterial OTUs were used as nodes in a bipartite graph, with edges connecting OTU nodes to the hosts in which they are found (*2*). Using 1900 V2 16*S* rRNA sequences from each mammalian host, the network shows clear separation of fecal communities by host diet (Fig. 2A), mirroring our earlier results based on smaller numbers of full-length 16*S* rRNA sequences (*1*).

We reasoned that the bipartite graph approach could also be used to connect mammalian samples to individual microbial gene functions from shotgun reads. The power of the bipartite graph approach is to represent both genes and mammalian species explicitly as nodes, thus visualizing which genes connect with which species. The clear separation by diet disappears when we consider gene functions (Fig. 2B and fig. S2), suggesting that rather than a diet- or physiology-specific set of genes, the relationship among mammalian gut microbiomes is that they share a large core repertoire of functions. We confirmed this result by plotting the frequency of shared taxa in the 39 mammalian fecal samples, and also species- and genus-level OTU bins (*2*). All of the curves demonstrate an essentially exponential decay as successive samples are added, with no OTUs found in more than 30 samples (Fig. 2C). However, the plot of KO frequency flattens out, with 35 KOs found in all samples. This effect cannot be due to differences in the number of OTUs relative to KOs: There are more OTUs than KOs, and fewer assigned species or assigned genera, yet all the taxonomic curves show the same rapid decay, unlike the KOs.

This result does not imply that there are no differences among the functional configurations of microbiomes of host species having different diets. Rather, it suggests that the differences between microbiomes probably stem from differing abundances of shared functions, such as enzymes that break down chemical substrates in the host diet. We identified 495 E.C.s with significantly different proportional abundance in the 7 carnivorous and 21 herbivorous mammalian microbiomes, using the program Shotgun FunctionalizeR (adjusted $P < 0.001$ after multiple hypothesis correction) (table S5) (*11*). Many of the enzymes distinguishing carnivorous and herbivorous fecal microbiomes are involved in amino acid metabolism. Microbiomes from herbivores were enriched in enzymes that map to biosynthetic reactions for 12 amino acids, whereas no carnivore samples were enriched in amino acid bio-

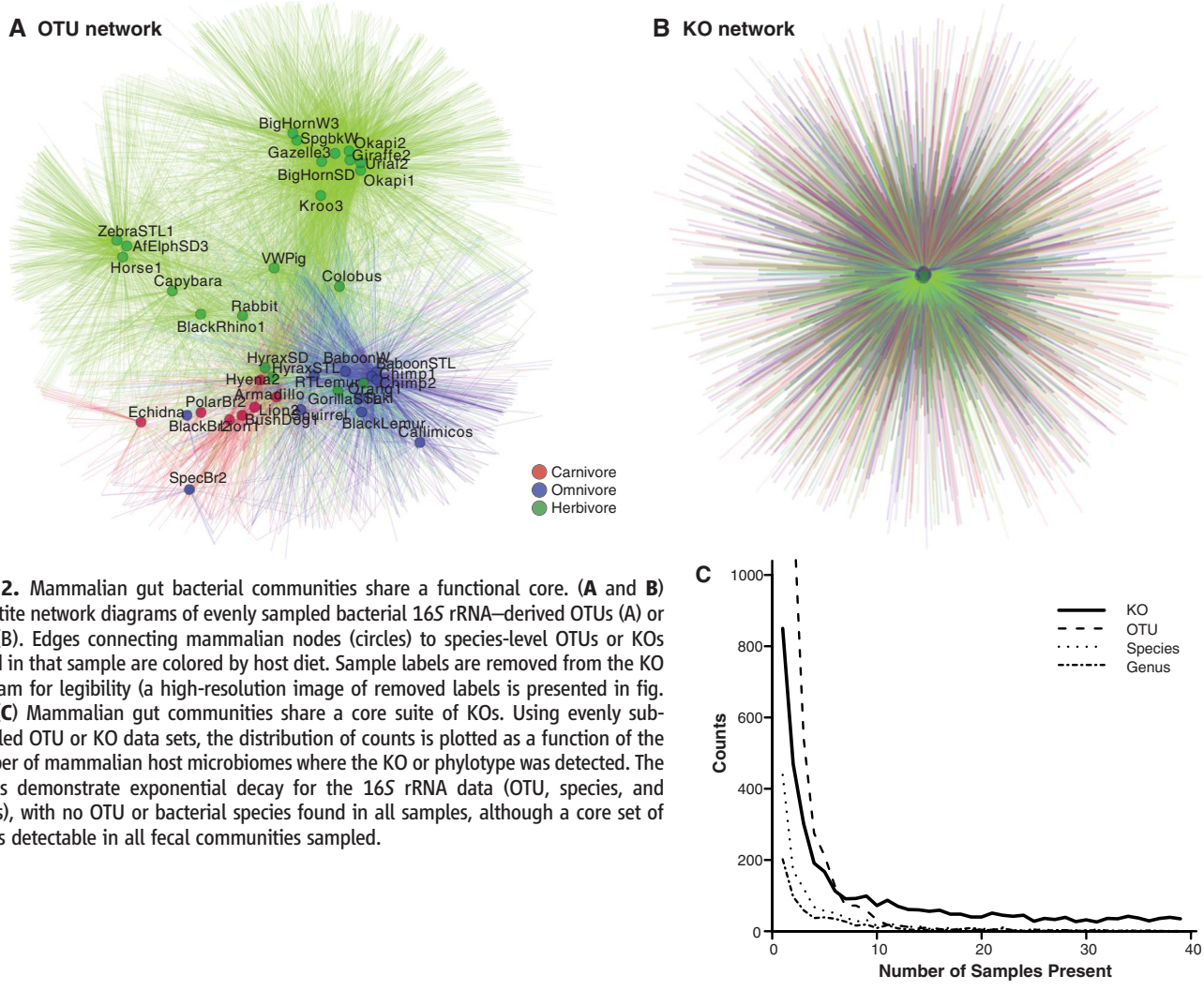

Fig. 2. Mammalian gut bacterial communities share a functional core. (**A** and **B**) Bipartite network diagrams of evenly sampled bacterial 16*S* rRNA–derived OTUs (A) or KOs (B). Edges connecting mammalian nodes (circles) to species-level OTUs or KOs found in that sample are colored by host diet. Sample labels are removed from the KO diagram for legibility (a high-resolution image of removed labels is presented in fig. S2). (**C**) Mammalian gut communities share a core suite of KOs. Using evenly subsampled OTU or KO data sets, the distribution of counts is plotted as a function of the number of mammalian host microbiomes where the KO or phylotype was detected. The results demonstrate exponential decay for the 16*S* rRNA data (OTU, species, and genus), with no OTU or bacterial species found in all samples, although a core set of KOs is detectable in all fecal communities sampled.

synthetic enzymes (table S6). In contrast, nine amino acid degradation pathways contained enzymes that were significantly increased in carnivores, whereas the only degradative enzymes whose representation was significantly greater in herbivores were those involved in the breakdown of branched-chain amino acids (Val, Leu, and Ile). Glutamate metabolism is particularly illustrative of these trends. Both the adenosine triphosphate (ATP)–dependent and ATP-independent pathways for glutamate biosynthesis are significantly increased in herbivore microbiomes, whereas the catabolic reactions to break down glutamate and glutamine are increased in carnivores (Fig. 3A). These results suggest that carnivorous microbiomes have specialized to degrade proteins as an energy source, whereas herbivorous communities have specialized to synthesize amino acid building blocks.

The distinctiveness of carnivorous and herbivorous microbiomes was also revealed at a central anaplerotic node (Fig. 3B). When gluconeogenesis is required, oxaloacetate (OAA) can be converted to phosphoenolpyruvate (PEP) and pyruvate. When tricarboxylic acid cycle intermediates are withdrawn for biosynthesis, they are replenished by converting PEP and pyruvate directly to OAA (*12*). All of the genes encoding

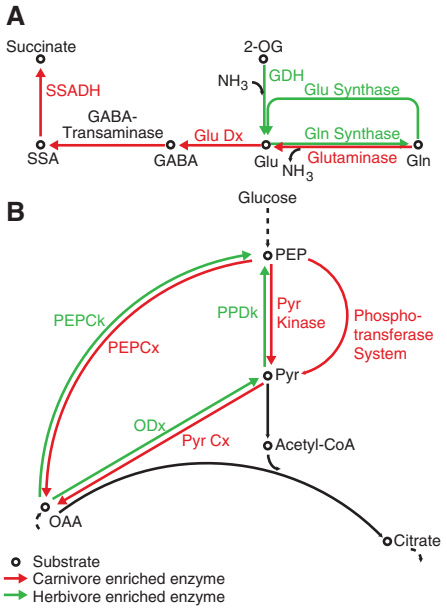

Fig. 3. Differences in metabolic features encoded in fecal microbiomes among herbivores versus carnivores. (**A**) Carnivorous and herbivorous microbiomes indicate opposing directionality for amino acid metabolism. Colored arrows denote enzyme functions whose representation is significantly ($P < 0.001$) greater in the fecal microbiomes of herbivores (green) or carnivores (red). (**B**) Carnivorous and herbivorous microbiomes suggest opposing directionality at the central PEP-pyruvate-OAA node. The coloring scheme is as in (A). Abbreviations: 2-OG, alpha-ketoglutarate; Ck, carboxykinase; Cx, carboxylase; DH, dehydrogenase; Dx, decarboxylase; GABA, γ-aminobutyrate; GDH, Glu DH; ODx, OAA Dx; PPDk, Pyr-phosphate dikinase; Pyr, pyruvate; SSA, succinate-semialdehyde.

enzymes catalyzing OAA production from pyruvate or PEP are significantly increased in the carnivore microbiomes, whereas the reverse reactions are catalyzed by enzymes whose representation is increased in herbivore microbiomes.

Our studies comparing mammalian species revealed a relationship between host diet and gut microbial community structure and function. We next asked whether similar trends could be detected using diet variation within a single free-living host species, namely humans. Quantitative studies of diet in most human populations are complicated by the known inaccuracy of self-reported data (*13*), so we turned to a group of adults known to keep meticulous records about their daily food composition and consumption. The selected cohort consisted of 18 lean members of the Calorie Restriction Society who typically measure and record all components of their diets on a daily basis with computer software to insure optimal nutrition despite reduced energy intake (*14*, *15*). We collected their dietary records for a 4-day period (conservatively encompassing at least one complete intestinal transit time) before obtaining a single fecal sample, and analyzed macro- and micronutrient consumption using a validated protocol (*2*, *16*). An average of 3642 ± 3826 bacterial V2 16*S* rRNA reads and 54,295 ± 28,086 shotgun reads were obtained per sample (tables S7 to S10).

Procrustes analysis revealed a significant association between the bacterial phylogenetic structure of their fecal communities (16*S* rRNA) and the functions encoded in their microbiomes [$P < 0.05$ for KOs, E.C.s, and CAZymes (glycoside hydrolases)]; not significant for peptidases ($P = 0.061$) (fig. S3). These results suggest that the processes that drive the functional differentiation of microbiomes within an individual host species may be fundamentally similar to those that drive their differentiation across mammalian evolution.

Documentation of the weight of each ingredient in each meal consumed by these individuals (table S7) allowed us to perform a follow-up analysis examining the impact on fecal bacterial community configuration of three dietary components (total protein, carbohydrate, and insoluble fiber intake). We chose these diet categories because protein intake is markedly different between carnivores and herbivores, and because an extensive literature exists about the impact of ingested polysaccharides and fiber on the gut microbiota (*17*). Linear regression of the three dietary categories against the position of each individual's microbiome along principal coordinate 1 of the PCoA plots revealed that total protein intake was significantly associated with KO data [adjusted linear regression coefficient of determination (R^2) value = 0.307, adjusted P value = 0.030] (*2*). In contrast, insoluble dietary fiber was significantly associated with bacterial OTU content (Bray-Curtis metric; adjusted R^2 value = 0.371; adjusted P value = 0.013) (table S11). These results confirm that within a single free-living species, both the structure and function of the gut microbiome are significantly associated with dietary intake.

Taken together with our prior work (*1*), these results teach us that even fecal samples from mammals living in zoos and human samples from a single self-selected population can provide insights into the factors driving the evolution of the gut microbiome. They also compel us, at a time when complete genomes are to be sequenced for 10,000 vertebrates (*18*), to take the next step and perform systematic studies that rigorously test specific mechanisms that drive the evolution of hosts and their (gut) microbial symbionts. These studies should be guided by experts who can choose taxa that radiated at different points in their evolutionary history, with parallel shifts in their diet, morphology, biogeography, or other key factors known or hypothesized to influence evolution. The results should help address questions such as what functional features in host intestinal environments (including the biochemical characteristics of mucosal surfaces) are related to the representation of specific bacterial taxa and microbiome functions, and how readily microbial populations have been acquired and reacquired during the course of vertebrate evolution. Additionally, our findings emphasize the need to sample humans across the globe with a variety of extreme diets and lifestyles, including relatively ancestral hunter-gatherer lifestyles, in order to provide new insights into the limits of variation within a host species and the possibility that our microbes, in coevolving with our bodies and our cultures, have helped shaped our physiological differences and environmental adaptations.

References and Notes

1. R. E. Ley *et al.*, *Science* **320**, 1647 (2008).
2. See supporting material on *Science* Online.
3. M. Kanehisa, S. Goto, *Nucleic Acids Res.* **28**, 27 (2000).
4. B. L. Cantarel *et al.*, *Nucleic Acids Res.* **37** (database issue), D233 (2009).
5. N. D. Rawlings, A. J. Barrett, A. Bateman, *Nucleic Acids Res.* **38** (database issue), D227 (2010).
6. D. H. Huson, A. F. Auch, J. Qi, S. C. Schuster, *Genome Res.* **17**, 377 (2007).
7. J. R. Hurley, R. B. Cattell, *Behav. Sci.* **7**, 258 (1962).
8. J. C. Gower, *Psychometrika* **40**, 33 (1975).
9. C. Lozupone, R. Knight, *Appl. Environ. Microbiol.* **71**, 8228 (2005).
10. T. E. Cerling, J. R. Ehleringer, J. M. Harris, *Philos. Trans. R. Soc. London Ser. B* **353**, 159, discussion 170 (1998).
11. E. Kristiansson, P. Hugenholtz, D. Dalevi, *Bioinformatics* **25**, 2737 (2009).
12. O. E. Owen, S. C. Kalhan, R. W. Hanson, *J. Biol. Chem.* **277**, 30409 (2002).
13. K. Poslusna, J. Ruprich, J. H. M. de Vries, M. Jakubikova, P. van't Veer, *Br. J. Nutr.* **101** (suppl. 2), S73 (2009).
14. L. Fontana, S. Klein, *JAMA* **297**, 986 (2007).
15. L. K. Heilbronn *et al.*, *JAMA* **295**, 1539 (2006).
16. S. F. Schakel, Y. A. Sievert, I. M. Buzzard, *J. Am. Diet. Assoc.* **88**, 1268 (1988).
17. H. J. Flint, *Adv. Appl. Microbiol.* **56**, 89 (2004).
18. Genome 10K Community of Scientists, *J. Hered.* **100**, 659 (2009).

Acknowledgments: We thank J. Manchester and S. Wagoner for technical assistance; B. Cantarel, V. Lombard, C. Rancurel, and P. Coutinho for CAZyme annotation; R. Ley and members of the Gordon lab for their suggestions; and S. Bircher, R. Ramey, M. Schlegel, M. Schrenzel, T. Tucker, and P. Turnbaugh for past help in procuring mammalian fecal samples. This work was supported by grants

from NIH (DK30292, DK70977, DK078669, and UL1 RR024992), the Crohn's and Colitis Foundation of America, and NIH Institutional Training Grant T32-A1007172 (to B.D.M.). The National Center for Biotechnology Information Sequence Read Archive accession number for the bacterial 16*S* rRNA and shotgun data sets related to our studies of mammalian and Calorie Restriction Society member human fecal microbiomes is SRA030940. Sequence data have also been deposited in MG-Rast with project accession numbers qiime:625, qiime:626, qiime:627, and qiime:628.

Supporting Online Material
www.sciencemag.org/cgi/content/full/332/6032/970/DC1
Materials and Methods
Figs. S1 to S3
Tables S1 to S11
References (*19*–*34*)

5 October 2010; accepted 13 April 2011
10.1126/science.1198719

The Toll-Like Receptor 2 Pathway Establishes Colonization by a Commensal of the Human Microbiota

June L. Round,[1]* S. Melanie Lee,[1] Jennifer Li,[1] Gloria Tran,[1] Bana Jabri,[2] Talal A. Chatila,[3] Sarkis K. Mazmanian[1]*

Mucosal surfaces constantly encounter microbes. Toll-like receptors (TLRs) mediate recognition of microbial patterns to eliminate pathogens. By contrast, we demonstrate that the prominent gut commensal *Bacteroides fragilis* activates the TLR pathway to establish host-microbial symbiosis. TLR2 on $CD4^+$ T cells is required for *B. fragilis* colonization of a unique mucosal niche in mice during homeostasis. A symbiosis factor (PSA, polysaccharide A) of *B. fragilis* signals through TLR2 directly on $Foxp3^+$ regulatory T cells to promote immunologic tolerance. *B. fragilis* lacking PSA is unable to restrain T helper 17 cell responses and is defective in niche-specific mucosal colonization. Therefore, commensal bacteria exploit the TLR pathway to actively suppress immunity. We propose that the immune system can discriminate between pathogens and the microbiota through recognition of symbiotic bacterial molecules in a process that engenders commensal colonization.

Throughout our lives, we continuously encounter microorganisms that range from those essential for health to those causing death (*1*). Consequently, our immune system is charged with the critical task of distinguishing between beneficial and pathogenic microbes. Toll-like receptors (TLRs) are evolutionarily conserved molecules that promote immune responses, and TLR signaling by innate immune cells is indispensable for proper activation of the immune system during infections. T cells also express functional TLRs (*2*–*4*), and TLR signaling has furthermore been shown to restrain immune responses (*5*). As symbionts and pathogens produce similar molecular patterns that are sensed by TLRs, the mechanisms by which our immune system differentiates between the microbiota and enteric infections remain unknown.

Whereas the intestinal microbiota contains hundreds of bacterial species and is integral to human health (*6*), the mucosal immune system employs an arsenal of responses to control enteric pathogens. Germ-free mice lack proinflammatory T helper 17 (T_H17) cells in the gut (*7*, *8*) (Fig. 1A), and only select symbiotic bacteria can induce T_H17 cells (*9*, *10*). Most microbes express common TLR ligands (e.g., peptidoglycan, unmethylated CpG, and lipoproteins); therefore, how do symbionts avoid triggering intestinal immunity in their mammalian hosts? We examined the hypothesis that the human gut commensal *Bacteroides fragilis* evolved molecular mechanisms to suppress T_H17 responses during homeostatic colonization. As predicted previously (*7*, *10*, *11*), we found that *B. fragilis* mono-associated animals did not induce T_H17 cell development in the colon compared to germ-free controls (Fig. 1A). The beneficial contributions of *B. fragilis* require a single immunomodulatory molecule named polysaccharide A (PSA), which prevents and cures inflammatory disease (*12*–*14*). Colonization with *B. fragilis* in the absence of PSA (*B. fragilis*ΔPSA), however, resulted in significant T_H17 cell responses in the gut (Fig. 1, A and B). Colonic lamina propria (LP) lymphocytes from *B. fragilis*ΔPSA mono-associated animals displayed increased secretion of interleukin-17A (IL-17A) in vitro (fig. S1) and elevated transcription of *Il17a* and the T_H17-specific lineage differentiation factor RORγt (*Rorc*) (Fig. 1, C and D) (*15*). Differences in T_H1 responses were not observed during *B. fragilis*ΔPSA colonization (fig. S2). Cells from *B. fragilis* mono-associated animals produced low amounts of IL-17A during in vitro T_H17 skewing assays, whereas $CD4^+$ T cells from *B. fragilis*ΔPSA animals display elevated IL-17A production (fig. S3). Administration of purified PSA to *B. fragilis*ΔPSA mono-associated animals suppresses T_H17 immunity (Fig. 1E). Thus, *B. fragilis* actively restrains T_H17 cell responses during colonization.

Recent studies have shown that certain gut bacteria can promote regulatory T cell (T_{reg}) induction (*11*, *14*). T_{regs} expressing the transcription factor Foxp3 (forkhead box P3) suppress proinflammatory T_H17 cell reactions. To test whether T_{regs} prevent immune responses during *B. fragilis* colonization, we reconstituted germ-free *Rag1*$^{-/-}$ mice with bone marrow from Foxp3-DTR (diphtheria toxin receptor) donors, which allowed for specific ablation of T_{regs} by administration of diphtheria toxin (DT) (*16*). Mice were mono-associated with *B. fragilis* to induce T_{reg} development (Fig. 1F). DT treatment of mice resulted in depletion of $Foxp3^+$ T cells (Fig. 1F), with a concomitant increase in T_H17 responses (Fig. 1G and fig. S4), which suggests that $Foxp3^+$ T_{regs} are required for suppression of T_H17 cells during *B. fragilis* colonization.

PSA is an immunomodulatory bacterial molecule that shapes host immune responses (*17*). Induction of IL-10 and interferon-γ (IFN-γ) from $CD4^+$ T cells by PSA requires TLR2 signaling (*14*, *18*). We sought to determine the mechanism whereby *B. fragilis* suppresses T_H17 cell responses by testing whether PSA functions through TLR2 signaling by dendritic cells (DCs) and/or $CD4^+$ T cells. PSA elicited a significant increase in IL-10 and IFN-γ production from mixed cultures of wild-type DCs and wild-type $CD4^+$ T cells in vitro (Fig. 2A and fig. S5). When *Tlr2*$^{-/-}$ T cells were cocultured with wild-type DCs, however, PSA-induced IL-10 production was reduced, whereas IFN-γ expression was not affected (Fig. 2A and fig. S5), which indicated that PSA required TLR2 expression on T cells to promote IL-10 production. IL-10 responses to PSA were specific to T cells (fig. S6). Consistent with previous findings (*18*), proinflammatory IFN-γ production was dependent on TLR2 signaling by DCs (fig. S5); however, IL-10 production was unaffected in cultures containing wild-type $CD4^+$ T cells and *Tlr2*$^{-/-}$ DCs (Fig. 2A). Therefore, TLR2 expression by T lymphocytes is necessary for IL-10 production by PSA.

$CD4^+$ T cells produce IL-10 in response to PSA in the absence of antigen-presenting cells (APCs) (Fig. 2B). Moreover, PSA induces IL-10 expression from purified T cells in a dose-dependent manner, whereas other TLR2 ligands do not (fig. S7). TLR2 can function as either a homodimer or a heterodimer with TLR1 or TLR6 (*19*). PSA could induce high amounts of IL-10 from wild-type, *Tlr1*$^{-/-}$, and *Tlr6*$^{-/-}$ $CD4^+$ T cells; however, IL-10 production was lost only from *Tlr2*$^{-/-}$ $CD4^+$ T cells and T cells deleted in the TLR adapter molecule MyD88 (Fig. 2B). To determine T_{reg} suppression as a function of cell-

[1]Division of Biology, California Institute of Technology, Pasadena, CA 91125, USA. [2]Department of Pathology, Department of Pediatrics, Department of Medicine, University of Chicago, Chicago, IL 60637, USA. [3]Division of Immunology, Allergy and Rheumatology, Department of Pediatrics, David Geffen School of Medicine at UCLA, Los Angeles, CA 90095, USA.

*To whom correspondence should be addressed. E-mail: jround@caltech.edu (J.L.R.); sarkis@caltech.edu (S.K.M.)

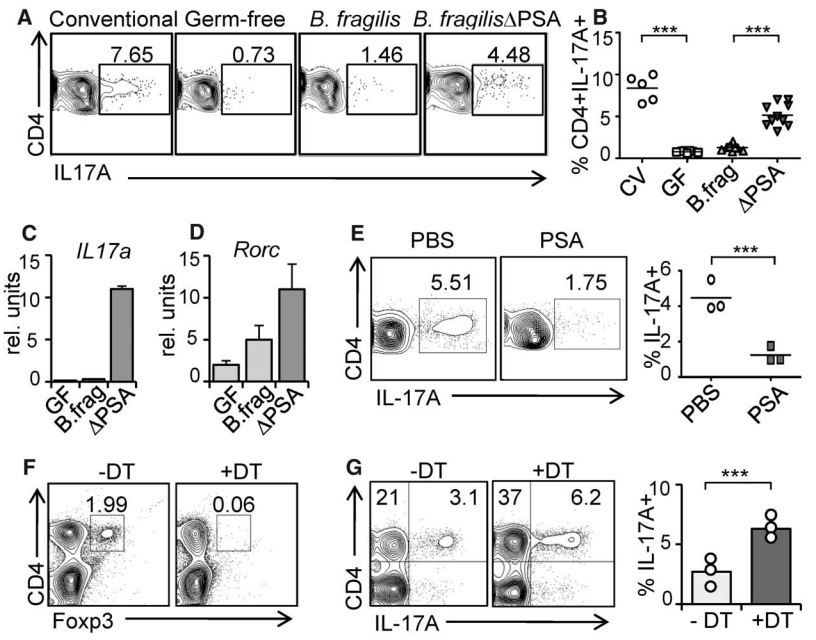

Fig. 1. PSA actively suppresses T_H17 cell development during *B. fragilis* colonization through Foxp3$^+$ T_{regs}. (**A**) Colonic lamina propria lymphocytes (LPLs) were harvested and stained with antibodies against CD4 and IL-17A and analyzed by flow cytometry. Numbers indicate the percentage of CD4$^+$IL-17A$^+$ (T_H17) cells. Conventional mice are specific pathogen free. (**B**) Compiled data from three independent experiments as in (A). CV, conventional; GF, germ-free; B.frag, *B. fragilis*; ΔPSA, *B. fragilis*ΔPSA. ***$P < 0.001$, two-way analysis of variance. (**C** and **D**) CD4$^+$ T cells were isolated from the mesenteric lymph nodes of the indicated animals. RNA was collected and used as a template to determine the relative levels of IL-17A (C) and RORγt (D) transcript. Error bars represent SDs from triplicate samples. The data are representative of three independent experiments. (**E**) *B. fragilis*ΔPSA mono-associated mice were treated with either phosphate-buffered saline (PBS) or PSA, and the LPLs were isolated and the percentage of CD4$^+$ IL-17A–producing cells was determined by flow cytometry. Each symbol represents an individual animal (n = 3 to 4 mice per group). ***$P < 0.001$. (**F** and **G**) Germ-free *Rag1*$^{-/-}$ animals were reconstituted with bone marrow from Foxp3-DTR mice and then mono-associated with *B. fragilis*. Animals were treated with either PBS (–DT) or diphtheria toxin (+DT) as described (*16*). Colonic LPLs were harvested after T_{reg} ablation and restimulated with phorbol 12-myristate 13-acetate (PMA)–ionomycin and brefeldin A. Cells were stained with antibodies to CD4, Foxp3, and IL-17A and analyzed by flow cytometry. (Right) Symbols represent T cell proportions from individual mice within a single experiment (n = 3 to 4 mice per group) and are representative of two independent trials. ***$P < 0.001$.

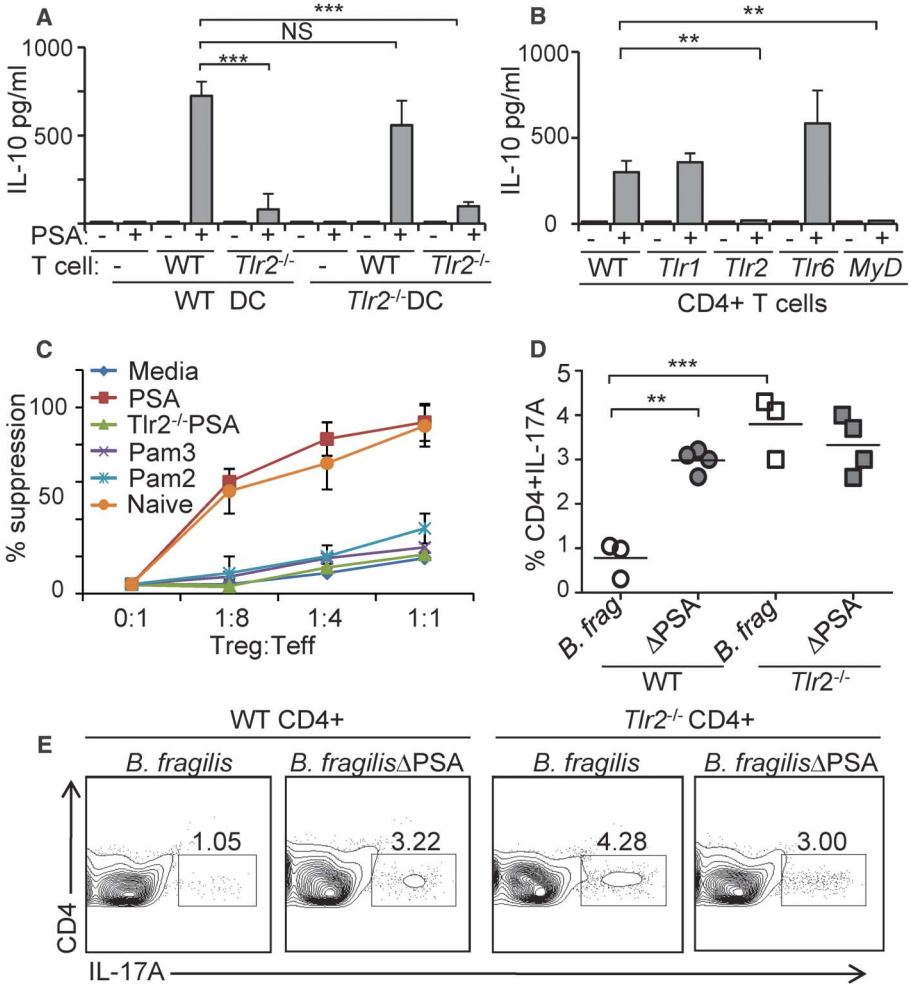

Fig. 2. PSA signals through TLR2 on CD4$^+$ T cells to suppress T_H17 cell responses. (**A**) Bone marrow–derived dendritic cells from wild-type (WT) or *Tlr2*$^{-/-}$ mice were incubated with splenic CD4$^+$ T cells. Amounts of secreted IL-10 were determined by enzyme-linked immunosorbent assay (ELISA). Error bars represent SDs from two independent assays performed in quadruplicate. ***$P < 0.001$; NS, not significant. (**B**) CD4$^+$ T cells were isolated from WT mice, and the indicated knockout mice and cells were stimulated as in (A). MyD is *Myd88*$^{-/-}$. IL-10 was assayed by ELISA. **$P < 0.01$. Error bars represent SDs for quadruplicate samples and are representative of two independent trials. (**C**) CD4$^+$Foxp3$^+$ T_{regs} were purified from Foxp3^{EGFP} mice (*26*) and *Tlr2*$^{-/-}$ X Foxp3^{EGFP} mice and stimulated with plate-bound antibodies against CD3 and recombinant TGF-β, with PSA or with the indicated TLR ligands. Equal numbers of live cultured T_{regs} were then incubated with CFSE (carboxyfluorescein diacetate succinimidyl ester)–pulsed responder cells (CD4$^+$Foxp3$^-$). Percent suppression is determined by the ratio of proliferating responder cells in each condition relative to proliferation in the absence of added T_{regs}. Error bars are SDs from a single experiment performed in duplicate and are representative of two independent trials. (**D** and **E**) Germ-free *Rag1*$^{-/-}$ animals were reconstituted with CD4$^+$ T cells from WT or *Tlr2*$^{-/-}$ mice and then mono-associated with either WT *B. fragilis* or *B. fragilis*ΔPSA. Colonic LPLs were isolated and analyzed for T_H17 cell proportions by flow cytometry. Plots are gated on CD4$^+$ cells. (D) Each symbol represents an individual animal (n = 3 to 4 mice per group), and data are representative of two independent trials. **$P < 0.01$; ***$P < 0.001$.

intrinsic TLR2 signaling, we measured proliferation of responder T cells after coculture with T_{regs} stimulated in vitro with PSA, or classical TLR2 ligands Pam3CysK or Pam2CysK. The proportion of $Foxp3^+$ T cells was equivalent under all conditions (fig. S8). PSA-treated T_{regs} displayed increased suppressive capacity compared to media or other TLR2 ligand–treated T_{regs} (Fig. 2C). IL-2 was not produced by T_{regs} during treatment with any of the TLR2 ligands, and IL-2 neutralization had no effect on in vitro suppression (fig. S9). Notably, the suppressive capacity of PSA-treated T_{regs} was lost when $Foxp3^+$ T cells were deficient in TLR2 (Fig. 2C). PSA likely directed the development of inducible T_{regs} by promoting the expression of IL-10, transforming growth factor–β2 (TGF-β2), and Foxp3 from purified $Foxp3^+$ T cells in a TLR2-dependent fashion (fig. S10). Collectively, these studies show that unlike other TLR2 ligands, PSA enhances T_{reg} function and gene expression in the absence of APCs through TLR2 signaling directly on $CD4^+Foxp3^+$ Treg cells.

We next determined whether PSA signals through TLR2 on $Foxp3^+$ T_{regs} during *B. fragilis* colonization of animals to suppress T_H17 cell responses. Germ-free *Rag1*$^{-/-}$ mice were reconstituted with purified $CD4^+$ T cells from wild-type or *Tlr2*$^{-/-}$ animals. Animals were subsequently mono-associated with either *B. fragilis* or *B. fragilis*ΔPSA. Unlike wild-type animals, IL-10–producing $Foxp3^+$ T_{regs} were not induced in the gut of *B. fragilis* mono-colonized animals that were reconstituted with *Tlr2*$^{-/-}$ $CD4^+$ T cells (fig. S11). Although we observed minimal T_H17 cell development in wild-type mice mono-associated with *B. fragilis*, T_H17 cell responses were significantly increased during colonization of animals that were reconstituted with *Tlr2*$^{-/-}$ $CD4^+$ T cells (Fig. 2, D and E). Furthermore, TLR2-deficient $CD4^+$ T cells from *B. fragilis* mono-associated mice produced more IL-17A compared to mice reconstituted with wild-type $CD4^+$ T cells (fig. S12). Collectively, these data demonstrate that *B. fragilis* requires TLR2 to induce $Foxp3^+$ T_{regs} during intestinal colonization and actively suppresses T_H17 responses through engagement of TLR2 specifically on T cells.

The intestinal microbiota occupies both mucosal and luminal niches during normal colonization; however, the biogeographic distributions of specific microbial species are poorly characterized. We reasoned that the functions of PSA were driven by an evolutionary impetus to prevent deleterious mucosal immune reactions to *B. fragilis*, enabling bacteria to associate with host tissue. Intriguingly, we discovered a population of bacteria that intimately associates with the intestinal epithelium (Fig. 3A). Whole-mount preparations of medial colons were probed for bacteria after labeling with *B. fragilis*–specific antisera (fig. S13). Three-dimensional reconstruction of confocal microscopic images revealed microcolonies of *B. fragilis* residing within colonic crypts (Fig. 3A). The amounts of *B. fragilis* associated with host tissue represented a fraction of total bacteria (Fig. 3, B and C), but likely are an important population that are in close proximity to the host immune system. We speculated that the amounts of tissue-associated bacteria would be sensitive to host immune responses such as T_H17 cell induction. Notably, animals colonized with *B. fragilis*ΔPSA displayed profoundly reduced numbers of tissue-associated bacteria when compared to animals colonized with wild-type *B. fragilis* (Fig. 3D). Treatment of *B. fragilis*ΔPSA–colonized animals with purified PSA corrected this defect and increased colonization of *B. fragilis*ΔPSA to wild-type bacterial levels (Fig. 3D). Only tissue-associated bacteria were affected, because no differences were observed in the amounts of bacteria in the gut lumen by either strain (fig. S14) (*17*). Collectively, these data identify a previously unappreciated mucosal niche for *B. fragilis* and reveal that PSA is required for maintaining host-bacterial symbiosis at the epithelial surface of the gut.

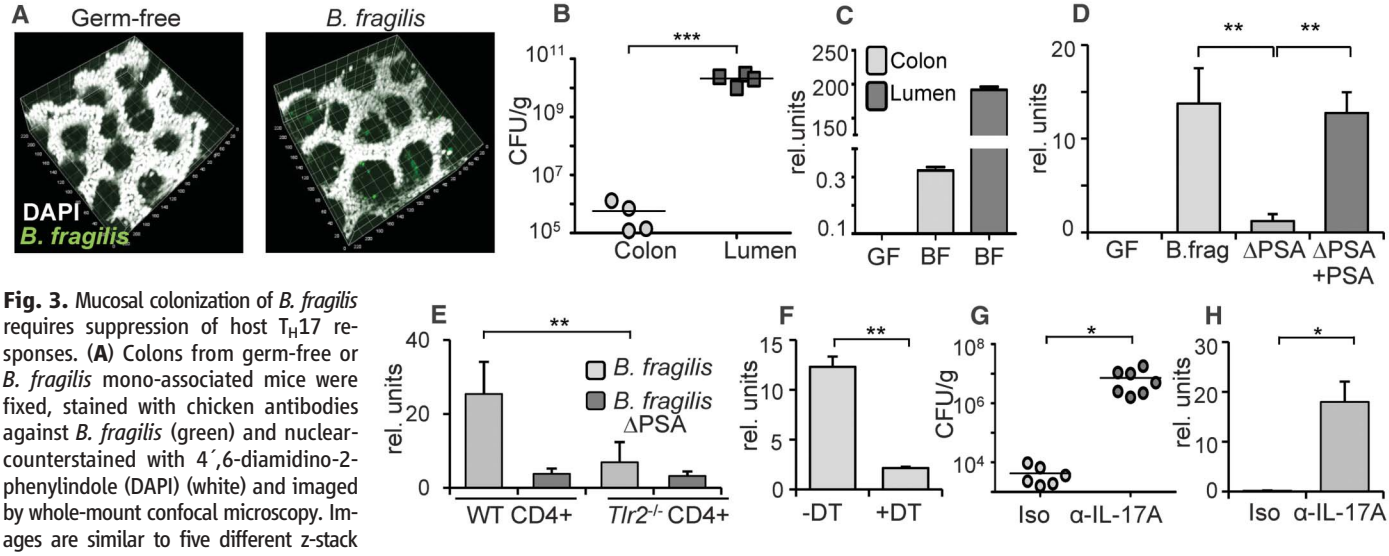

Fig. 3. Mucosal colonization of *B. fragilis* requires suppression of host T_H17 responses. (**A**) Colons from germ-free or *B. fragilis* mono-associated mice were fixed, stained with chicken antibodies against *B. fragilis* (green) and nuclear-counterstained with 4′,6-diamidino-2-phenylindole (DAPI) (white) and imaged by whole-mount confocal microscopy. Images are similar to five different z-stack images per colon and representative of five mice. (**B**) Colon sections or luminal contents from *B. fragilis* mono-associated mice were homogenized and serially diluted to obtain live bacterial counts. CFUs (colony-forming units) per gram of tissue were determined after microbiologic plating. Each symbol represents an individual animal (n = 3 to 4 animals per group) and is representative of three independent trials. ***$P < 0.001$. (**C**) Quantitative reverse transcription–polymerase chain reaction (qRT-PCR) analysis was performed with *Bacteriodes*-specific primers on RNA extracted from colon tissue or luminal contents. GF, germ-free; BF, *B. fragilis*. Error bars represent SDs from individual mice in the same experiment and are representative of two independent trials. (**D**) qRT-PCR analysis for *B. fragilis* was performed on RNA extracted from colon homogenates from indicated animals. The bar furthest to the right shows colonization of *B. fragilis*ΔPSA in animals orally treated with purified PSA. GF, germ-free; B.frag, *B. fragilis*; ΔPSA, *B. fragilis*ΔPSA. Data are shown for four animals per group and are representative of two independent trials. **$P < 0.01$. (**E**) Germ-free *Rag1*$^{-/-}$ animals were reconstituted with *Tlr2*$^{-/-}$ or WT $CD4^+$ T cells and colonized with either WT *B. fragilis* or *B. fragilis*ΔPSA. Colons were prepared and analyzed as in (D). **$P < 0.01$. (**F**) Germ-free *Rag1*$^{-/-}$ animals were reconstituted with Foxp3-DTR bone marrow and colonized with *B. fragilis*. Two months after reconstitution animals were treated with either PBS (–DT) or with diphtheria toxin (+DT), and colons were prepared as described in (D). **$P < 0.01$. (**G** and **H**) Neutralization of IL-17A increases *B. fragilis* colonization. Germ-free animals were colonized with *B. fragilis*ΔPSA and treated with either an antibody that neutralizes IL-17A (α-IL-17A) or an isotype control (Iso). Colon homogenates were analyzed by live bacterial plating (G) or qRT-PCR (H) as described in (B) and (C). Each symbol in (G) represents an individual animal. Error bars in (H) show the SDs from individual animals and are compiled data from two independent trials with three or four animals per group. *$P < 0.05$.

Our findings suggest that PSA induces T_{regs} through TLR2 signaling to suppress T_H17 cell responses and promote mucosal colonization by *B. fragilis*. To test this model, we measured colonization levels of *B. fragilis* in *Rag1*$^{-/-}$ mice reconstituted with TLR2-deficient CD4$^+$ T cells. Tissue association by wild-type *B. fragilis* in the colon was reduced to the levels of *B. fragilis*ΔPSA in these mice (Fig. 3E and fig. S15). Moreover, Foxp3$^+$ T_{reg} ablation in *B. fragilis* mono-associated animals resulted in significantly reduced amounts of tissue-associated *B. fragilis* (Fig. 3F), without affecting bacterial numbers in the lumen of the gut (fig. S16). Finally, to functionally determine the role of IL-17 responses in mucosal association, we treated *B. fragilis*ΔPSA mono-associated animals with a neutralizing antibody to IL-17A. Whereas the amounts of *B. fragilis*ΔPSA in isotype control–treated animals remained low, neutralization of IL-17A resulted in a 1000-fold increase in tissue-associated bacteria (Fig. 3, G and H). These data indicate that IL-17 suppression by PSA is required by *B. fragilis* during association with its host. Therefore, unlike pathogens that trigger inflammatory responses through TLRs to clear infections, symbiotic colonization by *B. fragilis* is actually enhanced via the TLR pathway. We conclude that PSA evolved to engender host-bacterial mutualism by inducing mucosal tolerance through TLR2 activation of T_{reg} cells.

The gastrointestinal tract represents a primary portal for entry by numerous pathogens. Toll-like receptors recognize MAMPs (microbial-associated molecular patterns) expressed by bacteria and coordinate a cascade of innate and adaptive immune responses that control infections (*20*). Although TLRs have classically been studied on innate immune cells, recent reports have demonstrated their expression by T cells in both mice and humans (*4*, *21*–*23*). As bacteria contain universally conserved MAMPs, how do commensal microbes, unlike pathogens, avoid triggering TLR activation? It is historically believed that the microbiota is excluded from the mucosal surface (*24*). However, certain symbiotic bacteria tightly adhere to the intestinal mucosa (*9*–*11*), and thus immunologic ignorance may not explain why inflammation is averted by the microbiota. Our study provides new insight into the mechanisms by which the immune system distinguishes between pathogens and symbionts. The functional activity of PSA on T_{regs} contrasts with the role of TLR2 ligands of pathogens, which elicit inflammation, and thus reveals an unexpected function for TLR signaling during homeostatic intestinal colonization by the microbiota. Although engagement of TLR2 by previously identified ligands is known to stimulate microbial clearance of pathogens, TLR signaling by PSA paradoxically allows *B. fragilis* persistence on mucosal surfaces. These results identify PSA as the incipient member of a new class of TLR ligands termed "symbiont-associated molecular patterns (SAMPs)" that function to orchestrate immune responses to establish host-commensal symbiosis. On the basis of the importance of the microbiota to mammalian health (*25*), evolution appears to have created molecular interactions that engender host-bacterial mutualism. In conclusion, our findings suggest that animals are not "hard-wired" to intrinsically distinguish pathogens from symbionts, and that microbial-derived mechanisms have evolved to actively promote immunologic tolerance to symbiotic bacteria. This concept suggests a reconsideration of how we define self versus nonself.

References and Notes

1. R. E. Ley, D. A. Peterson, J. I. Gordon, *Cell* **124**, 837 (2006).
2. S. Manicassamy, B. Pulendran, *Semin. Immunol.* **21**, 185 (2009).
3. M. Fukata *et al.*, *J. Immunol.* **180**, 1886 (2008).
4. J. M. Reynolds *et al.*, *Immunity* **32**, 692 (2010).
5. I. Caramalho *et al.*, *J. Exp. Med.* **197**, 403 (2003).
6. P. B. Eckburg *et al.*, *Science* **308**, 1635 (2005).
7. I. I. Ivanov *et al.*, *Cell Host Microbe* **4**, 337 (2008).
8. K. Atarashi *et al.*, *Nature* **455**, 808 (2008).
9. V. Gaboriau-Routhiau *et al.*, *Immunity* **31**, 677 (2009).
10. I. I. Ivanov *et al.*, *Cell* **139**, 485 (2009).
11. K. Atarashi *et al.*, *Science* **331**, 337 (2011).
12. S. K. Mazmanian, J. L. Round, D. L. Kasper, *Nature* **453**, 620 (2008).
13. J. Ochoa-Repáraz *et al.*, *Mucosal Immunol.* **3**, 487 (2010).
14. J. L. Round, S. K. Mazmanian, *Proc. Natl. Acad. Sci. U.S.A.* **107**, 12204 (2010).
15. Materials and methods are available as supporting material on *Science* Online.
16. J. M. Kim, J. P. Rasmussen, A. Y. Rudensky, *Nat. Immunol.* **8**, 191 (2006).
17. S. K. Mazmanian, C. H. Liu, A. O. Tzianabos, D. L. Kasper, *Cell* **122**, 107 (2005).
18. Q. Wang *et al.*, *J. Exp. Med.* **203**, 2853 (2006).
19. C. A. Janeway Jr., R. Medzhitov, *Annu. Rev. Immunol.* **20**, 197 (2002).
20. R. Medzhitov, *Nature* **449**, 819 (2007).
21. H. Liu, M. Komai-Koma, D. Xu, F. Y. Liew, *Proc. Natl. Acad. Sci. U.S.A.* **103**, 7048 (2006).
22. R. P. Sutmuller *et al.*, *J. Clin. Invest.* **116**, 485 (2006).
23. S. Babu, C. P. Blauvelt, V. Kumaraswami, T. B. Nutman, *J. Immunol.* **176**, 3885 (2006).
24. L. V. Hooper, *Nat. Rev. Microbiol.* **7**, 367 (2009).
25. K. Smith, K. D. McCoy, A. J. Macpherson, *Semin. Immunol.* **19**, 59 (2007).
26. W. Lin *et al.*, *Nat. Immunol.* **8**, 359 (2007).

Acknowledgments: We thank S. W. McBride and Y. Shen (California Institute for Technology) for help with bacterial colonization and germ-free studies. We are grateful to A. Rudensky [Memorial Sloan-Kettering Cancer Center and Howard Hughes Medical Institute (HHMI)] for the gift of Foxp3-DTR mice and L. Hooper (University of Texas Southwestern and HHMI) for germ-free *Rag1*$^{-/-}$ mice. We thank members of the Mazmanian laboratory for their critical review of the manuscript. B.J. acknowledges support from the Crohn's and Colitis Foundation of America (CCFA) (award 2831) and T.A.C acknowledges support from the NIH (grant AI 080002). J.L.R. is a Merck Fellow of the Jane Coffin Childs Memorial Fund. S.K.M. is a Searle Scholar. This work was supported by funding from the NIH (grants DK 078938, DK 083633, AI 088626), the Damon Runyon Cancer Research Foundation, and the CCFA (award 2405) to S.K.M. J.L.R. and S.K.M. have a patent application (PCT/US2008/082928) on the use of PSA as a therapy for inflammatory bowel disease. The authors have no competing financial interests related to this publication.

Supporting Online Material

www.sciencemag.org/cgi/content/full/science.1206095/DC1
Materials and Methods
Figs. S1 to S16

15 February 2011; accepted 6 April 2011
Published online 21 April 2011;
10.1126/science.1206095

A Packing Mechanism for Nucleosome Organization Reconstituted Across a Eukaryotic Genome

Zhenhai Zhang,[1]* Christian J. Wippo,[2]* Megha Wal,[1] Elissa Ward,[1] Philipp Korber,[2]† B. Franklin Pugh[1]†

Near the 5′ end of most eukaryotic genes, nucleosomes form highly regular arrays that begin at canonical distances from the transcriptional start site. Determinants of this and other aspects of genomic nucleosome organization have been ascribed to statistical positioning, intrinsically DNA-encoded positioning, or some aspect of transcription initiation. Here, we provide evidence for a different explanation. Biochemical reconstitution of proper nucleosome positioning, spacing, and occupancy levels was achieved across the 5′ ends of most yeast genes by adenosine triphosphate–dependent trans-acting factors. These transcription-independent activities override DNA-intrinsic positioning and maintain uniform spacing at the 5′ ends of genes even at low nucleosome densities. Thus, an active, nonstatistical nucleosome packing mechanism creates chromatin organizing centers at the 5′ ends of genes where important regulatory elements reside.

Statistical positioning depends on the presence of a genomic barrier within a linear array of nucleosomes (*1*). Nucleosomes within the array will passively align at regular intervals from the barrier, independent of sequence or other external factors, rather than arrange randomly. Nucleosome organization in vivo displays patterns that are consistent with statistical

positioning (*2*–*4*). Yet studies have suggested that as much as half of all nucleosome positions are "encoded" in the DNA sequence (*5*, *6*), because nucleosome occupancy reconstituted in vitro with purified genomic DNA and histones is similar to that in vivo. However, occupancy and positioning are distinct metrics of nucleosome organization (fig. S1). Nucleosome positions around transcription start sites (TSS) in vivo are different from in vitro positions (*7*–*9*) (Fig. 1A), which has led to the suggestion that transcription promotes nucleosome organization in vivo (*7*, *10*).

To determine what is needed to reconstitute proper nucleosome positions across all genes, we added whole-cell extracts to nucleosomes reconstituted on genomic DNA (*11*). To facilitate visualization of nucleosome patterns, genes were clustered based on their in vivo nucleosome organization (Fig. 1B, left panel). We produced an equivalently ordered "native" nucleosome pattern (Fig. 1B, right panel), in which chromatin was first isolated from cells without prior cross-linking, then cross-linked in vitro, as a positive control for in vitro reconstitution. The native pattern was stable (fig. S4) and similar to the in vivo pattern (Fig. 1B).

We reevaluated the intrinsically DNA-encoded organization of nucleosomes in these five clusters in three ways: (i) existing datasets were re-examined (*6*, *7*), (ii) nucleosomes within native chromatin were allowed to redistribute to their thermodynamically favored DNA-guided positions by incubation in 600 mM NaCl, and (iii) purified *Drosophila* histones were deposited by salt gradient dialysis (SGD) onto recombinant plasmid libraries (1:1 histone/DNA ratio), containing 10- to 30-kb inserts of *Saccharomyces* genomic DNA.

These experiments recapitulated some of the more prominent features of the native patterns, including nucleosome-free promoter regions (NFRs) and nucleosome positions and occupancy at certain canonical locations, as evident by the similarity of some peaks and troughs between data sets (fig. S5). However, most positions were not predominantly sequence-intrinsic. Thus, sequence-intrinsic cues contribute to nucleosome exclusion at the 5′ ends of genes but are very limited in defining nucleosome occupancy and positioning in adjacent regions and are negligible for positioning further into the coding regions.

Poly(dA:dT) tracts are a major intrinsic determinant of low nucleosome levels in yeast promoters (*12*–*14*) but have not been linked to positioning of adjacent nucleosomes. We find a strong correlation between the consensus positions of poly(dA:dT) tracts and +1 nucleosomes

[1]Center for Eukaryotic Gene Regulation, Department of Biochemistry and Molecular Biology, The Pennsylvania State University, University Park, PA 16802, USA. [2]Adolf-Butenandt-Institut, Universität München, Munich, 80336, Germany.

*These authors contributed equally to this work.
†To whom correspondence should be addressed. E-mail: bfp2@psu.edu (B.F.P.); pkorber@lmu.de (P.K.)

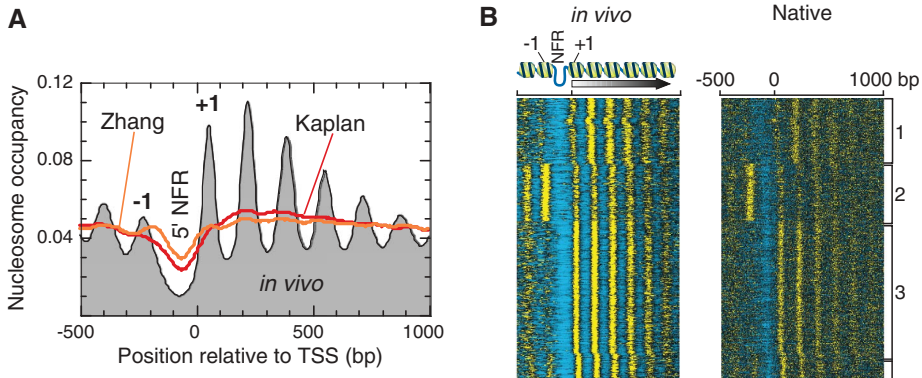

Fig. 1. Nucleosome organization around the 5′ ends of genes is not reconstituted in vitro with purified histones alone. (**A**) Composite distribution of nucleosome midpoints, assembled in vivo or in vitro (*6*, *7*), around transcriptional start sites. (**B**) Cluster view showing five in vivo patterns of nucleosome organization (left panel) and further characterized in fig. S3. All other cluster plots were ordered identically. A total of 4785 genes (rows) are aligned by their TSS. Yellow, black, and blue indicate a high, medium, and low occupancy level (tag counts), respectively.

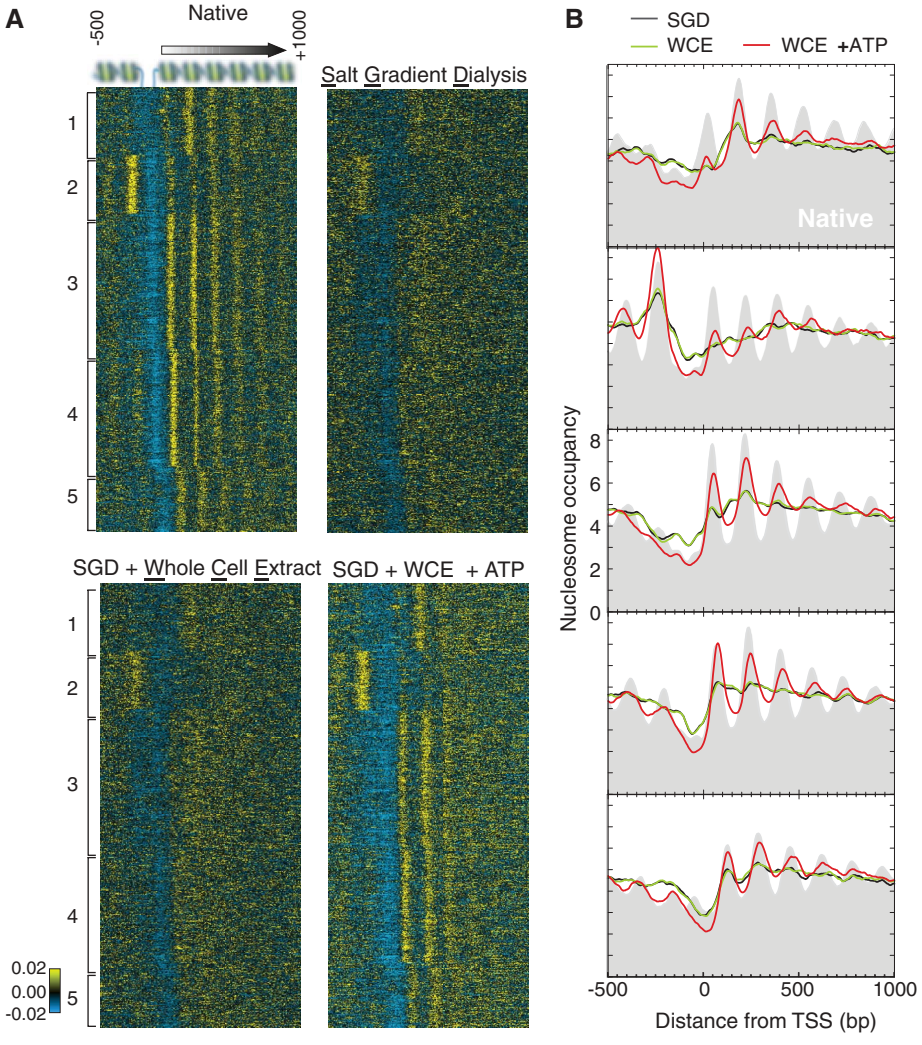

Fig. 2. Nucleosome organization around the 5′ ends of genes is reconstituted with whole-cell extracts and ATP. (**A**) Cluster plot and (**B**) corresponding composite plots of nucleosomes reconstituted by SGD. This reconstituted chromatin was either left untreated (SGD) or incubated with yeast whole-cell extracts in the absence (WCE) or presence (WCE+ATP) of ATP.

(fig. S6). Thus, poly(dA:dT) tracts may contribute to positioning of the +1 nucleosome.

Statistical positioning requires fixed barriers as sole guides of nucleosome positioning and sufficiently high nucleosome density such that one nucleosome sterically restricts the position of a neighboring nucleosome (*1*). Three of the in vitro reconstitution experiments (SGD, 600 mM, and Zhang *et al.*) (fig. S5) seemingly met these criteria: (i) the NFRs, which may serve as barriers, were largely recapitulated, and (ii) the histone:DNA ratio was sufficiently high (1:1) to promote statistical positioning. Yet, in conflict with statistical positioning, no regular arrays aligned at the canonical +1 position were observed. Even thermal reequilibration of nucleosomes (*15*, *16*) did not allow statistical positioning to occur, because extended incubation of the SGD material at 55°C did not generate uniformly positioned arrays (fig. S7). The failure to achieve statistical positioning with only histones and DNA suggests that sequence-guided placement of each nucleosome predominates in vitro over statistical positioning.

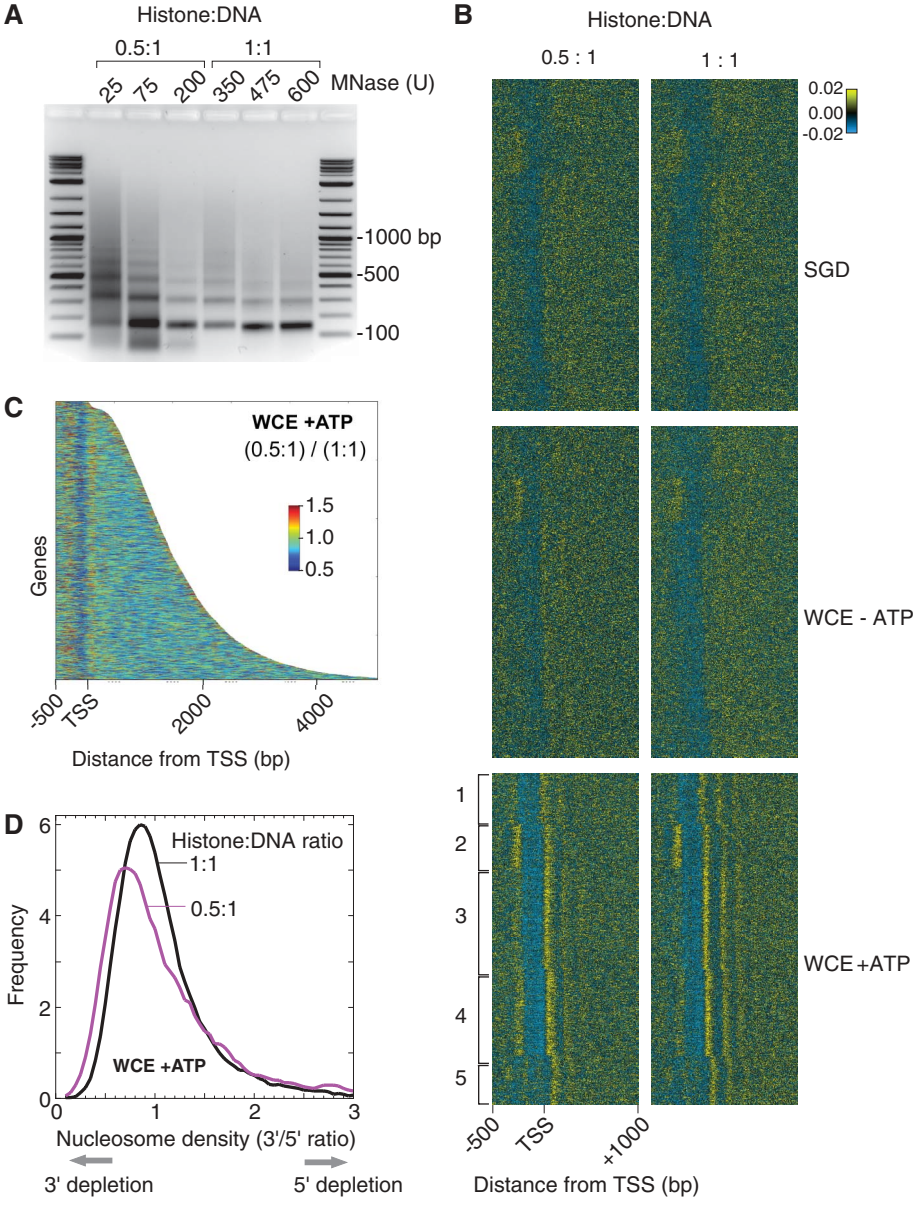

Fig. 3. Evidence that nucleosomes are actively packed against a barrier. (**A**) Ethidium bromide stained gel of SGD chromatin assembled at the indicated histone:DNA ratio (characterized in fig. S9), treated with whole-cell extracts and ATP, and then digested with micrococcal nuclease (MNase). (**B**) Cluster plots of nucleosomes reconstituted at 0.5:1 and 1:1 histone:DNA mass ratios. The bin-by-bin ratio of the bottom two panels to each other is shown in (**C**), but sorted by gene length. Data beyond the termination site is not shown. (**D**) Frequency distribution of 3′ histone density to 5′ histone density, on a per gene basis. The 3′ region is from +140 bp to the transcript termination site, whereas the 5′ region is from −20 to +140, relative to the TSS.

Given the central role adenosine triphosphate (ATP)–dependent chromatin remodeling complexes play in nucleosome organization (*17*), we considered that proper reconstitution of nucleosome positions might require ATP and trans-acting factors. The addition of whole-cell extracts plus ATP to the SGD material reconstituted nucleosome positions and occupancy levels around the 5′ ends of nearly all 4,785 tested yeast genes (Fig. 2). This was strictly ATP-dependent as incubation with extract in the absence of ATP had virtually no effect on nucleosome organization.

This reconstitution of in vivo–like nucleosome positioning did not require the other nucleoside triphosphates (*11*), indicating that transcription and DNA replication is not the predominant means by which nucleosomes become organized around genes, as originally demonstrated on *PHO5* (*18*). Moreover, the transcription initiation complex is not an obvious barrier against which nucleosomes are organized, because the TATA box position did not correlate with the position of the +1 nucleosome (fig. S8), and canonical nucleosome positioning is maintained in vivo at genes having little or no transcription (*3*). However, the binding site positions for Reb1, which is not part of the transcription machinery but functions similar to poly(dA:dT) tracts (*19*), did correlate with +1 positioning.

The data thus far argue against a DNA-intrinsic or transcription-based mechanism for organizing nucleosomes around the 5′ ends of genes but are entirely consistent with ATP-facilitated statistical positioning. For example, chromatin remodeling complexes could use ATP hydrolysis to override the DNA-intrinsic positioning landscape, thereby providing free bidirectional fluidity to nucleosomes that is only impeded by barriers. Although we favor the involvement of a remodeler adenosine triphosphatase (ATPase), we cannot formally exclude a kinase.

Statistical positioning predicts that internucleosomal spacing within arrays should be inversely related to nucleosome density (*1*), yet the cluster plots in Figs. 1 and 2 indicate that nucleosomal spacing is largely constant regardless of local nucleosome density (i.e., the periodicity of the yellow stripes is independent of the intensity of the yellow). As a direct test, we reconstituted ATP-dependent positioning on genomic DNA assembled at half the global histone:DNA density (0.5:1 instead of 1:1). Spacing remained largely unaltered [~165 base pairs (bp)], both globally (Fig. 3A) and in relation to a reference point like the TSS (Fig. 3B). Thus, a key test of statistical positioning failed.

Due to the bidirectional fluidity of nucleosomes inherent to the statistical positioning model, nucleosome density should remain relatively uniform, albeit periodic, outside of the barrier. This was not observed at the lower histone:DNA ratio. Instead, there was a decrease in nucleosome density in the NFR and internal to genes compared to the +1 nucleosome position. This was

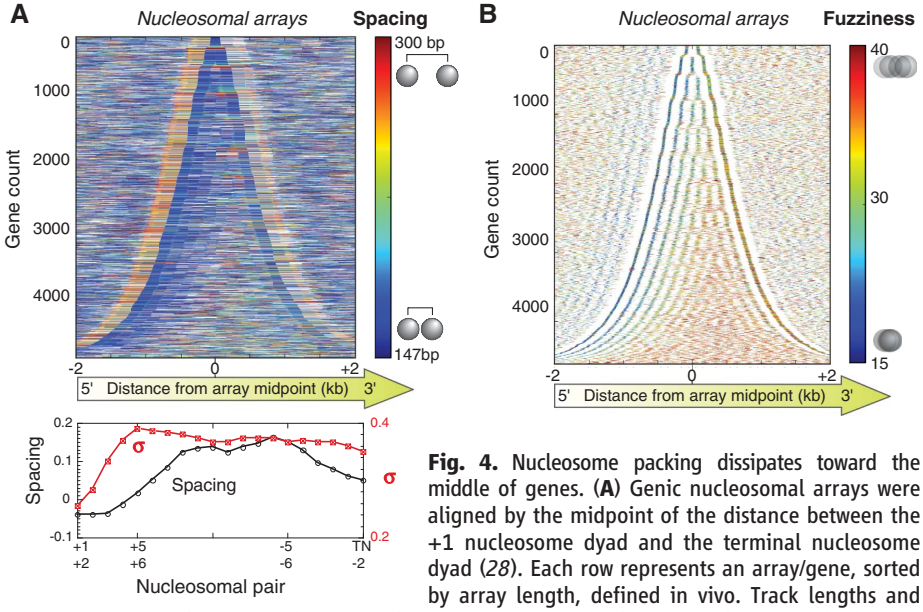

Fig. 4. Nucleosome packing dissipates toward the middle of genes. (**A**) Genic nucleosomal arrays were aligned by the midpoint of the distance between the +1 nucleosome dyad and the terminal nucleosome dyad (*28*). Each row represents an array/gene, sorted by array length, defined in vivo. Track lengths and coloring represent the spacing between adjacent nucleosome dyads measured in vivo. The bottom graph plots the median spacing (black) as well as its standard deviation, starting from the +1 nucleosome to the terminal nucleosome (TN). Median spacing is represented as the fractional change from the canonical 165 bp. (**B**) Same as (A), except that the track midpoints report the dyad position of each nucleosome measurement. Track lengths and heat map colors represent the standard deviation (fuzziness) of each cluster of tags measured in vivo.

evident on genes analyzed individually (Fig. 3C) or on aggregated data (Fig. 3D), suggesting that nucleosomes are actively packed against barriers at the 5′ ends of genes using ATP. This would occur at the expense of more distal nucleosomes under conditions of low nucleosome density. This model does not exclude bidirectional fluidity, but does implicate net directionality of nucleosome packing (fig. S10). This packing mechanism is consistent with previously proposed spacing mechanisms (*20*–*23*) but differs by the addition of a barrier and directionality. Together they provide constant spacing close to the barrier regardless of nucleosome density.

To analyze the packing mechanism further, we examined internucleosomal spacing in vivo along genic nucleosome arrays (Fig. 4A). The average spacing was relatively narrow and uniform from nucleosomes +1 through +4, and to a lesser extent also at the 3′ end. Spacing was, on average, wider but more variable toward the middle of longer genes, and thus less definable. This is not in conflict with the uniform spacing (peak-to-peak distances) in composite plots (e.g., Fig. 1A), because such measurements reflect modal internucleosomal distances (i.e., the most common spacing), rather than the average spacing. Modal internucleosomal distances are expected to remain constant along arrays until spacing activities and/or the influence of the barriers have fully dissipated. The wider and more variable spacing toward the middle of genes suggested that the active packing mechanism at 5′ barriers dissipates toward the middle of genes. The ATP-dependent packing activities may be constrained to position about four nucleosomes, because this was the extent to which ATP reconstituted proper positioning (Fig. 2).

More distally from barriers, nucleosome positioning may gradually transition to other mechanisms, for example through sequence-intrinsic preferences. If well-positioned nucleosomes resulted, then such positioning would be manifested as low fuzziness (standard deviation of sequencing tag positions) (*24*). However, nucleosome fuzziness increased toward the middle of genes, with some skewing toward the 3′ end (Fig. 4B). Thus, mechanisms outside the 5′ packing activity (and to a lesser extent at the 3′ end as well), whether active or passive, do not produce well-positioned nucleosomes.

Nucleosome positioning at the 5′ ends of most genes appears to be driven by ATP-dependent activities that directionally package nucleosomes against a 5′ barrier (and to a lesser extent 3′ barriers). Such nucleosome placement is not likely to be static and may involve dynamic exchange with free histones (*25*, *26*). Accordingly, the active nucleosome organization in vivo may be at steady state, under the continuous expense of energy, rather than at equilibrium (*27*). This barrier-packing combination may constitute an organizing center that operates for a limited distance to buffer nucleosome organization at the 5′ ends of genes from fluctuations in histone levels both globally and locally during DNA replication and transcription. If replication transiently decreases nucleosome density by half and if 5′ nucleosome packing operates faster than replication-dependent nucleosome assembly, old nucleosomes would be enriched toward the 5′ ends and new histones mainly would be deposited in the middle to 3′ ends of genes. A 5′ packing mechanism may also serve to regulate access to transcriptional start sites. Furthermore, the control of nucleosome positioning at each gene by a single organizing center would minimize evolutionary constraints on coding sequences that might otherwise occur if positioning was intrinsically encoded by the DNA sequence.

References and Notes

1. R. D. Kornberg, L. Stryer, *Nucleic Acids Res.* **16**, (14A), 6677 (1988).
2. G. C. Yuan *et al.*, *Science* **309**, 626 (2005).
3. T. N. Mavrich *et al.*, *Genome Res.* **18**, 1073 (2008).
4. W. Möbius, U. Gerland, *PLOS Comput. Biol.* **6**, e1000891 (2010).
5. E. Segal *et al.*, *Nature* **442**, 772 (2006).
6. N. Kaplan *et al.*, *Nature* **458**, 362 (2009).
7. Y. Zhang *et al.*, *Nat. Struct. Mol. Biol.* **16**, 847 (2009).
8. A. Stein, T. E. Takasuka, C. K. Collings, *Nucleic Acids Res.* **38**, 709 (2010).
9. A. Hughes, O. J. Rando, *J. Biol.* **8**, 96 (2009).
10. A. Weiner, A. Hughes, M. Yassour, O. J. Rando, N. Friedman, *Genome Res.* **20**, 90 (2010).
11. Materials and methods are available as supporting material on *Science* Online.
12. J. D. Anderson, J. Widom, *Mol. Cell. Biol.* **21**, 3830 (2001).
13. V. Iyer, K. Struhl, *EMBO J.* **14**, 2570 (1995).
14. R. M. Raisner *et al.*, *Cell* **123**, 233 (2005).
15. K. Luger, T. J. Rechsteiner, T. J. Richmond, *Methods Enzymol.* **304**, 3 (1999).
16. A. Flaus, T. Owen-Hughes, *Mol. Cell. Biol.* **23**, 7767 (2003).
17. G. R. Schnitzler, *Cell Biochem. Biophys.* **51**, 67 (2008).
18. P. Korber, W. Hörz, *J. Biol. Chem.* **279**, 35113 (2004).
19. P. D. Hartley, H. D. Madhani, *Cell* **137**, 445 (2009).
20. P. D. Varga-Weisz *et al.*, *Nature* **388**, 598 (1997).
21. G. LeRoy, G. Orphanides, W. S. Lane, D. Reinberg, *Science* **282**, 1900 (1998).
22. T. Ito, M. Bulger, M. J. Pazin, R. Kobayashi, J. T. Kadonaga, *Cell* **90**, 145 (1997).
23. T. Tsukiyama, J. Palmer, C. C. Landel, J. Shiloach, C. Wu, *Genes Dev.* **13**, 686 (1999).
24. I. Albert *et al.*, *Nature* **446**, 572 (2007).
25. A. Rufiange, P. E. Jacques, W. Bhat, F. Robert, A. Nourani, *Mol. Cell* **27**, 393 (2007).
26. M. F. Dion *et al.*, *Science* **315**, 1405 (2007).
27. E. Segal, J. Widom, *Trends Genet.* **25**, 335 (2009).
28. C. Vaillant *et al.*, *Genome Res.* **20**, 59 (2010).

29. We thank the members of the Penn State Center for Eukaryotic Gene Regulation and of the Molecular Biology Unit of the Adolf-Butenandt-Institut for valuable discussion and support. We are grateful to D. Blaschke for technical assistance and to S. Holmberg for the gift of the *S. cerevisiae* library. This work was supported by grant HG004160 from the National Institutes of Health to B.F.P.; and by the German Research Community (SFB/TR5) and the Epigenome Network of Excellence in the Sixth Framework Programme of the European Community (NET grant), both to P.K. Sequencing data are available at ArrayExpress under accession number: SRA030538.1.

Supporting Online Material

www.sciencemag.org/cgi/content/full/332/6032/977/DC1
Materials and Methods
Figs. S1 to S10
References

10.1126/science.1200508

Structures of the Bacterial Ribosome in Classical and Hybrid States of tRNA Binding

Jack A. Dunkle,[1]* Leyi Wang,[2] Michael B. Feldman,[2,3] Arto Pulk,[1] Vincent B. Chen,[4] Gary J. Kapral,[4] Jonas Noeske,[1] Jane S. Richardson,[4] Scott C. Blanchard,[2] Jamie H. Doudna Cate[1,5]†

During protein synthesis, the ribosome controls the movement of tRNA and mRNA by means of large-scale structural rearrangements. We describe structures of the intact bacterial ribosome from *Escherichia coli* that reveal how the ribosome binds tRNA in two functionally distinct states, determined to a resolution of ~3.2 angstroms by means of x-ray crystallography. One state positions tRNA in the peptidyl-tRNA binding site. The second, a fully rotated state, is stabilized by ribosome recycling factor and binds tRNA in a highly bent conformation in a hybrid peptidyl/exit site. The structures help to explain how the ratchet-like motion of the two ribosomal subunits contributes to the mechanisms of translocation, termination, and ribosome recycling.

Protein biosynthesis by the ribosome proceeds in defined phases of initiation, protein elongation, termination, and ribosome recycling (*1*). Understanding the molecular mechanism of translation requires high-resolution descriptions of the motions in the ribosome that enable key translational events (*1*–*3*). A ratchet-like rotation of the small ribosomal subunit relative to the large ribosomal subunit (*4*) is crucial to the positioning of tRNAs in intermediate—or hybrid—binding sites, in which the 3′-CCA termini and acceptor stems of tRNA advance by one site on the large subunit while the anticodon elements of tRNA remain fixed on the small subunit (*5*). Binding of tRNAs in hybrid sites is central to mRNA and tRNA movements on the ribosome when they are translocated after each peptide bond is formed, during termination, and during ribosome recycling (*6*, *7*). However, the molecular basis for ribosome positioning of tRNAs in hybrid sites has been unclear.

Atomic-resolution x-ray crystal structures of the bacterial ribosome with ligands bound have revealed molecular details of conformational rearrangements taking place in the unrotated ribosome (*1*). The first molecular descriptions of intermediate states of ribosome ratchet-like rotation at atomic resolution were provided by x-ray crystal structures of the *Escherichia coli* 70*S* ribosome (*8*), with additional substeps proposed on the basis of cryogenic electron microscopy (cryo-EM) reconstructions (*9*). A posttranslocation rotated state of the ribosome was recently identified by means of cryo-EM (*10*), in a conformation similar to that of the *Saccharomyces cerevisiae* 80*S* ribosome in the absence of bound substrates (*11*, *12*).

After the termination of protein synthesis, ribosome recycling is required to free ribosomes from the mRNA transcript to enable further rounds of translation. In bacteria and organelles, ribosome recycling factor (RRF) binds in the tRNA-binding cleft of the 70*S* ribosome at the interface of the large (50*S*) and small (30*S*) subunits and interacts with the 50*S* subunit peptidyl transferase center (PTC) (*13*, *14*). In so doing, RRF sterically occludes deacylated tRNA binding in the peptidyl-tRNA site (P site, P/P configuration) to favor tRNA positioning in the hybrid peptidyl/exit tRNA-binding site (P/E configuration) (Fig. 1A) (*13*, *15*, *16*). In the P/E configuration, tRNA is bound simultaneously to the P site of the small (30*S*) subunit and to the E site of the large (50*S*) subunit (*5*). Binding of the guanosine triphosphatase (GTPase) elongation

[1]Departments of Molecular and Cell Biology and Chemistry, University of California at Berkeley, Berkeley, CA 94720, USA. [2]Department of Physiology and Biophysics, Weill Cornell Medical College of Cornell University, New York, NY 10065, USA. [3]Weill Cornell/Rockefeller University/Sloan-Kettering Tri-Institutional MD-PhD Program, New York, NY 10065, USA. [4]Department of Biochemistry, Duke University Medical Center, Durham, NC 27710, USA. [5]Physical Biosciences Division, Lawrence Berkeley National Laboratory, Berkeley, CA 94720, USA.

*Present address: Department of Biochemistry, Emory University School of Medicine, Atlanta, GA 30322, USA.
†To whom correspondence should be addressed. E-mail: jcate@lbl.gov

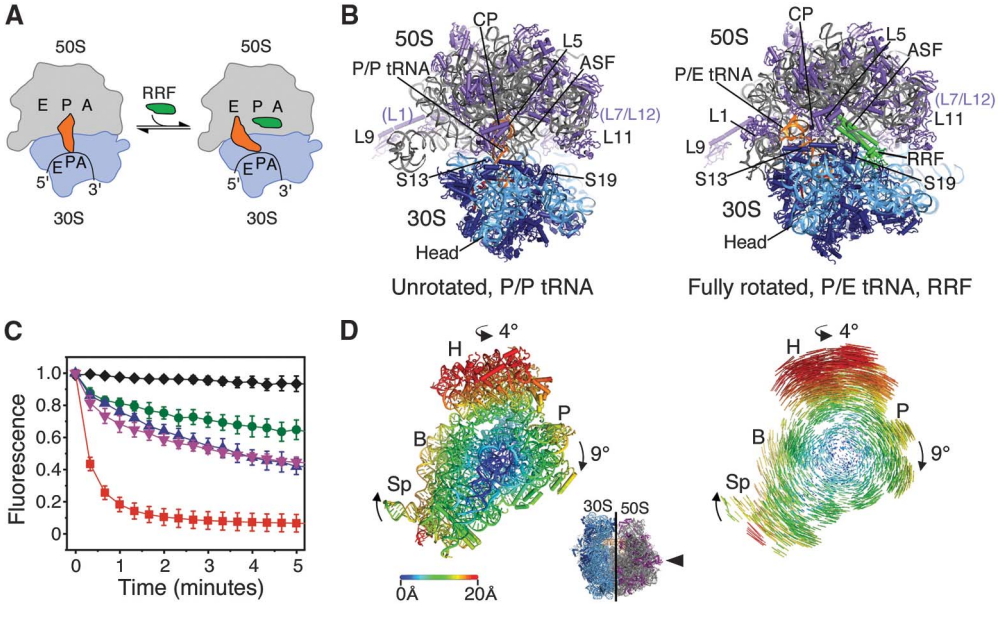

Fig. 1. Ribosome recycling in bacteria and organelles. (**A**) Steps of ribosome recycling. After termination, ribosomes with deacylated tRNA in the P site undergo a structural rearrangement to a fully rotated state in which tRNA adopts a P/E hybrid state of binding and RRF is bound in the 50*S* P site. EF-G then catalyzes subunit dissociation. (**B**) Global views of the ribosome in a posttermination state (L) and intermediate state of recycling (R). The small subunit rRNA and proteins are colored light and dark blue, respectively, with the large subunit rRNA and proteins colored gray and purple, respectively. Bound tRNA (orange), mRNA (dark red), and RRF (green) are also shown. (**C**) The dependence of subunit release on RRF, EF-G, and GTP under crystallographic buffer conditions. Release was monitored by the loss of Cy5-labeled L1 fluorescence in 50*S* subunits from surface-immobilized ribosome complexes carrying Cy3-labeled $tRNA^{Phe}$ in the P site. Complexes were imaged in the absence of factors (black diamonds) or in the presence of 10 μM RRF (green circles), 20 μM EF-G/2 mM GTP (purple inverted triangles), 10 μM RRF/20 μM EF-G/2 mM GDPNP (blue triangles), or 10 μM RRF/20 μM EF-G/2 mM GTP (red squares). Data reflect the mean ± SD of normalized Cy5 fluorescence intensity as a function of time from three experimental replicates. (**D**) Conformational changes in the 70*S* ribosome during inter-subunit rotation. (Inset) View of the 30*S* subunit from the perspective of the 50*S* subunit. Shifts between equivalent RNA phosphorus atoms and protein Cα atoms in the unrotated (R_0) and fully rotated (R_F) states are color coded as indicated by the scale. Ribosomes were superimposed by using the 50*S* subunit as the frame of reference (*38*). Difference vectors between equivalent phosphorus or Cα atoms of the 30*S* subunits in the unrotated and fully rotated ribosome structures are shown on the right.

factor–G (EF-G) to the RRF-ribosome complex and subsequent guanosine 5′-triphosphate (GTP) hydrolysis lead to the dissociation of ribosomal subunits (*17*).

We determined structures of the intact *E. coli* 70*S* ribosome at a resolution of ~3.2 Å (tables S1 and S2) (*12*) using crystals that contain two independent copies of the ribosome per asymmetric unit in a "top-top" polysome configuration (*18*). One ribosome adopts an unrotated state, with $tRNA^{Phe}$ bound in the peptidyl-tRNA (P/P) binding site (Fig. 1B) (*19*) that mimics a posttermination state of the translation cycle. The second ribosome adopts a fully rotated conformation that contains $tRNA^{Phe}$ bound in the hybrid P/E binding site and RRF bound at the ribosomal subunit interface (Fig. 1B). This structure is thought to represent an early intermediate in bacterial ribosome recycling (Fig. 1A) (*15*). Under these buffer conditions, single-molecule fluorescence resonance energy transfer (smFRET) measurements showed RRF achieved approximately 50% maximal stabilization of the fully rotated, P/E hybrid configuration of the posttermination complex (fig. S1) and supported EF-G– and GTP hydrolysis–dependent ribosome recycling (Fig. 1C and fig. S1) (*12*).

When compared with the posttermination ribosome complex, the 30*S* subunit of the RRF-bound ribosome is rotated ~9° relative to the 50*S* subunit. An approximately orthogonal rotation of the head domain of the 30*S* subunit of ~4° swivels the head domain in the direction of the ribosomal E site on the 50*S* subunit. These motions of the 30*S* subunit into the rotated state result in shifts at the periphery of the ribosome of more than 20 Å (Fig. 1D) that direct deacylated P-site tRNA into the P/E hybrid site. The tRNA anticodon stem-loop (ASL) and mRNA move laterally by ~6 Å relative to the 50*S* subunit, coupled to the motion of the 30*S* subunit platform domain (Figs. 1D and 2A). When tRNA moves into the P/E site from the P/P site, the tRNA ASL remains in contact with the 30*S* subunit head and platform domains (Fig. 2B and fig. S2A) (*19*) but breaks its interactions with 23*S* ribosomal RNA (rRNA) helix H69 in the large subunit (*19*) (Fig. 2B and movie S1).

Bound in the hybrid P/E site, $tRNA^{Phe}$ is severely kinked at the junction between the ASL and D stem when compared with $tRNA^{Phe}$ bound in the P/P site. Although the conformation of the anticodon and two closing base pairs of the ASL region remain essentially unchanged, the major groove widens by ~4 Å at the junction of the ASL and D stem (Fig. 2C and fig. S2). The kink between the ASL and D stems allows the acceptor stem of P/E tRNA to swing by ~37° into the 50*S* E site (Fig. 2D) (*12*). This abrupt kink contrasts with the more distributed bend that occurs in mRNA-decoding complexes bound to elongation factor EF-Tu [A/T state, (*20*, *21*)], in which tRNA bends in the opposite direction. Comparing P/E tRNA with A/T tRNA, the total extent of tRNA bending at the ASL/D-stem junction amounts to ~70° (Fig. 2D and movie S1).

In the large subunit E site, P/E tRNA contacts the ribosome in a similar manner to tRNA bound in the E/E site (Fig. 2B) (*19*). Nucleotides G2112 and G2168 in 23*S* rRNA, part of the protein L1-containing arm of the 50*S* subunit, stack on the D-loop and T-loop of P/E tRNA (Figs. 1B and 2B) (*22*). Consistent with biochemical studies of the mechanism of translocation (*23*), nucleotide A76 at the acceptor end of P/E tRNA stacks between nucleotides in helix H88 of 23*S* rRNA (Fig. 2B and fig. S3), where the terminal ribose engages the Watson-Crick face of nucleotide C2394 (*19*, *23*). In contrast to the positioning of C75 in E-site tRNA in the bacterium *Thermus thermophilus* (*19*) and in the archaeal large subunit (*24*), in the *E. coli* ribosome, nucleotide C75 in P/E tRNA stacks on nucleotide A2432 in 23*S* rRNA, away from the tRNA acceptor stem (fig. S3). The striking divergence of the 50*S* E site contacts contrasts with the high level of conservation in the peptidyl transferase center, supporting the notion that the ribosomal E site evolved relatively late and has continued to diverge (*19*, *25*).

The molecular contacts between the two ribosomal subunits are composed of both rRNA and ribosomal proteins, with the central contacts, or bridges, conserved across kingdoms (*11*, *26*). In the fully rotated state, the pivot point for intersubunit ratcheting occurs at bridge B3 (Fig. 3A and fig. S4), which maintains the same conformation and contacts when compared with the unrotated ribosome (*26*). Bridge B3 is composed of a cross-strand adenosine-stacking motif (*27*), in which residues A1418 and A1483 within helix 44 (h44) of 16*S* rRNA in the 30*S* subunit dock into the minor groove of helix 71 (H71) in 23*S* rRNA of the 50*S* subunit. Residues A1418 and A1483 lie within adjacent sheared G-A base pairs that coordinate an inner-sphere magnesium ion that possibly contributes to subunit association in all organisms (Fig. 3B) (*26*, *28*).

In the aminoacyl-tRNA (A) and P sites, bridge B2a involves contacts between 23*S* rRNA helix H69 in the 50*S* subunit and 16*S* rRNA residues at the end of helix h44 in the 30*S* subunit that are preserved in both the unrotated and fully rotated states of the ribosome (Fig. 3A). In both states, residue A1913 of H69 penetrates the minor groove of the h44 mRNA decoding site. However, in going from the unrotated to fully rotated state, the P-site tRNA anticodon, mRNA (Fig. 2A), and the end of helix h44 move laterally by ~6 Å toward the E site (Fig. 3C). The interactions between H69 and h44 are maintained during this movement because of a ~5 Å compression of H69 (Fig. 3C and movie S2). In part, this compression is enabled by disruption of the terminal base pair (C1925-G1929) of H69 and extrusion of the nearly universally conserved uridine U1926 (*29*) from the tight U-turn motif at the base of H69 (fig. S5 and movie S2) (*25*).

The observed conformational rearrangements in bridge B2a may help explain how antibiotics such as viomycin that target translocation stabi-

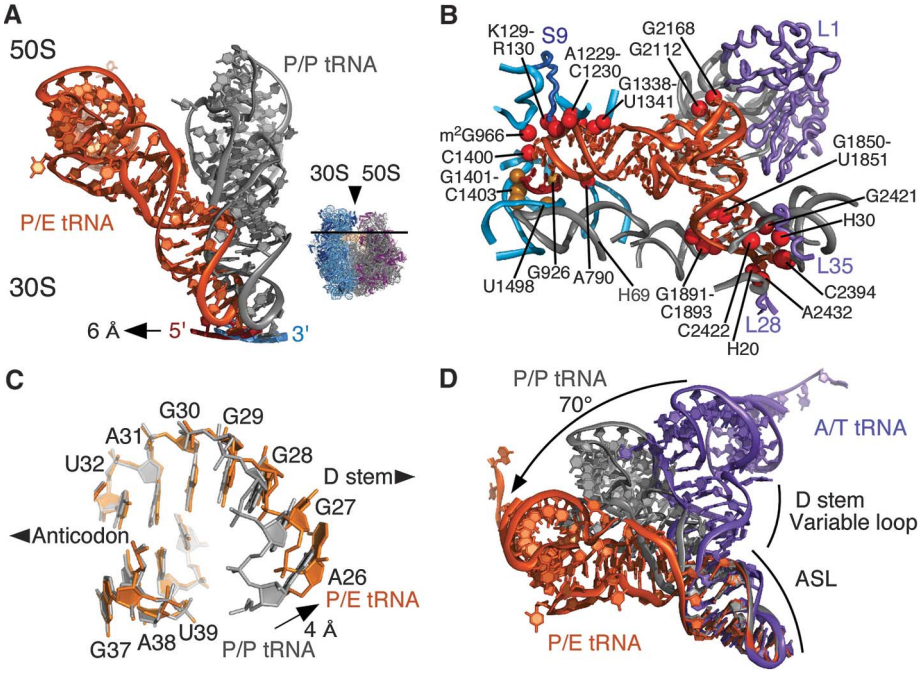

Fig. 2. Conformation of tRNA in the P/E hybrid state. (**A**) Movement of P/E tRNA and mRNA toward the E site when compared with P/P tRNA and mRNA. The direction of view is shown to the right. (**B**) View of mRNA and P/E tRNA interactions with the 30*S* subunit P site and 50*S* subunit E site. Residues that contact mRNA (gold) and P/E tRNA (red) are shown. Colors for the ribosome, mRNA, and tRNA are as in Fig. 1. (**C**) View of the P/E tRNA ASL/D stem junction (orange). P/P tRNA (gray) is shown for comparison, with an arrow indicating the widening of the helix major groove. (**D**) Comparison of ASL/D stem junctions between P/E tRNA (orange), P/P tRNA (gray), and A/T tRNA (purple). A/T tRNA structure is a homology model adapted from (*12*, *21*). The bending angle for the A/T to P/E conformational change (70°) is shown.

lize the fully rotated state of the ribosome (*30*, *31*). Viomycin and the related antibiotic capreomycin bind to the ribosome in the vicinity of nucleotide A1913 in 23*S* rRNA (*32*), the only nucleotide whose contacts with h44 change appreciably during inter-subunit rotation. Aminoglycosides such as neomycin, which bind to two sites in bridge B2a (*33*, *34*), may favor the fully rotated state of the ribosome by stabilizing the compressed conformation of helix H69.

On the opposite end of the tRNA-binding cleft, bridge B7a is disrupted by the rotation of the 30*S* platform domain (Fig. 1D). In the unrotated state, nucleotide A702 in 16*S* rRNA stacks on an A-A dinucleotide platform near the end of helix H68 of 23*S* rRNA (*12*, *35*). This interaction involves a hydrogen bond between N1 of A702 and G1846 in 23*S* rRNA (*25*). Consistent with chemical probing data used to identify hybrid tRNA-binding sites (*5*), rotation of the 30*S* platform domain into the fully rotated position results in a ~13 Å displacement of A702 away from H68 that exposes the base pairing face of A702 to solvent (Fig. 3D). Consistent with biochemical observations (*36*), H68 moves in the opposite direction by 2 to 3 Å to pack in the minor groove of the acceptor stem of P/E tRNA (Fig. 3D), probably helping to stabilize tRNA in the P/E hybrid site.

The absence of bridge B7a in the fully rotated state appears to be partially compensated for by new contacts between protein L2 in the large subunit and helices h23 and h24 in 16*S* rRNA (bridges B7b and B7c) (Fig. 3A). However, the key stabilizing contact to the 30*S* platform region in both the unrotated and fully rotated ribosome configurations remains bridge B4, which in bacteria involves intimate contacts between the hairpin loop at the end of helix H34 in 23*S* rRNA of the large subunit and protein S15 in the small subunit. Helix H34 bends by ~7 Å, or 12°, during inter-subunit rotation and slightly adjusts how nucleotide A715 packs on the hydrophobic surface of protein S15 (Fig. 3E) (*25*). Compensation for the loss of bridge B7a in the fully rotated state may also result from the formation of more extensive interactions between the 30*S* subunit body domain and the 50*S* subunit near bridge B8. In bridge B8, large subunit proteins L14 and L19 interact more closely with helices h8 and h14 in the 30*S* subunit (Fig. 3A).

In the fully rotated state, the head domain of the 30*S* subunit swivels as a rigid body in the direction of tRNA movement, rearranging bridge B1b to place the central alpha helix of protein S13 directly across from protein L5 in the 50*S* subunit (Fig. 1B) (*37*). This lateral change in protein S13 position correlates with tRNA binding in the hybrid P/E site and may help control the position of tRNAs on the ribosome (*38*). Thus, the contacts between protein S13 and protein L5 probably play an important role in the ribosome ratcheting mechanism. Consistent with this view, deletions in protein S13 result in more rapid and lower fidelity translocation of mRNA and tRNA (*39*). Mutations in the other major contact between the 30*S* subunit head domain and helix H38 in the 50*S* subunit, bridge B1a, have a similar effect (*40*).

In the fully rotated ribosome, RRF binds in the P-site and A-site cleft of the 50*S* subunit, precluding tRNA binding in either site. Its three-helix bundle domain (domain I) runs nearly parallel to the subunit interface, with alpha helix 3 packed tightly against helix H71 in 23*S* rRNA (Fig. 4A). Mutations in this region result in lethal or temperature-sensitive phenotypes (*41*). In addition, conserved amino acids within the tip of RRF domain I (*42*) interact with rRNA nucleotides of the universally conserved P loop element of the peptidyl transferase center (Fig. 4A). These sets of interactions appear to be the same in both the unrotated and fully rotated states of the ribosome (*33*, *43*), suggesting that they are necessary but not sufficient for the recycling mechanism.

Additional points of contact between RRF and the fully rotated ribosome occur between

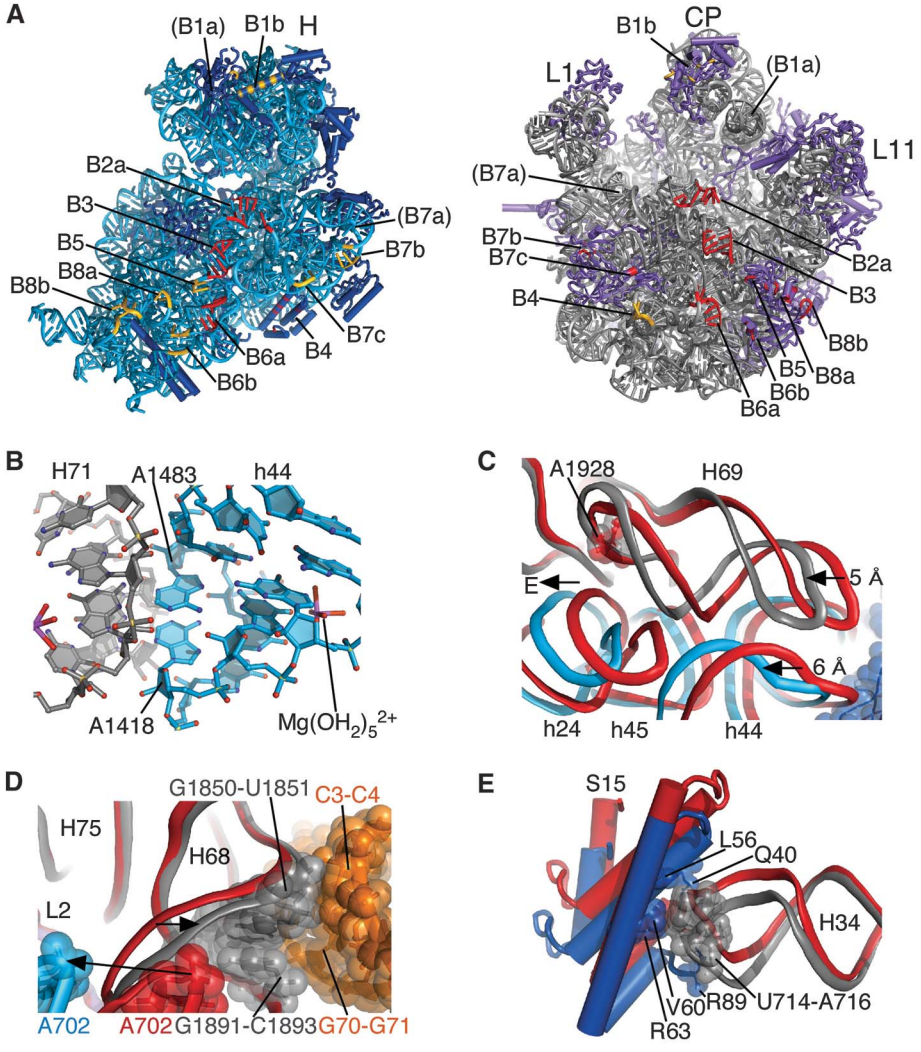

Fig. 3. Inter-subunit contacts in the fully rotated state. (**A**) Global view of inter-subunit contacts of the fully rotated state. Elements in each ribosomal subunit that contact rRNA in opposite subunit are color-coded red, whereas elements in each subunit that contact ribosomal proteins in the opposite subunit are color-coded gold. rRNAs and proteins are colored as in Fig. 1. Bridge numbering is adapted from (*11*, *26*). The tip of helix H38 in bridge B1a is disordered in the present structures. The 30*S* subunit head region (H) and 50*S* subunit central protuberance (CP), L1 and L11 arms are labeled for reference. (**B**) Bridge B3 serves as the pivot of inter-subunit rotation. The Mg^{2+} ion involved in inner-sphere coordination to the tandem sheared GA pairs in 16*S* rRNA and a fully hydrated Mg^{2+} ion in 23*S* rRNA are also shown. rRNAs are colored as in Fig. 1. (**C**) Compression of helix H69 in 23*S* rRNA because of inter-subunit rotation. The direction of view is similar to Fig. 1. Color coding of the fully rotated ribosome (R) is as in Fig. 1, with unrotated ribosome (U) in red. Nucleotide A1928 in 23*S* rRNA, nearly invariant in position, is shown for reference. Helices in 16*S* rRNA are labeled "h" and in 23*S* rRNA are labeled "H." (**D**) Movement of H68 because of disruption of A702 interactions and packing with P/E tRNA. Nucleotides involved in H68 packing with P/E tRNA are indicated. Elements of the fully rotated ribosome are colored as in Fig. 1. Elements of the unrotated ribosome are shown in red. Arrows indicate movement from the unrotated to fully rotated state. (**E**) Bridge B4 in the fully rotated state compared with that in the unrotated state (R_0, red). Residues involved in direct contact in the fully rotated state are shown. Coloring for the fully rotated state is as in Fig. 1.

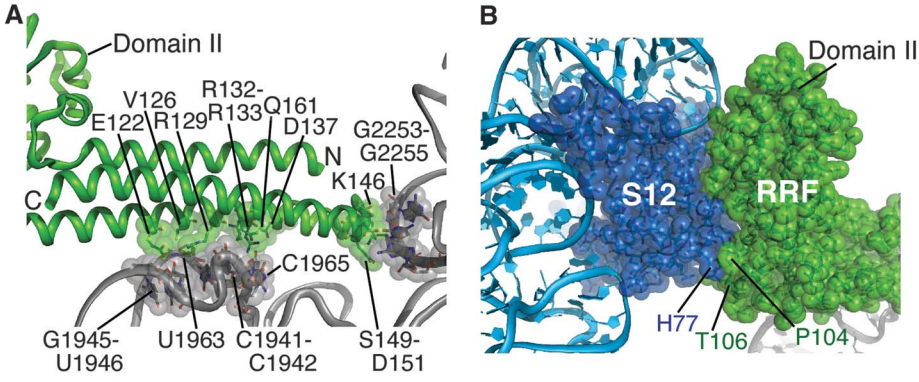

Fig. 4. RRF interactions with the ribosome in the fully rotated state. (**A**) Contacts between RRF domain I and the P and A sites of the 50*S* subunit. Amino acids in RRF (green) and nucleotides in 23*S* rRNA (gray) in direct contact are shown. Helix H69 and the 30*S* subunit are behind the view shown. (**B**) Contacts between RRF and protein S12 in the 30*S* subunit. Amino acids at the junction of RRF domains I and II that interact closely with S12 are indicated. RRF, S12, and rRNAs are colored as in Fig. 1.

conserved amino acids near the junction of domains I and II in RRF and ribosomal protein S12 of the small subunit (Fig. 4B) (*42*). Domain II of RRF is more constrained in its position in the ratcheted state as compared with its location in the unratcheted ribosome (*33*, *43*). As suggested by cryo-EM reconstructions of the ribosome in complexes with RRF (*14*, *15*), RRF domain II probably serves a steric function in ribosome recycling. Docking of EF-G from a cryo-EM reconstruction of the ribosome in a rotated conformation related to translocation (*10*) onto the ratcheted 70*S* ribosome structure determined here shows substantial overlap between domain II of RRF and domains IV and V of EF-G (fig. S6). Thus, EF-G binding to the RRF-bound ribosome probably entails large-scale rearrangements in RRF, EF-G, and the ribosome (*15*).

When compared with other structures, the structure of the fully rotated state of the ribosome provides critical insights into the molecular description of the ratcheting mechanism in translation. Because simple mRNAs can be translated in the absence of exogenous factors like EF-G (*44*), the ribosome itself serves as a Brownian ratchet (*2*, *45*), with tRNA substrates probably serving as the "teeth." A notable feature of the ratcheting mechanism is the use of RNA secondary structural elements to control large-scale conformational rearrangements in the ribosome. These include RNA stem-loops in bridges B2a and B4 that adjust as the 30*S* subunit rotates relative to the 50*S* subunit (*8*, *11*, *15*, *46*, *47*); helix H68 in 23*S* rRNA adjacent to bridge B7a and P/E tRNA; RNA helices H76 and H42 in the L1 and L11 arms of the large subunit, respectively (*1*, *2*, *11*, *37*, *48*); and helix h28 in 16*S* rRNA which directs swiveling of the 30*S* subunit head domain (*25*). Helix h28 probably serves as the "spring" in the ratcheting process, helping to position the "pawl" between the small subunit P and E sites (*3*, *10*, *25*, *45*). The hinge-like motion in P/E tRNA observed here, when compared with P/P tRNA, suggests that the conserved tertiary structure of tRNA is required not only for mRNA decoding (*20*, *21*, *49*) but also for translocation, termination, and ribosome recycling (*10*, *50*). Intact P-site tRNA is required for translocation (*51*), a requirement that may in part be due to a need for a large distortion of tRNA in the P/E binding site. This distortion may be used to tune the energetics of the transition between the pretranslocation state and posttranslocation state of the ribosome. Future structural studies of ribosome complexes with EF-G will be required to explain how this factor controls the conformational events described here to accelerate translocation and ribosome recycling.

References and Notes

1. T. M. Schmeing, V. Ramakrishnan, *Nature* **461**, 1234 (2009).
2. J. B. Munro, K. Y. Sanbonmatsu, C. M. Spahn, S. C. Blanchard, *Trends Biochem. Sci.* **34**, 390 (2009).
3. J. A. Dunkle, J. H. Cate, *Annu. Rev. Biophys.* **39**, 227 (2010).
4. J. Frank, R. K. Agrawal, *Nature* **406**, 318 (2000).
5. D. Moazed, H. F. Noller, *Nature* **342**, 142 (1989).
6. Y. P. Semenkov, M. V. Rodnina, W. Wintermeyer, *Nat. Struct. Biol.* **7**, 1027 (2000).
7. A. V. Zavialov, M. Ehrenberg, *Cell* **114**, 113 (2003).
8. W. Zhang, J. A. Dunkle, J. H. Cate, *Science* **325**, 1014 (2009).
9. N. Fischer, A. L. Konevega, W. Wintermeyer, M. V. Rodnina, H. Stark, *Nature* **466**, 329 (2010).
10. A. H. Ratje *et al.*, *Nature* **468**, 713 (2010).
11. A. Ben-Shem, L. Jenner, G. Yusupova, M. Yusupov, *Science* **330**, 1203 (2010).
12. Materials and methods are available as supporting material on *Science* Online.
13. L. Lancaster, M. C. Kiel, A. Kaji, H. F. Noller, *Cell* **111**, 129 (2002).
14. R. K. Agrawal *et al.*, *Proc. Natl. Acad. Sci. U.S.A.* **101**, 8900 (2004).
15. N. Gao *et al.*, *Mol. Cell* **18**, 663 (2005).
16. S. H. Sternberg, J. Fei, N. Prywes, K. A. McGrath, R. L. Gonzalez Jr., *Nat. Struct. Mol. Biol.* **16**, 861 (2009).
17. A. Savelsbergh, M. V. Rodnina, W. Wintermeyer, *RNA* **15**, 772 (2009).
18. F. Brandt *et al.*, *Cell* **136**, 261 (2009).
19. M. Selmer *et al.*, *Science* **313**, 1935 (2006).
20. T. M. Schmeing *et al.*, *Science* **326**, 688 (2009).
21. R. M. Voorhees, T. M. Schmeing, A. C. Kelley, V. Ramakrishnan, *Science* **330**, 835 (2010).
22. Single-letter abbreviations for the amino acid residues are as follows: A, Ala; C, Cys; D, Asp; E, Glu; F, Phe; G, Gly; H, His; I, Ile; K, Lys; L, Leu; M, Met; N, Asn; P, Pro; Q, Gln; R, Arg; S, Ser; T, Thr; V, Val; W, Trp; and Y, Tyr. Single-letter abbreviations for nucleotide residues are as follows: A, adenosine; C, cytidine; G, guanosine; and U, uridine.
23. R. Lill, J. M. Robertson, W. Wintermeyer, *EMBO J.* **8**, 3933 (1989).
24. T. M. Schmeing, P. B. Moore, T. A. Steitz, *RNA* **9**, 1345 (2003).
25. K. Bokov, S. V. Steinberg, *Nature* **457**, 977 (2009).
26. B. S. Schuwirth *et al.*, *Science* **310**, 827 (2005).
27. J. H. Cate *et al.*, *Science* **273**, 1678 (1996).
28. C. L. Shenvi, K. C. Dong, E. M. Friedman, J. A. Hanson, J. H. Cate, *RNA* **11**, 1898 (2005).
29. J. J. Cannone *et al.*, *BMC Bioinformatics* **3**, 2 (2002).
30. D. N. Ermolenko *et al.*, *Nat. Struct. Mol. Biol.* **14**, 493 (2007).
31. P. V. Cornish, D. N. Ermolenko, H. F. Noller, T. Ha, *Mol. Cell* **30**, 578 (2008).
32. R. E. Stanley, G. Blaha, R. L. Grodzicki, M. D. Strickler, T. A. Steitz, *Nat. Struct. Mol. Biol.* **17**, 289 (2010).
33. M. A. Borovinskaya *et al.*, *Nat. Struct. Mol. Biol.* **14**, 727 (2007).
34. M. B. Feldman, D. S. Terry, R. B. Altman, S. C. Blanchard, *Nat. Chem. Biol.* **6**, 54 (2010).
35. J. H. Cate *et al.*, *Science* **273**, 1696 (1996).
36. J. S. Feinberg, S. Joseph, *Proc. Natl. Acad. Sci. U.S.A.* **98**, 11120 (2001).
37. M. Valle *et al.*, *Cell* **114**, 123 (2003).
38. J. Frank, H. Gao, J. Sengupta, N. Gao, D. J. Taylor, *Proc. Natl. Acad. Sci. U.S.A.* **104**, 19671 (2007).
39. A. R. Cukras, R. Green, *J. Mol. Biol.* **349**, 47 (2005).
40. T. Komoda *et al.*, *J. Biol. Chem.* **281**, 32303 (2006).
41. L. Janosi *et al.*, *J. Mol. Biol.* **295**, 815 (2000).
42. H. Ashkenazy, E. Erez, E. Martz, T. Pupko, N. Ben-Tal, *Nucleic Acids Res.* **38** (Web Server issue), W529 (2010).
43. A. Weixlbaumer *et al.*, *Nat. Struct. Mol. Biol.* **14**, 733 (2007).
44. L. P. Gavrilova, O. E. Kostiashkina, V. E. Koteliansky, N. M. Rutkevitch, A. S. Spirin, *J. Mol. Biol.* **101**, 537 (1976).
45. A. S. Spirin, *J. Biol. Chem.* **284**, 21103 (2009).
46. S. R. Connell *et al.*, *Mol. Cell* **25**, 751 (2007).
47. C. M. Spahn *et al.*, *EMBO J.* **23**, 1008 (2004).
48. M. Valle *et al.*, *Nat. Struct. Biol.* **10**, 899 (2003).
49. M. Valle *et al.*, *EMBO J.* **21**, 3557 (2002).
50. W. Li, J. Frank, *Proc. Natl. Acad. Sci. U.S.A.* **104**, 16540 (2007).
51. S. Joseph, H. F. Noller, *EMBO J.* **17**, 3478 (1998).

52. We thank K. Hamadani for purified RRF; K. Nierhaus for $tRNA^{Phe}$ overexpression plasmids; K. Frankel, S. Classen, and G. Meigs for help with data measurement at the SIBYLS and 8.3.1 beamlines at the Advanced Light Source (ALS); R. Kanagalaghatta, D. Neau, F. Murphy, and I. Kourinov for help with data measurement at ID-24 at the Advanced Photon Source (APS); J. Headd for help with Phenix refinement; and J. Holton for useful crystallographic discussions. We also thank J. Doudna and H. Noller for helpful comments on the manuscript. Atomic coordinates and structure factors are deposited in the Protein Data Bank (accession codes 3R8N and 3R8S for the fully rotated state R_F, 3R8O and 3R8T for the unrotated state R_0). This work was funded by the National Institutes of Health (GM65050 to J.H.D.C., GM079238 to S.C.B, and GM074127-04S1, GM088674, and P01-GM63210 project IV to J.S.R.), National Cancer Institute grant CA92584 for the SIBYLS and 8.3.1 beam lines at the ALS, and National Center for Research Resources grant RR-15301 for the Northeastern Collaborative Access Team beam lines at 24-ID at APS, and by the U.S. Department of Energy (DE-AC03 76SF00098 for the SIBYLS and 8.3.1 beamlines at the ALS, and DE-AC02-06CH11357 for the APS). M.B.F. is a trainee in the Weill Cornell/Rockefeller University/Sloan-Kettering Tri-Institutional MD-PhD Program supported by NIH Medical Scientist Training Program grant GM07739. J.N. is supported by a Human Frontiers in Science Program Postdoctoral Fellowship.

Supporting Online Material

www.sciencemag.org/cgi/content/full/332/6032/981/DC1
Materials and Methods
Figs. S1 to S6
Tables S1 to S3
References
Movies S1 and S2

10 January 2011; accepted 6 April 2011
10.1126/science.1202692

DUAL-MEMBRANE SYRINGE FILTERS

The Phenex-GF/NY dual-membrane syringe filters are designed for viscous, particulate-laden samples. The new filter incorporates a glass layer, through which the sample passes first for elimination of heavy particulates, increasing the effectiveness of the second, nylon fiber membrane. By removing particulates from the sample, the syringe filter prevents buildup and blockage of chromatography columns and frits while minimizing wear and tear on injection valves. Proper sample filtration can ultimately reduce system downtime and component replacement. Ideal for any applications with highly viscous or heavily particulate-laden samples, such as foods, biological fluids, soil, and fermentation broths, Phenex-GF/NY performs at higher capacity than nylon-only filters and requires less hand pressure to filter the sample. Phenex syringe filters are optimized for superior flow rates and high throughput. Target applications include food and beverage, and environmental testing.

Phenomenex

For info: 310-212-0555 | www.phenomenex.com

PROTEASE INHIBITOR COCKTAIL

FOCUS ProteaseArrest is a ready-to-use, 100x concentrated broad range protease inhibitor cocktail that is fully compatible with 2D electrophoresis and subsequent mass spectrometry. The protease inhibitor cocktail contains reversible and irreversible inhibitors of serine, cysteine, calpain, and metalloproteases. Due to the optimized concentration of the various inhibitors, FOCUS ProteaseArrest shows excellent inhibition of protease activities and is therefore suitable for the protection of protein samples from animal tissues, plants, yeast, and bacteria. FOCUS ProteaseArrest is compatible with 2D electrophoresis as it uses an alternative to EDTA as an inhibitor of metalloproteases. The absence of EDTA allows for optimal action of nucleases or removing nucleic acids from the samples. For additional convenience, OneQuant ProteaseArrest is available as a single use aliquot suitable for >95 percent protease inhibition in 10 ml solutions.

G-Biosciences

For info: 800-628-7730 | www.gbiosciences.com

KINASE ENRICHMENT KITS

The Thermo Scientific Pierce Kinase Enrichment Kits use novel ATP- and ADP-based probes developed by ActivX Biosciences to covalently modify active sites of ATPases, including kinases, chaperones, and metabolic enzymes. The probes feature a desthiobiotin tag, a biotin analog, attached to the nucleotide. The nucleotide binds to the active site of the kinase, whereas the desthiobiotin tag allows for capture and enrichment of the bound kinase. The desthiobiotin tag binds less tightly to biotin-binding proteins, making the capture bond easily reversible by biotin displacement, low pH, or heat. The isolated proteins then can be further studied by Western blot analysis or mass spectrometry. The system is useful for inhibitor profiling and IC_{50} determinations. The Pierce Kinase Enrichment Kit is available with either an ActivX ATP- or ADP-based probe and includes all labeling and enrichment reagents. Both ActivX Probes are also available separately.

Thermo Fisher Scientific

For info: 800-874-3723 | www.thermoscientific.com/pierce

THERMO-CONDUCTIVE PLATE HOLDER

Used as an interface between a microplate and crushed ice, the BioCision CoolSink thermo-conductive plate holder provides fast equilibration of all wells to below 4°C and excellent well-to-well temperature uniformity. Many experimental and clinical applications require low-temperature control for culture plates. Placing a plate on BioCision's thermo-conductive CoolSink and then putting the assembly on ice brings all wells to or below 4°C. This setup provides a very simple way for researchers to ensure that all their samples are treated uniformly with no "plate edge effect." CoolSink is an ideal tool for increasing the reproducibility of results in a variety of applications, such as cell-based assays, ELISA, FACS staining and analysis, migration or adhesion studies, temperature shift assays, or any work with temperature-sensitive biomarkers.

BioCision

For info: 888-478-2221 | www.biocision.com

PHOSPHOPEPTIDE ENRICHMENT KIT

Recently, titanium dioxide (TiO_2) has been demonstrated to enrich phosphopeptides from complex peptide mixtures. This methodology has provided a solution for this challenging analytical task; however, the technology has not been optimized. Protea Biosciences has improved upon its previously existing TiO_2 product with the release of the new TiO_2 SpinTip Sample Prep Kit (SP-154). This kit contains tips and reagents for the enrichment of phosphopeptides from complex mixtures such as protein digest samples. The reformulated reagent solutions are specially formulated to maximize the retention of phosphorylated peptides, while simultaneously minimizing the retention of nonphosphorylated peptides.

Protea Biosciences

For more info: 877-776-8321 | www.proteabio.com

OXYGEN FLASK COMBUSTION UNIT

The Oxygen Flask Combustion Unit (OFCU-1) provides a highly safe tool for preparing samples for elemental analysis of halogens, sulfur, phosphorus, and a number of metals using the Schöniger flask method. The Schöniger flask method is a well-proven technique for combusting samples prior to elemental analysis by ion chromatography or titration. The durably constructed OFCU-1 copes easily with a wide range of sample types and is very simple to set up, use, and maintain. Built with operator safety in mind, the OFCU-1 remotely ignites samples inside a safety interlocked chamber using focused infrared heat from two tungsten-halogen lamps. Integral pressure vents ensure safe release of excess reaction pressure. A thick black acrylic observation window is provided on the OFCU-1 to allow users to visually check ignition has taken place.

Exeter Analytical

For info: 978-251-1411 | www.exeteranalytical.co.uk

Electronically submit your new product description or product literature information! Go to **www.sciencemag.org/products/newproducts.dtl** for more information.

Newly offered instrumentation, apparatus, and laboratory materials of interest to researchers in all disciplines in academic, industrial, and governmental organizations are featured in this space. Emphasis is given to purpose, chief characteristics, and availability of products and materials. Endorsement by *Science* or AAAS of any products or materials mentioned is not implied. Additional information may be obtained from the manufacturer or supplier.

POSITIONS OPEN

SENIOR SCIENTIST

The Department of Neurology at Columbia University, the NewYork-Presbyterian Hospital, and the Taub Institute for Research on Alzheimer's Disease and the Aging Brain are recruiting a senior scientist to take the lead on understanding the pathogenesis of neurodegenerative disorders. We seek an individual with outstanding experience and excellent references to lead a program specifically dedicated to studying the pathogenesis of disorders such as Alzheimer's disease, Parkinson's disease, and related diseases affecting the nervous system. This position will focus on the molecular mechanisms that underlie neurodegeneration and inform the design of potential therapeutics. Protected research time and appropriate resource support will be provided.

M.D. and board certified in neurology. Faculty rank is expected to be at the **ASSOCIATE PROFESSOR** or **PROFESSOR LEVEL,** commensurate with experience and achievement. Assistant professor–level candidates must provide evidence of research accomplishments and have some teaching experience. External research funding is preferred.

Qualified candidates should send a letter of interest and curriculum vitae in Word format to:

Richard Mayeux, M.D., M.Sc.
Department of Neurology
622 West 168th Street, P&S Box 16
New York, NY 10032
E-mail: rpm2@columbia.edu

Apply electronically through **website: https://academicjobs.columbia.edu/applicants/Central?quickFind=54655.**

Columbia University is an Affirmative Action/Equal Opportunity Employer.

POSTDOCTORAL RESEARCH SCIENTIST
Position - Columbia University
Multiphoton quantum state for optical metrology

Applications are invited for a Postdoctoral Research Scientist Position at Columbia University, in the area of entangled photon generation and nonclassical imaging. Qualified candidates must have a Ph.D. with background in optics or photonics, with demonstrated ability to conduct outstanding research, and be a U.S. citizen. Both experimental and theoretical advances are possible, including high-rate, high-quality entangled multiphoton generation, semiconductor chip-based measurements, novel protocols for measurements, and photon indistinguishability. More information on the Wong group can be found at **website: http://www.columbia.edu/cu/nanohv/.** Successful candidates will interact with the principal investigator, research scientists, graduate students, and external collaborators. Targeted start date is approximately July 2011 with possible flexibility. Interested candidates please contact **Professor Chee Wei Wong, e-mail: cww2104@columbia.edu, telephone: +1-212-854-4275.**

A **POSTDOCTORAL RESEARCH ASSOCIATE** position is available July 1 in the Department of Emergency Medicine at the University of Nebraska Medical Center. The study focuses on the signal transduction for lowered cell excitability of arterial baroreceptor neurons in chronic heart failure. Applicants must have a M.D. or Ph.D. in Medicine/Physiology or related field. The successful applicants will be expected to master general electrophysiological technique, molecular methods, and intricate animal surgical procedures. Previous experience with aortic depressor nerve and renal sympathetic nerve recordings is preferred. Interested applicants should submit: a letter describing research interests, a current curriculum vitae, and information of three referees. Application should be sent electronically to **Yulong Li,** M.D., Ph.D., Assistant Professor of Emergency Medicine and Physiology, Department of Emergency Medicine, University of Nebraska Medical Center, Omaha, NE 68198-5850, **e-mail: yulongli@unmc.edu** or to **Laura Robinson,** MPA, Administrator, Department of Emergency Medicine, University of Nebraska Medical Center, Omaha, NE 68198-1150, **e-mail: lmrobins@unmc.edu.** *Individuals from diverse backgrounds are encouraged to apply.*

POSITIONS OPEN

FACULTY POSITION in Neurology

The Department of Neurology at Columbia University and the NewYork-Presbyterian Hospital are recruiting an individual to develop a clinical and research program in Neuro-Oncology. The ideal candidate should have experience working in a dedicated Neuro-Oncology program. The incumbent provides clinical care to adults with primary CNS tumors and neurological complications of systemic cancer. In a leadership role, he/she is responsible for the development and direction of a comprehensive Neuro-Oncology Program that incorporates all state-of-the-art elements for the diagnosis and treatment of all CNS tumors as well as an active clinical research component. Protected research time and appropriate resource support will be provided.

M.D. and board certified in neurology and medical oncology. Faculty rank is expected to be at the **ASSISTANT** or **ASSOCIATE PROFESSOR** level, commensurate with experience and achievement. Assistant professor-level candidates must provide evidence of research accomplishments and have some teaching experience. External research funding is preferred.

Qualified candidates should send a letter of interest and curriculum vitae in Word format to:

Richard Mayeux, M.D., M.Sc.
Department of Neurology
622 West 168th Street, P&S Box 16
New York, NY 10032
E-mail: rpm2@columbia.edu

Apply electronically through **website: https://academicjobs.columbia.edu/applicants/Central?quickFind=54654.**

Columbia University is an Affirmative Action/Equal Opportunity Employer.

NEUROLOGIST

The Department of Neurology at Columbia University and the New York Presbyterian has an open faculty position to develop a clinical program in Multiple Sclerosis. We are looking for a board certified Neurologist with experience in treating Multiple Sclerosis. The position will round out a revamped multispecialty neurology practice that will serve as the cornerstone of the outpatient service. Protected research time for clinical trials and appropriate resource support will be provided.

M.D. and board certified in Neurology with experience in Multiple Sclerosis is required. Faculty rank is expected to be at the **ASSISTANT** or **ASSOCIATE PROFESSOR** level, commensurate with experience and achievement. Assistant Professor level candidates must provide evidence of training, and have some teaching experience.

Qualified candidates should send a letter of interest and curriculum vitae in Word format to:

Richard Mayeux, M.D., M.Sc.
Department of Neurology
622 West 168th Street, P&S Box 16
New York, NY 10032
E-mail: rpm2@columbia.edu

Apply electronically through **website: https://academicjobs.columbia.edu/applicants/Central?quickFind=54688.**

Columbia University is an Affirmative Action/Equal Opportunity Employer.

FACULTY POSITION
Institute of Molecular and Cellular Biology
National Taiwan University

The institute is seeking an outstanding individual to fill a full-time faculty position available on August 1, 2012. The level of appointment is open. The specific research area should be related to molecular or cellular biology. Candidates must have a Ph.D. degree and postdoctoral experience is preferred. Applicants should submit curriculum vitae, research and teaching plans, and three recommendation letters by November 10, 2011, to: **Faculty Search Committee, Institute of Molecular and Cellular Biology, National Taiwan University, No.1, Section 4, Roosevelt Road, Taipei, Taiwan 10617. Website: http://cell.lifescience.ntu.edu.tw/english/index.htm.**

Scientist

Who we are
At Roche, 80,000 people across 150 countries are pushing back the frontiers of healthcare. Working together, we've become one of the world's leading research-focused healthcare groups. Our success is built on innovation, curiosity and diversity, and on seeing each other's differences as an advantage. To innovate healthcare, Roche has ambitious plans to keep learning and growing – and is seeking people who have the same goals for themselves.

The headquarters in Basel is one of Roche's largest sites, over 8,000 people from approximately 80 countries work at Roche Basel. Favored by its geographic location in the heart of Europe, the Basel area is one of the most dynamic economic regions in Switzerland – a great place to live and work.

The Position
We are looking for a highly motivated neuroscientist to join in preclinical neuroscience research to deepen our understanding of pathological mechanisms in Alzheimer's Disease and Parkinson's Disease.
- You will conduct research in the cell biology to discover novel targets and their mode of action. Research activities include sub-cellular imaging using state-of-the-art microscopy to reveal modulation of neuronal targets or pathways in response to candidate drug treatment
- As a member of drug-discovery teams you will identify and evaluate new drug targets by in vitro and in vivo testing
- You are expected to conduct laboratory research with responsibility for the design, execution and analysis of cellular imaging studies

Who you are
- You have a PhD in neurobiology or cell biology and practical knowledge in state-of-the-art light microscopy imaging and image processing with a strong link to applications in the central nervous system
- You have a proven record of research experience in neuronal cell biology and excellent understanding of the principles that regulate intra-neuronal trafficking
- You are familiar with concepts and conduct of intracellular labelling and quantitative analysis of cells and tissues by confocal microscopy. You are familiar with image processing software
- Experience in live cell imaging, synapse analysis, and high resolution or time resolved molecular imaging modalities is a plus.
- You are flexible, have strong team and excellent communication skills in English

Job ID No.: 38102551145820110408
Contact HR: M. Steininger, Phone: +41 61 687 48 94

The next step is yours. To apply online for this position visit www.careers.roche.ch

Roche is an Equal Opportunity Employer

Sustainable Cropping and Food Systems (Assistant/Associate Professor)
Sociology of Food Systems (Assistant Professor)
Cornell University

Cornell University, located in Ithaca, New York, is an inclusive, dynamic, and innovative Ivy League university and New York's land-grant institution. Its staff, faculty, and students impart an uncommon sense of larger purpose and contribute creative ideas and best practices to further the university's mission of teaching, research, and outreach.

The College of Agriculture and Life Sciences at Cornell University is seeking applicants for two tenure-track positions related to a new initiative in sustainable agriculture and food systems. A position in Sustainable Cropping and Food Systems will be filled in the Department of Crop and Soil Sciences and a position in Sociology of Food Systems will be filled in the Department of Development Sociology. Both positions have 50% Teaching and 50% Research responsibilities and both appointments will be on an academic year (~9.0 month) basis. Qualified applicants must have a demonstrated ability to establish a distinguished record of scholarship with clear relevance to food system issues, and demonstrated ability to participate in and/or lead interdisciplinary projects.

Applicants for the **Sustainable Cropping and Food Systems** position (Assistant/Associate Professor) will be expected to teach an introductory course on Sustainable Agriculture, and an upper-level course related to cropping systems and food production. The individual is expected to develop an internationally-recognized research program involving field-based efforts in sustainable cropping systems and other biophysical aspects of cropping and food systems with a primary focus on field crops. More information on the position can be found at **http://css.cals.cornell.edu**. Candidates are requested to submit to Sue Bishop **(skp5@cornell.edu)** a letter of application, detailed resume, research and teaching statements, copies of university transcripts, copies of up to two publications, and names and contact information for three references combined into a single file in PDF format. Reviews will start after August 1, 2011. Inquiries may be sent to **Professor Harold van Es, Chair of Crop and Soil Sciences (hmv1@cornell.edu; 1-607-255-5459)**.

Applicants for the **Sociology of Food Systems** position (Assistant Professor) will be expected to develop an internationally recognized and externally funded research program on the social organization of food systems. Teaching will consist of 2.5 courses per year focusing on the social organization and restructuring of food systems in the U.S. and/or internationally. More information on food system and other related research, teaching, and outreach in Development Sociology can be found at **http://devsoc.cals.cornell.edu**. Candidates are requested to submit a cover letter stating why she/he is a good candidate for this tenure-track position, together with a curriculum vitae, a brief research plan, and a statement of teaching interests and experience. All application materials, including the cover letter, curriculum vitae, research plan, statement of teaching interest, selected reprints, and names and addresses of three individuals who may be contacted to provide letters of recommendation, should be incorporated into a single PDF file and submitted electronically to **Ms. Cynthia Twardokus (ct259@cornell.edu)**. Reviews will start after July 15, 2011. Inquiries may be sent to **Professor Philip McMichael, Development Sociology, Search Committee Chair (pdm1@cornell.edu)**.

College of Agriculture and Life Sciences
Developing Leaders. Improving Lives. Shaping the Future.

Cornell University
Cornell University is an affirmative action/ equal opportunity employer and educator

Full /Associate Professor Positions
At School of Public Health, Nanjing Medical University

Position Summary:
Nanjing Medical University School of Public Health is located in Nanjing, the scenic capital of Jiangsu Province, China. It is one of the 5 top well-known schools of public health in China and has developed rapidly in scientific research and personnel training in recent years. In order to accelerate the development of the school, we are searching for colleagues to join us at the associate or full professor levels with very competitive offers including start money and settle down costs. Opportunities are available in all areas of preventive medicine, especially in the following areas: Infectious diseases (e.g. HBV, HIV, TB) epidemiology, non-infectious diseases (CVD, diabetes or cancer) epidemiology, biostatistics or bioinformatics, occupational medicine and environmental health, toxicology, nutrition and food safety, social medicine and health education, and other related areas.

Requirements/Qualifications:
- Has been working as an assistant professor or higher in the universities or institutes abroad or has been completed post-doctoral training with outstanding academic records. Young investigators are preferred.

For more detail information, please visit the following website in Chinese: **http://gwxy.njmu.edu.cn/**.

Contact:
Ms. Huijuan Zhu
School of Public Health, Nanjing Medical University
140 Hanzhong Road, Nanjing, Jiangsu Province, 210029, China
Tel: +86-25-86862925
Fax: +86-25-86527613
E-mail: **gwxy@njmu.edu.cn**

VCU
Virginia Commonwealth University

Faculty Position in Bioinformatics

The Center for the Study of Biological Complexity at Virginia Commonwealth University (**www.vcu.edu/csbc/**) invites applications for a Bioinformaticist. The successful candidate will hold a PhD in a relevant field, and have a demonstrated ability to develop a strong, internationally recognized, independent and innovative research program. He or she will collaborate with and complement the strengths of existing faculty in synergistic and complementary interdisciplinary research efforts including applying bioinformatics approaches to the study of complex biological systems including microbial genomics or systematics, host-pathogen interactions, metagenomics, comparative genomics and related areas. The successful candidate will also provide leadership and enthusiasm in our efforts to guide the next generation of bioinformaticists, through innovative undergraduate and graduate courses and research mentoring. Preference will be given to individuals exhibiting skills in algorithm design and development for the analysis, interpretation, and visualization of multi-scale/multi-dimensional biological datasets, simulation of complex biological systems, or other relevant areas of computational biology and bioinformatics.

Teaching responsibilities are likely to include courses in bioinformatics algorithm design and development, manipulation and analysis of biological sequence data, and offerings in the area of the candidate's interest.

This is a twelve-month, tenure eligible position at a rank of assistant, associate or full professor, depending on the experience and track record of the applicant. The successful candidate must have demonstrated experience working in and fostering a diverse faculty, staff, and student environment or a commitment to do so as a faculty member at VCU. Competitive start-up funds are available.

Please submit a letter of interest, a statement of research and teaching interests and experience, curriculum vitae, and contact information for at least three references, by electronic mail, to Edwina Hunter (**ehunter3@vcu.edu**), Center for the Study of Biological Complexity, Virginia Commonwealth University, Richmond, Virginia. For submission deadline and additional details, please visit **http://www.pubinfo.vcu.edu/facjobs/** and click on "Life Sciences".

Virginia Commonwealth University is an Equal Opportunity/Affirmative Action employer. Women, minorities and persons with disabilities are strongly encouraged to apply.

Assistant Professor
Department of Food Science
College of Agriculture and Life Sciences (CALS)
Teaching (50%) Research (50%)
Tenure Track – 9 month appointment
Cornell University – Stocking Hall – Ithaca, New York

Cornell University, located in Ithaca, New York, is an inclusive, dynamic, and innovative Ivy League university and New York's land-grant institution. Its staff, faculty, and students impart an uncommon sense of larger purpose and contribute creative ideas and best practices to further the university's mission of teaching, research, and outreach.

The Department of Food Science seeks an Assistant Professor in the area of **Biology of Food Perception**s. This position offers a unique opportunity for a creative scholar to develop a cutting edge, multidisciplinary teaching and research program for the study of human perception of foods and food components. Cornell's outstanding students and faculty, world-class applied and basic research programs, and a new Food Science building scheduled to open in 2013 provide an ideal environment for scholarship in this area.

The position includes a teaching component (50% effort) with the following responsibilities:

- Teach a senior undergraduate course in Sensory Evaluation of Food, develop and teach a course in the individual's area of expertise, and contribute lectures on human perception of foods in other departmental courses.
- Provide high quality teaching and advising for students enrolled in Food Science undergraduate and graduate degree programs.

The position also includes a research component (50% effort) focusing on human perceptions of foods and food components. The successful candidate will be expected to:

- Develop a world class, externally funded research program to study human perceptions of foods and food components, with a focus on the biological and biochemical mechanisms involved in response to stimuli. Possible research areas include but are not limited to: identification and structural characterization of chemoreceptor proteins in the mouth and nose; relationship between genetic variation in trigeminal, taste, and odor chemoreceptors and food perception or preference; impact of sodium reduction on flavor perception in the context of whole foods; effects of flavor perception on satiety; effects of flavor compounds on gene expression and implications for obesity prevention; genomics of perceptions in human populations; or physiology and aging of human sensory perception.
- Establish collaborative research relationships with Cornell colleagues in food science and related disciplines such as nutrition, genomics, biochemistry, neurobiology, plant breeding, chemistry and chemical biology.

Qualifications: Doctoral degree and post-doctoral research experience in one or more of the following fields: neurobiology, molecular biology and genetics, biochemistry, cognitive psychology, physiology of human perception, food science, nutrition or a related field.

A record of excellence in scholarship as evidenced by publications in peer-reviewed journals.

Preferences: Demonstrated success in securing competitive grants preferred. Prior teaching experience is highly desirable.

Application procedure: Qualified candidates should send a letter of application, curriculum vitae, selected reprints, academic transcripts, statement of research goals and plans, statement of teaching philosophy, and three letters of recommendation to:

Dr. Carmen I. Moraru, Search Committee Chair
Department of Food Science
Cornell University
Ithaca, NY 14853

Email: cim24@cornell.edu
Phone: 607-255-8121

Review of applications will begin on August 1, 2011 and will continue until the appropriate candidate is selected.

Cornell University seeks to meet the needs of dual career couples, has a Dual Career program, and is a member of the Upstate New York Higher Education Recruitment Consortium which assists with dual career searches. Visit **http://www.unyherc.org** to see positions available in higher education in the upstate New York area.

College of Agriculture and Life Sciences
Developing Leaders. Improving Lives. Shaping the Future.

Cornell University
Cornell University is an affirmative action/ equal opportunity employer and educator

Tenure Track Faculty Evolutionary Medicine & Information Biology

Children's Hospital of Philadelphia (CHOP)

The Children's Hospital of Philadelphia and the Department of Pathology and Laboratory Medicine at the University of Pennsylvania's School of Medicine seeks candidates for several Assistant, Full, and/or Associate Professor positions in the tenure track. Rank will be commensurate with experience. The successful applicant will have experience in the field of Evolutionary Medicine & Information Biology. Applicants must have a Ph.D. or M.D./Ph.D. degree and have demonstrated excellent qualifications in Education and Research. Clinicians, additionally, must demonstrate excellent qualifications in clinical care and be eligible for licensure in the Commonwealth of Pennsylvania.

These positions are based at The Children's Hospital of Philadelphia Center for Mitochondrial and Epigenomic Medicine. Research is oriented toward the application of quantitative and information approaches to understanding the role of bioenergetic dysfunction in the etiology of pediatric and adult complex diseases, cancer and aging. Individuals with expertise in the areas of information sciences, evolutionary biology, population genetics, and mitochondrial biology and bioenergetics will be considered. Since the ultimate goals of the Center are in developing more effective diagnoses and treatments of complex diseases, expertise pertinent to these goals will be relevant.

The successful candidate will be expected to develop and/or maintain an independently funded research laboratory and individuals with clinical expertise will be expected to participate in the Center's and Department's clinical and/or diagnostic programs in Mitochondrial Medicine. Assumption of additional educational and administrative duties will also be expected consistent with a tenure track faculty member.

Apply for this position online at:
http://www.med.upenn.edu/apps/faculty_ad/index.php/g/d2626

The University of Pennsylvania and The Children's Hospital of Philadelphia are equal opportunity, affirmative action employers. Women and minority candidates are strongly encouraged to apply.

Penn University of Pennsylvania

The Children's Hospital *of* Philadelphia®

Tenure Track Faculty Mitochondrial and Epigenomic Medicine

Children's Hospital of Philadelphia (CHOP)

The Children's Hospital of Philadelphia and the Department of Pathology and Laboratory Medicine at the University of Pennsylvania's School of Medicine seeks candidates for several Assistant, Full, and/or Associate Professor positions in the tenure track. Rank will be commensurate with experience. The successful applicant will have experience in the field of Mitochondrial and Epigenomic Medicine. Applicants must have an M.D and/or Ph.D or equivalent degree and have demonstrated excellent qualifications in Education and Research. Clinicians, additionally, must demonstrate excellent qualifications in clinical care and be eligible for licensure in the Commonwealth of Pennsylvania.

These positions are based at The Children's Hospital of Philadelphia Center for Mitochondrial and Epigenomic Medicine. Research is oriented toward advancing our understanding in the role of bioenergetic dysfunction in the etiology of pediatric and adult complex diseases, cancer and aging with the ultimate goal of developing more effective diagnoses and treatments for bioenergetic disease. Expertise in mitochondrial DNA and/or nuclear DNA genetics, gene regulation, and epigenetics as well as in bioenergetics and mitochondrial molecular biology will be appropriate for these positions. Strong consideration will be given to the candidate's research credentials and in the case of clinicians, to their expertise in the diagnosis and treatment of complex diseases of potential mitochondrial and epigenomic etiology.

The successful candidate will be expected to develop and/or maintain an independently funded research laboratory and individuals with clinical expertise will be expected to participate in the Center's and Department's clinical and/or diagnostic programs in Mitochondrial Medicine. Assumption of additional educational and administrative duties will also be expected consistent with a tenure track faculty member.

Apply for this position online at:
http://www.med.upenn.edu/apps/faculty_ad/index.php/g/d2627

The University of Pennsylvania and The Children's Hospital of Philadelphia are equal opportunity, affirmative action employers. Women and minority candidates are strongly encouraged to apply.

Penn University of Pennsylvania

The Children's Hospital *of* Philadelphia®

Columbia University's Department of Pathology and Cell Biology, Division of Immunogenetics, invites applications for four positions as follows:

1. **Two Staff Associate positions** to perform and interpret histocompatibility tests; perform molecular HLA typing and flow cytometry crossmatching; coordinate quality assurance operations; and train new personnel.
2. **One Staff Associate position** to perform flow cytometric analysis of clinical specimens using a wide array of cytometry based assays; report results, communicate with referring physicians, and participate in the development of new laboratory protocols.
3. **One Senior Staff Associate position** to conduct immunophenotypic analysis and functional assays for the characterization of leukemia/lymphoma, immunodeficiency, pre- and post- transplant status; coordinate QC/QA operations, manage laboratory databases and implement new methods of technology.

Minimum requirements are: BS degree and four years experience in cellular immunology and/or molecular genetics or eight years of experience for a Senior Staff Associate. Expertise in flow cytometry and/or histocompatibility testing is essential. The candidate should be certified by the New York State Department of Health as a laboratory technician or technologist. These positions require working evenings and/or weekend hours.

Interested applicants should apply online at: **academicjobs.columbia.edu/applicants/Central?quickFind=54679**.

Columbia University is an Equal Opportunity/Affirmative Action Employer.

PURDUE UNIVERSITY

Assistant Professor, Industrial and Physical Pharmacy

Seeking applications to fill a full-time tenure track (9 months, academic year) faculty position in the general area of pharmaceutical solids and manufacturing. Expected to establish an externally funded research program, teach courses in the undergraduate, graduate and professional programs, and collaborate on various research activities within the university including the multi-university NSF funded Engineering Research Center (ERC) on Structured Organic Particulate Systems (C-SOPS) (**http://ercforsops.org/**). The candidate should have expertise in fundamental and applied research related to the development, design, analysis and manufacturing of pharmaceutical products. Representative areas of interest include: pharmaceutical materials science; solid state chemistry of pharmaceutical systems; process analytical technologies and quality by design applied to manufacturing processes; particle technology; fundamentals of unit operations associated with drug substance and drug product manufacture; pharmaceutical engineering. Purdue University is an ADVANCE institution.

Qualifications: The candidate must hold a PhD degree in a relevant discipline which would include pharmaceutical sciences, engineering or chemistry, have an outstanding academic record, an exceptional potential for world-class research and a commitment to both undergraduate and graduate education.

Application: Submit electronically to **mhurt@purdue.edu** a curriculum vitae, a letter of interest providing a summary of qualifications for the position, a description of research interests and goals, a statement of teaching philosophy, and the names and contact information for three references. Application review will begin **September 1, 2011**, and will continue until the position is filled. For further information please contact **Mary Ellen Hurt, Assistant Professor Search Committee, Department of Industrial and Physical Pharmacy, College of Pharmacy, Purdue University, West Lafayette, IN 47907-2091; mhurt@purdue.edu**. A background check required for employment.

Purdue University is an Equal Opportunity/Equal Access/Affirmative Action Employer, fully committed to achieving a diverse workforce.

Georgia Health Sciences University

MEDICAL COLLEGE OF GEORGIA CANCER CENTER
Faculty Position in Proteomics and Metabolomics

The Georgia Health Sciences University, Medical College of Georgia, Cancer Center is seeking applications for a position at the Assistant or Associate Professor level in the field of cancer Proteomics/ Metabolomics. Previous experience in this area is essential. Academic rank will be commensurate with experience. The successful candidate will join a team of experts in genomics and epigenomics to undertake a systems biology analysis of human cancer. It is anticipated that applicants would have a strong history of collaborative research, publications and NIH funding, ideally from NCI. A competitive start-up package is available to support this position.

A detailed description of the Georgia Health Sciences University, Medical College of Georgia, Cancer Center faculty and facilities is available at **http://www.georgiahealth.edu/cancer/**.

Inquiries should be addressed to **Dr. John K. Cowell**, Chair of the Search Committee, at **jcowell@georgiahealth.edu** and should include detailed CV, names of three referees and a statement of research plans and career objectives. Additionally, all interested candidates should apply online at **http://www.georgiahealth.edu/facultyjobs/**, Requisition (reference) **#5410**.

Application Deadline: Until Filled

Georgia Health Sciences University is an Equal Opportunity and Equal Access Institution; AA/EEO/Equal Access or AA/EEO/Equal Access/ADA Employer.

POSITIONS OPEN

CLINICAL RESEARCHERS

The Department of Neurology at Columbia University and the NewYork-Presbyterian Hospital are recruiting a new head for the division of Movement Disorders that will form part of the newly structured Center for Neurodegenerative Disorders. The ideal candidate is an accomplished researcher in clinical or basic research, with experience training fellows who have obtained independent funding. Protected research time and appropriate resource support will be provided.

M.D., board certified in neurology, with specialty training in movement disorders (fellowship or equivalent). Faculty rank is expected to be at the **ASSOCIATE** or **FULL PROFESSOR** level, commensurate with experience and achievement. External research funding is preferred.

Qualified candidates should send a letter of interest and curriculum vitae in Word format to:

Karen Marder, M.D.
MPH 622 West 168th Street
P&S Box 16
New York, NY 10032
E-mail: ksm1@columbia.edu

Apply electronically through **website: https://academicjobs.columbia.edu/applicants/Central?quickFind=54687.**

Columbia University is an Affirmative Action/Equal Opportunity Employer.

PEDIATRIC NEUROLOGIST

The Department of Neurology at Columbia University and the NewYork-Presbyterian Hospital announce the recruitment for a board certified child neurologist to lead the division of Pediatric Neurology through its next phase of growth and build upon a solid patient base and restructured multidisciplinary physician and medical professional group. Protected research time and appropriate resource support will be provided.

M.D. and board certified in child neurology. Faculty rank is expected to be at the **ASSISTANT** or **ASSOCIATE PROFESSOR** level, commensurate with experience and achievement. Assistant Professor–level candidates must provide evidence of research accomplishments and have some teaching experience. External research funding is preferred.

Qualified candidates should send a letter of interest and curriculum vitae in Word format to:

Mitchell Elkind, M.D.
Department of Neurology
622 West 168th Street, P&S Box 16
New York, NY 10032
E-mail: mse13@columbia.edu

Apply electronically through **website: https://academicjobs.columbia.edu/applicants/Central?quickFind=5466.**

Columbia University is an Affirmative Action/Equal Opportunity Employer.

POSTDOCTORAL FELLOW
Lung Fibrosis

Position available (Medical University of South Carolina Rheumatology Division) offering a high quality of life in beautiful Charleston, SC. Translational research on novel treatments for currently untreatable lung diseases is supported by a new grant. Applicants should be able to work with a team and have the ability and motivation to make independent intellectual contributions. Handling mice required. *U.S. Citizens or Permanent Residents preferred.* Submit curriculum vitae, references, and cover letter to **Stanley Hoffman** at **e-mail: hoffmas@musc.edu.**

POSTDOCTORAL POSITION

Postdoctoral position is available at the Burnett School of Biomedical Sciences, College of Medicine, University of Central Florida, Orlando, Florida, to investigate the nature of genes involved in Tuberculosis latency using recently developed in vitro models of latency (*PLoS One* e6077, 2009; *PLoS Pathog.* 2011, in press). Send curriculum vitae and references electronically to **Dr. P.E. Kolattukudy, e-mail: pk@ucf.edu.**

The University of Central Florida is an Equal Opportunity, Equal Access, and Affirmative Action Employer. As a member of the Florida State University System, all application materials and selection procedures are available for public review.

POSITIONS OPEN

The University of Texas at Austin seeks applications for the position of **DIRECTOR** of the Marine Science Institute and Chairman of the Department of Marine Science to continue its growth as a leading coastal marine laboratory on the Gulf of Mexico. Applicants must be accomplished and respected researchers in marine science with a solid record of scholarly achievements. Candidates with strong leadership qualities, familiarity with multi-disciplinary programs, and an interest in promoting the diverse research and academic activities of the Institute are urged to apply. A proven record in managing departmental or programmatic administration and supporting staff would be desirable. The Director holds the Nancy Lee and Perry Bass Regents Administrative Chair in Marine Science and a tenured appointment at the rank of Professor in the Department of Marine Science. Details of the position and the Institute are available at **website: http://www.utmsi.utexas.edu/hr/director.pdf.**

Candidate selection will begin August 1, 2011 and the search will remain open until an appointment is made. Applications should include a letter of interest, curriculum vitae, names and addresses of five references, and can be sent electronically to **e-mail: facsearch@utlists.utexas.edu** or mailed to: **Director Search Committee, The University of Texas at Austin, Marine Science Institute, 750 Channel View Dr., Port Aransas, Texas 78373-5015.**

Background check conducted on applicant selected. The University of Texas at Austin is an Affirmative Action/Equal Opportunity Employer.

cell sciences®

cytokine center

Browse our web site of recombinant proteins, including cytokines, growth factors, chemokines and neurotrophins. Daily shipping and competitive pricing are offered. Bulk quantities of many proteins available. Cell Sciences also carries corresponding antibodies and ELISA kits.

www.cellsciences.com

LIST OF PROTEINS

4-1BBL
4-1BB Receptor
6 Ckine
ACAD8
ACAT2
gAcrp30/Adipolean
Activin A
ACY1
ADAT1
Adiponectin
ADRP
AITRL
Akt1
Alpha-Feto Protein (AFP)
Alpha-Galactosidase A
Angiopoietin-1 (Ang-1)
Angiopoietin-2 (Ang-2)
Angiostatin K1-3
Annexin-V
apo-SAA
Apoliprotein A-1
Apoliprotein E2
Apoliprotein E3
Apoliprotein E4
APRIL
Artemin
ATF2
Aurora A
Aurora B
BAFF
BAFF Receptor
BCA-1 / BLC / CXCL13
BCMA
BD-1
BD-2
BD-3
BDNF
Bivalirudin
BMP-2
BMP-4
BMP-7
BMP-13
sBMPR-1A
Brain Natriuretic Protein
BRAK
Breast Tumor Antigen
C5a
C5L2 Peptide
C-10
C-Reactive Protein
C-Src
Calbindin D-9K
Calbindin D-28K
Calbindin D-29K
Calmodulin
Calcitonin Acetate
Carbonic Anhydrase III
Carcino-embryonic Antigen
Cardiotrophin-1
Caspase-3
Caspase-6
CD4
CD14
CD22
CD40 Ligand / TRAP
CD95 / sFas Ligand
CD105 / Endoglin
CHIPS
CNTF
Collagen
CREB
CTACK/CCL27
CTGF
CTGFL/WISP-2
CTLA-4/Fc
CXCL16
Cytokeratin 8
DEP-1
Desmopressin
Disulfide Oxidoreductase
E-selectin
ECGF
EGF
Elafin/SKALP
EMAP-II
ENA-78
Endostatin
Enteropeptidase
Eotaxin
Eotaxin-2
Eotaxin-3 (TSC)
EPHB2
EPHB4
Eptifbatide
Erk-2
Erythropoietin (EPO)
Exodus-2
Fas Ligand
Fas Receptor
FGF-1 (acidic)
FGF-2 (basic)
FGF-4
FGF-5
FGF-6
FGF-7/ KGF
FGF-8
FGF-9
FGF-10
FGF-16
FGF-17
FGF-18
FGF-19
FGF-20
sFGFR-1 (IIIc) / Fc Chimera
sFGFR-2 (IIIc) / Fc Chimera
sFGFR-3 / Fc Chimera
sFGFR-4 / Fc Chimera
sFlt-1 (native)
sFlt-1 (D3)
sFlt-1 (D4)
sFlt-1 (D5)
sFlt-1 (D7)
Flt3-Ligand
sFlt-4
sFlt-4/ Fc Chimera
Follistatin
FSH
Fractalkine/ CX3C
G-CSF
α-Galactosidase A
Galectin-1
Galectin-3
Gastrointestinal CA
GCP-2
GDF-3
GDF-9
GDF-11
GDNF
GLP-1
Glucagon
Goserelin
GM-CSF
GPBB
GROα
GROβ
GROγ
GRO/MGSA
Growth Hormone
Growth Hormone BP
GST-p21/WAF-1
HB-EGF
HCC-1
HGF
Histdyl-tRNA synthetase
Histrelin
HRG1-β1
I-309
I-TAC
IFN-α
IFN-α A
IFN-α 2a
IFN-α 2b
IFN-β
IFN-γ
IFN-Omega
IGF-I
IGF-II
proIGF-II
IGFBP-1
IGFBP-2
IGFBP-3
IGFBP-4
IGFBP-4
IGFBP-5
IGFBP-6
IGFBP-7
IL-1α
IL-1β
IL-2
IL-3
IL-4
sIL-4 Receptor
IL-5
IL-6
sIL-6 Receptor
IL-7
IL-8 (72 a.a.)
IL-8 (77 a.a.)
IL-9
IL-10
IL-11
IL-12
IL-13
IL-13 analog
IL-15
IL-16 (121 a.a.)
IL-16 (130 a.a.)
IL-17
IL-17B
IL-17D
IL-17E
IL-17F
IL-19
IL-20
IL-22
IL-31
Insulin
IP-10
JE
JNK2a1
JNK2a2
KC / CXCL1
KGF
L-asparaginase
LAG-1
LALF Peptide
LAR-PTP
LC-1
LBP
LD-78β
LDH
LEC/NCC-4
Leptin
LIGHT
LIX
LKM
LL-37
Lymphotactin
sLYVE-1
M-CSF
MCP-1 (MCAF)
MCP-2
MCP-3
MCP-4
MCP-5
MDC (67 a.a.)
MDC (69 a.a.)
MDH
MEC
Mek-1
MIA
Midkine
MIG / CXCL9
MIP-1α / CCL3
MIP-1β / CCL4
MIP-3 / CCL23
MIP-3α / CCL20
MIP-3β / CCL19
MIP-4 (PARC) / CCL18
MIP-5 / CCL15
MMP-3
MMP-7
MMP-13
Myostatin
Nanog
NAP-2
Neurturin
NFAT-1
beta-NGF
NOGGIN
NOV
NP-1
NT-1/BCSF-3
NT-3
NT-4
Ocreotide
Oncostatin M
Osteoprotegerin (OPG)
OTOR
Oxytocin
p38-α
Parathyroid Hormone
PDGF-AA
PDGF-AB
PDGF-BB
Persephin
PF-4
PIGF-1
PIGF-2
PKA α-subunit
PKC-α
PKC-γ
Pleiotrophin
PLGF-1
Polymyxin B (PMB)
PRAS40
PRL-1
PRL-2
PRL-3
Prokineticin-2
Prolactin
Protirelin
PTHrP
PTP1B
PTP-IA2
PTP-MEG2
PTP-PEST
sRANK
sRANKL
RANTES
RELM-α
RELM-β
Resistin
RPTPβ
RPTPγ
RPTPμ
SCF
SCGF-α
SCGF-β
SDF-1α
SDF-1β
Secretin
SF20
SHP-2
STAT1
c-Src
TACI
TARC
TC-PTP
TECK
TFF2
TGF-α
TGF-β1
TGF-β2
TGF-β3
Thymosin α1
sTIE-1/Fc Chimera
sTIE-2/Fc Chimera
TL-1A
TNF-α
TNF-β
sTNFR1
sTNFR2
TPO
TRAIL/Apo2L
sTRAIL R-1 (DR4)
sTRAIL R-2 (DR5)
TSH
TSLP
TWEAK
TWEAK Receptor
Urokinase
VEGF121
VEGF145
VEGF165
VEGF-C
VEGF-C I525
EG-VEGF
VEGF-E
HB-VEGF-E
sVEGFR-1
sVEGFR-2
sVEGFR-3
WISP-1
WISP-2
WISP-3
WNT-1

CELL SCIENCES INC • 480 NEPONSET STREET, BUILDING 12A, CANTON, MA 02021 • INFO@CELLSCIENCES.COM

TOLL FREE: (888) 769-1246 • TEL: (781) 828-0610 • FAX: (781) 828-0542 • WEB: WWW.CELLSCIENCES.COM

Submission deadline August 1

Your name here.

The GE & Science Prize for Young Life Scientists. Because brilliant ideas build better realities.

Imagine standing on the podium at the Grand Hotel in Stockholm, making your acceptance speech for the GE & Science Prize for Young Life Scientists. Imagine having your essay read by your peers around the world. Imagine discussing your work in a seminar with other prize winners and Nobel Laureates. Imagine what you could do with the $25,000 prize money. Now stop imagining. If you were awarded your Ph.D. in molecular biology in 2010, then submit your 1000-word essay by August 1, and you can make it a reality.

Want to build a better reality? Go to www.gescienceprize.org

GE & Science Prize for Young Life Scientists

imagination at work

Science AAAS

* For the purpose of this prize, molecular biology is defined as "that part of biology which attempts to interpret biological events in terms of the physico-chemical properties of molecules in a cell".

(McGraw-Hill Dictionary of Scientific and Technical Terms, 4th Edition).

28-9402-06AB

EPITOMICS®
Better Antibodies · Better Science

Now Available
2500 RABBIT MONOCLONALS
Over 9000 Antibodies Total

THE RABBIT MONOCLONAL ADVANTAGE

	RABBIT MONOCLONAL	MOUSE MONOCLONAL
ANTIGEN RECOGNITION	Excellent response to a wide range of antigens	Limited immuno response
AFFINITIES	Picomolar (10^{-12} kD M) possible	Nanomolar (~10^{-9} kD M)
APPLICATIONS	Westerns, ELISA, Flow Cytometry, IP, IHC, ICC - Excellent results in IHC	Westerns, ELISA, Flow Cytometry, IP - Not suitable for mouse studies
IHC		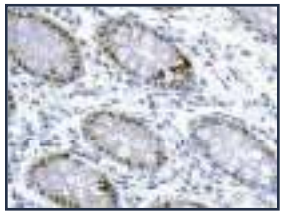

What is the Rabbit Monoclonal Advantage ?

Rabbit Monoclonal Antibodies (RabMAbs®) provide the combined benefits of superior antigen recognition of the rabbit immune system with the specificity and consistency of a monoclonal antibody, bringing you the highest quality antibody possible.

Find out more @ www.epitomics.com/comparison

Paraffin-embedded human colon tissue stained with Epitomics' CDX2 RabMAb (Cat.# 2475-1) and Vendor A's CDX2 Mouse Monoclonal under optimal conditions

SPECIAL OFFER **$99 ANTIBODY SPECIAL**

Find out more @ www.epitomics.com/products/promo

For updates and special offers
Follow us on: twitter
www.twitter.com/epitomics_inc

www.epitomics.com

US & Canada | 1-877-772-2622
Outside NA | 650-583-6688

abcam®

What color will help you today?

Abcam offers a variety of conjugated secondary antibodies that complement our products in a wide range of applications.

- Monoclonal and polyclonal antibodies
- Large selection of host and target species
- Conjugated to high quality fluorochromes
- Pre-adsorbed
- F(ab) and F(ab')$_2$ fragments

Learn more about DyLight® at **www.abcam.com/DyLight**

DyLight® is a trademark of Thermo Fisher Scientific Inc. and its subsidiaries.

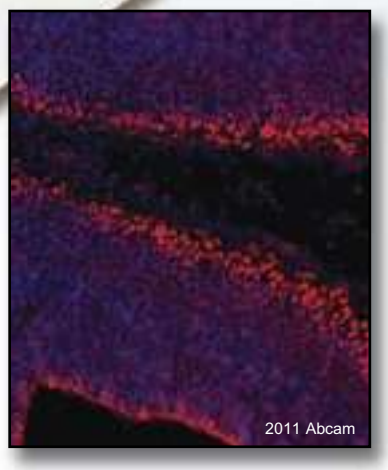

This image is courtesy of an Abreview in which an E14 mouse brain sample was stained with a primary Rabbit anti-Clim1 antibody. The secondary antibody used was **ab96921**, a Donkey polyclonal secondary antibody to Rabbit IgG - H&L (DyLight® 594) **pre-adsorbed** against 8 species. The blue staining is DAPI.

One*Taq*™ DNA Polymerase

The ONE polymerase for your endpoint PCR needs

- Robust yield with minimal optimization
- Ideal for routine, AT- or GC-rich templates
- Hot start and master mix versions available

NEW ENGLAND BioLabs® Inc.
enabling technologies in the life sciences

Request a sample at
www.neb.com/OneTaq

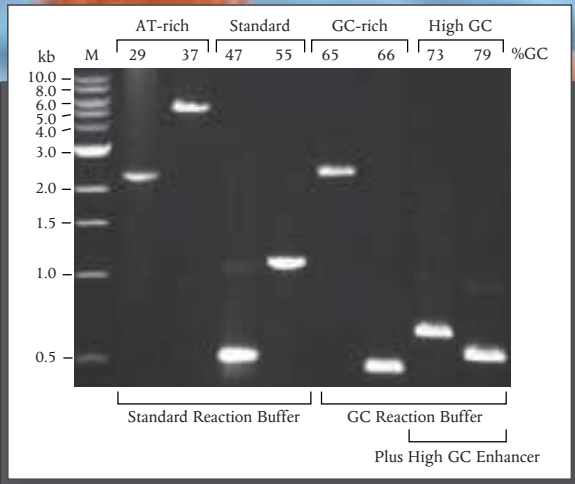

Amplification of a selection of sequences with varying AT and GC content from human and C. elegans genomic DNA, using OneTaq DNA Polymerase.

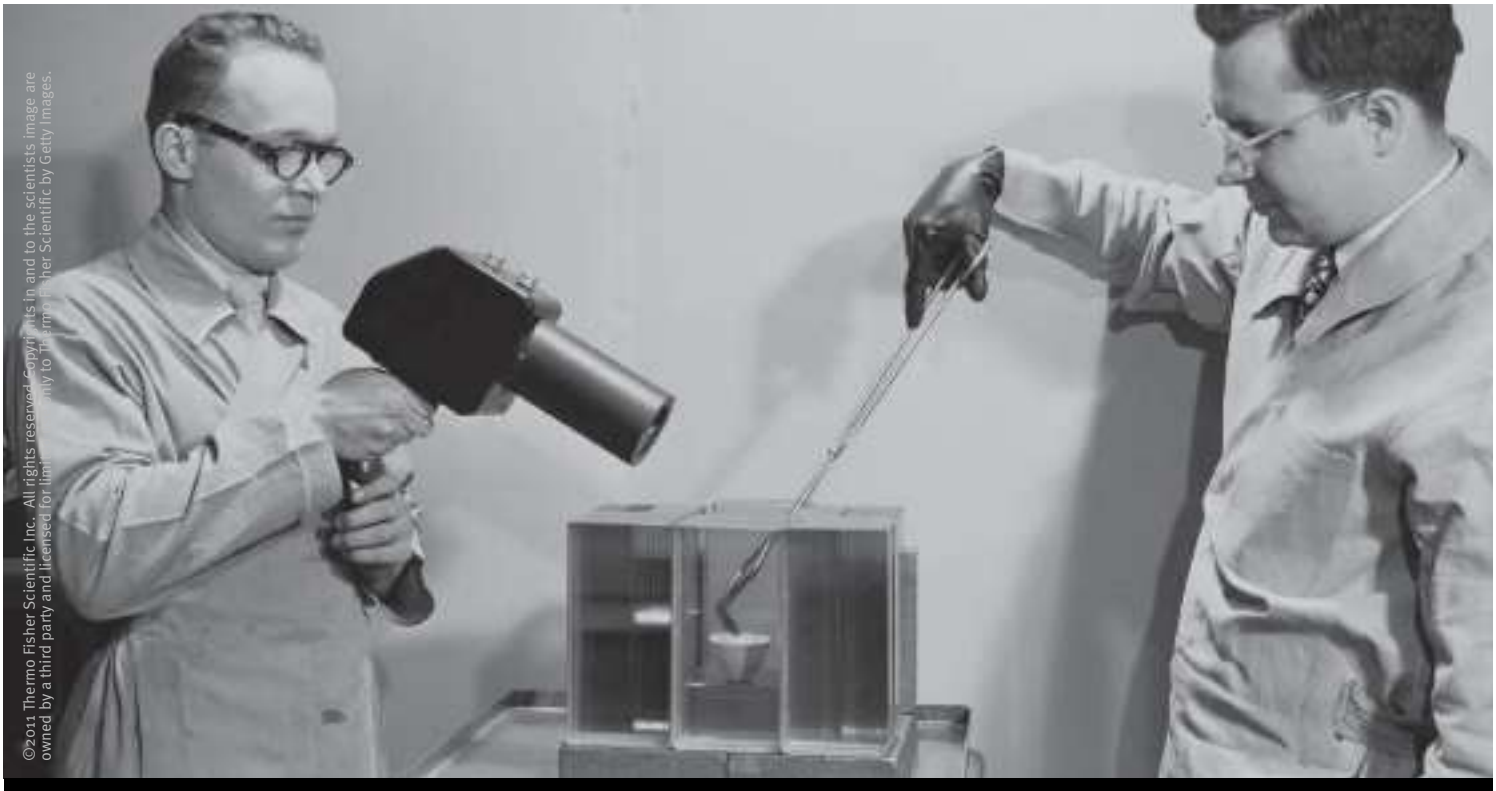

Limited by an outdated PCR system?

You can run 15 minute PCR protocols and use 50% less consumables and energy by getting away from the old standard. Choose Thermo Scientific Piko Thermal Cyclers, Phusion reagents, and ultra thin wall (UTW) plastic consumables for the most rapid and accurate PCR results. These technologically advanced components can be used individually to improve your current workflow, or as a complete solution for advanced PCR.

- Ultra fast PCR cycling protocols optimized to ‹15 minutes
- 96-well PCR runs using 50% less plastics, reagents and energy
- PCR kits that allow amplification directly from plant, blood, and tissue samples

Start your PCR experiment today
www.thermoscientific.com/advancedpcr

Everything for PCR
Thermo Scientific PCR portfolio has everything you need for successful PCR including industry leading reagents, high-quality instruments and trusted plastic consumables.

Moving science forward

Thermo SCIENTIFIC
Part of Thermo Fisher Scientific

华大基因 BGI Premier Scientific Partner

Accurate Reliable Efficient

Sequencing

Accelerate Your Scientific Exploration

tech@genomics.cn www.genomics.cn

Locations: China (Mainland, Hong Kong), North America (Boston), Europe (Copenhagen)

“A dream told me to do it.”

Dr. Carl Alving on his inspiration for inventing the vaccine patch.

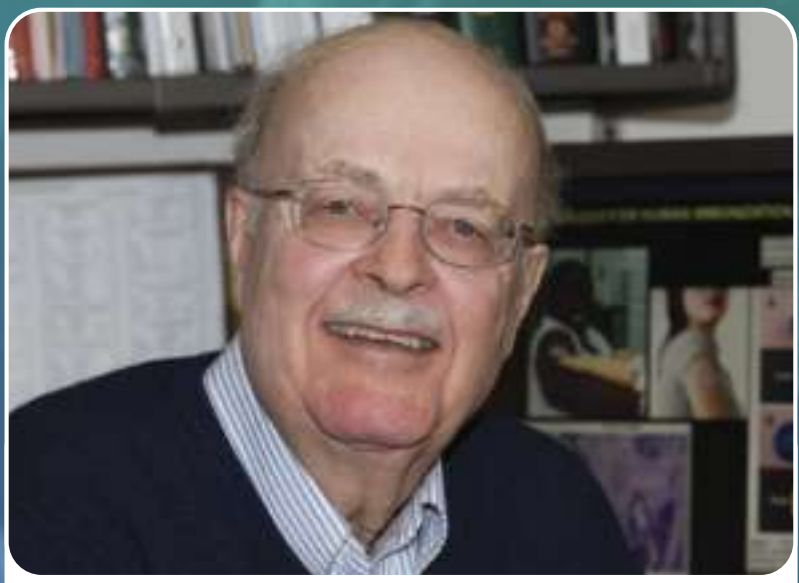

Carl R. Alving, M.D.
Chief of the Department of Adjuvant & Antigen Research, Division of Retrovirology
at the Walter Reed Army Institute of Research
AAAS member

MemberCentral is the new website that looks at science through the eyes of AAAS members. It celebrates their achievements—like Dr. Alving’s vaccine patch—and their shared belief in the transformative power of science. Use **Member**Central to connect with other members, learn about work being done in other fields, and get fresh perspectives on issues ranging from speciation to STEM education.

Visit **Member**Central today and get to know the AAAS member community in a whole new way.

AAAS MEMBERCENTRAL

MemberCentral.aaas.org

Blogs | Videos | Webinars | Discounts | Downloads | Community

Eppendorf Consumables – it's Your sample

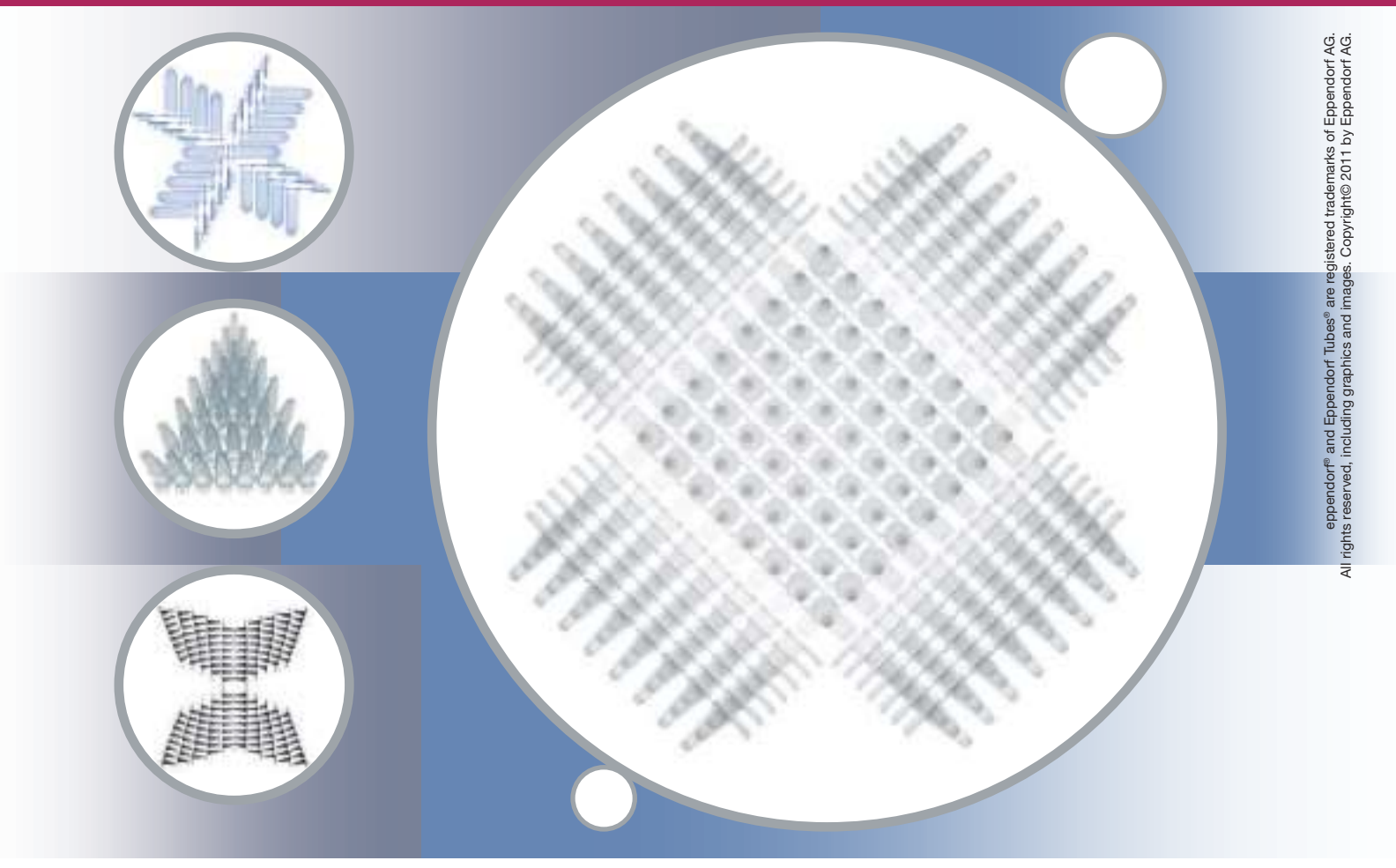

Go for Unaffected Assay Results!

Choose the right tubes for your experiments

Laboratory consumables can affect bioassays!
Reaction tubes for storing and processing samples should be selected carefully as they can influence the quality and reproducibility of your entire workflow. Original Eppendorf Tubes are produced without additives that have been shown to influence bioassay results, offer proven mechanical stability, superior technical performance and batch certified purity levels.

Original Eppendorf Tubes® :
Developed with your research results in mind!

- No slip agents, no plasticizers or biocides used at any time of the production process
- No leaching of UV-absorbing substances that can affect DNA quantifications
- Automated manufacturing under clean-room conditions to eliminate human interaction as source for contamination

Experience Eppendorf quality consumables and order your free sample on:
www.eppendorf.com/consumables

eppendorf
In touch with life

Your local distributor www.eppendorf.com/worldwide · Application Support: support@eppendorf.com
Eppendorf AG · Germany · Tel: +49 40 538 01-0 · Eppendorf North America, Inc. · USA · Tel: +1 800 645 3050
Eppendorf Asia Pacific Headquarters · Malaysia · Tel: +60 3 8023 2769

DUAL-MEMBRANE SYRINGE FILTERS

The Phenex-GF/NY dual-membrane syringe filters are designed for viscous, particulate-laden samples. The new filter incorporates a glass layer, through which the sample passes first for elimination of heavy particulates, increasing the effectiveness of the second, nylon fiber membrane. By removing particulates from the sample, the syringe filter prevents buildup and blockage of chromatography columns and frits while minimizing wear and tear on injection valves. Proper sample filtration can ultimately reduce system downtime and component replacement. Ideal for any applications with highly viscous or heavily particulate-laden samples, such as foods, biological fluids, soil, and fermentation broths, Phenex-GF/NY performs at higher capacity than nylon-only filters and requires less hand pressure to filter the sample. Phenex syringe filters are optimized for superior flow rates and high throughput. Target applications include food and beverage, and environmental testing.

Phenomenex

For info: 310-212-0555 | www.phenomenex.com

PROTEASE INHIBITOR COCKTAIL

FOCUS ProteaseArrest is a ready-to-use, 100x concentrated broad range protease inhibitor cocktail that is fully compatible with 2D electrophoresis and subsequent mass spectrometry. The protease inhibitor cocktail contains reversible and irreversible inhibitors of serine, cysteine, calpain, and metalloproteases. Due to the optimized concentration of the various inhibitors, FOCUS ProteaseArrest shows excellent inhibition of protease activities and is therefore suitable for the protection of protein samples from animal tissues, plants, yeast, and bacteria. FOCUS ProteaseArrest is compatible with 2D electrophoresis as it uses an alternative to EDTA as an inhibitor of metalloproteases. The absence of EDTA allows for optimal action of nucleases or removing nucleic acids from the samples. For additional convenience, OneQuant ProteaseArrest is available as a single use aliquot suitable for >95 percent protease inhibition in 10 ml solutions.

G-Biosciences

For info: 800-628-7730 | www.gbiosciences.com

KINASE ENRICHMENT KITS

The Thermo Scientific Pierce Kinase Enrichment Kits use novel ATP- and ADP-based probes developed by ActivX Biosciences to covalently modify active sites of ATPases, including kinases, chaperones, and metabolic enzymes. The probes feature a desthiobiotin tag, a biotin analog, attached to the nucleotide. The nucleotide binds to the active site of the kinase, whereas the desthiobiotin tag allows for capture and enrichment of the bound kinase. The desthiobiotin tag binds less tightly to biotin-binding proteins, making the capture bond easily reversible by biotin displacement, low pH, or heat. The isolated proteins then can be further studied by Western blot analysis or mass spectrometry. The system is useful for inhibitor profiling and IC_{50} determinations. The Pierce Kinase Enrichment Kit is available with either an ActivX ATP- or ADP-based probe and includes all labeling and enrichment reagents. Both ActivX Probes are also available separately.

Thermo Fisher Scientific

For info: 800-874-3723 | www.thermoscientific.com/pierce

THERMO-CONDUCTIVE PLATE HOLDER

Used as an interface between a microplate and crushed ice, the BioCision CoolSink thermo-conductive plate holder provides fast equilibration of all wells to below 4°C and excellent well-to-well temperature uniformity. Many experimental and clinical applications require low-temperature control for culture plates. Placing a plate on BioCision's thermo-conductive CoolSink and then putting the assembly on ice brings all wells to or below 4°C. This setup provides a very simple way for researchers to ensure that all their samples are treated uniformly with no "plate edge effect." CoolSink is an ideal tool for increasing the reproducibility of results in a variety of applications, such as cell-based assays, ELISA, FACS staining and analysis, migration or adhesion studies, temperature shift assays, or any work with temperature-sensitive biomarkers.

BioCision

For info: 888-478-2221 | www.biocision.com

PHOSPHOPEPTIDE ENRICHMENT KIT

Recently, titanium dioxide (TiO_2) has been demonstrated to enrich phosphopeptides from complex peptide mixtures. This methodology has provided a solution for this challenging analytical task; however, the technology has not been optimized. Protea Biosciences has improved upon its previously existing TiO_2 product with the release of the new TiO_2 SpinTip Sample Prep Kit (SP-154). This kit contains tips and reagents for the enrichment of phosphopeptides from complex mixtures such as protein digest samples. The reformulated reagent solutions are specially formulated to maximize the retention of phosphorylated peptides, while simultaneously minimizing the retention of nonphosphorylated peptides.

Protea Biosciences

For more info: 877-776-8321 | www.proteabio.com

OXYGEN FLASK COMBUSTION UNIT

The Oxygen Flask Combustion Unit (OFCU-1) provides a highly safe tool for preparing samples for elemental analysis of halogens, sulfur, phosphorus, and a number of metals using the Schöniger flask method. The Schöniger flask method is a well-proven technique for combusting samples prior to elemental analysis by ion chromatography or titration. The durably constructed OFCU-1 copes easily with a wide range of sample types and is very simple to set up, use, and maintain. Built with operator safety in mind, the OFCU-1 remotely ignites samples inside a safety interlocked chamber using focused infrared heat from two tungsten-halogen lamps. Integral pressure vents ensure safe release of excess reaction pressure. A thick black acrylic observation window is provided on the OFCU-1 to allow users to visually check ignition has taken place.

Exeter Analytical

For info: 978-251-1411 | www.exeteranalytical.co.uk

Electronically submit your new product description or product literature information! Go to **www.sciencemag.org/products/newproducts.dtl** for more information.

Newly offered instrumentation, apparatus, and laboratory materials of interest to researchers in all disciplines in academic, industrial, and governmental organizations are featured in this space. Emphasis is given to purpose, chief characteristics, and availability of products and materials. Endorsement by *Science* or AAAS of any products or materials mentioned is not implied. Additional information may be obtained from the manufacturer or supplier.

The Proteomics of Posttranslational Modifications

Unraveling Cellular Signaling Through Mass Spectrometry

Webinar

June 8, 2011

12 noon ET, 9 am PT,
5 pm UK, 6pm CEST

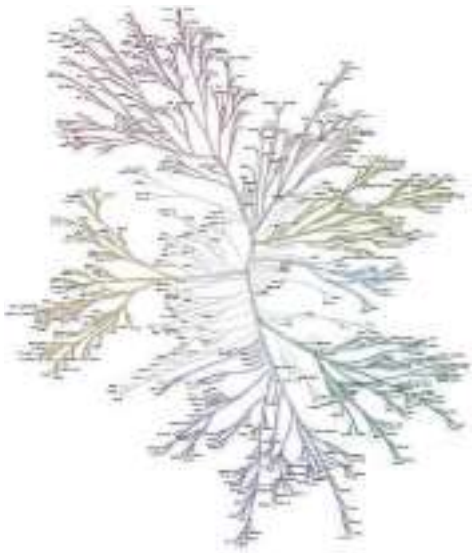

Posttranslational modifications—including phosphorylation, acetylation, and ubiquitination—allow for the fine-tuning of signaling pathways and networks within cells. Mass spectrometry-based proteomics techniques are powerful tools for the investigation of these networks. Dynamic protein phosphorylation is a key cellular regulatory mechanism, and the characterization of global phosphorylation profiles using large-scale proteomic approaches, including antibody-based phosphopeptide enrichment, has proven informative. Acetylation has also been studied using these approaches—as histone deacetylase inhibitors gain clinical importance, the need to better characterize their mechanism of action has accelerated lysine acetylation proteomics research. Further, ubiquitination is gaining growing attention as an important mechanism for both signal transduction and proteolytic degradation. Most recently, new ubiquitin affinity reagents, such as the ubiquitin remnant antibody, have become available, allowing for the identification of hundreds of ubiquitinylated lysine residues in human cells.

During this webinar, viewers will:

- Obtain an overview of posttranslational mechanisms and their role in cellular signaling
- Learn about technologies for studying and characterizing these modifications
- See how the latest technologies are being applied by experts in the field to cellular signaling research
- Have the opportunity to put their question to the expert panel live and in real time.

Participating Experts

Matthias Mann, Ph.D.
Max Planck Institute
of Biochemistry
Martinsried, Germany

Samie Jaffrey, M.D., Ph.D.
Weill Cornell Medical College
New York, NY

Akhilesh Pandey, M.D., Ph.D.
Johns Hopkins Medical Institutes
Baltimore, MD

REGISTER NOW!

Sign Up At:
www.sciencemag.org/webinar

Brought to you by the
AAAS/*Science* Business Office

Science
AAAS

Webinar sponsored by

Cell Signaling
TECHNOLOGY

Efficient protein transfers in 3 minutes.

That's **transferapidly**.

The Trans-Blot® Turbo™ transfer system — the next innovation in protein transfers for western blotting. Get more blots done faster without compromising on performance and transfer efficiency.

Accelerate your western blotting with:

- **Turbo Transfers** — total protein transfer in as little as 3 min using the convenient and ready-to-use Trans-Blot Turbo Transfer Packs
- **Superior Transfer Efficiency** — up to 6x the transfer efficiency compared to the iBlot dry blotting system; efficient transfer of high- and low-MW proteins
- **High Throughput** — transfers up to 4 mini/2 midi gels simultaneously
- **System Flexibility** — can run traditional semi-dry protocols using standard membranes, paper, and buffers

Make the change to our Trans-Blot Turbo system. Call your Bio-Rad sales representative or visit **www.TransBlotTurbo.com**.

Research. Together.

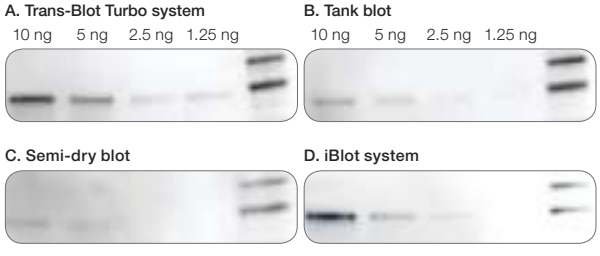

Superior transfer efficiency. Serial dilutions of transferrin were separated on a Criterion™ TGX™ 4–20% gel and transferred using four different techniques. **A**, Trans-Blot Turbo system (25 V for 7 min); **B**, tank blotting (100 V for 30 min); **C**, semi-dry (25 V for 30 min); **D**, iBlot (P3 for 7 min).